SANDIA REPORT

SAND2011-6031
Unlimited Release
Printed August 2011

Atom-to-Continuum Methods for Gaining a Fundamental Understanding of Fracture

Reese E. Jones, Jonathan A. Zimmerman, Jeremy A. Templeton, Xiaowang Zhou, Neville R. Moody, E. David Reedy Jr., Christopher J. Kimmer, Terry J. Delph, Jay Oswald, Ted Belytschko, Jeffrey T. Lloyd, and David L. McDowell

Prepared by
Sandia National Laboratories
Albuquerque, New Mexico 87185 and Livermore, California 94550

Sandia National Laboratories is a multi-program laboratory managed and operated by Sandia Corporation, a wholly owned subsidiary of Lockheed Martin Corporation, for the U.S. Department of Energy's National Nuclear Security Administration under contract DE-AC04-94AL85000.

Issued by Sandia National Laboratories, operated for the United States Department of Energy by Sandia Corporation.

Available to DOE and DOE contractors from
U.S. Department of Energy
Office of Scientific and Technical Information
P.O. Box 62
Oak Ridge, TN 37831

Telephone: (865) 576-8401
Facsimile: (865) 576-5728
E-Mail: reports@adonis.osti.gov
Online ordering: http://www.osti.gov/bridge

Available to the public from
U.S. Department of Commerce
National Technical Information Service
5285 Port Royal Rd
Springfield, VA 22161

Telephone: (800) 553-6847
Facsimile: (703) 605-6900
E-Mail: orders@ntis.fedworld.gov
Online ordering: http://www.ntis.gov/help/ordermethods.asp?loc=7-4-0#online

SAND2011-6031
Unlimited Release
Printed August 2011

Atom-to-Continuum Methods for Gaining a Fundamental Understanding of Fracture

Reese E. Jones, Jonathan A. Zimmerman, Jeremy A. Templeton,
Xiaowang Zhou, Neville R. Moody, E. David Reedy Jr.
Sandia National Laboratories
Livermore, CA 94551
rjones@sandia.gov

Christopher J. Kimmer
Indiana University Southeast
New Albany, IN

Terry J. Delph
Lehigh University
Bethlehem, PA 18015

Jay Oswald, Ted Belytschko
Northwestern University
Evanston, IL 60208

Jeffrey T. Lloyd, David L. McDowell
Georgia Institute of Technology
Atlanta, GA 30332

Abstract

This report describes an Engineering Sciences Research Foundation (ESRF) project to characterize and understand fracture processes via molecular dynamics modeling and atom-to-continuum methods. Under this aegis we developed new theory and a number of novel techniques to describe the fracture process at the atomic scale. These developments ranged from a material-frame connection between molecular dynamics and continuum mechanics to an atomic level **J** integral. Each of the developments build upon each other and culminated in a cohesive zone model derived from atomic information and verified at the continuum scale.

Acknowledgments

We gratefully acknowledge helpful discussions and technical assistance from the following individuals: Douglas J. Bammann, Youping Chen, James W. Foulk III, Robert J. Hardy, Richard B. Lehoucq, Alex J. Lindblad, Alejandro Mota, Steven J. Plimpton, Jeffrey M. Rickman, Aidan P. Thompson, Gregory J. Wagner, and Edmund B. Webb III. Support for this project was provided by Sandia's Engineering Sciences Research Foundation and the Enabling Predictive Simulation Research Institute (EPSRI).

Contents

List of Figures

List of Tables

Chapter 1

Introduction

This report describes an Engineering Sciences Research Foundation (ESRF) project to characterize and understand fracture processes via molecular dynamics modeling and atom-to-continuum methods. The effort is predicated on the idea that processes and information at the atomic level are missing in engineering scale simulations of fracture, and, moreover, are necessary for these simulations to be predictive.

In this project we developed considerable new theory and a number of novel techniques in order to describe the fracture process at the atomic scale. Chapter 2 gives a detailed account of the material-frame connection between molecular dynamics and continuum mechanics we constructed in order to best use atomic information from solid systems. With this framework, in Chapter 3, we were able to make a direct and elegant extension of the classical **J** down to simulations on the scale of nanometers with a discrete atomic lattice. The technique was applied to cracks and dislocations with equal success and displayed high fidelity with expectations from continuum theory. Then, as a prelude to extension of the atomic **J** to finite temperatures, we explored the quasi-harmonic models as efficient and accurate surrogates of atomic lattices undergoing thermo-elastic processes (Chapter 4). With this in hand, in Chapter 5 we provide evidence that, by using the appropriate energy potential, the atomic **J** integral we developed is calculable and accurate at finite/room temperatures. In Chapter 6, we return in part to the fundamental efforts to connect material behavior at the atomic scale to that of the continuum. In this chapter, we devise theory that predicts the onset of instability characteristic of fracture/failure via atomic simulation. In Chapters 7 and 8, we describe the culmination of the project in connecting atomic information to continuum modeling. In these chapters we show that cohesive zone models are: (a) derivable from molecular dynamics in a robust and systematic way, and (b) when used in the more efficient continuum-level finite element technique provide results that are comparable and well-correlated with the behavior at the atomic-scale. Moreover, we show that use of these same cohesive zone elements is feasible at scales very much larger than that of the lattice. Finally, in Chapter 9 we describe our work in developing the efficient non-reflecting boundary conditions necessary to perform transient fracture and shock simulation with molecular dynamics.

Chapter 2

A material frame approach for evaluating continuum variables in atomistic simulations

Principal Authors: Jonathan A. Zimmerman, Reese E. Jones, and Jeremy A. Templeton

In this chapter, we present a material frame formulation analogous to the spatial frame formulation developed by Hardy, whereby expressions for continuum mechanical variables such as stress and heat flux are derived from atomic scale quantities intrinsic to molecular simulation. This formulation is ideally suited for developing an atomistic-to-continuum correspondence for solid mechanics problems. We derive expressions for the first Piola-Kirchhoff (P-K) stress tensor and the material frame heat flux vector directly from the momentum and energy balances using localization functions in a reference configuration. The resulting P-K stress tensor, unlike the Cauchy expression, has no explicit kinetic contribution. The referential heat flux vector likewise lacks the kinetic contribution appearing in its spatial frame counterpart. Using a proof for a special case and molecular dynamics simulations, we show that our P-K stress expression nonetheless represents a full measure of stress that is consistent with both the system virial and the Cauchy stress expression developed by Hardy. We also present an expanded formulation to define continuum variables from micromorphic continuum theory, which is suitable for the analysis of materials represented by directional bonding at the atomic scale.

2.1 Introduction

Continuum theory has been used for decades to analyze and predict the mechanics of materials and structures. However, as technologies shrink to the nanometer range, quantities such as stress and strain become ill defined and the application of continuum mechanics in nanomechanical frameworks becomes suspect. This brings into question whether the traditional design tools used for manufacturing can be applied to micro or nano electro-mechanical systems. And while atomic scale modeling and simulation methods, *e.g.* molecular dynamics, have provided a wealth of information for such systems, the use of such methods has not been standardized. Certainly, the use of continuum mechanics methods would be invaluable provided that clear connections between nanoscale mechanics and engineering scale analysis can be made.

The development of definitions for continuum variables that are calculable within an atomic system has a long and rich history. In the late 19^{th} century, Clausius [31] and Maxwell [125, 126] simultaneously developed the virial theorem (VT) to define the stress applied to the surface of a fixed volume containing interacting particles and a non-zero temperature. Since these initial efforts, there have been many subsequent works to improve on this definition [27, 35, 71, 83, 118, 136, 138, 143, 163, 170, 188, 200, 213–215, 222], most of which have occurred in the last quarter of the 20^{th} century and have continued into the 21^{st} century. The articles cited here have addressed important issues such as the consistency of stress expressions with the mechanical concept of a force acting on a unit area, the validity of an atomic stress based on the VT, and the role of both spatial and time averaging. For brevity, we refer the reader to the discussions in [222] and [200] for more information.

Among these efforts is the notable work by Hardy and colleagues [71–73]. Hardy's formalism uses a finite valued and finite ranged localization function in lieu of the Dirac delta function [83] to establish a self-consistent manner of distributing discrete atomic contributions to thermomechanical fields. While the range and form of the localization function can be selected arbitrarily, the resulting expression for, say, the stress has a certain amount of regularity with varying sized support regions given reasonable choices for the form. Hardy's original formulation is based on the Eulerian or spatial configuration where localization volumes are essentially control volumes fixed in space that matter occupies at a particular time. Hence, Hardy's expressions for stress and heat flux contain both potential (based on derivatives of potential energy) and kinetic (based on the flux of momentum or energy through the localization volume) terms. The validity of kinetic contributions to stress has been an issue of some contention, and has been examined in detail by such authors as Zhou [214] and Murdoch [138].

An alternative approach that obviates the separation of potential and kinetic contributions to stress is to construct a similar formulation to Hardy's in the Lagrangian or material frame. In the material frame, an appropriate stress measure is the 1^{st} Piola-Kirchhoff tensor $\mathbf{P}$, which represents the amount of current force exerted on a unit area as measured in the reference configuration. Expressions to calculate $\mathbf{P}$ have been developed by Andia *et al.* [7, 8, 36, 37]; however, their definition is constructed as a system average, *i.e.* a single value representative of the average stress state for a cell with periodic boundary conditions. In addition, Andia *et al.* make the distinction between internal and external forces, separating the interactions between atoms within the cell and the interactions between atoms with "ghost" atoms located across the periodic boundaries. This distinction is not made in many of the approaches mentioned earlier, and application of this concept is not straightforward for the localization volume framework of Hardy.

In this paper, we present a material frame formulation analogous to the one developed by Hardy for the spatial frame. This formulation relies on a mapping from reference to current positions of material points. It is ideally suited for developing an atomistic-to-continuum correspondence for solid mechanics problems as it contains atom-to-material point mapping functions that need only be calculated once for a given simulation. Also, it easily links to concepts and variables used within continuum constitutive models such as the deformation gradient. In Section 2.2, we derive an expression for P-K stress and the referential heat flux directly from the momentum and energy balances using localization functions in a zero temperature reference configuration. Neither

the P-K stress nor the referential heat flux vector have explicit dependence on kinetic energy. Nevertheless, we demonstrate that the derived P-K stress is consistent with the Hardy expression for Cauchy stress using a proof based on a system average in Section 2.2.4, as well as pointing out the obvious connection between the continuum versions of these two quantities which are derived directly from the appropriate balance laws. Furthermore, we employ molecular dynamics simulations discussed in Section 2.3 to verify that our stress expression is consistent even for systems where the kinetic portion of the Cauchy stress is a significant fraction of the total value. As a further extension of this work, we also present an expanded formulation to define continuum variables from micromorphic continuum theory in Section 2.4. This extension relies crucially on the Lagrangian framework we develop and shows that our formulation is useful for the analysis of materials represented by directional bonding at the atomic scale.

2.2 Formulation for Standard Continuum Mechanics

Before we begin our formulation, we define the notation for spatial and temporal derivatives and operators used in this paper. Letting the notations $\widetilde{\mathbf{g}}$ and $\hat{\mathbf{g}}$ refer to $\mathbf{g}$ as a function of the spatial coordinate $\mathbf{x}$ or the material coordinate $\mathbf{X}$, respectively, we can write $\mathbf{g} = \widetilde{\mathbf{g}}(\mathbf{x},t) = \widetilde{\mathbf{g}}(\hat{\mathbf{x}}(\mathbf{X},t),t) = \hat{\mathbf{g}}(\mathbf{X},t)$, for any scalar, vector or tensor function $\mathbf{g}$. With this notation we can define the spatial frame and material frame divergences to be $\nabla_{\mathbf{x}} \cdot \widetilde{\mathbf{g}}$ and $\nabla_{\mathbf{X}} \cdot \hat{\mathbf{g}}$, and likewise define the spatial frame and material frame gradients as $\nabla_{\mathbf{x}}\widetilde{\mathbf{g}}$ and $\nabla_{\mathbf{X}}\hat{\mathbf{g}}$. In the following, this explicit notation will not be used; rather, it will be clear from context whether the field referred to is a function of the spatial configuration or the material configuration, as is customary in the continuum mechanics literature, *e.g.* [68, 119]. Also, it is understood that if $\mathbf{g}(\mathbf{X},t)$ is a tensor of "mixed" character, *e.g.* the 1^{st} Piola-Kirchhoff stress tensor, then the expression $\nabla_{\mathbf{X}} \cdot \mathbf{g}$ is defined to be consistent with the index notation $g_{iJ,J}$, where lower-case Roman letters denote spatial frame indices and upper-case Roman letters denote material frame indices, with both types of subscripts referring to the Cartesian coordinate components of vector or tensor quantities. Regarding derivatives in time, we express the partial time derivative of $\widetilde{\mathbf{g}}(\mathbf{x},t)$ as $\frac{\partial \mathbf{g}}{\partial t} \equiv \left.\frac{\partial \mathbf{g}}{\partial t}\right|_{\mathbf{x}}$ and the full or material time derivative as $\frac{d\mathbf{g}}{dt} \equiv \left.\frac{\partial \mathbf{g}}{\partial t}\right|_{\mathbf{X}}$. As usual, these two time derivatives are related through the expression $\frac{d\mathbf{g}}{dt} = \frac{\partial \mathbf{g}}{\partial t} + \nabla_{\mathbf{x}}\mathbf{g} \cdot \mathbf{v}$.

2.2.1 Balance Laws

We begin by modifying Hardy's formulation for the Lagrangian or material frame. Hardy's work uses the balance equations for mass, linear momentum and energy. These are expressed in a spatial configuration as follows:

$$\frac{\partial \rho}{\partial t} + \nabla_{\mathbf{x}} \cdot (\rho \mathbf{v}) = 0 \tag{2.1}$$

$$\frac{\partial (\rho \mathbf{v})}{\partial t} = \nabla_{\mathbf{x}} \cdot (\boldsymbol{\sigma} - \rho \mathbf{v} \otimes \mathbf{v}) + \rho \mathbf{b} \tag{2.2}$$

$$\frac{\partial(\rho e)}{\partial t} = \nabla_{\mathbf{x}} \cdot (\boldsymbol{\sigma} \cdot \mathbf{v} - \rho e \mathbf{v} - \mathbf{q}) + \rho \mathbf{b} \cdot \mathbf{v} + \rho h \tag{2.3}$$

These expressions can be manipulated to use the full or material time derivative $\frac{d}{dt}$ instead of the partial time derivative $\frac{\partial}{\partial t}$:

$$\frac{d\rho}{dt} + \rho \nabla_{\mathbf{x}} \cdot \mathbf{v} = 0 \tag{2.4}$$

$$\rho \frac{d\mathbf{v}}{dt} = \nabla_{\mathbf{x}} \cdot \boldsymbol{\sigma} + \rho \mathbf{b} \tag{2.5}$$

$$\rho \frac{d\varepsilon}{dt} = \boldsymbol{\sigma} : \nabla_{\mathbf{x}} \mathbf{v} - \nabla_{\mathbf{x}} \cdot \mathbf{q} + \rho h \tag{2.6}$$

In equations (2.1) through (2.6) ρ is mass density, $\mathbf{v}$ is velocity, $\boldsymbol{\sigma}$ is Cauchy stress, $\mathbf{b}$ is body force per unit mass, e is total energy per unit mass, ε is internal energy per unit mass (total energy contains contributions from both internal energy and continuum kinetic energy: $e = \varepsilon + \frac{1}{2}v^2$), $\mathbf{q}$ is heat flux and h is energy generation per unit mass. Equations (2.1) - (2.3) are commonly used in fluid dynamics analyses whereas equations (2.4) - (2.6) are typically used to solve solid mechanics problems. Nevertheless, the variables used within all of these equations are defined with respect to the current/spatial configuration, *i.e.* variables are functions of spatial coordinate $\mathbf{x}$ and time t.

These variables and equations can also be expressed with respect to the reference/material configuration:

$$\frac{d\rho_0}{dt} = 0 \tag{2.7}$$

$$\rho_0 \frac{d\mathbf{v}}{dt} = \nabla_{\mathbf{X}} \cdot \mathbf{P} + \rho_0 \mathbf{b} \tag{2.8}$$

$$\rho_0 \frac{d\varepsilon}{dt} = \mathbf{P} : \frac{d\mathbf{F}}{dt} - \nabla_{\mathbf{X}} \cdot \mathbf{Q} + \rho_0 h \tag{2.9}$$

In these equations, ρ_0 is reference mass density (mass per unit reference volume), $\mathbf{P}$ is 1^{st} Piola-Kirchhoff stress (force per unit reference area), $\mathbf{F}$ is the deformation gradient ($\frac{\partial \mathbf{x}}{\partial \mathbf{X}}$), and $\mathbf{Q}$ is the reference heat flux (energy per unit reference area per unit time). These variables in equations (2.7)-(2.9) are all functions of the reference coordinate $\mathbf{X}$ and time t, with the material time derivative retaining its earlier definition, $\frac{d\mathbf{g}(\mathbf{X},t)}{dt} = \left.\frac{\partial \mathbf{g}}{\partial t}\right|_{\mathbf{X}}$. Although different in form and functional dependencies, all three sets of equations, (2.1)-(2.3), (2.4)-(2.6), and (2.7)-(2.9), represent the same fundamental balance laws and are derivable from one another as shown in standard texts on continuum mechanics, *e.g.* [68, 119].

2.2.2 Densities and Localization

We consider a body to be a system of N atoms which are interacting with each other through some inter-atomic potential energy formulation. Each atom α is characterized by its mass m^α, its position in the reference configuration $\mathbf{X}^\alpha$, its position in the current configuration $\mathbf{x}^\alpha(t)$, its velocity $\mathbf{v}^\alpha(t) = \frac{d\mathbf{x}^\alpha}{dt}$, and a displacement $\mathbf{u}^\alpha(t) \equiv \mathbf{x}^\alpha(t) - \mathbf{X}^\alpha$. Herein, any superscripted, lowercase Greek letter will be used to refer to a particular atom.

In Hardy's formulation, two views of the material system are considered. One perspective is the continuum, where quantities are point-wise functions of time and position. These quantities include mass density $\rho_0(\mathbf{X},t)$, momentum density $\mathbf{p}_0(\mathbf{X},t)$, and energy density $\rho_0 e(\mathbf{X},t)$. The other perspective is that the material system contains atoms, each of which has its own mass, momentum, potential energy and kinetic energy. In order to connect the two views, Hardy uses a localization function ψ which spatially averages the properties of the atoms, and allows many atoms to contribute to a continuum property at a specific position and time. In his original formulation, Hardy expressed ψ as a function of current position. In our derivation, we instead choose it to be a function of reference position. The three key relations analogous to Hardy's spatial forms are:

$$\rho_0(\mathbf{X}) = \sum_{\alpha=1}^{N} m^\alpha \psi(\mathbf{X}^\alpha - \mathbf{X}) \tag{2.10}$$

$$\mathbf{p}_0(\mathbf{X},t) = \sum_{\alpha=1}^{N} m^\alpha \mathbf{v}^\alpha \psi(\mathbf{X}^\alpha - \mathbf{X}) \tag{2.11}$$

$$\rho_0(\mathbf{X}) e(\mathbf{X},t) = \sum_{\alpha=1}^{N} \left\{ \frac{1}{2} m^\alpha (v^\alpha)^2 + \phi^\alpha \right\} \psi(\mathbf{X}^\alpha - \mathbf{X}). \tag{2.12}$$

A few important things to note:

- The localization function $\psi(\mathbf{r})$ is non-negative,[1] *i.e.* $\psi(\mathbf{r}) \geq 0$.
- $\psi(\mathbf{r})$ has dimensions of inverse volume.
- $\psi(\mathbf{r})$ is a normalized function, thus

  $$\int_\Omega \psi(\mathbf{r}) d^3 r = 1, \tag{2.13}$$

  where $\Omega \subset R^3$ is the domain of interest containing the collection of atoms.
- In equation (2.12), the total potential energy density of the system is expressed as the summation of individual atomic potential energies, ϕ_α.
- The velocity field $\mathbf{v}$ is defined by the expression

  $$\mathbf{v}(\mathbf{X},t) \equiv \frac{\mathbf{p}_0(\mathbf{X},t)}{\rho_0(\mathbf{X})} = \frac{\sum_{\alpha=1}^{N} m^\alpha \mathbf{v}^\alpha \psi(\mathbf{X}^\alpha - \mathbf{X})}{\sum_{\alpha=1}^{N} m^\alpha \psi(\mathbf{X}^\alpha - \mathbf{X})}. \tag{2.14}$$

  which is effectively a mass weighted average. With velocity defined in this manner, the displacement field $\mathbf{u}$ can be defined as

  $$\mathbf{u}(\mathbf{X},t) = \frac{\sum_{\alpha=1}^{N} m^\alpha \mathbf{u}^\alpha \psi(\mathbf{X}^\alpha - \mathbf{X})}{\sum_{\alpha=1}^{N} m^\alpha \psi(\mathbf{X}^\alpha - \mathbf{X})}, \tag{2.15}$$

[1] While it is possible to choose localization functions that are not non-negative (as discussed on p. 77 of [137]), in practice this is rarely done as it contains the potential to admit unbounded values for the extremum. In such instances, additional regularity requirements are needed.

which is consistent with the velocity field defined in (2.14), *i.e.* $\mathbf{v} = \frac{d\mathbf{u}}{dt}$. With a displacement field we can construct the motion of material points $\mathbf{X}$ from reference to current configuration as a function of time in the usual way $\mathbf{x}(\mathbf{X},t) = \mathbf{X} + \mathbf{u}(\mathbf{X},t)$. Furthermore, we can apply the differential operator $\nabla_{\mathbf{X}}$ to (2.15) to define a displacement gradient,

$$\nabla_{\mathbf{X}}\mathbf{u} = \frac{\sum_{\alpha=1}^{N} m^{\alpha}\left(\mathbf{u}^{\alpha} - \mathbf{u}(\mathbf{X},t)\right) \otimes \nabla_{\mathbf{X}}\psi(\mathbf{X}^{\alpha} - \mathbf{X})}{\sum_{\alpha=1}^{N} m^{\alpha}\psi(\mathbf{X}^{\alpha} - \mathbf{X})}, \tag{2.16}$$

which then can be used to form a locally defined deformation gradient $\mathbf{F}(\mathbf{X},t) = \mathbf{1} + \nabla_{\mathbf{X}}\mathbf{u}$. However, this use of Hardy localization places additional requirements on the smoothness and exact form of ψ. For example, a so-called "top hat" or radial Heaviside function that is constant and non-zero only in compact region would not produce smooth, continuous displacement gradients.

The question arises: can one relate a Lagrangian/referential field $\hat{g}(\mathbf{X},t)$ derived from atomic data to an Eulerian/spatial field $\tilde{g}(\mathbf{x},t)$ derived from the same data. First, let us examine the mass density starting with the referential definition (2.10). To map this referential function into a spatial one we need to transform the localization function ψ and its base point $\mathbf{X}$ to the current configuration. Given a reference configuration for the atoms $\{\mathbf{X}^{\alpha}\}$, which defines the atomic displacements $\mathbf{u}^{\alpha}(t) = \mathbf{x}^{\alpha}(t) - \mathbf{X}^{\alpha}$, we can construct the continuum/coarse-scale motion $\mathbf{x}(\mathbf{X},t) = \mathbf{u}(\mathbf{X},t) + \mathbf{X}$ from the field $\mathbf{u}$ defined by Equation (2.15). Then

$$\psi_{\mathbf{X}} = \psi_{\mathbf{X}(\mathbf{x},t)} \equiv \psi^{t}_{\mathbf{x}} \tag{2.17}$$

where $\psi^{t}_{\mathbf{x}}$ is the deformed version of $\psi_{\mathbf{X}}$ which is not equivalent to $\psi_{\mathbf{x}}$ in general, please refer to the schematic in Figure 2.1. Here, we have introduced new notation, e.g. $\psi_{\mathbf{X}}(\mathbf{X}^{\alpha}) = \psi(\mathbf{X}^{\alpha} - \mathbf{X})$, to make clear that the function ψ on $\mathbb{R}^3$ transforms differently than its argument $\mathbf{X}^{\alpha}$ in going from reference to current configuration, *i.e.* the kernel transforms with the displacement field and the atoms follow their particular trajectory. To first order, *i.e.* where the kernel radius is small enough relative to the spatial gradient of the motion $\mathbf{F}$,

$$\int_{\Omega_0} \psi_{\mathbf{X}}(\mathbf{Y})\, d^3Y = \int_{\Omega} \psi^{t}_{\mathbf{x}}(\mathbf{y}) \frac{1}{\det\mathbf{F}}\, d^3y \approx \frac{1}{\det\mathbf{F}} \int_{\Omega} \psi^{t}_{\mathbf{x}}(\mathbf{y})\, d^3y \tag{2.18}$$

and $(\det\mathbf{F})\psi_{\mathbf{x}} \approx \psi^{t}_{\mathbf{x}}$ since $\int_{\Omega_0} \psi_{\mathbf{X}}(\mathbf{X})\, d^3X = \int_{\Omega} \psi_{\mathbf{x}}(\mathbf{x})\, d^3x = 1$. With this in hand, we have the usual relation between referential and spatial mass density

$$\rho_0(\mathbf{X}) = \sum_{\alpha=1}^{N} m^{\alpha}\psi_{\mathbf{X}}(\mathbf{X}^{\alpha}) = \sum_{\alpha=1}^{N} m^{\alpha}\psi^{t}_{\mathbf{x}}(\mathbf{x}^{\alpha}) \approx \det\mathbf{F} \sum_{\alpha=1}^{N} m^{\alpha}\psi_{\mathbf{x}}(\mathbf{x}^{\alpha}) = \det\mathbf{F}(\mathbf{X},t)\, \rho(\mathbf{X},t) \tag{2.19}$$

This derivation can also be directly applied to the momentum and energy densities which were defined as primary fields in (2.11) and (2.12). Please note that, despite the mapping of $\psi_{\mathbf{X}}$ to $\psi^{t}_{\mathbf{x}}$ by the coarse-scale motion, the same atoms may not contribute to the density of corresponding points $\mathbf{X}$ and $\mathbf{x}$. For solids,[2] where the discrepancies in coarse motion $\mathbf{x}(\mathbf{X}^{\alpha},t)$ and the atomic trajectory

[2]Fluids and granular materials will be touched on in the Discussion at the end of the paper.

$\mathbf{x}^\alpha(t)$ are small and of a thermal nature, there should not be significant changes in the set of atoms that contribute the densities calculated with $\psi_{\mathbf{X}}$ or $\psi^t_{\mathbf{x}}$.[3] Now turning to the derived velocity (2.14) and displacement (2.15) fields, we see that they are simply ratios of the momentum to mass density and hence the determinant factors $\det\mathbf{F}$ drop out so that

$$\hat{\mathbf{u}}(\mathbf{X},t) = \frac{\sum_{\alpha=1}^N m^\alpha \mathbf{u}^\alpha \psi_{\mathbf{X}}(\mathbf{X}^\alpha)}{\sum_{\alpha=1}^N m^\alpha \psi_{\mathbf{X}}(\mathbf{X}^\alpha)} = \frac{\sum_{\alpha=1}^N m^\alpha \mathbf{u}^\alpha \psi^t_{\mathbf{x}}(\mathbf{x}^\alpha)}{\sum_{\alpha=1}^N m^\alpha \psi^t_{\mathbf{x}}(\mathbf{x}^\alpha)} \approx \frac{\det\mathbf{F}\sum_{\alpha=1}^N m^\alpha \mathbf{u}^\alpha \psi_{\mathbf{x}}(\mathbf{x}^\alpha)}{\det\mathbf{F}\sum_{\alpha=1}^N m^\alpha \psi_{\mathbf{x}}(\mathbf{x}^\alpha)} = \tilde{\mathbf{u}}(\mathbf{x},t) \quad (2.20)$$

for instance. As will be made clear in Section 2.2.4, the connection between Lagrangian and Eulerian fluxes such as stress, is made through the correspondence between the continuum balance laws (2.1-2.3) and (2.7-2.9).

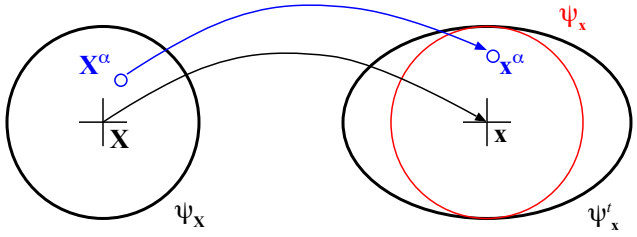

Figure 2.1. Schematic showing the motion of atom $\alpha : \mathbf{X}^\alpha \to \mathbf{x}^\alpha$ and a nearby point $\mathbf{X} \to \mathbf{x}$. Also shown are the support of the localization function in the reference configuration $\psi_{\mathbf{X}}$ and its image in the current $\psi^t_{\mathbf{x}}$ which is subject to deformation. For comparison the undeformed kernel $\psi_{\mathbf{x}}$ identical to $\psi_{\mathbf{X}}$ but centered at $\mathbf{x}$ in the current configuration is also shown.

On closing this section, we note that in his earlier works [71, 73], Hardy established an important property of the localization function ψ. Given regularity of ψ, a bond function $B^{\alpha\beta}(\mathbf{X})$ between atoms α and β can be defined by the expression

$$B^{\alpha\beta}(\mathbf{X}) \equiv \int_0^1 \psi(\lambda\mathbf{X}^{\alpha\beta} + \mathbf{X}^\beta - \mathbf{X})d\lambda, \quad (2.21)$$

where $\mathbf{X}^{\alpha\beta} = \mathbf{X}^\alpha - \mathbf{X}^\beta$. By taking the derivative of $\psi(\lambda\mathbf{X}^{\alpha\beta} + \mathbf{X}^\beta - \mathbf{X})$ with respect to λ,

$$\frac{\partial\psi(\lambda\mathbf{X}^{\alpha\beta} + \mathbf{X}^\beta - \mathbf{X})}{\partial\lambda} = -\mathbf{X}^{\alpha\beta}\cdot\nabla_{\mathbf{X}}\psi(\lambda\mathbf{X}^{\alpha\beta} + \mathbf{X}^\beta - \mathbf{X}), \quad (2.22)$$

and then integrating from $\lambda = 0$ to $\lambda = 1$, one obtains the identity:

$$\psi(\mathbf{X}^\alpha - \mathbf{X}) - \psi(\mathbf{X}^\beta - \mathbf{X}) = -\mathbf{X}^{\alpha\beta}\cdot\nabla_{\mathbf{X}}B^{\alpha\beta}(\mathbf{X}). \quad (2.23)$$

We will revisit the connection between the bond function in the reference and current configuration in Section 2.2.4.

[3] An alternate viewpoint considering only the transformation of discrete values of the localization function following the trajectories of the relevant atoms $\psi_{\mathbf{X}}(\mathbf{X}_\alpha)$ from the reference to current, would not lead to any change in the set of atoms but says nothing about points in space not occupied by atoms nor provides a simple route to (2.18).

2.2.3 Energy and Force Assumptions

Hardy makes four key assumptions about the forms of the energies of, and forces on, the atoms in the system. The first is that the total potential energy of the system, Φ, can be considered to be the summation of individual potential energies of each atom within the system,

$$\Phi = \sum_{\alpha=1}^{N} \phi^{\alpha}. \tag{2.24}$$

The usual procedure for constructing ϕ^{α} is to partition the energies per bond to each of the constituent atoms such that the partition factors add to one.

The second assumption is that the force on any atom can be expressed by the summation

$$\mathbf{f}^{\alpha} \equiv -\frac{\partial \Phi}{\partial \mathbf{x}^{\alpha}} = \sum_{\beta \neq \alpha}^{N} \mathbf{f}^{\alpha\beta}. \tag{2.25}$$

Although it is not always clear what the physical meaning of $\mathbf{f}^{\alpha\beta}$ is, this partition can always be made. When Φ is the summation of pair potentials, $\phi^{\alpha} = \frac{1}{2}\sum_{\beta\neq\alpha}^{N} \phi^{\alpha\beta}(x^{\alpha\beta})$ where $x^{\alpha\beta} = \|\mathbf{x}^{\alpha\beta}\|$ and $\mathbf{x}^{\alpha\beta} \equiv \mathbf{x}^{\alpha} - \mathbf{x}^{\beta}$, or for the Embedded Atom Method (EAM) [57], $\mathbf{f}^{\alpha\beta}$ obviously means the force exerted on atom α by atom β. However, for some multi-body potentials, such as the 3-body term in the Stillinger-Weber potential [177], the meaning is not so straight-forward; nevertheless, the force partition (2.25) can be constructed. This partition is not unique; more discussion of this fact will be given in Sections 2.2.4 and 2.4.3.

The third assumption Hardy makes is that the atomic potential energies depend only on the relative inter-atomic distances, $\phi^{\alpha} = \phi^{\alpha}(x^{\alpha\beta}, x^{\alpha\gamma}, \ldots, x^{\beta\gamma})$, so

$$\mathbf{f}^{\alpha} = -\sum_{\beta\neq\alpha}^{N} \frac{\partial \Phi}{\partial x^{\alpha\beta}} \frac{\mathbf{x}^{\alpha\beta}}{x^{\alpha\beta}} = -\sum_{\beta\neq\alpha}^{N}\sum_{\gamma=1}^{N} \frac{\partial \phi^{\gamma}}{\partial x^{\alpha\beta}} \frac{\mathbf{x}^{\alpha\beta}}{x^{\alpha\beta}}. \tag{2.26}$$

This expression includes the possibility that $\alpha = \gamma$. While it is clear that radially-symmetric potentials such as Lennard-Jones [109, 110] and EAM satisfy this assumption, it is also true that potential energies that depend on bond orientations satisfy this as well. For the 3-body term in the Stillinger-Weber potential [177], it can be shown by way of the law of cosines, which relates the bond angles to relative inter-atomic distances, that this third assumption is valid.

Finally, the fourth assumption made is that each atomic potential energy depends only on the distances between the atom under consideration and all other atoms, $\phi^{\alpha} = \phi^{\alpha}(x^{\alpha\beta}, x^{\alpha\gamma}, \ldots, x^{\alpha N})$. Thus, the force between atoms α and β can be expressed as

$$\mathbf{f}^{\alpha\beta} = -\left\{ \frac{\partial \phi^{\alpha}}{\partial x^{\alpha\beta}} + \frac{\partial \phi^{\beta}}{\partial x^{\alpha\beta}} \right\} \frac{\mathbf{x}^{\alpha\beta}}{x^{\alpha\beta}} = -\mathbf{f}^{\beta\alpha}. \tag{2.27}$$

Clearly, while pair potentials and EAM qualify for this assumption, the potential of Stillinger-Weber does not since the angle between atoms α, β, γ depends on all three relative distances including $x^{\beta\gamma}$. This should in no-way imply that the quantity $\mathbf{f}^{\alpha\beta}$ cannot be defined. Rather, we

merely note that for some choices of inter-atomic potential Hardy's fourth assumption does not appear to be applicable. This point will be further addressed in Section 2.4.

2.2.4 Derivation of Continuum Expressions

Here we apply the kinematic definitions (2.10-2.12) to the balance laws (2.7-2.9) in order to define the referential fluxes of stress and heat. We also make connections between these fluxes and their spatial counterparts through the well-known Piola transform which is ultimately derived from the relations between the respective balance laws, (2.7-2.9) and (2.1-2.3).

Balance of Mass

Inspection of equation (2.10) reveals that

$$\frac{d\rho_0}{dt} = 0,$$

since locations of atoms in the reference configuration, $\{\mathbf{X}^\alpha\}$, are fixed.

Balance of Linear Momentum

Starting with Hardy's expression for momentum density (2.11),

$$\begin{aligned}\rho_0 \frac{d\mathbf{v}}{dt} = \frac{d\mathbf{p}_0}{dt} &= \frac{d}{dt}\left\{\sum_{\alpha=1}^{N} m^\alpha \mathbf{v}^\alpha \psi(\mathbf{X}^\alpha - \mathbf{X})\right\} \\ &= \sum_{\alpha=1}^{N} m^\alpha \frac{d\mathbf{v}^\alpha}{dt}\psi(\mathbf{X}^\alpha - \mathbf{X}) \\ &= \sum_{\alpha=1}^{N} \left(\mathbf{f}^\alpha + m^\alpha \mathbf{b}^\alpha\right)\psi(\mathbf{X}^\alpha - \mathbf{X}),\end{aligned}$$

where we have applied Newton's 2^{nd} law for each atom and divided the total force on atom α into the sum of total internal force $\mathbf{f}^\alpha$ and the body force $m^\alpha \mathbf{b}^\alpha$. The internal force term on the RHS of the above expression can be combined with Hardy's second force assumption to obtain,

$$\sum_{\alpha=1}^{N} \mathbf{f}^\alpha \psi(\mathbf{X}^\alpha - \mathbf{X}) = \sum_{\alpha=1}^{N}\sum_{\beta\neq\alpha}^{N} \mathbf{f}^{\alpha\beta}\psi(\mathbf{X}^\alpha - \mathbf{X}).$$

Since α and β run over all atoms in the system, they are considered dummy indices and can be switched. By doing this, and using the symmetry condition, (2.27), one obtains

$$\sum_{\alpha=1}^{N} \mathbf{f}^\alpha \psi(\mathbf{X}^\alpha - \mathbf{X}) = \frac{1}{2}\sum_{\alpha=1}^{N}\sum_{\beta\neq\alpha}^{N} \mathbf{f}^{\alpha\beta}\left(\psi(\mathbf{X}^\alpha - \mathbf{X}) - \psi(\mathbf{X}^\beta - \mathbf{X})\right).$$

Using this with expression (2.23), the time derivative of the momentum density becomes

$$\rho_0 \frac{d\mathbf{v}}{dt} = \sum_{\alpha=1}^{N} \left(\frac{1}{2} \sum_{\beta \neq \alpha}^{N} \mathbf{f}^{\alpha\beta} \left(-\mathbf{X}^{\alpha\beta} \cdot \nabla_{\mathbf{X}} B^{\alpha\beta}(\mathbf{X}) \right) + m^{\alpha} \mathbf{b}^{\alpha} \psi(\mathbf{X}^{\alpha} - \mathbf{X}) \right) \tag{2.28}$$

$$= \nabla_{\mathbf{X}} \cdot \left(-\frac{1}{2} \sum_{\alpha=1}^{N} \sum_{\beta \neq \alpha}^{N} \mathbf{f}^{\alpha\beta} \otimes \mathbf{X}^{\alpha\beta} B^{\alpha\beta}(\mathbf{X}) \right) + \sum_{\alpha=1}^{N} m^{\alpha} \mathbf{b}^{\alpha} \psi(\mathbf{X}^{\alpha} - \mathbf{X}). \tag{2.29}$$

Comparing equation (2.29) with the continuum balance of momentum (2.8), we observe that in order for these expressions to be consistent with one another,

$$\mathbf{P}(\mathbf{X},t) = -\frac{1}{2} \sum_{\alpha=1}^{N} \sum_{\beta \neq \alpha}^{N} \mathbf{f}^{\alpha\beta} \otimes \mathbf{X}^{\alpha\beta} B^{\alpha\beta}(\mathbf{X}), \tag{2.30}$$

and

$$\mathbf{b}(\mathbf{X},t) = \frac{1}{\rho_0(\mathbf{X})} \sum_{\alpha=1}^{N} m^{\alpha} \mathbf{b}^{\alpha} \psi(\mathbf{X}^{\alpha} - \mathbf{X}) = \frac{\sum_{\alpha=1}^{N} m^{\alpha} \mathbf{b}^{\alpha} \psi(\mathbf{X}^{\alpha} - \mathbf{X})}{\sum_{\alpha=1}^{N} m^{\alpha} \psi(\mathbf{X}^{\alpha} - \mathbf{X})}. \tag{2.31}$$

For pair and other central force potentials (e.g., EAM),

$$\mathbf{P} = \frac{1}{2} \sum_{\alpha=1}^{N} \sum_{\beta \neq \alpha}^{N} \left\{ \frac{\partial \phi^{\alpha}}{\partial x^{\alpha\beta}} + \frac{\partial \phi^{\beta}}{\partial x^{\alpha\beta}} \right\} \frac{\mathbf{x}^{\alpha\beta} \otimes \mathbf{X}^{\alpha\beta}}{x^{\alpha\beta}} B^{\alpha\beta}(\mathbf{X}). \tag{2.32}$$

This expression can be further simplified by splitting this expression into two terms, switching the dummy indices used in one of the terms, and using the relations $x^{\beta\alpha} = x^{\alpha\beta}$, $\mathbf{x}^{\beta\alpha} = -\mathbf{x}^{\alpha\beta}$, $\mathbf{X}^{\beta\alpha} = -\mathbf{X}^{\alpha\beta}$ and $B^{\beta\alpha} = B^{\alpha\beta}$ to obtain

$$\mathbf{P} = \sum_{\alpha=1}^{N} \sum_{\beta \neq \alpha}^{N} \frac{\partial \phi^{\beta}}{\partial x^{\alpha\beta}} \frac{\mathbf{x}^{\alpha\beta} \otimes \mathbf{X}^{\alpha\beta}}{x^{\alpha\beta}} B^{\alpha\beta}(\mathbf{X}). \tag{2.33}$$

It is interesting to note that equation (2.30) shows that $\mathbf{P}$ is connected to the underlying atomic displacements through the inter-atomic forces $\mathbf{f}^{\alpha\beta}$. It is also through this connection that $\mathbf{P}$ is implicitly dependent on thermal motion of the atomic system. Our expression defines stress without the need to necessarily define a deformation gradient field or a hyperelastic stored energy function.

Also note that equation (2.30) contains only force terms on the right-hand side; no explicit dependence on velocity is present,[4] unlike the Cauchy stress expression

$$\boldsymbol{\sigma}(\mathbf{x},t) = -\frac{1}{2} \sum_{\alpha=1}^{N} \sum_{\beta \neq \alpha}^{N} \mathbf{f}^{\alpha\beta} \otimes \mathbf{x}^{\alpha\beta} \tilde{B}^{\alpha\beta}(\mathbf{x}) - \sum_{\alpha=1}^{N} m^{\alpha} \mathbf{w}^{\alpha} \otimes \mathbf{w}^{\alpha} \tilde{\psi}(\mathbf{x}^{\alpha} - \mathbf{x}) \tag{2.34}$$

from the Eulerian analysis [71, 73]. The relative velocity $\mathbf{w}^{\alpha}$ is defined

$$\mathbf{w}^{\alpha}(\mathbf{x},t) \equiv \mathbf{v}^{\alpha} - \mathbf{v}(\mathbf{x},t) \ . \tag{2.35}$$

[4]The P-K expression (2.30) also differs from the Cauchy expression (2.34) in that it gives a zero value for the somewhat degenerate case of a non-interacting gas regardless of temperature.

and has the property

$$\sum_{\alpha=1}^{N} m^{\alpha}\mathbf{w}^{\alpha}\tilde{\psi}(\mathbf{x}^{\alpha}-\mathbf{x}) = \mathbf{0} \tag{2.36}$$

by virtue of the Eulerian analogue of the definition (2.14). Note that $\tilde{\psi}$ and $\tilde{B}$ are the localization and bond functions expressed in units of inverse current/deformed volume rather than units of inverse reference/undeformed volume.

In addition to the well-known connection between the continuum measures of stress, $\mathbf{P}$ and $\boldsymbol{\sigma}$, we now show that our expression for $\mathbf{P}$ given in equation (2.30) can be directly related to Hardy's Cauchy stress expression (2.34) in a manner consistent with this connection. Given the continuum Piola transformation[5] from 1^{st} P-K stress to Cauchy stress, $\boldsymbol{\sigma} = \frac{1}{J}\mathbf{P}\cdot\mathbf{F}^{T}$ where $J \equiv \det\mathbf{F}$, we produce

$$\frac{1}{J}\mathbf{P}\cdot\mathbf{F}^{T} = -\frac{1}{J}\sum_{\alpha=1}^{N}\sum_{\beta\neq\alpha}^{N}\frac{1}{2}\mathbf{f}^{\alpha\beta}\otimes\mathbf{X}^{\alpha\beta}B^{\alpha\beta}(\mathbf{X})\cdot\mathbf{F}^{T}. \tag{2.37}$$

In order to simplify this equation, we assert that the position of each atom can be decomposed into a rigid body translation, $\mathbf{r}(t)$, a homogeneous deformation $\mathbf{F}$ relative to the material point $\mathbf{X}$, plus a perturbation due to thermal fluctuations and/or inhomogeneities in the deformation field,

$$\mathbf{x}^{\alpha} = \mathbf{r}(t) + \mathbf{F}(\mathbf{X},t)\cdot\mathbf{X}^{\alpha} + \mathbf{z}^{\alpha}(\mathbf{X},t), \tag{2.38}$$

where $\mathbf{z}^{\alpha}$ is merely the remainder of $\mathbf{x}^{\alpha}$ with respect to the expansion of $\mathbf{x}^{\alpha}$ to first order in $\mathbf{X}^{\alpha}$. We define $\boldsymbol{\Xi}^{\alpha} = \mathbf{X}^{\alpha} - \mathbf{X}$ where now $\mathbf{X}$ satisfies the relation

$$\mathbf{X} = \frac{1}{\rho_0(\mathbf{X})}\sum_{\alpha=1}^{N} m^{\alpha}\mathbf{X}^{\alpha}\psi(\mathbf{X}^{\alpha}-\mathbf{X}). \tag{2.39}$$

This relation enforces the restriction that material points $\mathbf{X}$ coincide with the centers of mass of the localization volumes they are associated with. This restriction apparently makes the selection of material points $\mathbf{X}$ non-trivial since (2.39) is an implicit relationship. However, since most crystal structures possess a high degree of symmetry, especially if an undeformed, defect-free configuration is used as a reference state, immediate selection of the appropriate locations of material points is possible and can be as dense as the lattice itself. Equation (2.39) allows us to write

$$\mathbf{v}^{\alpha} = \frac{d\mathbf{r}}{dt} + \frac{d\mathbf{F}}{dt}\cdot\mathbf{X}^{\alpha} + \frac{d\mathbf{z}}{dt}^{\alpha} = \frac{d\mathbf{r}}{dt} + \frac{d\mathbf{F}}{dt}\cdot\mathbf{X} + \frac{d\mathbf{F}}{dt}\cdot\boldsymbol{\Xi}^{\alpha} + \frac{d\mathbf{z}}{dt}^{\alpha} \tag{2.40}$$

and then to identify

$$\mathbf{w}^{\alpha} = \frac{d\mathbf{F}}{dt}\boldsymbol{\Xi}^{\alpha} + \frac{d\mathbf{z}}{dt}^{\alpha} \tag{2.41}$$

with the part of the velocity $\mathbf{v}^{\alpha}$ that satisfies (2.36). Since $\mathbf{x}^{\alpha\beta} = \mathbf{F}\cdot\mathbf{X}^{\alpha\beta} + \mathbf{z}^{\alpha\beta}$, we can recast (2.37)

[5]The Piola transform comes directly from Nanson's formula $d\mathbf{a} = \det(\mathbf{F})\mathbf{F}^{-T}d\mathbf{A}$ which relates the change in directed area elements from reference to current configuration by way of the deformation gradient.

as

$$\begin{aligned}\frac{1}{J}\mathbf{P}\cdot\mathbf{F}^T &= -\frac{1}{2J}\sum_{\alpha=1}^{N}\sum_{\beta\neq\alpha}^{N}\mathbf{f}^{\alpha\beta}\otimes\left(\mathbf{x}^{\alpha\beta}-\mathbf{z}^{\alpha\beta}\right)B^{\alpha\beta}(\mathbf{X}) \\ &= -\frac{1}{2J}\sum_{\alpha=1}^{N}\sum_{\beta\neq\alpha}^{N}\mathbf{f}^{\alpha\beta}\otimes\mathbf{x}^{\alpha\beta}B^{\alpha\beta}(\mathbf{X})+\frac{1}{2J}\sum_{\alpha=1}^{N}\sum_{\beta\neq\alpha}^{N}\mathbf{f}^{\alpha\beta}\otimes\mathbf{z}^{\alpha\beta}B^{\alpha\beta}(\mathbf{X}).\end{aligned} \tag{2.42}$$

If we now examine the special case of a full system average such that $\frac{1}{J}B^{\alpha\beta}=1/V$ for all points in a system with finite volume V, the Piola transformed $\mathbf{P}$ from (2.42) becomes

$$\frac{1}{J}\mathbf{P}\cdot\mathbf{F}^T = -\frac{1}{2V}\sum_{\alpha=1}^{N}\sum_{\beta\neq\alpha}^{N}\mathbf{f}^{\alpha\beta}\otimes\mathbf{x}^{\alpha\beta}+\frac{1}{2V}\sum_{\alpha=1}^{N}\sum_{\beta\neq\alpha}^{N}\mathbf{f}^{\alpha\beta}\otimes\mathbf{z}^{\alpha\beta}, \tag{2.43}$$

and the Cauchy stress (2.34) becomes

$$\boldsymbol{\sigma} = -\frac{1}{2V}\sum_{\alpha=1}^{N}\sum_{\beta\neq\alpha}^{N}\mathbf{f}^{\alpha\beta}\otimes\mathbf{x}^{\alpha\beta}-\frac{1}{V}\sum_{\alpha=1}^{N}m^{\alpha}\mathbf{w}^{\alpha}\otimes\mathbf{w}^{\alpha}. \tag{2.44}$$

The difference between these two expressions, (2.43) and (2.44), is

$$\begin{aligned}\frac{1}{J}\mathbf{P}\cdot\mathbf{F}^T-\boldsymbol{\sigma} &= \frac{1}{V}\sum_{\alpha=1}^{N}\frac{1}{2}\sum_{\beta\neq\alpha}^{N}\mathbf{f}^{\alpha\beta}\otimes\mathbf{z}^{\alpha\beta}+\sum_{\alpha=1}^{N}m^{\alpha}\mathbf{w}^{\alpha}\otimes\mathbf{w}^{\alpha} \\ &= \frac{1}{V}\sum_{\alpha=1}^{N}\left(\mathbf{f}^{\alpha}\otimes\mathbf{z}^{\alpha}+m^{\alpha}\mathbf{w}^{\alpha}\otimes\mathbf{w}^{\alpha}\right)\end{aligned} \tag{2.45}$$

after using the identity

$$\begin{aligned}\frac{1}{2}\sum_{\alpha=1}^{N}\sum_{\beta\neq\alpha}^{N}\mathbf{f}^{\alpha\beta}\otimes\mathbf{z}^{\alpha\beta} &= \frac{1}{2}\sum_{\alpha=1}^{N}\sum_{\beta\neq\alpha}^{N}\mathbf{f}^{\alpha\beta}\otimes(\mathbf{z}^{\alpha}-\mathbf{z}^{\beta}) \\ &= \frac{1}{2}\Big(\sum_{\alpha=1}^{N}\sum_{\beta\neq\alpha}^{N}\mathbf{f}^{\alpha\beta}\otimes\mathbf{z}^{\alpha}+\sum_{\alpha=1}^{N}\sum_{\beta\neq\alpha}^{N}\mathbf{f}^{\beta\alpha}\otimes\mathbf{z}^{\beta}\Big)=\sum_{\alpha=1}^{N}\mathbf{f}^{\alpha}\otimes\mathbf{z}^{\alpha}\end{aligned} \tag{2.46}$$

which results simply from the manipulation of dummy indices, the definition (2.25) and the sym-

metry condition (2.27). In the absence of a body force ($\mathbf{f}^\alpha = m^\alpha \frac{d\mathbf{v}^\alpha}{dt}$) then

$$\begin{aligned}
\Big\langle \sum_{\alpha=1}^{N} \mathbf{f}^\alpha \otimes \mathbf{z}^\alpha \Big\rangle &= \Big\langle \frac{d}{dt} \sum_{\alpha=1}^{N} m^\alpha \mathbf{v}^\alpha \otimes \mathbf{z}^\alpha \Big\rangle - \Big\langle \sum_{\alpha=1}^{N} m^\alpha \mathbf{v}^\alpha \otimes \frac{d\mathbf{z}^\alpha}{dt} \Big\rangle \\
&= -\Big\langle \sum_{\alpha=1}^{N} m^\alpha \mathbf{v}^\alpha \otimes \frac{d\mathbf{z}^\alpha}{dt} \Big\rangle \\
&= -\Big\langle \sum_{\alpha=1}^{N} m^\alpha \big(\mathbf{v} + \mathbf{w}^\alpha\big) \otimes \big(\mathbf{w}^\alpha - \frac{d\mathbf{F}}{dt}\boldsymbol{\Xi}^\alpha\big) \Big\rangle \\
&= -\Big\langle \mathbf{v} \otimes \sum_{\alpha=1}^{N} m^\alpha \mathbf{w}^\alpha \Big\rangle + \Big\langle \mathbf{v} \otimes \frac{d\mathbf{F}}{dt} \sum_{\alpha=1}^{N} m^\alpha \boldsymbol{\Xi}^\alpha \Big\rangle \\
&\quad - \Big\langle \sum_{\alpha=1}^{N} m^\alpha \mathbf{w}^\alpha \otimes \mathbf{w}^\alpha \Big\rangle + \Big\langle \sum_{\alpha=1}^{N} m^\alpha \mathbf{w}^\alpha \otimes \frac{d\mathbf{F}}{dt}\boldsymbol{\Xi}^\alpha \Big\rangle \\
&= -\Big\langle \sum_{\alpha=1}^{N} m^\alpha \mathbf{w}^\alpha \otimes \mathbf{w}^\alpha \Big\rangle + \Big\langle \sum_{\alpha=1}^{N} m^\alpha \mathbf{w}^\alpha \otimes \frac{d\mathbf{F}}{dt}\boldsymbol{\Xi}^\alpha \Big\rangle
\end{aligned} \tag{2.47}$$

given the definition of $\boldsymbol{\Xi}^\alpha$, and the fact that time averages $\langle \bullet \rangle$ of exact differentials of bounded quantities are zero. The identity (2.47) is a simply a version of the virial theorem and if we assume a steady state, where $\frac{d\mathbf{F}}{dt}$ must be zero, then we have

$$\Big\langle \sum_{\alpha=1}^{N} \mathbf{f}^\alpha \otimes \mathbf{z}^\alpha \Big\rangle + \Big\langle \sum_{\alpha=1}^{N} m^\alpha \mathbf{w}^\alpha \otimes \mathbf{w}^\alpha \Big\rangle = \mathbf{0} \,, \tag{2.48}$$

This does not mean that $\mathbf{F}$ is necessarily fixed at the identity; rather, it means that (2.48) is satisfied only for truly steady systems. Now we can return to (2.45) and show that the (time-averaged) expressions for the transformed 1^{st} Piola-Kirchhoff stress and the Cauchy stress are consistent:

$$\Big\langle \frac{1}{J}\mathbf{P} \cdot \mathbf{F}^T - \boldsymbol{\sigma} \Big\rangle = \frac{1}{V} \Big\langle \sum_{\alpha=1}^{N} \mathbf{f}^\alpha \otimes \mathbf{z}^\alpha + m^\alpha \mathbf{w}^\alpha \otimes \mathbf{w}^\alpha \Big\rangle = \mathbf{0} \tag{2.49}$$

by use of (2.48).

The main difficulty in extending this proof to the general case is that the atoms contributing to the sums in (2.34) and (2.37) may be different depending on how atoms are flowing through space. Moreover, mapping the reference frame function $B^{\alpha\beta}(\mathbf{X}) = B^{\alpha\beta}_{\mathbf{X}}$ to the spatial $\tilde{B}^{\alpha\beta}(\mathbf{x}) = B^{\alpha\beta}_{\mathbf{x}}$ is non-trivial (as alluded to in Section 2.2.2). Rather than attempting to do this analysis, in Section 2.3 we will explore how the expression for $\mathbf{P}$ in equation (2.30) performs for cases where the thermal fluctuations are significant, and compare our results with expectations from continuum mechanics and with the usual Hardy definition for Cauchy stress.

Balance of Energy

Starting with the Lagrangian expression for the system energy (2.12),

$$\begin{aligned}\frac{d(\rho_0 e)}{dt} = \rho_0 \frac{de}{dt} &= \frac{d}{dt}\left\{\sum_{\alpha=1}^{N}\left\{\frac{1}{2}m^\alpha (v^\alpha)^2 + \phi^\alpha\right\}\psi(\mathbf{X}^\alpha - \mathbf{X})\right\} \\ &= \sum_{\alpha=1}^{N}\left\{m^\alpha\left(\frac{d\mathbf{v}^\alpha}{dt}\cdot\mathbf{v}^\alpha\right) + \frac{d\phi^\alpha}{dt}\right\}\psi(\mathbf{X}^\alpha - \mathbf{X}) \\ &= \sum_{\alpha=1}^{N}\left\{(\mathbf{f}^\alpha + m^\alpha\mathbf{b}^\alpha)\cdot\mathbf{v}^\alpha + \frac{d\phi^\alpha}{dt}\right\}\psi(\mathbf{X}^\alpha - \mathbf{X}).\end{aligned}$$

By imposing the second and third force assumptions, this simplifies to

$$\rho_0\frac{de}{dt} = \nabla_{\mathbf{X}}\cdot\left(\sum_{\alpha=1}^{N}\sum_{\beta\neq\alpha}^{N}\sum_{\gamma\neq\alpha}^{N}\left(\frac{\partial\phi^\gamma}{\partial x^{\alpha\beta}}\frac{\mathbf{x}^{\alpha\beta}}{x^{\alpha\beta}}\cdot\mathbf{v}^\alpha\right)\mathbf{X}^{\alpha\gamma}B^{\alpha\gamma}(\mathbf{X})\right) + \sum_{\alpha=1}^{N} m^\alpha\mathbf{b}^\alpha\cdot\mathbf{v}^\alpha\psi(\mathbf{X}^\alpha - \mathbf{X}). \tag{2.50}$$

Equation (2.50) can be further simplified by using the fourth force assumption:

$$\rho_0\frac{de}{dt} = \nabla_{\mathbf{X}}\cdot\left(\sum_{\alpha=1}^{N}\sum_{\beta\neq\alpha}^{N}\sum_{\gamma\neq\alpha}^{N}\left(\frac{\partial\phi^\gamma}{\partial x^{\alpha\beta}}\left(\delta_{\alpha\gamma}+\delta_{\beta\gamma}\right)\frac{\mathbf{x}^{\alpha\beta}}{x^{\alpha\beta}}\cdot\mathbf{v}^\alpha\right)\mathbf{X}^{\alpha\gamma}B^{\alpha\gamma}(\mathbf{X})\right) + \sum_{\alpha=1}^{N} m^\alpha\mathbf{b}^\alpha\cdot\mathbf{v}^\alpha\psi(\mathbf{X}^\alpha - \mathbf{X}) \tag{2.51}$$

$$= \nabla_{\mathbf{X}}\cdot\left(\sum_{\alpha=1}^{N}\sum_{\beta\neq\alpha}^{N}\left(\frac{\partial\phi^\beta}{\partial x^{\alpha\beta}}\frac{\mathbf{x}^{\alpha\beta}}{x^{\alpha\beta}}\cdot\mathbf{v}^\alpha\right)\mathbf{X}^{\alpha\beta}B^{\alpha\beta}(\mathbf{X})\right) + \sum_{\alpha=1}^{N} m^\alpha\mathbf{b}^\alpha\cdot\mathbf{v}^\alpha\psi(\mathbf{X}^\alpha - \mathbf{X}) \tag{2.52}$$

To proceed further, we separate atomic motion from continuum motion in two ways. First, we split the atomic velocities $\mathbf{v}^\alpha$ into the continuum velocity $\mathbf{v}(\mathbf{X},t)$ and a relative velocity $\mathbf{w}^\alpha(\mathbf{X},t)$ as in (2.35). Next we recall that earlier we recognized that the total energy, e contains contributions from both internal energy and continuum-scale kinetic energy. We separate this using the expression $e = \varepsilon + \frac{1}{2}v^2$:

$$\rho_0\frac{de}{dt} = \rho_0\frac{d\varepsilon}{dt} + \rho_0\frac{d\mathbf{v}}{dt}\cdot\mathbf{v} \tag{2.53}$$

Application of (2.53) to the LHS of (2.52) and (2.35) to the RHS of (2.52) produces:

$$\begin{aligned}
\rho_0 \frac{d\varepsilon}{dt} + \rho_0 \frac{d\mathbf{v}}{dt} \cdot \mathbf{v} &= \nabla_{\mathbf{X}} \cdot \left(\sum_{\alpha=1}^{N} \sum_{\beta \neq \alpha}^{N} \left(\frac{\partial \phi^{\beta}}{\partial x^{\alpha\beta}} \frac{\mathbf{x}^{\alpha\beta}}{x^{\alpha\beta}} \cdot (\mathbf{v} + \mathbf{w}^{\alpha}) \right) \mathbf{X}^{\alpha\beta} B^{\alpha\beta}(\mathbf{X}) \right) \\
&\quad + \sum_{\alpha=1}^{N} m^{\alpha} \mathbf{b}^{\alpha} \cdot (\mathbf{v} + \mathbf{w}^{\alpha}) \psi(\mathbf{X}^{\alpha} - \mathbf{X}) \\
&= \nabla_{\mathbf{X}} \cdot (\mathbf{v} \cdot \mathbf{P}) + \nabla_{\mathbf{X}} \cdot \left(\sum_{\alpha=1}^{N} \sum_{\beta \neq \alpha}^{N} \left(\frac{\partial \phi^{\beta}}{\partial x^{\alpha\beta}} \frac{\mathbf{x}^{\alpha\beta}}{x^{\alpha\beta}} \cdot \mathbf{w}^{\alpha} \right) \mathbf{X}^{\alpha\beta} B^{\alpha\beta}(\mathbf{X}) \right) \\
&\quad + \rho_0 \mathbf{b} \cdot \mathbf{v} + \sum_{\alpha=1}^{N} m^{\alpha} \mathbf{b}^{\alpha} \cdot \mathbf{w}^{\alpha} \psi(\mathbf{X}^{\alpha} - \mathbf{X}) \\
&= (\nabla_{\mathbf{X}} \mathbf{v}) : \mathbf{P} + \mathbf{v} \cdot (\nabla_{\mathbf{X}} \cdot \mathbf{P} + \rho_0 \mathbf{b}) + \nabla_{\mathbf{X}} \cdot \left(\sum_{\alpha=1}^{N} \sum_{\beta \neq \alpha}^{N} \left(\frac{\partial \phi^{\beta}}{\partial x^{\alpha\beta}} \frac{\mathbf{x}^{\alpha\beta}}{x^{\alpha\beta}} \cdot \mathbf{w}^{\alpha} \right) \mathbf{X}^{\alpha\beta} B^{\alpha\beta}(\mathbf{X}) \right) \\
&\quad + \sum_{\alpha=1}^{N} m^{\alpha} \mathbf{b}^{\alpha} \cdot \mathbf{w}^{\alpha} \psi(\mathbf{X}^{\alpha} - \mathbf{X})
\end{aligned}$$

Using the balance of linear momentum equation (2.8), this simplifies to

$$\rho_0 \frac{d\varepsilon}{dt} = (\nabla_{\mathbf{X}} \mathbf{v}) : \mathbf{P} + \nabla_{\mathbf{X}} \cdot \left(\sum_{\alpha=1}^{N} \sum_{\beta \neq \alpha}^{N} \left(\frac{\partial \phi^{\beta}}{\partial x^{\alpha\beta}} \frac{\mathbf{x}^{\alpha\beta}}{x^{\alpha\beta}} \cdot \mathbf{w}^{\alpha} \right) \mathbf{X}^{\alpha\beta} B^{\alpha\beta}(\mathbf{X}) \right) + \sum_{\alpha=1}^{N} m^{\alpha} \mathbf{b}^{\alpha} \cdot \mathbf{w}^{\alpha} \psi(\mathbf{X}^{\alpha} - \mathbf{X}). \tag{2.54}$$

Since the $\nabla_{\mathbf{X}}$ and $\frac{d}{dt}$ operators are commutative, $\nabla_{\mathbf{X}} \mathbf{v} = \frac{d\mathbf{F}}{dt}$. Hence,

$$\rho_0 \frac{d\varepsilon}{dt} = \mathbf{P} : \frac{d\mathbf{F}}{dt} - \nabla_{\mathbf{X}} \cdot \mathbf{Q} + \rho_0 h, \tag{2.55}$$

where

$$\mathbf{Q}(\mathbf{X}, t) = - \sum_{\alpha=1}^{N} \sum_{\beta \neq \alpha}^{N} \left(\frac{\partial \phi^{\beta}}{\partial x^{\alpha\beta}} \frac{\mathbf{x}^{\alpha\beta}}{x^{\alpha\beta}} \cdot \mathbf{w}^{\alpha} \right) \mathbf{X}^{\alpha\beta} B^{\alpha\beta}(\mathbf{X}) \tag{2.56}$$

is the heat flux as expressed in the reference configuration. We note that like the expression for stress this expression contains only a potential term and not a kinetic term, unlike the spatial frame heat flux expression derived by Hardy [159]. Nevertheless, thermal motion does enter this expression through the derivatives of the potential energy, the inter-atomic positions $\mathbf{x}^{\alpha\beta}$, and the relative velocities $\mathbf{w}^{\alpha}$.

Comparison of (2.54) with (2.55) also produces the relation defining energy generation per unit mass:

$$h(\mathbf{X}, t) = \frac{1}{\rho_0(\mathbf{X})} \sum_{\alpha=1}^{N} m^{\alpha} \mathbf{b}^{\alpha} \cdot \mathbf{w}^{\alpha} \psi(\mathbf{X}^{\alpha} - \mathbf{X}) = \frac{\sum_{\alpha=1}^{N} m^{\alpha} \mathbf{b}^{\alpha} \cdot \mathbf{w}^{\alpha} \psi(\mathbf{X}^{\alpha} - \mathbf{X})}{\sum_{\alpha=1}^{N} m^{\alpha} \psi(\mathbf{X}^{\alpha} - \mathbf{X})} \tag{2.57}$$

We note that for a uniform body force field this term simplifies to zero. This term would be also be negligible for a non-uniform body force field for which significant variations in the field are defined at larger length scales that the localization volume size associated with ψ. However,

for situations where **b** truly varies from atom to atom, it appears that the work done by the field against the relative velocity field generates energy. The term h may also be related to other energy source terms that can be introduced into the atomic energy, although none are present in the above analysis.

Hardy and colleagues also derived [159] an expression for temperature by considering the equipartition theorem and the kinetic energy associated with atomic velocities relative to the velocity of the continuum at a spatial point,

$$\mathrm{T}(\mathbf{x},t) = \frac{1}{3k_B} \frac{\sum_{\alpha=1}^{N} m^{\alpha} \left(w^{\alpha}\right)^2 \psi(\mathbf{x}^{\alpha} - \mathbf{x})}{\sum_{\alpha=1}^{N} \psi(\mathbf{x}^{\alpha} - \mathbf{x})}, \tag{2.58}$$

which is a simple weighted average as opposed to the volume average in (2.10) for example. Here k_B is Boltzman's constant. Similarly, we can define a temperature field using our densities expressed in the reference configuration,

$$\mathrm{T}(\mathbf{X},t) = \frac{1}{3k_B} \frac{\sum_{\alpha=1}^{N} m^{\alpha} \left(w^{\alpha}\right)^2 \psi(\mathbf{X}^{\alpha} - \mathbf{X})}{\sum_{\alpha=1}^{N} \psi(\mathbf{X}^{\alpha} - \mathbf{X})}. \tag{2.59}$$

This definition is consistent with the allocation of $\frac{1}{2}k_BT$ of kinetic energy per degree of freedom for an atomic system. For solids, this allocation is somewhat inexact due to constraints, e.g. periodic boundary conditions, that may be acting on the system, but this difference is minimal for systems where the number of atoms is much larger than the number of constraints.

2.3 Evaluation of Material Frame Expressions

In this section, we examine the behavior of our P-K stress expression for several molecular dynamics simulations. These simulations will confirm that our expression for P-K stress is consistent with both the virial stress and the Cauchy stress expression defined by Hardy.[6] All of our simulations involve system of copper modeled using the EAM potential by Foiles *et al.* [57]. This potential creates an equilibrium, face-centered-cubic crystal of Cu of lattice parameter equal to 3.615 Å at zero temperature. For molecular dynamics simulations, a timestep of 0.001 ps is used.

Calculations are done using specialized routines written for ParaDyn [167] and the Large-scale Atomic/Molecular Massively Parallel Simulator (LAMMPS)[168], molecular simulation codes developed at Sandia National Laboratories. For the analyses presented in this section, the choice of the zero temperature, undeformed system is used as our material configuration. The rationale for this selection will be elaborated upon in the subsequent discussion section.

[6] In this section, all calculations of Cauchy stress ($\boldsymbol{\sigma}$) are determined using equation (2.34), where the fixed spatial point **x** coincides with the material point **X** used to calculate **P** via equation (2.30).

2.3.1 Stress for a constrained finite temperature system

In this and the following section, we present simulations of a system containing 4,000 atoms (10 x 10 x 10 unit cells), where periodic boundary conditions are enforced on all sides of the simulation box. Two sets of calculations are performed: one using a single point in the center of system with a spherical localization volume of radius 15 Å and a quartic polynomial localization function, and another using a step function where both ψ and $B^{\alpha\beta}$ equal the quantity V_0^{-1} (where V_0 is the system size at zero temperature and deformation).

We first examine the situation where our system is constrained to remain at the reference volume, but heated to a finite, non-zero temperature. In this instance $\mathbf{F} = \mathbf{1}$ and $J = 1$; hence, the values of 1^{st} P-K and Cauchy stress should coincide. Unless otherwise stated, the results presented here refer to the continuum stress measures evaluated for the single point simulations. The results obtained in the step-based simulations were similar in all cases, with stress values much closer in agreement to the system virial as one would expect since all atoms and bonds contribute uniformly in that analysis.

Figure 2.2 shows the variation of instantaneous pressure with time for a system that is heated to 100 K. 'Pressure' in this case refers to the negative of the hydrostatic stress for each stress measure, *i.e.* the P-K pressure equals $-\frac{1}{3}\text{Trace}(\mathbf{P}) = -\frac{1}{3}P_{kk}$, the Cauchy pressure equals $-\frac{1}{3}\text{Trace}(\boldsymbol{\sigma})$ and the same relation is used for the system virial. The distributions of P-K and Cauchy nearly perfectly

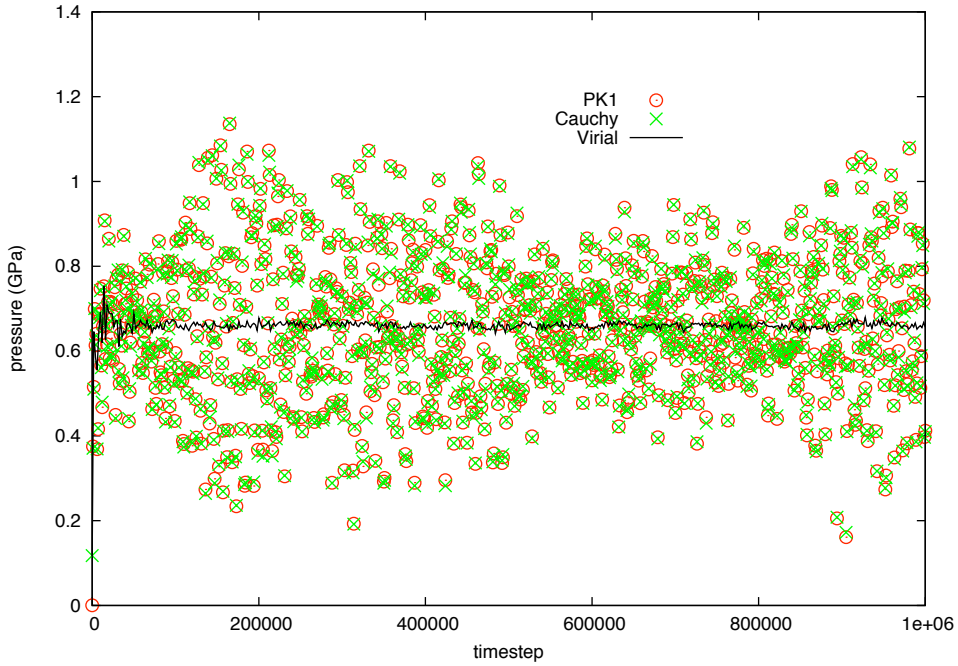

Figure 2.2. Variation of instantaneous pressure with time for a constrained system at 100 K.

overlap with one another, and both distributions are centered around the virial distribution. Also, since the volume of material used for evaluation is a subset of the whole system, the variations from the mean value are larger in magnitude for both P-K and Cauchy pressures as compared with the variation observed in the virial. It is interesting to note that while the mathematical analysis presented in the previous section showed that the P-K and Cauchy stress expressions agree with one another (through the $J\boldsymbol{\sigma} = \mathbf{P} \cdot \mathbf{F}^T$ transformation) only if a long time average is taken, Figure 2.2 shows that close agreement also exists for stress evaluations at specific instants in time. We suspect that this is due to the ensemble averaging provided by the Hardy method.

The agreement between our stress measures and the virial is easier to see by using the data in Figure 2.2 to calculate cumulative time averaged pressures. Figure 2.3 shows the variation of these time averaged pressures with time for the same duration, 10^6 timesteps. This figure shows that

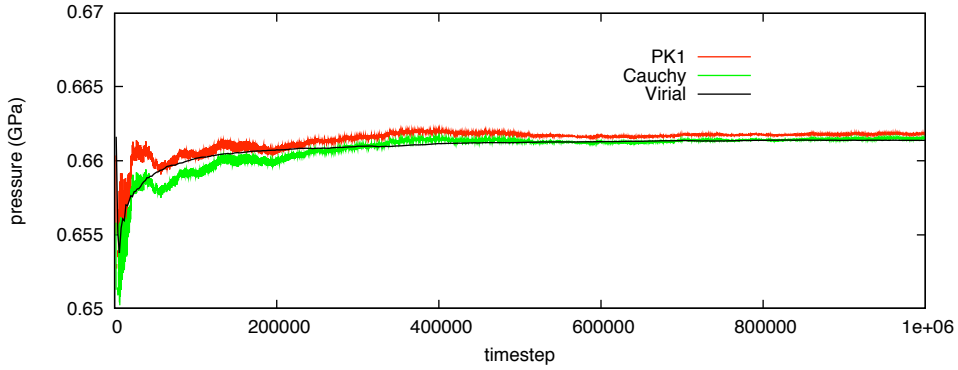

Figure 2.3. Variation of time averaged pressure with time for a constrained system at 100 K.

the time averaged pressures essentially converge within 500,000 timesteps (0.5 ns), and that the converged values of P-K, Cauchy and virial pressures are very close to one another. This agreement is more clearly shown in Table 2.1, which compares the converged values of P-K pressure (after 10^6 timesteps) with the virial pressure for both the point-based analysis shown in Figure 2.3 and the step-based analysis. We note in Table 2.1 that the percent difference between P-K and virial pressures is much less than 1%, and that this difference is smaller for the step-based analysis (which uses all atoms in the system) than for the point-based analysis.

Table 2.1 also shows the converged time averaged pressures for systems heated to 300 K and 675 K, values approximately 22% and 50%, respectively, of the melting temperature of copper. It can be seen that the agreement between P-K pressure and the virial remains excellent even at these high temperatures and stress levels. This close agreement is emphasized in Figure 2.4, which graphically shows the variation of pressure with increasing temperature for this constrained system. It was also observed that, at the highest temperature simulated of 675 K, agreement between the P-K pressure and the virial improved if a longer time average is taken.

The above analyses show that our derived expression for P-K stress is consistent with a thermo-

Table 2.1. Time averaged pressures after 10^6 timesteps for constrained volume simulations.

Temperature (K)	Point / Step	virial pressure (GPa)	P-K pressure (GPa)	% difference
100	Point	0.6613775	0.6618136	0.06653
100	Step	0.6614168	0.6613937	-0.00350
300	Point	1.944335	1.944422	0.00448
300	Step	1.944465	1.944413	-0.00264
675	Point	4.335872	4.334868	-0.02316
675	Step	4.335840	4.336577	0.01699

mechanical measure of stress despite the fact that it contains only a potential and not a kinetic term, unlike the Cauchy stress expression derived by Hardy. The small level of error between P-K stress and the system virial noted in Table 2.1 is much smaller than the amount of stress attributed to the kinetic part of Hardy's Cauchy stress or the virial itself. That kinetic part is approximately equal to 0.1169 GPa, 0.3507 GPa and 0.7891 GPa for the temperatures considered (100 K, 300 K and 675 K, respectively). Comparison of these values with the virial pressure listed for each temperature, given in Table 2.1, shows that they are significant fractions of the virial, about 17.7%, 18.0% and 18.2%, respectively. This finding confirms that for cases where the kinetic contribution to the stress tensor is significant, the P-K stress expression yields a full measure of stress in agreement with the expression for the total Cauchy stress, which explicitly includes this kinetic contribution.

2.3.2 Finite temperature deformation

For the situation of a constrained volume, the values of P-K and Cauchy stress were not anticipated to differ by any significant amount. However, we have yet to consider a case for which deformation occurs and the two values should be related by the Piola transform $\boldsymbol{\sigma} = \frac{1}{J}\mathbf{P}\cdot\mathbf{F}^T$. We now examine the scenario where our system starts out at zero temperature, is heated over the course of 10^6 timesteps (1 ns) to a finite temperature but allowed to expand in order to maintain a condition of zero pressure, is equilibrated for an additional 10^6 timesteps at that non-zero temperature and zero pressure, and is then triaxially stretched an additional 1% or 5% from this expanded state.

Figure 2.5 shows the variation of the hydrostatic stresses for $\mathbf{P}$, $\boldsymbol{\sigma}$ (as measured using the original Hardy formulation) and the system virial for a stretch of 1% after equilibration at 100 K. In this section, we plot and discuss only values measured from the simulations performed with the point-based analysis; however, values calculated with step-based analysis were virtually the same. Figure 2.5 shows large variations in the instantaneous estimates of $\mathbf{P}$ and $\boldsymbol{\sigma}$ as compared with the system virial. It is observed that this variation stays within a limit of approximately $\pm$ 15% of the long time average after 400,000 timesteps (0.4 ns) have elapsed. As expected, the values of $\mathbf{P}$ are slightly higher than the values of $\boldsymbol{\sigma}$ and the virial. Figure 2.6 compares the transformed stress $\frac{1}{J}\mathbf{P}\cdot\mathbf{F}^T$ to the Cauchy stress and virial, and demonstrates that the transformed P-K stress is in close correspondence with the Cauchy measure. In this figure, we see that the distributions of

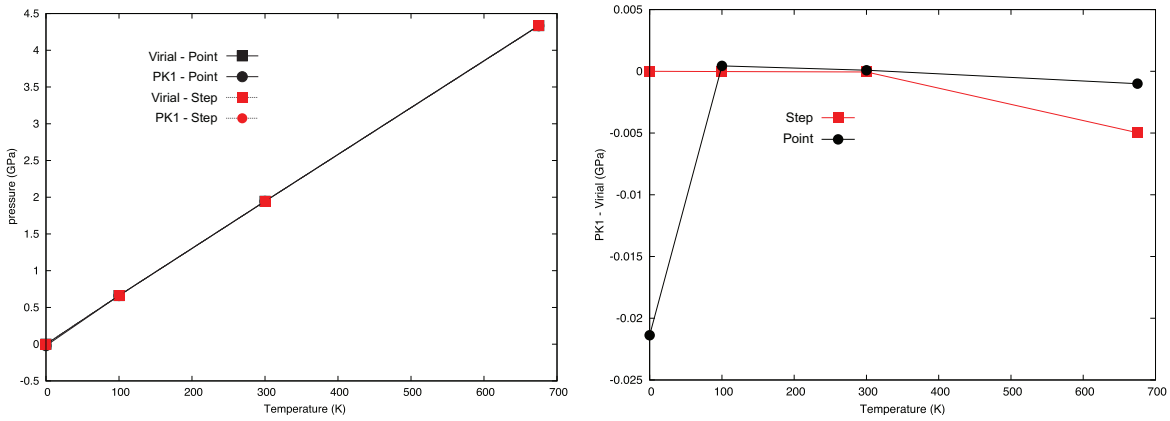

Figure 2.4. (a) Time averaged pressures after 10^6 timesteps for constrained volume simulations performed at various temperatures. (b) Differences between P-K and virial measures of pressure at various temperatures.

transformed Piola-Kirchhoff stress and Cauchy stress nearly perfectly overlap with one another, and both distributions are centered around the virial distribution. Again, we note that although the mathematical analysis presented in the previous section showed that the P-K and Cauchy stress expressions agree with one another only if a long time average is taken, Figure 2.6 shows that close agreement also exists for stress evaluations at specific instants in time.

Figure 2.7 shows the cumulative time averages of the four stress values (**P**, σ, virial and transformed **P**). It is observed that the system virial approaches its long time average in a short amount of time, $\sim$ 20,000 timesteps (0.02 ns), and that both the Cauchy stress and transformed P-K stress approach this same value within approximately 200,000 timesteps (0.2 ns). The P-K stress also approaches its own long time average within this same amount of time, and the value is appropriately higher. Values of these long time averages are listed in Table 2.2. These results clearly show a negligible difference between the transformed P-K stress value and the virial of the system. Thus, we again conclude that our derived expression is consistent with the continuum relation between Cauchy and P-K stress despite the absence of a kinetic term.

In addition to our simulation results for the case of 1% stretch at 100 K, Table 2.2 also shows results for systems heated to 300 K and 675 K for stretches of both 1% and 5% following thermal equilibration at zero pressure. We observe that in all cases, the difference between the hydrostatic virial stress and the hydrostatic transformed P-K stress is very small with a difference of, at most, 1%. The results in Figures 2.8(a) and (b) show near perfect agreement of the virial and the transformed P-K stress across a range of temperatures.[7]

[7]These figures reveal that at higher temperatures a lower amount of stress is produced within the system. This result can be attributed to the temperature dependence of the elastic constants that softens (decreases) their value with

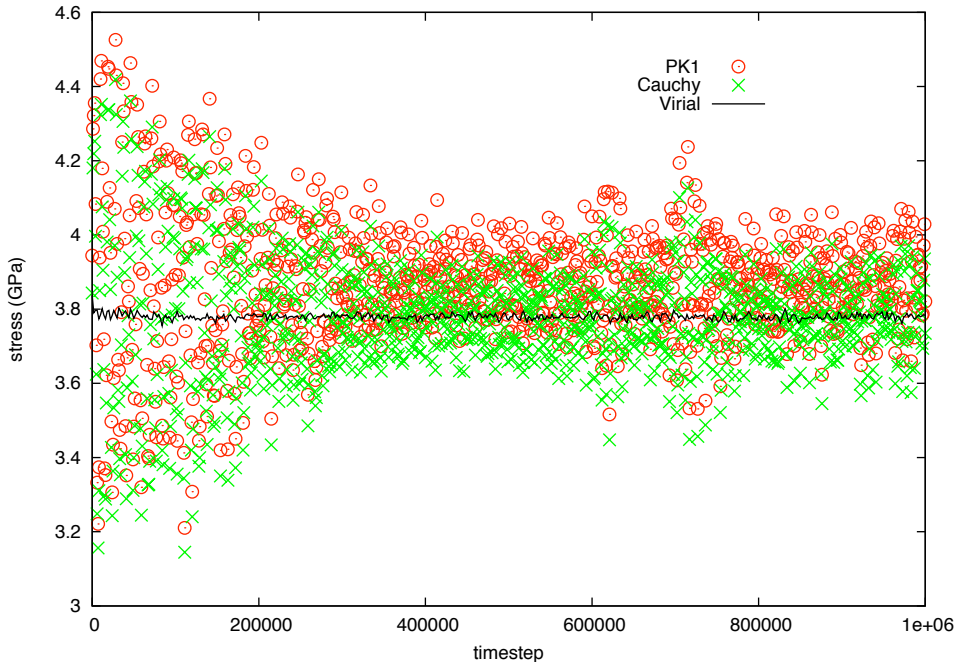

Figure 2.5. Variation of the instantaneous hydrostatic stresses for $\mathbf{P}$ [eqn. (2.30)], $\boldsymbol{\sigma}$ [eqn. (2.34)] and the system virial for a stretch of 1% after equilibration at 100 K and zero pressure.

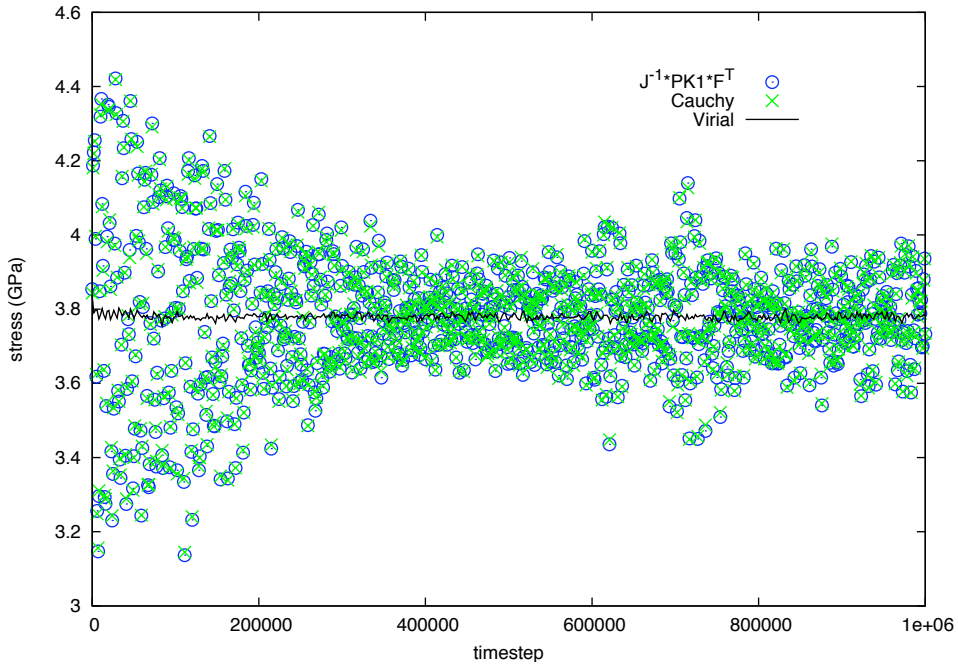

Figure 2.6. Variation of the instantaneous hydrostatic stresses for $\frac{1}{J}\mathbf{P}\cdot\mathbf{F}^T$, $\boldsymbol{\sigma}$ and the system virial for a stretch of 1% after equilibration at 100 K and zero pressure.

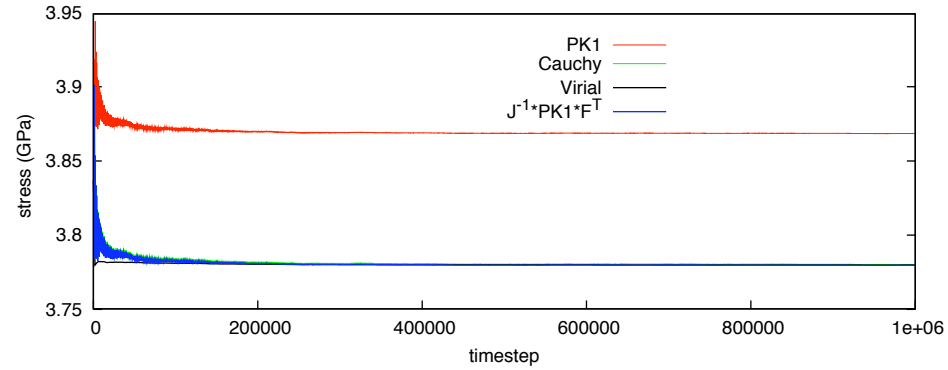

(a)

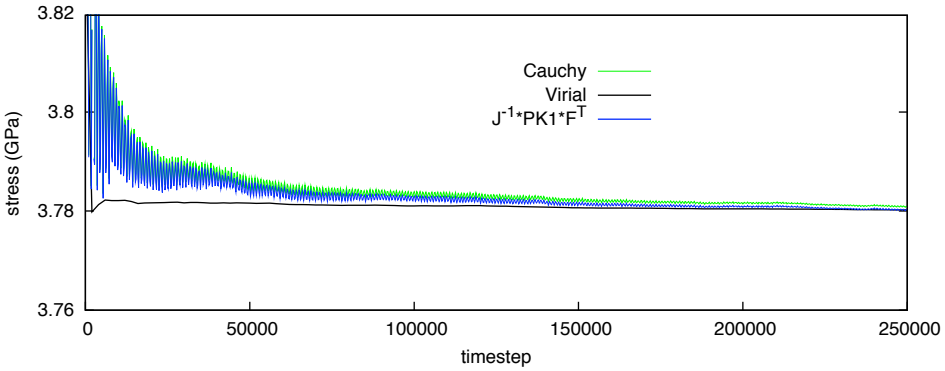

(b)

Figure 2.7. (a) Variation of time averaged hydrostatic stress measures with time for a stretch of 1% after equilibration at 100 K and zero pressure. (b) Close-up of (a) for the first 250,000 timesteps.

2.3.3 Tensile stretching of a center-cracked body

The previous two examples show that our formulation enables the calculation of 1^{st} Piola-Kirchhoff stress that is consistent with estimates of the Cauchy stress, either using the system virial or the original Hardy formulation. However, these examples only produce a single value of stress representative of the entire system, *i.e.* systems subjected to a homogeneous deformation state. The strength of our formulation lies in its ability to produce a field of spatially varying values of stress for cases where an inhomogeneous deformation is produced.

The Hardy formalism has much in common with the data reduction and smoothing technique called Moving Least Squares (MLS) [105]. For instance, (2.15) can been seen as the solution to a weighted least-squares problem using a lumped version of the least squares matrix [197]. Although effective, it becomes expensive to recalculate, say (2.15) at every sample point of interest in a

increasing temperature.

Table 2.2. Time averaged stresses after 10^6 timesteps for simulations of a heated and triaxially strained system. Here,'% difference' refers to the difference between transformed P-K stress (the 6^{th} column) and the virial.

T (K)	Point / Step	total strain	virial (GPa)	P-K (GPa)	$\frac{1}{J}$(P-K)$\mathbf{F}^T$	% difference
0	Point	0.01	3.876275	3.954033	3.876123	-0.00394
0	Step	0.01	3.876273	3.954190	3.876277	-0.00009
0	Point	0.05	14.70036	16.20713	14.70035	-0.00009
0	Step	0.05	14.70036	16.20710	14.70032	-0.00026
100	Point	0.01168	3.779846	3.868452	3.779658	-0.00499
100	Step	0.01163	3.782552	3.871040	3.782538	-0.00038
100	Point	0.05169	14.26000	15.77334	14.26085	0.00597
300	Point	0.01495	3.581698	3.690054	3.582124	0.01190
300	Step	0.01495	3.579387	3.687273	3.579472	0.002386
300	Point	0.05515	13.30167	14.80901	13.30142	-0.00186
675	Point	0.02174	3.194773	3.334715	3.194304	-0.01469
675	Step	0.02174	3.194821	3.303813	3.164701	-0.94278
675	Point	0.06221	11.33258	12.78735	11.33345	0.00768

simulation with large spatial variations. Instead we choose to sample on a collection of points $I = 1..M$ on a regular grid and then use finite element shape functions $N_I(\mathbf{X})$ to construct an approximation to the field of interest, for example the displacement field

$$\mathbf{u}(\mathbf{X},t) = \sum_{I=1}^{M} \mathbf{u}_I(t) N_I(\mathbf{X}) = \sum_{I=1}^{M} \frac{\sum_{\alpha=1}^{N} m^\alpha \mathbf{u}^\alpha \psi(\mathbf{X}^\alpha - \mathbf{X}_I)}{\sum_{\alpha=1}^{N} m^\alpha \psi(\mathbf{X}^\alpha - \mathbf{X}_I)} N_I(\mathbf{X}) \tag{2.60}$$

where we can define and store the matrices $\psi_{I\alpha} = \psi(\mathbf{X}^\alpha - \mathbf{X}_I)$ and $B_{I\alpha\beta} = B^{\alpha\beta}(\mathbf{X}_I)$. This also gives us a second way to estimate the displacement gradient (2.16) by taking the gradient of the interpolation $N_I(\mathbf{X})$.

In this section, we examine a system containing a center crack and compare the inhomogeneous stress fields that arise due to tensile stretching. Our system consists 9,840 atoms, approximately 20 x 20 x 6 unit cells, that contains a center crack 4 unit cells wide in the center. We acknowledge that this is a small and highly constrained system, and use it only as a means to show our ability to estimate spatially varying stress fields. The crack is created by excluding interactions between atoms above the center-plane of the system (and within the 4 unit cell width) and atoms below the center-plane. Periodic boundary conditions are used in the horizontal and thickness directions, while atoms within 2 unit cells of the system's upper and lower boundaries are controlled by prescribing a fixed velocity of ± 0.1 Å/ps, respectively. Given the dimensions of our system, this produces an approximate strain rate of initial value 3.46 x 10^{-3} ps^{-1} = 3.46 x 10^9 sec^{-1}. Before inducing the stretching, our system is relaxed using a conjugate gradient minimization algorithm in order to relax the upper, lower and crack boundaries and set the reference configuration.

To calculate stress at material points, we use localization volumes consisting of rectangular

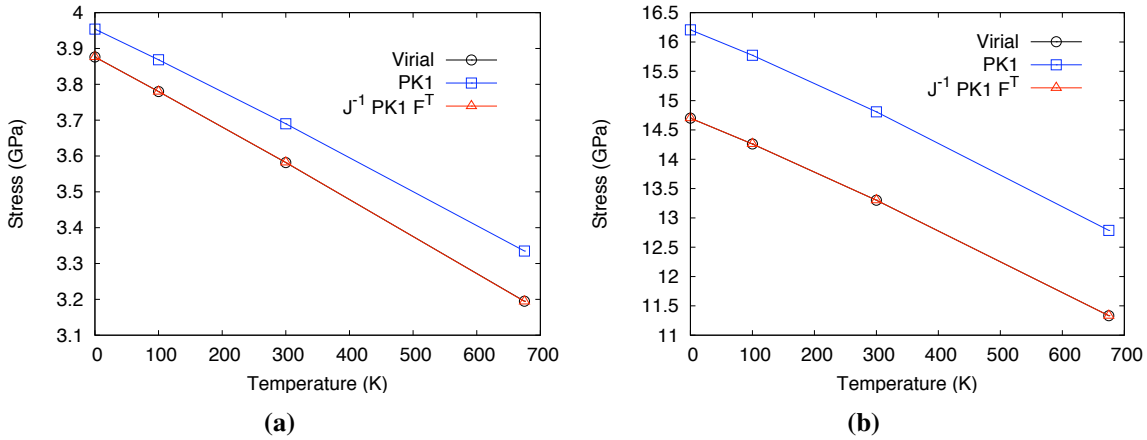

Figure 2.8. Variation of time-averaged hydrostatic stress measures after 10^6 timesteps with temperature for a stretch of (a) 1%, and (b) 5 % after equilibration at that temperature.

parallelepipeds, and localization functions that are multiples of three linear shape functions, one for each orthogonal direction, as in the finite element method. For this system, our mesh consists of 10 x 15 x 1 = 150 elements where our mesh extends beyond the atomic system in the vertical direction by 2.5 unit cells at both the upper and lower boundaries.

Figure 2.9 shows the displaced atoms, colored by the values of the component u_y of their displacement vector, as well as u_y displacement field evaluated at nodes and interpolated through elements, for the center-cracked body vertically stretched by approximately 6.9%. The left portion of Figure 2.9 clearly shows that the nodal values of displacement agree with the values of nearby atoms, while the right portion displays a displacement field consistent with expectations from fracture mechanics. It is interesting to note that the normalization present in equation (2.15) enables approximately correct values of u_y to be calculated at nodes bordering the boundaries of the atomic system, even though 1/2 of each node's localization volume is empty. This is because the normalization produces a displacement value corresponding to the center of mass of the localization volume and assigns that value to the node. And, since each element only contains a small number of atoms, the difference between the nodal position and the center of mass position is relatively small. Obviously, special care should be taken to use small elements near the boundary of an enclosed atomistic system, or near any region for which mass is unevenly distributed within the localization volume in the reference configuration. Nodes with localization volumes that are completely empty of atoms are assigned a zero value.

Figure 2.10 shows the fields of P_{yy} and σ_{yy} for the same stretch state of 6.9%. These fields are consistent with expectations from fracture mechanics, possessing features such as zero stress in the crack opening region and concentrations of tensile stress near the crack tips. Consistency between our formulation and Hardy's is shown by the qualitative similarity of the fields, with values of σ_{yy} having, in general, a slightly higher magnitude than the corresponding value of P_{yy}. Quantitative

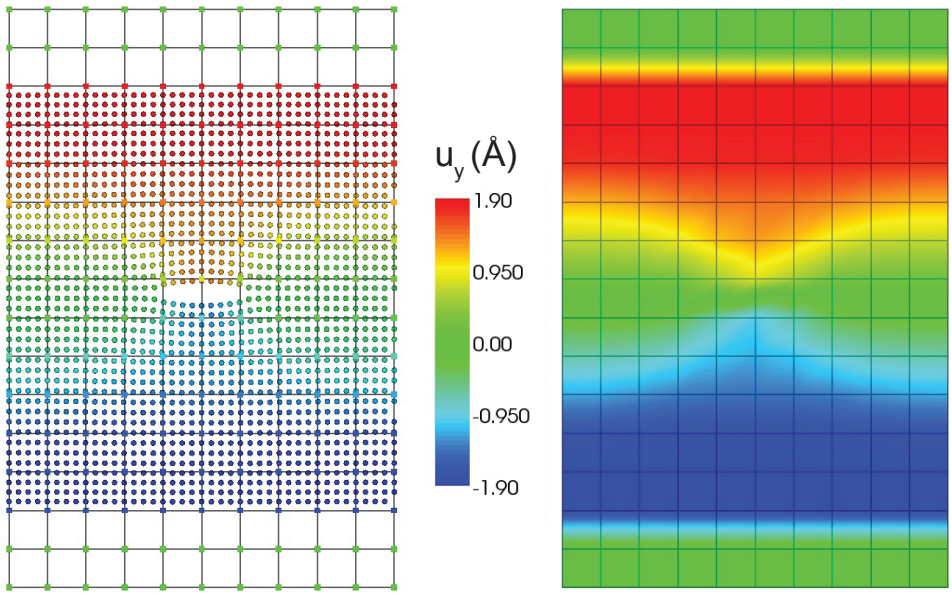

Figure 2.9. Displacement field u_y for a center-cracked body vertically stretched 6.9%. Left: Atoms pictured with overlaying mesh and nodes. Right: Mesh elements showing contours of continuum displacement field; mesh is shown with gray lines to identify elements.

consistency can be evaluated by comparing the values at a specific material point. We choose a node near the crack tip, at a position of {21.69 Å, 10.845 Å, 10.845 Å} (6 elements down from the top of the system, and 2 elements from the right edge). At this node, the value of P_{yy} equals 9.40327 GPa, and the value of σ_{yy} is 10.0719 GPa. Using our method to estimate displacement gradient $\nabla_{\mathbf{X}}\mathbf{u}$, and by using the relation $\mathbf{F} = \mathbf{1} + \nabla_{\mathbf{X}}\mathbf{u}$, the value of transformed P-K stress is calculated to be 9.48638 GPa. This value is somewhat lower than the expected value from the Hardy expression (a difference of about -5.81%). However, our earlier simulation examples indicate that this agreement may improve if the system is fixed at a given (inhomogeneous) deformation state and stress values are time averaged for periods $\sim$ 1 ns. It may also be the case that displacement gradient values are actually higher in magnitude than estimated here due to the small size of the system and the use of (relatively) large localization volumes near the crack tip, *i.e.* the estimated displacement gradient also has errors associated with it.

2.4 Formulation for a Micromorphic Continuum

In Section 2.2.3, we noted that Hardy makes four assumptions about the forms of the energies of, and forces on, the atoms in the system. We also noted that arbitrary multi-body potentials do not necessarily satisfy all four assumptions. For example, the Stillinger-Weber potential for silicon

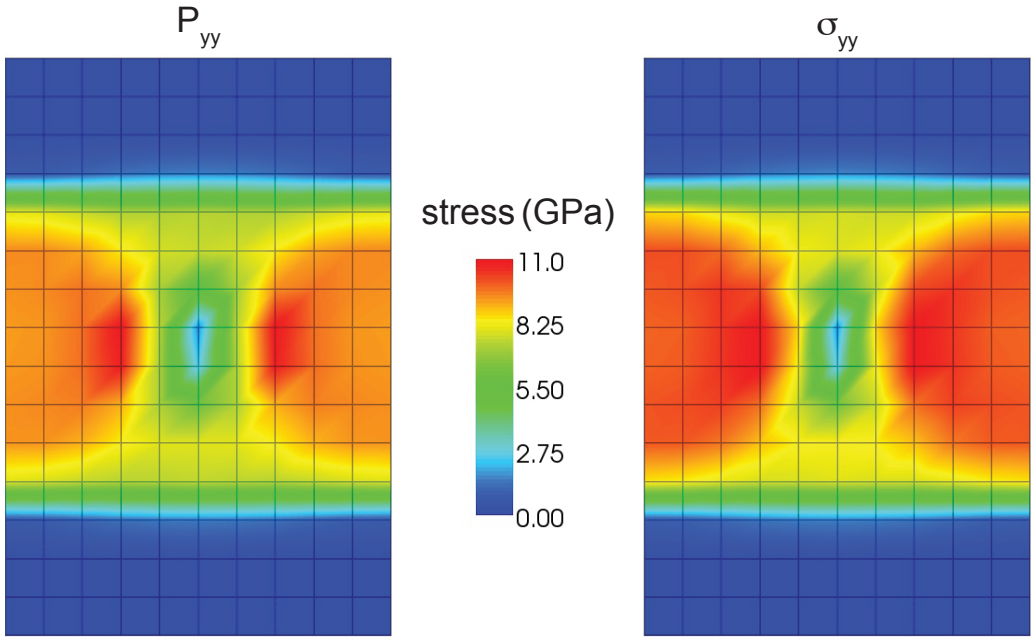

Figure 2.10. Stress fields for a center-cracked body vertically stretched 6.9%. Left: Mesh elements showing contours of continuum field P_{yy}. Right: Mesh elements showing contours of continuum field σ_{yy} as determined from the original Hardy formulation. In both pictures, the mesh is shown with gray lines to identify elements.

[177], contains a 3-body term that violates the fourth assumption. This assumption is pivotal as it leads to a simplified form of the inter-atomic force between two atoms, which is then used to isolate the expression for stress in the balance of energy. Without this relationship, it is not straightforward to show that the stress expression derived from momentum balance also satisfies energy balance.

This issue has been examined further by both Delph [40] and Chen [24]. In his work, Delph uses the linear momentum balance to derive a generalized expression for stress that includes multi-body terms up to N^{th} order (where N is the number of atoms in the system). However, this same expression is not present within his analysis of the balance of energy. On the other hand, Chen restricts her analysis to consider only potentials with 2-body and 3-body terms, such as the aforementioned Stillinger-Weber potential and the potential by Tersoff [180, 181]. While Chen does manage to show that the stress expression defined by linear momentum appears in the energy balance, her derivation is unclear in its consistency with regard to the expression for the inter-atomic force between two atoms.

We hypothesize that the difficulties experienced by both Delph and Chen are due to the underlying assumption that potential energies that use multi-body terms representative of directional bonding constitute a standard continuum at the microscopic scale. Rather, we conjecture that an

enhanced continuum theory is required in order to represent such a material. One such theory is that of a micromorphic continuum as put forth by Eringen [46, 47]. This theory is attractive as it is based on the supposition of microscopic deformations and rotations and includes the concepts of asymmetric stress and a couple stress tensor, both of which act to balance angular or rotational momentum in a body. Such concepts would seemingly be vital when defining volumes associated with continuum material points of arbitrary size and shape for a material governed by directional bonding between atoms. (This point is further addressed in the Appendix.)

In this section, we apply our material frame version of the Hardy formulation to the set of balance laws for a micromorphic continuum. The choice of a material frame analysis is not happenstance; indeed, the authors have attempted to perform a spatial frame analysis consistent with the original formulation by Hardy. However, this analysis is not trivial as an inconsistency exists between the notion of a fixed spatial point $\mathbf{x}$ from the Hardy formulation with the material point $\bar{\mathbf{x}}$ of Eringen's theory. In micromorphic theory, $\bar{\mathbf{x}}$ represents the center of mass of a "microvolume" or "microelement" at the current state of deformation. However, Hardy's analysis requires that $\mathbf{x}$ represent a fixed spatial point. Combining the two formulations requires the introduction of additional terms to account for the offset of the center of mass from the spatial point $\mathbf{x}$. We have thus far been unable to define a unambiguous set of balance laws that includes such additional variables. Eringen's original derivation for balance laws in the material frame, as shown in [47], does include such variables. For a material frame analysis (as presented in Section 2.2), this inclusion is unnecessary: a set of material points $\mathbf{X}$ can be selected that satisfy the center of mass requirement and these points remain fixed over time in the reference configuration. This statement is not true for spatial points that coincide with the material points when the system occupies the reference configuration as, at a later time, they will no longer represent mass centers.

Before proceeding, we note that Chen and Lee previously performed an analysis to connect atomistic quantities to micromorphic theory [25, 26]. In their work, they consider both instantaneous and time-averaged forms of thermomechanical variables and the consistency of these variables with the balance laws for a micromorphic continuum. However, their analysis was performed using a mixture of material and spatial frames as they use the spatial forms of the balance laws and consider current positions of microelements but define quantities relative to fixed sets of atoms associated with each microelement. In addition, they use the original form of Eringen's theory without consideration of the mass center issue discussed above. Our work will involve manipulation of the material frame versions of the balance laws, thereby avoiding this inconsistency. It is worth noting that Zhou and McDowell considered a similar "equivalent continuum" analysis for a micropolar continuum [215] (a continuum with microelements that undergo rigid rotations only), but proceeded in an entirely different manner than we do or that Chen and Lee have. Also, Murdoch has performed an analysis in which he defined a couple stress tensor that satisfies a moment of momentum balance [136]. It will be seen that our expression for couple stress contains significant differences as compared to Murdoch's expression, and that, unlike Murdoch, we consider the full set of micromorphic balance laws as established by Eringen.

2.4.1 Balance Laws

The material frame balance laws for a micromorphic continuum, as derived by Eringen in [47], are as follows:

$$\frac{d\rho_0}{dt} = 0 \tag{2.61}$$

$$\rho_0 \frac{d\mathbf{I}}{dt} = 0 \tag{2.62}$$

$$\rho_0 \frac{d\mathbf{v}}{dt} = \nabla_{\mathbf{X}} \cdot \mathbf{P} + \rho_0 \mathbf{b} \tag{2.63}$$

$$\rho_0 \frac{d^2\boldsymbol{\chi}}{dt^2} \cdot \mathbf{I} = \nabla_{\mathbf{X}} \cdot \mathbf{M} + \mathbf{P} - \bar{\mathbf{P}} + \rho_0 \mathbf{c} \tag{2.64}$$

$$\rho_0 \frac{d\varepsilon}{dt} = \mathbf{P} : \frac{d\mathbf{F}}{dt} + \mathbf{M} : \left(\nabla_{\mathbf{X}} \frac{d\boldsymbol{\chi}}{dt}\right) + \left(\bar{\mathbf{P}} - \mathbf{P}\right) : \frac{d\boldsymbol{\chi}}{dt} - \nabla_{\mathbf{X}} \cdot \mathbf{Q} + \rho_0 h \tag{2.65}$$

where $\mathbf{I}$ is the micro-inertia tensor, $\boldsymbol{\chi}$ is the micro-deformation gradient, and $\mathbf{M}$ is the couple stress tensor.[8] The stress $\bar{\mathbf{P}}$ is a quantity related to $\mathbf{P}$ in the sense that the latter is considered by Eringen to be a surface averaged limit of a traction while the former is a volume averaged limit of that same traction (for a more precise explanation, the reader is referred to reference [47]). We note that the total energy contains contributions from internal energy, continuum translational kinetic energy and continuum micro-rotational kinetic energy: $e = \varepsilon + \frac{1}{2}v^2 + \frac{1}{2}\mathbf{I} : \left(\frac{d\boldsymbol{\chi}}{dt}^T \cdot \frac{d\boldsymbol{\chi}}{dt}\right)$.[9] These equations appear in a more generalized form in [47]; however, to simplify our analysis we have made the assumption of Cartesian coordinates (instead of curvilinear coordinates) and do not separate out intrinsic surface energy density. We also assume that the material points $\mathbf{X}$ coincide with the centers of mass of the localization volumes they are associated with, as in (2.39). Hence,

$$\mathbf{X} = \frac{1}{\rho_0(\mathbf{X})} \sum_{\alpha=1}^{N} m^\alpha \mathbf{X}^\alpha \psi(\mathbf{X}^\alpha - \mathbf{X}) = \frac{\sum_{\alpha=1}^{N} m^\alpha \mathbf{X}^\alpha \psi(\mathbf{X}^\alpha - \mathbf{X})}{\sum_{\alpha=1}^{N} m^\alpha \psi(\mathbf{X}^\alpha - \mathbf{X})}. \tag{2.66}$$

The consequences of this assumption were mentioned earlier in this paper.

2.4.2 Densities

The expressions for ρ_0, $\mathbf{p}_0$ and $\rho_0 e$ defined in equations (2.10), (2.11) and (2.12), respectively, are reused for the micromorphic formulation. In addition, we define the following expression for micro-inertia tensor $\mathbf{I}$:

$$\rho_0 \mathbf{I}(\mathbf{X}) = \sum_{\alpha=1}^{N} m^\alpha \boldsymbol{\Xi}^\alpha \otimes \boldsymbol{\Xi}^\alpha \psi(\mathbf{X}^\alpha - \mathbf{X}) \tag{2.67}$$

[8] As the couple stress is a third order tensor, the divergence operator is taken to act on the outermost index of $\mathbf{M}$, *i.e.* $\nabla_{\mathbf{X}} \cdot \mathbf{M} = M_{iJK,K}$.

[9] Note that in equation (2.65), the notation $\mathbf{A} : \mathbf{B}$ represents the quantity $\sum_{i=1}^{3}\sum_{J=1}^{3} A_{iJ}B_{iJ}$ when $\mathbf{A}$ and $\mathbf{B}$ are second order tensors and the quantity $\sum_{i=1}^{3}\sum_{J=1}^{3}\sum_{K=1}^{3} A_{iJK}B_{iJK}$ when $\mathbf{A}$ and $\mathbf{B}$ are third order tensors.

In this expression, $\boldsymbol{\Xi}^\alpha \equiv \mathbf{X}^\alpha - \mathbf{X}$ using Eringen's notation.[10] We also note that micro-inertia is the second moment of mass for the localization volume centered at $\mathbf{X}$ (using relative position vectors $\boldsymbol{\Xi}^\alpha$), while mass density is the zeroth moment. Equation (2.66) can be used to show that the first moment of mass is, in-fact, zero:

$$\begin{aligned}
\sum_{\alpha=1}^{N} m^\alpha \boldsymbol{\Xi}^\alpha \psi(\mathbf{X}^\alpha - \mathbf{X}) &= \sum_{\alpha=1}^{N} m^\alpha \left(\mathbf{X}^\alpha - \mathbf{X}\right) \psi(\mathbf{X}^\alpha - \mathbf{X}) \\
&= \sum_{\alpha=1}^{N} m^\alpha \mathbf{X}^\alpha \psi(\mathbf{X}^\alpha - \mathbf{X}) - \sum_{\alpha=1}^{N} m^\alpha \mathbf{X} \psi(\mathbf{X}^\alpha - \mathbf{X}) \\
&= \rho_0 \mathbf{X} - \mathbf{X} \left(\sum_{\alpha=1}^{N} m^\alpha \psi(\mathbf{X}^\alpha - \mathbf{X}) \right) \\
&= \rho_0 \mathbf{X} - \rho_0 \mathbf{X} = 0
\end{aligned}$$

We also define a micro-rotational momentum tensor $\boldsymbol{\Upsilon}$,

$$\rho_0 \boldsymbol{\Upsilon}(\mathbf{X}, t) = \sum_{\alpha=1}^{N} m^\alpha \mathbf{v}^\alpha \otimes \boldsymbol{\Xi}^\alpha \psi(\mathbf{X}^\alpha - \mathbf{X}). \tag{2.68}$$

As for standard continuum theory, there are several interesting aspects of this expression. Consistency between equations (2.64) and (2.68) requires that $\boldsymbol{\Upsilon} = \frac{d\boldsymbol{\chi}}{dt} \cdot \mathbf{I}$. This makes sense; just as we earlier defined a continuum velocity field as the product of linear momentum density and the inverse of the mass density, now we define a "micro-deformational velocity tensor" ($\frac{d\boldsymbol{\chi}}{dt}$) as the product of micro-rotational momentum tensor and the inverse of the micro-inertia tensor:

$$\frac{d\boldsymbol{\chi}}{dt}(\mathbf{X}, t) = (\rho_0 \boldsymbol{\Upsilon}) \cdot (\rho_0 \mathbf{I})^{-1} = \left(\sum_{\alpha=1}^{N} m^\alpha \mathbf{v}^\alpha \otimes \boldsymbol{\Xi}^\alpha \psi(\mathbf{X}^\alpha - \mathbf{X}) \right) \cdot \left(\sum_{\alpha=1}^{N} m^\alpha \boldsymbol{\Xi}^\alpha \otimes \boldsymbol{\Xi}^\alpha \psi(\mathbf{X}^\alpha - \mathbf{X}) \right)^{-1}. \tag{2.69}$$

We also note that since the only time-dependent quantities in the above expression are the individual atomic velocities, we can integrate the expression to obtain the micro-deformation gradient,

$$\boldsymbol{\chi}(\mathbf{X}, t) = \left(\sum_{\alpha=1}^{N} m^\alpha \mathbf{x}^\alpha \otimes \boldsymbol{\Xi}^\alpha \psi(\mathbf{X}^\alpha - \mathbf{X}) \right) \cdot \left(\sum_{\alpha=1}^{N} m^\alpha \boldsymbol{\Xi}^\alpha \otimes \boldsymbol{\Xi}^\alpha \psi(\mathbf{X}^\alpha - \mathbf{X}) \right)^{-1}. \tag{2.70}$$

Using the expression $\mathbf{X}^\alpha = \mathbf{X} + \boldsymbol{\Xi}^\alpha$ with equation (2.66), we notice that $\boldsymbol{\chi} \to \mathbf{1}$ in the limit of zero deformation. We can use (2.69) and (2.70) to estimate the micro-gyration tensor defined by Eringen,

$$\boldsymbol{\nu} \equiv \frac{d\boldsymbol{\chi}}{dt} \cdot \boldsymbol{\chi}^{-1} = \left(\sum_{\alpha=1}^{N} m^\alpha \mathbf{v}^\alpha \otimes \boldsymbol{\Xi}^\alpha \psi(\mathbf{X}^\alpha - \mathbf{X}) \right) \cdot \left(\sum_{\alpha=1}^{N} m^\alpha \mathbf{x}^\alpha \otimes \boldsymbol{\Xi}^\alpha \psi(\mathbf{X}^\alpha - \mathbf{X}) \right)^{-1}. \tag{2.71}$$

Comparison of this expression with the expression by Chen and Lee [25] shows that our formulation, while similar, does display significant differences.

[10] Recall that this same definition was used in (2.39).

2.4.3 Derivation of Continuum Expressions

Balance of Mass and Micro-Inertia

As before, inspection of equation (2.10) reveals that $\frac{d\rho_0}{dt} = 0$. Similarly, we notice that the expression for micro-inertia given in equation (2.67) contains no atomic variables that are time-dependent. Hence,

$$\rho_0 \frac{d\mathbf{I}}{dt} = \frac{d\left(\rho_0 \mathbf{I}\right)}{dt} = 0.$$

Balance of Linear Momentum

We choose not to repeat the derivation shown in Section 2.2.4, but merely refer to our derived expressions for the 1^{st} Piola-Kirchhoff stress tensor in equation (2.30),

$$\mathbf{P}(\mathbf{X},t) = -\frac{1}{2}\sum_{\alpha=1}^{N}\sum_{\beta\neq\alpha}^{N} \mathbf{f}^{\alpha\beta} \otimes \mathbf{X}^{\alpha\beta} B^{\alpha\beta}(\mathbf{X}),$$

and the body force vector in equation (2.31),

$$\mathbf{b}(\mathbf{X},t) = \frac{\sum_{\alpha=1}^{N} m^{\alpha}\mathbf{b}^{\alpha}\psi(\mathbf{X}^{\alpha}-\mathbf{X})}{\sum_{\alpha=1}^{N} m^{\alpha}\psi(\mathbf{X}^{\alpha}-\mathbf{X})}.$$

We note that in this derivation it was not necessary to define the quantity $\mathbf{f}^{\alpha\beta}$, but merely acknowledge the relations $\mathbf{f}^{\alpha} = \sum_{\beta\neq\alpha}^{N} \mathbf{f}^{\alpha\beta}$ and $\mathbf{f}^{\beta\alpha} = -\mathbf{f}^{\alpha\beta}$. We will address the specific form of $\mathbf{f}^{\alpha\beta}$ in a later section.

Balance of Rotational Momentum

We start with the expression for micro-rotational momentum given in (2.68) and take its time derivative:

$$\begin{aligned}
\rho_0 \frac{d^2\boldsymbol{\chi}}{dt^2}\cdot\mathbf{I} &= \frac{d}{dt}\left(\rho\frac{d\boldsymbol{\chi}}{dt}\cdot\mathbf{I}\right) \\
&= \frac{d}{dt}\left(\rho_0\boldsymbol{\Upsilon}\right) \\
&= \frac{d}{dt}\left(\sum_{\alpha=1}^{N} m^{\alpha}\mathbf{v}^{\alpha}\otimes\boldsymbol{\Xi}^{\alpha}\psi(\mathbf{X}^{\alpha}-\mathbf{X})\right) \\
&= \sum_{\alpha=1}^{N} m^{\alpha}\frac{d\mathbf{v}^{\alpha}}{dt}\otimes\boldsymbol{\Xi}^{\alpha}\psi(\mathbf{X}^{\alpha}-\mathbf{X}) \\
&= \sum_{\alpha=1}^{N} \left(\mathbf{f}^{\alpha}+m^{\alpha}\mathbf{b}^{\alpha}\right)\otimes\boldsymbol{\Xi}^{\alpha}\psi(\mathbf{X}^{\alpha}-\mathbf{X})
\end{aligned}$$

By using the relation $\mathbf{f}^{\alpha} = \sum_{\beta\neq\alpha}^{N} \mathbf{f}^{\alpha\beta}$ and acknowledging that α and β are dummy indices, one obtains:

$$\rho_0 \frac{d^2\boldsymbol{\chi}}{dt^2} \cdot \mathbf{I} = \frac{1}{2} \sum_{\alpha=1}^{N} \sum_{\beta\neq\alpha}^{N} \mathbf{f}^{\alpha\beta} \otimes \left(\boldsymbol{\Xi}^{\alpha} \psi(\mathbf{X}^{\alpha} - \mathbf{X}) - \boldsymbol{\Xi}^{\beta} \psi(\mathbf{X}^{\beta} - \mathbf{X}) \right) + \sum_{\alpha=1}^{N} m^{\alpha} \mathbf{b}^{\alpha} \otimes \boldsymbol{\Xi}^{\alpha} \psi(\mathbf{X}^{\alpha} - \mathbf{X}) \tag{2.72}$$

In order to use the relationship shown in equation (2.23), we rearrange the first term on the RHS of (2.72) (labeled RHS_1 for convenience) into the following expression:

$$\mathrm{RHS}_1 = \frac{1}{2} \sum_{\alpha=1}^{N} \sum_{\beta\neq\alpha}^{N} \mathbf{f}^{\alpha\beta} \otimes \left(\mathbf{X}^{\alpha} \psi(\mathbf{X}^{\alpha} - \mathbf{X}) - \mathbf{X}^{\beta} \psi(\mathbf{X}^{\beta} - \mathbf{X}) - \mathbf{X} \left[\psi(\mathbf{X}^{\alpha} - \mathbf{X}) - \psi(\mathbf{X}^{\beta} - \mathbf{X}) \right] \right)$$

This can now be simplified to

$$\mathrm{RHS}_1 = \sum_{\alpha=1}^{N} \sum_{\beta\neq\alpha}^{N} \mathbf{f}^{\alpha\beta} \otimes \mathbf{X}^{\alpha} \psi(\mathbf{X}^{\alpha} - \mathbf{X}) + \frac{1}{2} \sum_{\alpha=1}^{N} \sum_{\beta\neq\alpha}^{N} \mathbf{f}^{\alpha\beta} \otimes \mathbf{X} \otimes \mathbf{X}^{\alpha\beta} \cdot \nabla_{\mathbf{X}} B^{\alpha\beta}(\mathbf{X}).$$

We then use the chain rule to bring the divergence operator to the outside of the second term. Hence,

$$\begin{aligned} \rho_0 \frac{d^2\boldsymbol{\chi}}{dt^2} \cdot \mathbf{I} = & \sum_{\alpha=1}^{N} \sum_{\beta\neq\alpha}^{N} \mathbf{f}^{\alpha\beta} \otimes \mathbf{X}^{\alpha} \psi(\mathbf{X}^{\alpha} - \mathbf{X}) \\ & + \nabla_{\mathbf{X}} \cdot \left(\frac{1}{2} \sum_{\alpha=1}^{N} \sum_{\beta\neq\alpha}^{N} \mathbf{f}^{\alpha\beta} \otimes \mathbf{X} \otimes \mathbf{X}^{\alpha\beta} B^{\alpha\beta}(\mathbf{X}) \right) \\ & - \frac{1}{2} \sum_{\alpha=1}^{N} \sum_{\beta\neq\alpha}^{N} \mathbf{f}^{\alpha\beta} \otimes \mathbf{X}^{\alpha\beta} B^{\alpha\beta}(\mathbf{X}) + \sum_{\alpha=1}^{N} m^{\alpha} \mathbf{b}^{\alpha} \otimes \boldsymbol{\Xi}^{\alpha} \psi(\mathbf{X}^{\alpha} - \mathbf{X}). \end{aligned} \tag{2.73}$$

At this point, we note that the third term on the RHS is none other than $\mathbf{P}$. Also, the first two terms on the RHS of equation (2.73) appear to lack frame invariance, *i.e.* the value of these terms will depend on the material frame coordinate origin. In order to correct this, we add (to the first term) and subtract (from the second term) the quantity

$$\nabla_{\mathbf{X}} \cdot \left(\frac{1}{2} \sum_{\alpha=1}^{N} \sum_{\beta\neq\alpha}^{N} \mathbf{f}^{\alpha\beta} \otimes \mathbf{X}^{\alpha} \otimes \mathbf{X}^{\alpha\beta} B^{\alpha\beta}(\mathbf{X}) \right),$$

and again use the relation in equation (2.23). This simplifies equation (2.73) to

$$\begin{aligned} \rho_0 \frac{d^2\boldsymbol{\chi}}{dt^2} \cdot \mathbf{I} = & \frac{1}{2} \sum_{\alpha=1}^{N} \sum_{\beta\neq\alpha}^{N} \mathbf{f}^{\alpha\beta} \otimes \mathbf{X}^{\alpha} \left(\psi(\mathbf{X}^{\alpha} - \mathbf{X}) + \psi(\mathbf{X}^{\beta} - \mathbf{X}) \right) \\ & + \nabla_{\mathbf{X}} \cdot \left(-\frac{1}{2} \sum_{\alpha=1}^{N} \sum_{\beta\neq\alpha}^{N} \mathbf{f}^{\alpha\beta} \otimes \boldsymbol{\Xi}^{\alpha} \otimes \mathbf{X}^{\alpha\beta} B^{\alpha\beta}(\mathbf{X}) \right) + \mathbf{P} + \sum_{\alpha=1}^{N} m^{\alpha} \mathbf{b}^{\alpha} \otimes \boldsymbol{\Xi}^{\alpha} \psi(\mathbf{X}^{\alpha} - \mathbf{X}). \end{aligned}$$

Finally, by separating the first term on the RHS into two separate terms, switching dummy indices α and β and using the relation $\mathbf{f}^{\beta\alpha} = -\mathbf{f}^{\alpha\beta}$, we arrive at

$$\begin{aligned}\rho_0 \frac{d^2\boldsymbol{\chi}}{dt^2} \cdot \mathbf{I} =& \frac{1}{2}\sum_{\alpha=1}^{N}\sum_{\beta\neq\alpha}^{N} \mathbf{f}^{\alpha\beta} \otimes \mathbf{X}^{\alpha\beta} \psi(\mathbf{X}^\alpha - \mathbf{X}) \\ &+ \nabla_{\mathbf{X}} \cdot \left(-\frac{1}{2}\sum_{\alpha=1}^{N}\sum_{\beta\neq\alpha}^{N} \mathbf{f}^{\alpha\beta} \otimes \boldsymbol{\Xi}^\alpha \otimes \mathbf{X}^{\alpha\beta} B^{\alpha\beta}(\mathbf{X}) \right) + \mathbf{P} + \sum_{\alpha=1}^{N} m^\alpha \mathbf{b}^\alpha \otimes \boldsymbol{\Xi}^\alpha \psi(\mathbf{X}^\alpha - \mathbf{X}).\end{aligned} \tag{2.74}$$

Comparing equation (2.74) with (2.64), we identify the expressions for couple stress,

$$\mathbf{M}(\mathbf{X},t) = -\frac{1}{2}\sum_{\alpha=1}^{N}\sum_{\beta\neq\alpha}^{N} \mathbf{f}^{\alpha\beta} \otimes \boldsymbol{\Xi}^\alpha \otimes \mathbf{X}^{\alpha\beta} B^{\alpha\beta}(\mathbf{X}), \tag{2.75}$$

for $\bar{\mathbf{P}}$,

$$\bar{\mathbf{P}}(\mathbf{X},t) = -\frac{1}{2}\sum_{\alpha=1}^{N}\sum_{\beta\neq\alpha}^{N} \mathbf{f}^{\alpha\beta} \otimes \mathbf{X}^{\alpha\beta} \psi(\mathbf{X}^\alpha - \mathbf{X}), \tag{2.76}$$

and for the body couple,

$$\mathbf{c}(\mathbf{X},t) = \frac{1}{\rho_0(\mathbf{X})}\sum_{\alpha=1}^{N} m^\alpha \mathbf{b}^\alpha \otimes \boldsymbol{\Xi}^\alpha \psi(\mathbf{X}^\alpha - \mathbf{X}) = \frac{\sum_{\alpha=1}^{N} m^\alpha \mathbf{b}^\alpha \otimes \boldsymbol{\Xi}^\alpha \psi(\mathbf{X}^\alpha - \mathbf{X})}{\sum_{\alpha=1}^{N} m^\alpha \psi(\mathbf{X}^\alpha - \mathbf{X})} \tag{2.77}$$

Before proceeding to the next section, we again point out that, with regard to the inter-atomic forces, we have only used the relations $\mathbf{f}^\alpha = \sum_{\beta\neq\alpha}^{N} \mathbf{f}^{\alpha\beta}$ and $\mathbf{f}^{\beta\alpha} = -\mathbf{f}^{\alpha\beta}$. We have not yet specified a form for the quantity $\mathbf{f}^{\alpha\beta}$.

Balance of Energy

As before, we begin with Hardy's expression for the system energy (2.12),

$$\begin{aligned}\rho_0 \frac{de}{dt} = \frac{d(\rho_0 e)}{dt} &= \frac{d}{dt}\left\{ \sum_{\alpha=1}^{N} \left\{ \frac{1}{2} m^\alpha (v^\alpha)^2 + \phi^\alpha \right\} \psi(\mathbf{X}^\alpha - \mathbf{X}) \right\} \\ &= \sum_{\alpha=1}^{N} \left\{ m^\alpha \left(\frac{d\mathbf{v}^\alpha}{dt} \cdot \mathbf{v}^\alpha \right) + \frac{d\phi^\alpha}{dt} \right\} \psi(\mathbf{X}^\alpha - \mathbf{X}) \\ &= \sum_{\alpha=1}^{N} \left\{ (\mathbf{f}^\alpha + m^\alpha \mathbf{b}^\alpha) \cdot \mathbf{v}^\alpha + \frac{d\phi^\alpha}{dt} \right\} \psi(\mathbf{X}^\alpha - \mathbf{X}) \\ &= \sum_{\alpha=1}^{N} \left\{ \mathbf{f}^\alpha \cdot \mathbf{v}^\alpha + \frac{d\phi^\alpha}{dt} \right\} \psi(\mathbf{X}^\alpha - \mathbf{X}) + \sum_{\alpha=1}^{N} m^\alpha \mathbf{b}^\alpha \cdot \mathbf{v}^\alpha \psi(\mathbf{X}^\alpha - \mathbf{X}).\end{aligned}$$

Using Hardy's second assumption, $\mathbf{f}^\alpha = \sum_{\eta=1}^{N} \mathbf{f}^{\alpha\eta}$, this can be also written as

$$\rho_0 \frac{de}{dt} = \sum_{\alpha=1}^{N} \left\{ \sum_{\eta\neq\alpha}^{N} \mathbf{f}^{\alpha\eta} \cdot \mathbf{v}^\alpha + \frac{d\phi^\alpha}{dt} \right\} \psi(\mathbf{X}^\alpha - \mathbf{X}) + \sum_{\alpha=1}^{N} m^\alpha \mathbf{b}^\alpha \cdot \mathbf{v}^\alpha \psi(\mathbf{X}^\alpha - \mathbf{X}). \tag{2.78}$$

In order to simplify the expression above, we must (as did Hardy) provide a relationship between the inter-atomic force $\mathbf{f}^{\alpha\eta}$ and the atomic potential energies ϕ^α and ϕ^η. Earlier, we noted that Hardy's third and fourth assumptions combined are only valid for pair and central force (*e.g.* EAM) potentials and not for potentials representative of directional bonding such as the Stillinger-Weber potential. Here, we substitute a new third assumption: each atom's potential energy depends only on the vectors that connect the atom under consideration to all other atoms. Hence, $\phi^\alpha = \phi^\alpha(\mathbf{x}^{\alpha\beta}, \mathbf{x}^{\alpha\gamma}, \ldots, \mathbf{x}^{\alpha N})$. We acknowledge that this form of ϕ^α is not invariant with respect to orientation of the coordinate system origin. (It is invariant with respect to translation.)[11] The actual form of ϕ^α is based on invariant arguments such as the angle between three neighboring atoms $\theta_\alpha^{\beta\gamma}$ which we express here in terms of relative position vectors, *i.e.* $\theta_\alpha^{\beta\gamma} = \frac{\mathbf{x}^{\beta\alpha} \cdot \mathbf{x}^{\gamma\alpha}}{\|\mathbf{x}^{\beta\alpha}\| \, \|\mathbf{x}^{\gamma\alpha}\|}$, for convenience in the subsequent mathematical developments. Using this new relation, the force between atoms α and η can be defined as

$$\mathbf{f}^{\alpha\eta} = -\left\{ \frac{\partial \phi^\alpha}{\partial \mathbf{x}^{\alpha\eta}} + \frac{\partial \phi^\eta}{\partial \mathbf{x}^{\alpha\eta}} \right\}, \tag{2.79}$$

our new fourth assumption.

Inserting equation (2.79) into the first term on the RHS of (2.78), this term (RHS_1) becomes the following:

$$\begin{aligned}
\mathrm{RHS}_1 &= \sum_{\alpha=1}^{N} \left\{ -\sum_{\eta\neq\alpha}^{N} \left\{ \frac{\partial \phi^\alpha}{\partial \mathbf{x}^{\alpha\eta}} + \frac{\partial \phi^\eta}{\partial \mathbf{x}^{\alpha\eta}} \right\} \cdot \mathbf{v}^\alpha + \frac{d\phi^\alpha}{dt} \right\} \psi(\mathbf{X}^\alpha - \mathbf{X}) \\
&= \sum_{\alpha=1}^{N} \left\{ -\sum_{\eta\neq\alpha}^{N} \left\{ \frac{\partial \phi^\alpha}{\partial \mathbf{x}^{\alpha\eta}} + \frac{\partial \phi^\eta}{\partial \mathbf{x}^{\alpha\eta}} \right\} \cdot \mathbf{v}^\alpha + \sum_{\eta\neq\alpha}^{N} \frac{\partial \phi^\alpha}{\partial \mathbf{x}^{\alpha\eta}} \cdot \mathbf{v}^{\alpha\eta} \right\} \psi(\mathbf{X}^\alpha - \mathbf{X}) \\
&= \sum_{\alpha=1}^{N} \sum_{\eta\neq\alpha}^{N} \left\{ -\frac{\partial \phi^\alpha}{\partial \mathbf{x}^{\alpha\eta}} \cdot \mathbf{v}^\alpha - \frac{\partial \phi^\eta}{\partial \mathbf{x}^{\alpha\eta}} \cdot \mathbf{v}^\alpha + \frac{\partial \phi^\alpha}{\partial \mathbf{x}^{\alpha\eta}} \cdot \mathbf{v}^\alpha - \frac{\partial \phi^\alpha}{\partial \mathbf{x}^{\alpha\eta}} \cdot \mathbf{v}^\eta \right\} \psi(\mathbf{X}^\alpha - \mathbf{X}) \\
&= \sum_{\alpha=1}^{N} \sum_{\eta\neq\alpha}^{N} \left\{ -\frac{\partial \phi^\eta}{\partial \mathbf{x}^{\alpha\eta}} \cdot \mathbf{v}^\alpha - \frac{\partial \phi^\alpha}{\partial \mathbf{x}^{\alpha\eta}} \cdot \mathbf{v}^\eta \right\} \psi(\mathbf{X}^\alpha - \mathbf{X}) \\
&= -\sum_{\alpha=1}^{N} \sum_{\eta\neq\alpha}^{N} \frac{\partial \phi^\eta}{\partial \mathbf{x}^{\alpha\eta}} \cdot \mathbf{v}^\alpha \psi(\mathbf{X}^\alpha - \mathbf{X}) - \sum_{\alpha=1}^{N} \sum_{\eta\neq\alpha}^{N} \frac{\partial \phi^\alpha}{\partial \mathbf{x}^{\alpha\eta}} \cdot \mathbf{v}^\eta \psi(\mathbf{X}^\alpha - \mathbf{X})
\end{aligned}$$

We now switch dummy indices on the right term of the above expression (*i.e.* $\alpha \leftrightarrow \eta$) and use the relation $\mathbf{x}^{\eta\alpha} = -\mathbf{x}^{\alpha\eta}$ to obtain

$$\mathrm{RHS}_1 = -\sum_{\alpha=1}^{N} \sum_{\eta\neq\alpha}^{N} \frac{\partial \phi^\eta}{\partial \mathbf{x}^{\alpha\eta}} \cdot \mathbf{v}^\alpha \left(\psi(\mathbf{X}^\alpha - \mathbf{X}) - \psi(\mathbf{X}^\eta - \mathbf{X}) \right). \tag{2.80}$$

[11] The Appendix of reference [222], discusses the fact that the system potential energy Φ must depend on its configuration through invariant quantities such as bond lengths, angles between bonds involving common atoms, areas and volumes.

Combining this result with equations (2.23) and (2.78), we arrive at

$$\rho_0 \frac{de}{dt} = \sum_{\alpha=1}^{N} \sum_{\eta \neq \alpha}^{N} \left(\frac{\partial \phi^{\eta}}{\partial \mathbf{x}^{\alpha\eta}} \cdot \mathbf{v}^{\alpha} \right) \left(\mathbf{X}^{\alpha\eta} \cdot \nabla_{\mathbf{X}} B^{\alpha\eta}(\mathbf{X}) \right) + \sum_{\alpha=1}^{N} m^{\alpha} \mathbf{b}^{\alpha} \cdot \mathbf{v}^{\alpha} \psi(\mathbf{X}^{\alpha} - \mathbf{X}). \tag{2.81}$$

As before, this can be modified to

$$\rho_0 \frac{de}{dt} = \nabla_{\mathbf{X}} \cdot \left(\sum_{\alpha=1}^{N} \sum_{\eta \neq \alpha}^{N} \left(\frac{\partial \phi^{\eta}}{\partial \mathbf{x}^{\alpha\eta}} \cdot \mathbf{v}^{\alpha} \right) \mathbf{X}^{\alpha\eta} B^{\alpha\eta}(\mathbf{X}) \right) + \sum_{\alpha=1}^{N} m^{\alpha} \mathbf{b}^{\alpha} \cdot \mathbf{v}^{\alpha} \psi(\mathbf{X}^{\alpha} - \mathbf{X}). \tag{2.82}$$

Similar to our material frame analysis of the balance of energy for standard continuum theory, we separate atomic motion from continuum motion by splitting the atomic velocities $\mathbf{v}^{\alpha}$. However, for a micromorphic continuum, this velocity becomes the sum of three terms,

$$\mathbf{v}^{\alpha} = \mathbf{v}(\mathbf{X}, t) + \frac{d\boldsymbol{\chi}}{dt}(\mathbf{X}, t) \cdot \boldsymbol{\Xi}^{\alpha} + \mathbf{w}^{\alpha}(\mathbf{X}, t), \tag{2.83}$$

where $\frac{d\boldsymbol{\chi}}{dt}(\mathbf{X}, t) \cdot \boldsymbol{\Xi}^{\alpha}$ now represents a continuum velocity associated with the microscale rotation and deformation of the microelement containing atom α. Substitution of this expression into (2.82), along with the aforementioned relation $e = \varepsilon + \frac{1}{2} v^2 + \frac{1}{2} \mathbf{I} : \left(\frac{d\boldsymbol{\chi}}{dt}^T \cdot \frac{d\boldsymbol{\chi}}{dt} \right)$, results in the following upon simplification:

$$\begin{aligned}
&\rho_0 \frac{d\varepsilon}{dt} + \rho_0 \frac{d\mathbf{v}}{dt} \cdot \mathbf{v} + \left(\rho_0 \frac{d^2\boldsymbol{\chi}}{dt^2} \cdot \mathbf{I} \right) : \frac{d\boldsymbol{\chi}}{dt} = \\
&\quad \nabla_{\mathbf{X}} \cdot \left(\mathbf{v} \cdot \left\{ \sum_{\alpha=1}^{N} \sum_{\eta \neq \alpha}^{N} \frac{\partial \phi^{\eta}}{\partial \mathbf{x}^{\alpha\eta}} \otimes \mathbf{X}^{\alpha\eta} B^{\alpha\eta}(\mathbf{X}) \right\} \right) \\
&\quad + \nabla_{\mathbf{X}} \cdot \left(\frac{d\boldsymbol{\chi}}{dt} : \left\{ \sum_{\alpha=1}^{N} \sum_{\eta \neq \alpha}^{N} \frac{\partial \phi^{\eta}}{\partial \mathbf{x}^{\alpha\eta}} \otimes \boldsymbol{\Xi}^{\alpha} \otimes \mathbf{X}^{\alpha\eta} B^{\alpha\eta}(\mathbf{X}) \right\} \right) \\
&\quad + \nabla_{\mathbf{X}} \cdot \left(\sum_{\alpha=1}^{N} \sum_{\eta \neq \alpha}^{N} \left(\frac{\partial \phi^{\eta}}{\partial \mathbf{x}^{\alpha\eta}} \cdot \mathbf{w}^{\alpha} \right) \mathbf{X}^{\alpha\eta} B^{\alpha\eta}(\mathbf{X}) \right) \\
&\quad + \rho_0 \mathbf{b} \cdot \mathbf{v} + \frac{d\boldsymbol{\chi}}{dt} : \left(\sum_{\alpha=1}^{N} m^{\alpha} \mathbf{b}^{\alpha} \otimes \boldsymbol{\Xi}^{\alpha} \psi(\mathbf{X}^{\alpha} - \mathbf{X}) \right) + \sum_{\alpha=1}^{N} m^{\alpha} \mathbf{b}^{\alpha} \cdot \mathbf{w}^{\alpha} \psi(\mathbf{X}^{\alpha} - \mathbf{X})
\end{aligned} \tag{2.84}$$

Equation (2.84) can be further simplified in two ways. On the LHS, the expressions $\rho_0 \frac{d\mathbf{v}}{dt}$ and $\rho_0 \frac{d^2\boldsymbol{\chi}}{dt^2} \cdot \mathbf{I}$ are replaced using the balance of linear and rotational momentum equations shown in equations (2.63) and (2.64), respectively. On the RHS, we can relate each divergence term to a corresponding continuum quantity. By using our new expression for inter-atomic forces defined in

equation (2.79), we notice that the 1^{st} Piola-Kirchhoff stress $\mathbf{P}$ is

$$\begin{aligned}
\mathbf{P} &= -\frac{1}{2}\sum_{\alpha=1}^{N}\sum_{\eta\neq\alpha}^{N}\mathbf{f}^{\alpha\eta}\otimes\mathbf{X}^{\alpha\eta}B^{\alpha\eta}(\mathbf{X}) \\
&= \frac{1}{2}\sum_{\alpha=1}^{N}\sum_{\eta\neq\alpha}^{N}\left\{\frac{\partial\phi^{\alpha}}{\partial\mathbf{x}^{\alpha\eta}}+\frac{\partial\phi^{\eta}}{\partial\mathbf{x}^{\alpha\eta}}\right\}\otimes\mathbf{X}^{\alpha\eta}B^{\alpha\eta}(\mathbf{X}) \\
&= \frac{1}{2}\left\{\sum_{\alpha=1}^{N}\sum_{\eta\neq\alpha}^{N}\frac{\partial\phi^{\alpha}}{\partial\mathbf{x}^{\alpha\eta}}\otimes\mathbf{X}^{\alpha\eta}B^{\alpha\eta}(\mathbf{X})+\sum_{\alpha=1}^{N}\sum_{\eta\neq\alpha}^{N}\frac{\partial\phi^{\eta}}{\partial\mathbf{x}^{\alpha\eta}}\otimes\mathbf{X}^{\alpha\eta}B^{\alpha\eta}(\mathbf{X})\right\} \\
&= \frac{1}{2}\left\{\sum_{\eta=1}^{N}\sum_{\alpha\neq\eta}^{N}\frac{\partial\phi^{\eta}}{\partial\mathbf{x}^{\eta\alpha}}\otimes\mathbf{X}^{\eta\alpha}B^{\eta\alpha}(\mathbf{X})+\sum_{\alpha=1}^{N}\sum_{\eta\neq\alpha}^{N}\frac{\partial\phi^{\eta}}{\partial\mathbf{x}^{\alpha\eta}}\otimes\mathbf{X}^{\alpha\eta}B^{\alpha\eta}(\mathbf{X})\right\} \\
&= \frac{1}{2}\left\{\sum_{\alpha=1}^{N}\sum_{\eta\neq\alpha}^{N}\frac{\partial\phi^{\eta}}{\partial\mathbf{x}^{\alpha\eta}}\otimes\mathbf{X}^{\alpha\eta}B^{\alpha\eta}(\mathbf{X})+\sum_{\alpha=1}^{N}\sum_{\eta\neq\alpha}^{N}\frac{\partial\phi^{\eta}}{\partial\mathbf{x}^{\alpha\eta}}\otimes\mathbf{X}^{\alpha\eta}B^{\alpha\eta}(\mathbf{X})\right\} \\
&= \sum_{\alpha=1}^{N}\sum_{\eta\neq\alpha}^{N}\frac{\partial\phi^{\eta}}{\partial\mathbf{x}^{\alpha\eta}}\otimes\mathbf{X}^{\alpha\eta}B^{\alpha\eta}(\mathbf{X}).
\end{aligned}$$

Hence,

$$\nabla_{\mathbf{X}}\cdot\left(\mathbf{v}\cdot\left\{\sum_{\alpha=1}^{N}\sum_{\eta\neq\alpha}^{N}\frac{\partial\phi^{\eta}}{\partial\mathbf{x}^{\alpha\eta}}\otimes\mathbf{X}^{\alpha\eta}B^{\alpha\eta}(\mathbf{X})\right\}\right)\rightarrow\nabla_{\mathbf{X}}\cdot(\mathbf{v}\cdot\mathbf{P})=\mathbf{P}:\frac{d\mathbf{F}}{dt}+\mathbf{v}\cdot(\nabla_{\mathbf{X}}\cdot\mathbf{P})\,. \tag{2.85}$$

Regarding the second divergence term in (2.84), we notice that the couple stress tensor (equation (2.75)) now has the form

$$\mathbf{M}=\frac{1}{2}\sum_{\alpha=1}^{N}\sum_{\eta\neq\alpha}^{N}\left\{\frac{\partial\phi^{\alpha}}{\partial\mathbf{x}^{\alpha\eta}}+\frac{\partial\phi^{\eta}}{\partial\mathbf{x}^{\alpha\eta}}\right\}\otimes\boldsymbol{\Xi}^{\alpha}\otimes\mathbf{X}^{\alpha\eta}B^{\alpha\eta}(\mathbf{X}).$$

Admittedly, it is not as easy to simplify this expression as it was to simplify the expression for $\mathbf{P}$. However, we note here that Delph asserted that any potential energy expression dependent on M atoms within the N-atom system is equally divided among the M atoms [40]. For example, the contribution for a 3-body energy term between atoms α, β and γ is divided equally into thirds for ϕ^{α}, ϕ^{β} and ϕ^{γ} respectively. Hence, this assertion results in the conclusion that while, in general, $\phi^{\alpha}\neq\phi^{\eta}$, it is the case that $\frac{\partial\phi^{\alpha}}{\partial\mathbf{x}^{\alpha\eta}}=\frac{\partial\phi^{\eta}}{\partial\mathbf{x}^{\alpha\eta}}$ since the portion of potential energy that provides non-zero values of this derivative is the same for both atoms α and η. Hence,

$$\mathbf{M}=\sum_{\alpha=1}^{N}\sum_{\eta\neq\alpha}^{N}\frac{\partial\phi^{\eta}}{\partial\mathbf{x}^{\alpha\eta}}\otimes\boldsymbol{\Xi}^{\alpha}\otimes\mathbf{X}^{\alpha\eta}B^{\alpha\eta}(\mathbf{X}),$$

and,

$$\begin{aligned}
\nabla_{\mathbf{X}}\cdot\left(\frac{d\boldsymbol{\chi}}{dt}:\left\{\sum_{\alpha=1}^{N}\sum_{\eta\neq\alpha}^{N}\frac{\partial\phi^{\eta}}{\partial\mathbf{x}^{\alpha\eta}}\otimes\boldsymbol{\Xi}^{\alpha}\otimes\mathbf{X}^{\alpha\eta}B^{\alpha\eta}(\mathbf{X})\right\}\right)&\rightarrow\nabla_{\mathbf{X}}\cdot\left(\frac{d\boldsymbol{\chi}}{dt}:\mathbf{M}\right) \\
&=\mathbf{M}:\left(\nabla_{\mathbf{X}}\frac{d\boldsymbol{\chi}}{dt}\right)+\frac{d\boldsymbol{\chi}}{dt}:(\nabla_{\mathbf{X}}\cdot\mathbf{M})
\end{aligned} \tag{2.86}$$

The third divergence term provides us with the definition for heat flux vector for a micromorphic system:

$$\mathbf{Q}(\mathbf{X},t) = -\sum_{\alpha=1}^{N}\sum_{\eta\neq\alpha}^{N}\left(\frac{\partial\phi^{\eta}}{\partial\mathbf{x}^{\alpha\eta}}\cdot\mathbf{w}^{\alpha}\right)\mathbf{X}^{\alpha\eta}B^{\alpha\eta}(\mathbf{X}) \tag{2.87}$$

Combining (2.85), (2.86) and (2.87) into equation (2.84), along with the earlier definitions for energy generation per unit mass (2.57) and body couple (2.77), we obtain:

$$\begin{aligned}\rho_0\frac{d\varepsilon}{dt} + (\nabla_{\mathbf{X}}\cdot\mathbf{P}+\rho_0\mathbf{b})\cdot\mathbf{v} + \left(\nabla_{\mathbf{X}}\cdot\mathbf{M}+\mathbf{P}-\bar{\mathbf{P}}+\rho_0\mathbf{c}\right):\frac{d\boldsymbol{\chi}}{dt} = \\ \mathbf{P}:\frac{d\mathbf{F}}{dt}+\mathbf{v}\cdot(\nabla_{\mathbf{X}}\cdot\mathbf{P})+\mathbf{M}:\left(\nabla_{\mathbf{X}}\frac{d\boldsymbol{\chi}}{dt}\right)+\frac{d\boldsymbol{\chi}}{dt}:(\nabla_{\mathbf{X}}\cdot\mathbf{M}) \\ -\nabla_{\mathbf{X}}\cdot\mathbf{Q}+\rho_0\mathbf{b}\cdot\mathbf{v}+\frac{d\boldsymbol{\chi}}{dt}:\rho_0\mathbf{c}+\rho_0 h\end{aligned} \tag{2.88}$$

Upon simplifying this equation, we obtain

$$\rho_0\frac{d\varepsilon}{dt} = \mathbf{P}:\frac{d\mathbf{F}}{dt}+\mathbf{M}:\left(\nabla_{\mathbf{X}}\frac{d\boldsymbol{\chi}}{dt}\right)+\left(\bar{\mathbf{P}}-\mathbf{P}\right):\frac{d\boldsymbol{\chi}}{dt}-\nabla_{\mathbf{X}}\cdot\mathbf{Q}+\rho_0 h, \tag{2.89}$$

which exactly matches the balance of energy equation derived by Eringen [47] and given earlier in equation (2.65).

2.5 Discussion

By constructing a material frame-based formalism similar to the spatial frame-based formalism developed by Hardy, we have derived expressions for continuum theory variables based on atomic-scale quantities. For an atomistic system governed by central force potentials, these expressions are based on conventional continuum theory and include the 1^{st} Piola-Kirchhoff stress tensor, a body force field, a heat flux vector field, and an energy generation rate. For an atomistic system where the inter-atomic potential is multi-body and directional in nature, these expressions are based on micromorphic continuum theory and also include a couple stress tensor and a body couple tensor field.

Our formulations are suitable for the analysis of solid mechanics problems for which rearrangement of the configuration due to large relative motions of neighboring atoms is minimal. For simulations involving fluid and gaseous states of matter the concepts of a reference configuration and deformation gradient are not well-defined. Hence, our formulations would have limited usefulness for these types of simulations. This would also be true for situations of dramatic molecular rearrangement, such as mixing (as happens in granular materials). For all of these cases, the original spatial frame formulation developed by Hardy would be appropriate. The difficulty inherent to developing a spatial frame formulation for a micromorphic continuum was discussed earlier, and more work is warranted to overcome this challenge. For the situation of plastic deformation, the use of the reference configuration should remain valid; however, this has yet to be verified and is deferred for future research.

Our expressions are distinct from both Hardy's original formulation, as well as the many other works discussed in the Introduction, as they are for material frame-based continuum variables. Exceptions to this are found in the text by Weiner [201, Chapter 4 and Appendix I in Chapter 6] and the articles by Andia and colleagues [7, 8, 36, 37]. As mentioned earlier, Andia *et al.* define an expression for P-K stress as a cell averaged quantity. Our expression is defined at a single material point and depends only on the size of the volume associated with that point in the sense that a minimum volume must be used to show consistency with expected continuum behavior. Additionally, both Andia *et al.* and Weiner make the distinction between internal and external forces, separating the interactions between atoms within the cell and the interactions between atoms with "ghost" atoms located across the periodic boundaries. This distinction is not needed for our approach.

The analyses presented in the Evaluation section clearly show that our derived expression for P-K stress is a full thermo-mechanical measure of stress despite the fact that it contains only a potential and not a kinetic term, unlike the Cauchy stress expression derived by Hardy. Our analysis also shows that our expression for $\mathbf{P}$ is consistent with Cauchy stress via the Piola transformation $\boldsymbol{\sigma} = \frac{1}{J}\mathbf{P}\cdot\mathbf{F}^T$. While, in the special case of a system average, Weiner's expression [201, Equation A44] is equivalent to our expression for $\mathbf{P}$ (2.30), we have gone one step further and made a strong connection between (2.30) and the expressions for Cauchy stress (2.34) and the virial.

In order to show the consistency of our expression with continuum thermodynamics, we chose our material configuration to be the zero temperature, undeformed state of the system simulated. Unlike conventional continuum mechanics where the choice of reference configuration and temperature is arbitrary, the selection of a zero temperature state as the reference configuration is mandatory for our formulation. This requirement was discussed by Weiner [201, Chapter 4], who noted that for the case of anharmonic pair potentials, a zero value of P-K stress is achieved only at zero temperature. This can be more easily understood by examining our expression for P-K stress,

$$\mathbf{P} = -\frac{1}{2}\sum_{\alpha=1}^{N}\sum_{\beta\neq\alpha}^{N}\mathbf{f}^{\alpha\beta}\otimes\mathbf{X}^{\alpha\beta}B^{\alpha\beta}(\mathbf{X}),$$

and comparing it with the expression derived by Hardy for Cauchy stress,

$$\boldsymbol{\sigma} = -\frac{1}{2}\sum_{\alpha=1}^{N}\sum_{\beta\neq\alpha}^{N}\mathbf{f}^{\alpha\beta}\otimes\mathbf{x}^{\alpha\beta}\tilde{B}^{\alpha\beta}(\mathbf{x}) - \sum_{\alpha=1}^{N}m^{\alpha}\mathbf{w}^{\alpha}\otimes\mathbf{w}^{\alpha}\tilde{\psi}(\mathbf{x}^{\alpha}-\mathbf{x}).$$

Here, we see that if we select the given current configuration to represent our material frame, the first term on the right-hand side of the Cauchy expression will exactly equal the full value of the P-K expression. However, this term will not equal zero for any system that has been equilibrated to a non-zero temperature. For that case, it is apparent that the second term on the right-hand side will be equal to a non-zero value. Ergo, the P-K and Cauchy stresses will differ by exactly this amount and the expected relationship between P-K and Cauchy stresses will not hold.

Although our continuum formulations are distinctly different from the works by Delph and Chen due to our use of a material frame basis, it is interesting to notice that our formulations offers two advantages. First, unlike in Delph's derivation, our stress expression appears in both the linear momentum and energy balance laws without modification. Second, unlike the work by Chen, the

balance laws our expressions satisfy are the same as from micromorphic continuum theory; no specialized "microscale balance laws" need to be postulated.

Our formulation, as applied to micromorphic theory, yields an expression for the couple stress tensor $\mathbf{M}$, equation (2.75). As couple stress has dimensions of stress times length, it is reasonable to ask if there is a characteristic length. The terms present in this expression include $\mathbf{f}^{\alpha\beta}$, $B^{\alpha\beta}(\mathbf{X})$, $\boldsymbol{\Xi}^{\alpha}$, and $\mathbf{X}^{\alpha\beta}$. The first of these, $\mathbf{f}^{\alpha\beta}$, is non-zero only for distances less than or equal to the cut-off distance of the inter-atomic potential used in the simulation. By comparison, $B^{\alpha\beta}(\mathbf{X})$ is non-zero over a region corresponding to the localization volume. The two remaining terms, $\boldsymbol{\Xi}^{\alpha}$ and $\mathbf{X}^{\alpha\beta}$, have no intrinsic length scale connected with them, as they span distances ranging from zero to the system size. Given the fact that both $\mathbf{f}^{\alpha\beta}$ and $B^{\alpha\beta}(\mathbf{X})$ go to zero outside their respective ranges, it is clear that the shorter of the two distances, *i.e.* the potential's cut-off distance or localization volume's size, constitutes an appropriate characteristic length. In most instances, the volume size is larger than the cut-off distance (a recommendation made in [222] for producing smooth continuum fields), and hence the latter defines the length scale for this microcontinuum.

Finally, in order to relate the material frame variables defined here to their spatial frame counterparts, it is necessary to define kinematic deformation variables such as the deformation gradient. It is interesting to note that few of the aforementioned articles establish such field variables. However, in equation (2.15) we define a displacement field $\mathbf{u}$ consistent with the same localization function and volumes used to define the thermodynamic variables. This field could easily be used to construct a locally-varying deformation gradient expression. Also, in equations (2.70) and (2.71) we derived expressions for the micro-deformation gradient $\boldsymbol{\chi}$ and micro-gyration tensor $\boldsymbol{\nu}$, respectively, the kinematic variables inherent to micromorphic continuum theory. It is interesting to note that if the relationship $\mathbf{x}^{\alpha} = \mathbf{x} + \boldsymbol{\xi}^{\alpha}$ is applied to equation (2.70), where $\boldsymbol{\xi}^{\alpha}$ is the spatial frame counterpart to $\boldsymbol{\Xi}^{\alpha}$, then it can also be shown that

$$\boldsymbol{\chi}(\mathbf{X},t) = \left(\sum_{\alpha=1}^{N} m^{\alpha} \boldsymbol{\xi}^{\alpha} \otimes \boldsymbol{\Xi}^{\alpha} \psi(\mathbf{X}^{\alpha} - \mathbf{X}) \right) \cdot \left(\sum_{\alpha=1}^{N} m^{\alpha} \boldsymbol{\Xi}^{\alpha} \otimes \boldsymbol{\Xi}^{\alpha} \psi(\mathbf{X}^{\alpha} - \mathbf{X}) \right)^{-1}. \tag{2.90}$$

This expression for micro-deformation gradient bears a strong resemblance to the expressions developed by both Horstemeyer *et al.* [66, 78, 79] and Zimmerman *et al.* [221, 223] to define an atomic-scale deformation gradient. Detailed comparisons between our micro-deformation gradient and the atomic-scale equivalent defined in these works is deferred for future work.

2.6 Appendix A

It can be shown that inter-atomic potentials representative of directional bonding will result in a non-symmetric Cauchy stress. To accomplish this, we use the "potential" portion of the Hardy expression, $\boldsymbol{\sigma} = -\frac{1}{2} \sum_{\alpha=1}^{N} \sum_{\beta \neq \alpha}^{N} \mathbf{f}^{\alpha\beta} \otimes \mathbf{x}^{\alpha\beta} \tilde{B}^{\alpha\beta}(\mathbf{x})$, combined with our new expression for $\mathbf{f}^{\alpha\beta} = -\left\{ \frac{\partial \phi^{\alpha}}{\partial \mathbf{x}^{\alpha\beta}} + \frac{\partial \phi^{\beta}}{\partial \mathbf{x}^{\alpha\beta}} \right\}$. As a simple case, we consider the interaction of only 3 atoms (α, β and δ) through a single 3-body potential energy term Φ,

$$\Phi = \Phi(\mathbf{x}^{\alpha\beta}, \mathbf{x}^{\alpha\delta}). \tag{A.1}$$

This form fits the case of the 3-body term in the Stillinger-Weber potential [177] where α is the center atom of the β-α-δ triplet and

$$\Phi(\mathbf{x}^{\alpha\beta},\mathbf{x}^{\alpha\delta}) = \varepsilon\lambda\exp(\frac{\gamma}{\frac{x^{\alpha\beta}}{\sigma}-a})\exp(\frac{\gamma}{\frac{x^{\alpha\gamma}}{\sigma}-a})\left\{\cos(\theta)+\frac{1}{3}\right\}^2, \tag{A.2}$$

where ε, λ, γ, σ and a are fitted material parameters and

$$\theta \equiv \arccos(\frac{\mathbf{x}^{\alpha\beta}\cdot\mathbf{x}^{\alpha\delta}}{x^{\alpha\beta}x^{\alpha\delta}}). \tag{A.3}$$

Using the relation $\phi^\alpha = \phi^\alpha(\mathbf{x}^{\alpha\beta},\mathbf{x}^{\alpha\gamma},\ldots,\mathbf{x}^{\alpha N})$, the full energy Φ is partitioned equally among the 3 atoms, $\phi^\alpha = \phi^\beta = \phi^\delta = \frac{1}{3}\Phi$. However, in order to correctly take partial derivatives of these individual energies, we must express the functional dependency for each energy correctly. For atom α, the expression is trivial,

$$\phi^\alpha = \frac{1}{3}\Phi(\mathbf{x}^{\alpha\beta},\mathbf{x}^{\alpha\delta}), \tag{A.4}$$

but for atoms β and δ, the expressions are

$$\phi^\beta = \phi^\beta(\mathbf{x}^{\beta\alpha},\mathbf{x}^{\beta\delta}) = \frac{1}{3}\Phi(\mathbf{x}^{\alpha\beta},\mathbf{x}^{\alpha\beta}+\mathbf{x}^{\beta\delta}) \tag{A.5}$$

$$\phi^\delta = \phi^\delta(\mathbf{x}^{\delta\alpha},\mathbf{x}^{\delta\beta}) = \frac{1}{3}\Phi(\mathbf{x}^{\alpha\delta}+\mathbf{x}^{\delta\beta},\mathbf{x}^{\alpha\delta}) \tag{A.6}$$

In these relations, we have substituted $\mathbf{x}^{\alpha\beta}+\mathbf{x}^{\beta\delta}$ for $\mathbf{x}^{\alpha\delta}$ in the expression for ϕ^β since it cannot depend directly on $\mathbf{x}^{\alpha\delta}$. Likewise for the ϕ^δ term, we have substituted $\mathbf{x}^{\alpha\delta}+\mathbf{x}^{\delta\beta}$ for $\mathbf{x}^{\alpha\beta}$. Obviously, clarity requires that any expression that uses Φ in a simple way must refer to its original form shown in (A.1). So, when partial derivatives are taken, they must include terms that may indirectly depend on certain variables. For example,

$$\frac{\partial\phi^\beta}{\partial\mathbf{x}^{\alpha\beta}} = \frac{1}{3}\left(\frac{\partial\Phi}{\partial\mathbf{x}^{\alpha\beta}}+\frac{\partial\Phi}{\partial\mathbf{x}^{\alpha\delta}}\frac{\partial\mathbf{x}^{\alpha\delta}}{\partial\mathbf{x}^{\alpha\beta}}\right) = \frac{1}{3}\left(\frac{\partial\Phi}{\partial\mathbf{x}^{\alpha\beta}}+\frac{\partial\Phi}{\partial\mathbf{x}^{\alpha\delta}}\right). \tag{A.7}$$

Equation (A.7) is easily understood. The first term inside the parentheses results from the derivative of Φ with respect to $\mathbf{x}^{\alpha\beta}$ as it appears explicitly within the normal functional form of Φ, but the second term is present because Φ also depends on $\mathbf{x}^{\alpha\delta}$, which itself depends on $\mathbf{x}^{\alpha\beta}$ through the relation $\mathbf{x}^{\alpha\delta} = \mathbf{x}^{\alpha\beta}+\mathbf{x}^{\beta\delta}$. Since

$$\frac{\partial\phi^\alpha}{\partial\mathbf{x}^{\alpha\beta}} = \frac{1}{3}\left(\frac{\partial\Phi}{\partial\mathbf{x}^{\alpha\beta}}\right), \tag{A.8}$$

we can now calculate $\mathbf{f}^{\alpha\beta}$ to be

$$\begin{aligned}\mathbf{f}^{\alpha\beta} &= -\left\{\frac{\partial\phi^\alpha}{\partial\mathbf{x}^{\alpha\beta}}+\frac{\partial\phi^\beta}{\partial\mathbf{x}^{\alpha\beta}}\right\}\\ &= -\left\{\frac{1}{3}\left(\frac{\partial\Phi}{\partial\mathbf{x}^{\alpha\beta}}\right)+\frac{1}{3}\left(\frac{\partial\Phi}{\partial\mathbf{x}^{\alpha\beta}}+\frac{\partial\Phi}{\partial\mathbf{x}^{\alpha\delta}}\right)\right\}\\ &= -\left\{\frac{2}{3}\frac{\partial\Phi}{\partial\mathbf{x}^{\alpha\beta}}+\frac{1}{3}\frac{\partial\Phi}{\partial\mathbf{x}^{\alpha\delta}}\right\}.\end{aligned} \tag{A.9}$$

Similarly, for this example

$$\mathbf{f}^{\alpha\delta} = -\left\{\frac{2}{3}\frac{\partial\Phi}{\partial\mathbf{x}^{\alpha\delta}} + \frac{1}{3}\frac{\partial\Phi}{\partial\mathbf{x}^{\alpha\beta}}\right\}, \tag{A.10}$$

It is interesting to note that the expression for $\mathbf{f}^{\alpha\beta}$ in (A.9) involves derivatives with respect to inter-atomic vectors other than just $\mathbf{x}^{\alpha\beta}$, and that it is not necessarily collinear with $\mathbf{x}^{\alpha\beta}$.

Combining the expressions in equations (A.9) and (A.10) with a similarly derived expression for $\mathbf{f}^{\beta\delta}$, the expression for Cauchy stress becomes:

$$\begin{aligned}
\boldsymbol{\sigma}(\mathbf{x},t) &= -\frac{1}{2}\sum_{\alpha=1}^{N}\sum_{\beta\neq\alpha}^{N}\mathbf{x}^{\alpha\beta}\otimes\mathbf{f}^{\alpha\beta}\tilde{B}^{\alpha\beta}(\mathbf{x}) \\
&= -\mathbf{x}^{\alpha\beta}\otimes\mathbf{f}^{\alpha\beta}\tilde{B}^{\alpha\beta}(\mathbf{x}) - \mathbf{x}^{\alpha\delta}\otimes\mathbf{f}^{\alpha\delta}\tilde{B}^{\alpha\delta}(\mathbf{x}) - \mathbf{x}^{\beta\delta}\otimes\mathbf{f}^{\beta\delta}\tilde{B}^{\beta\delta}(\mathbf{x}) \\
&= \mathbf{x}^{\alpha\beta}\otimes\left\{\frac{2}{3}\frac{\partial\Phi}{\partial\mathbf{x}^{\alpha\beta}} + \frac{1}{3}\frac{\partial\Phi}{\partial\mathbf{x}^{\alpha\delta}}\right\}\tilde{B}^{\alpha\beta}(\mathbf{x}) + \mathbf{x}^{\alpha\delta}\otimes\left\{\frac{1}{3}\frac{\partial\Phi}{\partial\mathbf{x}^{\alpha\beta}} + \frac{2}{3}\frac{\partial\Phi}{\partial\mathbf{x}^{\alpha\delta}}\right\}\tilde{B}^{\alpha\delta}(\mathbf{x}) \\
&\quad + \mathbf{x}^{\beta\delta}\otimes\left\{-\frac{1}{3}\frac{\partial\Phi}{\partial\mathbf{x}^{\alpha\beta}} + \frac{1}{3}\frac{\partial\Phi}{\partial\mathbf{x}^{\alpha\delta}}\right\}\tilde{B}^{\beta\delta}(\mathbf{x}),
\end{aligned} \tag{A.11}$$

which can be simplified to

$$\begin{aligned}
\boldsymbol{\sigma}(\mathbf{x},t) &= \mathbf{x}^{\alpha\beta}\otimes\left\{\frac{2}{3}\frac{\partial\Phi}{\partial\mathbf{x}^{\alpha\beta}} + \frac{1}{3}\frac{\partial\Phi}{\partial\mathbf{x}^{\alpha\delta}}\right\}\tilde{B}^{\alpha\beta}(\mathbf{x}) + \mathbf{x}^{\alpha\delta}\otimes\left\{\frac{1}{3}\frac{\partial\Phi}{\partial\mathbf{x}^{\alpha\beta}} + \frac{2}{3}\frac{\partial\Phi}{\partial\mathbf{x}^{\alpha\delta}}\right\}\tilde{B}^{\alpha\delta}(\mathbf{x}) \\
&\quad + \left\{\mathbf{x}^{\alpha\delta} - \mathbf{x}^{\alpha\beta}\right\}\otimes\left\{-\frac{1}{3}\frac{\partial\Phi}{\partial\mathbf{x}^{\alpha\beta}} + \frac{1}{3}\frac{\partial\Phi}{\partial\mathbf{x}^{\alpha\delta}}\right\}\tilde{B}^{\beta\delta}(\mathbf{x}).
\end{aligned} \tag{A.12}$$

To proceed further, we assume that the potential function Φ can be expressed an an alternative function $\tilde{\Phi}$ that depends only on the invariants $x^{\alpha\beta}$, $x^{\alpha\delta}$ and θ (as defined in equation (A.3)):

$$\Phi = \Phi(\mathbf{x}^{\alpha\beta},\mathbf{x}^{\alpha\delta}) = \tilde{\Phi}(x^{\alpha\beta},x^{\alpha\delta},\cos\theta). \tag{A.13}$$

This assumption is certainly true for the Stillinger-Weber 3-body term (A.2) and can be generalized for other potentials representative of directional bonding. Using (A.13), we obtain the relations

$$\begin{aligned}
\frac{\partial\Phi}{\partial\mathbf{x}^{\alpha\beta}} &= \frac{\partial\tilde{\Phi}}{\partial x^{\alpha\beta}}\frac{\mathbf{x}^{\alpha\beta}}{x^{\alpha\beta}} + \frac{\partial\tilde{\Phi}}{\partial c_\theta}\left[\frac{\mathbf{x}^{\alpha\delta}}{x^{\alpha\beta}x^{\alpha\delta}} - \frac{c_\theta}{x^{\alpha\beta}}\frac{\mathbf{x}^{\alpha\beta}}{x^{\alpha\beta}}\right] \\
\frac{\partial\Phi}{\partial\mathbf{x}^{\alpha\delta}} &= \frac{\partial\tilde{\Phi}}{\partial x^{\alpha\delta}}\frac{\mathbf{x}^{\alpha\delta}}{x^{\alpha\delta}} + \frac{\partial\tilde{\Phi}}{\partial c_\theta}\left[\frac{\mathbf{x}^{\alpha\beta}}{x^{\alpha\beta}x^{\alpha\delta}} - \frac{c_\theta}{x^{\alpha\delta}}\frac{\mathbf{x}^{\alpha\delta}}{x^{\alpha\delta}}\right],
\end{aligned} \tag{A.14}$$

where c_θ represents $\cos\theta$. Substituting the above relations into equation (A.12), we clearly see that the expression for $\boldsymbol{\sigma}(\mathbf{x},t)$ will contain many terms that are non-symmetric. Specifically, the quantities $\mathbf{x}^{\alpha\beta}\otimes\mathbf{x}^{\alpha\delta}$ and $\mathbf{x}^{\alpha\delta}\otimes\mathbf{x}^{\alpha\beta}$ will both be present but will not have the same scalar coefficient, a requirement for a symmetric tensor.

One result we can obtain is the expression for the average stress, $\bar{\boldsymbol{\sigma}}(t)$, for the entire volume V of the system. Integrating both sides of equation (A.12), we obtain

$$\begin{aligned}\bar{\boldsymbol{\sigma}}(t) &= \frac{1}{V}\left(\mathbf{x}^{\alpha\beta}\otimes\left\{\frac{2}{3}\frac{\partial\Phi}{\partial\mathbf{x}^{\alpha\beta}}+\frac{1}{3}\frac{\partial\Phi}{\partial\mathbf{x}^{\alpha\delta}}\right\}+\mathbf{x}^{\alpha\delta}\otimes\left\{\frac{1}{3}\frac{\partial\Phi}{\partial\mathbf{x}^{\alpha\beta}}+\frac{2}{3}\frac{\partial\Phi}{\partial\mathbf{x}^{\alpha\delta}}\right\}\right.\\ &\qquad\left.+\left\{\mathbf{x}^{\alpha\delta}-\mathbf{x}^{\alpha\beta}\right\}\otimes\left\{-\frac{1}{3}\frac{\partial\Phi}{\partial\mathbf{x}^{\alpha\beta}}+\frac{1}{3}\frac{\partial\Phi}{\partial\mathbf{x}^{\alpha\delta}}\right\}\right)\\ &= \frac{1}{V}\left(\mathbf{x}^{\alpha\beta}\otimes\frac{\partial\Phi}{\partial\mathbf{x}^{\alpha\beta}}+\mathbf{x}^{\alpha\delta}\otimes\frac{\partial\Phi}{\partial\mathbf{x}^{\alpha\delta}}\right)\end{aligned} \tag{A.15}$$

Substitution of (A.14) into (A.15), along with simplification of terms, results in the expression

$$\begin{aligned}\bar{\boldsymbol{\sigma}}(t) = \frac{1}{V}\left(\left[\frac{\partial\tilde{\Phi}}{\partial x^{\alpha\beta}}-\frac{\partial\tilde{\Phi}}{\partial c_\theta}\frac{c_\theta}{x^{\alpha\beta}}\right]\frac{\mathbf{x}^{\alpha\beta}\otimes\mathbf{x}^{\alpha\beta}}{x^{\alpha\beta}}+\left[\frac{\partial\tilde{\Phi}}{\partial x^{\alpha\delta}}-\frac{\partial\tilde{\Phi}}{\partial c_\theta}\frac{c_\theta}{x^{\alpha\delta}}\right]\frac{\mathbf{x}^{\alpha\delta}\otimes\mathbf{x}^{\alpha\delta}}{x^{\alpha\delta}}\right.\\ \left.+\frac{\partial\tilde{\Phi}}{\partial c_\theta}\frac{\left\{\mathbf{x}^{\alpha\beta}\otimes\mathbf{x}^{\alpha\delta}+\mathbf{x}^{\alpha\delta}\otimes\mathbf{x}^{\alpha\beta}\right\}}{x^{\alpha\beta}x^{\alpha\delta}}\right).\end{aligned} \tag{A.16}$$

Clearly, the average stress for the system is a symmetric quantity. This explains why standard continuum theory adequately describes the deformation of directional bonded materials such as silicon. At the macroscopic scale, asymmetries in stress are probably minor and unnoticeable. However, at the microscopic scale, these asymmetries may be significant and indicative of the need for a microcontinuum theory.

Chapter 3

The construction and application of an atomistic J-integral via Hardy estimates of continuum fields

Principal Authors: Reese E. Jones and Jonathan A. Zimmerman

In this chapter, we apply a Lagrangian kernel-based estimator of continuum fields to atomic data in order to estimate the **J**-integral for the analysis of cracks and dislocations. We show that this method has the properties of: consistency between the energy, stress and deformation fields; path independence of the contour integrals of the Eshelby stress; and excellent correlation with linear elastic fracture mechanics theory for appropriately constructed simulations. We discuss the appropriate reference configuration and reference energy for this type of analysis. Lastly, we use canonical examples to demonstrate that the proposed method is a direct and rational approach for estimating the configurational forces on atomic defects.

3.1 Introduction

At the macro-scale, Eshelbian mechanics has found myriad applications ranging from the analysis of defects to the modeling of the dynamics of phase boundaries [69]. With the advent of nanoscience and nanotechnology, there is strong motivation to extend its application to the nanoscale where issues of dissipation, compatibility, and isotropy are of both scientific and practical interest. For example, with an accurate measure of the atomic configurational forces we can construct traction-separation laws for macroscale closures of fracture problems and estimate resistance limits for defects propagating in complex environments, *e.g.*composed of clusters and aggregates of defects and dislocations, via simulation.

Eshelby's seminal work [48, 49] lead to Rice's well-known **J**-integral [152] of fracture mechanics and can be connected to Peach and Koehler's work [149] on the force on dislocations. The **J**-integral is a path independent contour or surface integral (in 2- or 3-dimensions, respectively) that evaluates the energetic driving force that acts to propagate an existing defect in a continuous medium. The **J**-integral is commonly used in numerical simulations of continuum mechanical deformation, such as the finite element method, to indicate when a critical loading state has been achieved that will result in crack growth. In the context of dislocations and linear elasticity, the **J**-integral represents the force to move a dislocation through the material in which it is embed-

ded. For both cracks and dislocations, the **J**-integral force is ultimately due to applied loads and interactions with other defects.

The use of molecular simulation methods to develop insight on mechanisms of fracture in materials has spawned numerous efforts to develop an "atomic-scale" **J**-integral, *i.e.* one estimated directly from atomistic information. The first such effort (known to the authors) is that of Inoue *et al.* [81, 82], who combined potential energy, the per-atom contribution to the virial and an estimate of the displacement gradient at an atom for designated atoms comprising a loop around a crack tip to calculate the "H-sum" parameter, an approximation for **J**. While the authors claim that this H-sum is path independent, their work clearly shows significant non-zero values of H for a closed path that does not enclose a crack tip.

Nakatani *et al.* [140, 141] attempted to avoid the difficulties that plague the calculation a contour integral by using a domain integral approach where atomic contributions to **J** are weighted spatially according to each atom's position within an annular region surrounding a crack tip. They examined how their estimate of **J** depended on the geometric features of the annular region. This work is interesting in two regards. First, the authors explicitly comment that an unloaded, uncracked system must be used to define a reference state with regard to strain energy density, with the exception of atoms at free surfaces where the reference energy is given by the surface energy. With regard to stress, they ascertain that the bulk lattice provides the appropriate reference value for every atom; whereas for energy, two different reference states are used. Second, Nakatani *et al.* show that their measurement of **J** agrees with the theoretical solution provided from linear elastic fracture mechanics (LEFM) only for small values of stress intensity factor, whereas for large deformation, deviation from the LEFM value occurs due to geometric nonlinearity. Both of these issues will be addressed later in this article. Jin and Yuan [86] and Khare *et al.* [93] have also used a domain integral approach for calculating an atomistic **J**-integral, where differences from the Nakatani *et al.* formulation are due to how strain energy density is calculated.

Xu *et al.* [205] presented calculations of **J** using an energy release rate form, *i.e.* energy per unit area created during crack advance, in order to estimate a critical value for the ductile fracture of a nickel crystal. Although fundamental in their approach, Xu *et al.* did not examine whether their metric is consistent with LEFM, nor with the contour-based methods that they cite, *e.g.* [81]. In addition, this approach is limited to defects that can propagate stably due to the need to make a finite difference approximation of the change in potential energy with respect to a (finite) change in crack length. As a consequence, it is clearly limited to estimating the critical value of **J**. No quantification of the driving force is possible prior to crack length extension. Also, it becomes complex in its application in the context of isolating the **J** of an individual defect in a group of defects, unlike contour based methods. In an attempt to use both atomistic and continuum simulation methods to characterize the fracture of a graphene sheet, Tsai *et al.* [189] have recently shown that calculation of such a strain energy release rate displays better agreement with a continuum model of fracture than using atomistic-based stress fields to directly estimate an appropriate stress intensity factor. For the latter method, these authors show that the near-tip stress fields display non-local behavior, making a quantitative estimate of stress intensity factor unreliable. However, calculations of energy release rate using both global and local techniques are in agreement with estimates made from their continuum model.

Finally, Choi and Kim [30] combined atomistics with anisotropic linear elasticity, a hybrid definition of atomic-scale deformation gradient, and an alternative contour integral to define their own metric of **J**. They too did not investigate consistency with LEFM, but rather focused on developing traction-separation relations for use in cohesive zone simulations.

In this article, we present a novel methodology for calculating the **J**-integral. We construct continuum variable fields from atomic data that are consistent with the continuum Euler balances of mass, momentum and energy, then use these fields in the traditional contour/surface integral expressions to estimate the **J**-integral. Our approach to estimate continuum fields from atomic data originated with Irving and Kirkwood's work [83] (which was later continued by Noll [143]). They established the consistency between Dirac delta weighted atomic point data and continuum fields through a correspondence between Newton's law governing the evolution of the particles and Euler's "hydrodynamic" balance laws governing the continuum. Hardy extended the averaging technique from Dirac delta weight functions to continuous kernels [71, 159], see also [200, 222] for review and applications. Hardy's and others' use of coarse-grained averages of atomic data has been shown by many researchers to be superior to per-atom data alone, in particular the atomic stress based on the virial theorem, with regards to producing results consistent with continuum mechanics theory. For example, Cormier *et al.* [35] showed that for the analysis of stress fields in the vicinity of an elastic inclusion, the use of coarse-graining produced fields closer in agreement with continuum estimates than did the per-atom virial stress. More recently, Admal and Tadmor [3] conducted an in-depth analytical and numerical study of how Hardy's expression for stress and the virial stress compare with each other and with other metrics used for estimating stress from atomistics. By examining cases of both homogeneous and inhomogeneous deformation, they conclude that the Hardy stress definition possesses higher accuracy and quicker convergence with averaging domain size than the other methods studied, including the coarse-grained (*i.e.* volume-averaged) virial stress.

Hardy's work, based in an Eulerian description of motion, was subsequently reformulated in the Lagrangian framework natural for solids by the authors in [224]. Given Eshelbian mechanics dependence on the material frame, it is rational to adopt the Lagrangian description. Our Lagrangian, kernel-based method, unlike that of previous work, has the benefits of preserving path independence down to a surprisingly small size. It must be emphasized that without this property any contour-based method that purports to give an estimate of **J** is questionable. In addition, the proposed method has excellent correspondence with linear elastic fracture and defect mechanics with regard to critical values and trends for idealized problems where there are analytical solutions. These properties will be demonstrated with numerical simulation of fundamental defect types in Section 3.5. Section 3.2 provides a brief summary of the continuum **J**-integral theory. Section 3.3 gives a concise summary of the continuum field estimators needed to calculate the **J**-integral and Section 3.4 discusses the various aspects of consistency, *e.g.*between stored energy and stress, needed to obtain accurate **J**-integral estimates from atomic data. As mentioned, in Section 3.5 representative simulations are given to validate the method and display its numerical properties. Lastly, the paper is concluded with a discussion of future work.

3.2 The Eshelby tensor

The Eshelby energy-momentum tensor $\mathcal{S}$ [48, 49] can be defined in terms of the free energy density Ψ, the deformation gradient $\mathbf{F}$ and the first Piola-Kirchhoff (PK) stress $\mathbf{P}$ as

$$\mathcal{S} = \Psi\mathbf{I} - \mathbf{F}^T\mathbf{P} \,. \tag{3.1}$$

The deformation gradient is a kinematic measure $\mathbf{F} = \boldsymbol{\nabla}_{\mathbf{X}}\boldsymbol{\chi}$ defined in terms of the motion $\mathbf{x} = \boldsymbol{\chi}(\mathbf{X},t)$ of material, with $\mathbf{X}$ being the reference position. It has many applications to the mechanics of defects, specifically in characterizing the evolution and propagation of cracks and dislocations, see, *e.g.*[69, 123]. Rice's directly related $\mathbf{J}$-integral [152] is defined as a boundary integral of $\mathcal{S}$

$$\mathbf{J} = \int_{\partial\Omega} \mathcal{S}\,\mathbf{N}\,dA = \int_{\partial\Omega} \Psi\mathbf{N} - \mathbf{F}^T\mathbf{P}\mathbf{N}\,dA \tag{3.2}$$

where the Eshelby stress acts on $\mathbf{N}$, the outward normal to the surface $\partial\Omega$ enclosing the region Ω in the reference configuration. For a region at a constant temperature and in equilibrium, this expression can be simplified to

$$\mathbf{J} = \int_{\partial\Omega} \Psi\mathbf{N} - \mathbf{H}^T\mathbf{P}\mathbf{N}\,dA = \int_{\partial\Omega} W\mathbf{N} - \mathbf{H}^T\mathbf{P}\mathbf{N}\,dA \tag{3.3}$$

The first equality requires equilibrium

$$\boldsymbol{\nabla}_{\mathbf{X}}\cdot\mathbf{P} = \mathbf{0} \quad \rightarrow \quad \int_{\partial\Omega} \mathbf{P}\mathbf{N}\,dA = \mathbf{0}\,, \tag{3.4}$$

and the relation between the deformation gradient $\mathbf{F}$ and the displacement gradient $\mathbf{H} = \mathbf{F} - \mathbf{I}$, with $\mathbf{u} = \mathbf{x} - \mathbf{X}$ being the displacement. The second equality requires that there is no heat flow, *i.e.* constant temperature, so the free energy density Ψ is equal to the internal energy density W with respect to the reference differential volume dV. The assumption of quasi-static motion at zero temperature will be used throughout the remainder of the paper.

As an aside, an Eulerian version of the J-integral can be derived using Nanson's formula, $\mathbf{n}\,da = \det(\mathbf{F})\,\mathbf{F}^{-T}\mathbf{N}dA$, so that (3.3) becomes

$$\begin{aligned}
\mathbf{J} &= \int_{\partial\Omega} \left(W\mathbf{I} - \mathbf{H}^T\mathbf{P}\right)\mathbf{N}\,dA \\
&= \int_{\partial\tilde{\Omega}} \left(W\mathbf{I} - \mathbf{F}^T\boldsymbol{\nabla}_{\mathbf{x}}^T\mathbf{u}\,\det(\mathbf{F})\,\mathbf{T}\mathbf{F}^{-T}\right)\frac{1}{\det(\mathbf{F})}\,\mathbf{F}^T\,\mathbf{n}\,da \\
&= \int_{\partial\tilde{\Omega}} \mathbf{F}^T\left(w\mathbf{I} - \boldsymbol{\nabla}_{\mathbf{x}}^T\mathbf{u}\,\mathbf{T}\right)\mathbf{n}\,da
\end{aligned}$$

given the Cauchy stress $\mathbf{T} = \frac{1}{\det(\mathbf{F})}\mathbf{P}\mathbf{F}^T$, energy density $w = \frac{1}{\det(\mathbf{F})}W$ in the current configuration occupied by $\tilde{\Omega}$, and spatial displacement gradient $\boldsymbol{\nabla}_{\mathbf{x}}\mathbf{u} = \mathbf{H}\mathbf{F}^{-1}$. Although attractive due to the usual connection between the Cauchy stress and the virial, this formulation still requires a reference configuration to define the displacement $\mathbf{u}$. As such, we use the material formulation, as is customary in the continuum mechanics community. It is also interesting to note that in [49], Eshelby derives

a spatial-frame version of the energy-momentum tensor $\boldsymbol{\Sigma} = w\mathbf{I} - \boldsymbol{\nabla}_{\mathbf{x}}^T \mathbf{u} \frac{\partial w}{\partial \boldsymbol{\nabla}_{\mathbf{x}} \mathbf{u}}$. However, the work-conjugate of displacement gradient $\frac{\partial w}{\partial \boldsymbol{\nabla}_{\mathbf{x}} \mathbf{u}}$ only equals the Cauchy stress in the small strain limit. This equality does not hold for general, finite deformation problems.

If the motion $\boldsymbol{\chi}$ is smooth enough in the region Ω for the application of the divergence theorem, the **J**-integral can be reinterpreted as the divergence of the Eshelby stress in the region bounded by $\partial\Omega$, *i.e.* $\int_{\partial\Omega} \mathcal{S}\mathbf{N}\, dA = \int_{\Omega} \boldsymbol{\nabla}_{\mathbf{X}} \cdot \mathcal{S}\, dV$. Given that the region is arbitrary, this statement can be localized to

$$\boldsymbol{\nabla}_{\mathbf{X}} \cdot \mathcal{S} = \boldsymbol{\nabla}_{\mathbf{X}} W - \boldsymbol{\nabla}_{\mathbf{X}} \mathbf{F}^T \mathbf{P} - \mathbf{F}^T \boldsymbol{\nabla}_{\mathbf{X}} \cdot \mathbf{P} = \mathbf{P} \boldsymbol{\nabla}_{\mathbf{X}} \mathbf{F} - \boldsymbol{\nabla}_{\mathbf{X}} \mathbf{F}^T \mathbf{P} = \mathbf{0} \tag{3.5}$$

assuming that the thermodynamic conjugacy between $\mathbf{P}$ and $\mathbf{F}$ holds, *i.e.*

$$\mathbf{P} = \frac{\partial W}{\partial \mathbf{F}} \,. \tag{3.6}$$

The last step in (3.5), *i.e.* $(P_{iB} F_{iB,A} - F_{iA,B} P_{iB}) = 0$, is only valid if the motion is twice differentiable *i.e.* $F_{iA,B} = x_{i,AB} = x_{i,BA} = F_{iB,A}$, so clearly the **J**-integral is sensitive to the compatibility of the motion. This result also leads directly to the fact that the **J**-integral around a closed region with a smooth motion is zero and consequently that $\mathbf{J}$ is path-independent for arbitrary contours around regions that contain singularities like cracks and dislocations.

It is well known that the Eshelby stress acts as a material force conjugate to the change in the reference configuration due to the evolution of a defect. Work conjugacy provides a fundamental definition for the Eshelby stress $\mathcal{S}$ and the **J**-integral. Starting with the total potential energy of a region Ω

$$\Pi(\mathbf{X}, \mathbf{x}, \mathbf{F}) = \int_{\Omega} W(\mathbf{X}, \mathbf{F})\, dV - \int_{\partial\Omega} \bar{\mathbf{p}} \cdot \mathbf{u}(\mathbf{x}, \mathbf{X})\, dA \tag{3.7}$$

where, here, body forces are omitted for simplicity and the applied boundary tractions $\bar{\mathbf{p}}$ are assumed to be independent of configuration $\mathbf{X}$. Now if a map $\boldsymbol{\varphi}_t(\mathbf{X})$ such that $\boldsymbol{\varphi}_t(\Omega) = \Omega$ is introduced to describe the configurational changes associated with the defect, the difference between the rates of change of $\Pi(\mathbf{X}, \boldsymbol{\chi}, \mathbf{F})$ and $\Pi(\boldsymbol{\varphi}_t(\mathbf{X}), \boldsymbol{\chi}, \mathbf{F})$ leads to the energy release rate

$$\dot{\Pi}(\boldsymbol{\varphi}_t(\mathbf{X}), \boldsymbol{\chi}, \mathbf{F}) - \dot{\Pi}(\mathbf{X}, \boldsymbol{\chi}, \mathbf{F}) = \int \left. \frac{\partial W}{\partial \mathbf{X}} \right|_{expl} \cdot \dot{\boldsymbol{\varphi}}\, dV \tag{3.8}$$

where

$$\left. \frac{\partial W}{\partial \mathbf{X}} \right|_{expl} \equiv \frac{\partial W(\mathbf{X}, \mathbf{F})}{\partial \mathbf{X}} = \frac{\partial W(\mathbf{X}, \mathbf{F}(\mathbf{X}))}{\partial \mathbf{X}} - \frac{\partial W(\mathbf{X}, \mathbf{F}(\mathbf{X}))}{\partial \mathbf{F}} : \boldsymbol{\nabla}_{\mathbf{X}} \mathbf{F} = \boldsymbol{\nabla}_{\mathbf{X}} \cdot \mathcal{S} \tag{3.9}$$

is work conjugate to the configurational change [49]. The **J**-integral is the resultant of these forces

$$\mathbf{J} = \int_{\partial\Omega} \mathcal{S}\mathbf{N}\, dA = \left. \frac{d\Pi}{d\mathbf{X}} \right|_{expl} \tag{3.10}$$

The details of Eshelbian mechanics specific to cracks and dislocations are given in Section 3.5.

3.3 Atom-based measures of continuum quantities

In order to measure the Eshelby stress field we need estimates of stored energy density W, the displacement gradient $\mathbf{H}$, and the first Piola-Kirchhoff stress $\mathbf{P}$. As mentioned in the Introduction, Hardy projection [71, 83, 224] has the advantage of being consistent with the continuum balance laws by extension of Irving and Kirkwood's seminal work [83] to continuous kernels. These kernels $\psi(\mathbf{x})$, also called "localization functions", have the basic properties:

$$\psi > 0 \tag{3.11}$$

$$\int_\Omega \psi \, dV = 1 \tag{3.12}$$

Given the material frame orientation of Eshelbian mechanics, we have chosen to use a Lagrangian description [224] of kinematic and dynamic quantities. In fact this choice is crucial in determining configurational forces like the $\mathbf{J}$-integral due to the fact that it naturally measures energy density, deformation and stress with respect to a given, fixed reference configuration.

In the following, Greek letters denote the label or index of a particular atom in the system. For instance, $\mathbf{x}^\alpha$ is the location of atom α.

3.3.1 Energy density

First, let us examine the stored energy density field W which can be defined as a local, weighted average of the potential energy per atom ϕ^α

$$W(\mathbf{X},t) = \sum_\alpha (\phi^\alpha(t) - \phi^\alpha_X)\, \psi(\mathbf{X} - \mathbf{X}^\alpha) = \sum_\alpha \phi^\alpha(t)\, \psi(\mathbf{X} - \mathbf{X}^\alpha) - W(\mathbf{X}) \tag{3.13}$$

where $\phi^\alpha_X = \phi^\alpha(\{\mathbf{X}^\beta\})$ in a fixed reference configuration $\{\mathbf{X}^\beta\}$, and $W(\mathbf{X}) = \sum_\alpha \phi^\alpha_X \psi(\mathbf{X} - \mathbf{X}^\alpha)$ by virtue of the fact that $\psi(\mathbf{X} - \mathbf{X}^\alpha)$ is independent of time. The field $W(\mathbf{X})$ is equal to the potential energy density for the zero temperature, perfect lattice configuration $\mathbf{X}^\alpha$. This reference configuration is not necessarily the initial configuration nor even occupiable from subsequent configurations of the system. This choice of zero point for $W(\mathbf{X},t)$ is necessary for $W(\mathbf{X},t) = 0$ to imply $\mathbf{P} = \mathbf{0}$, *i.e.* an unloaded reference state in a homogeneous system. (Readers are referred to the more elaborate discussion of this choice of reference configuration in [224].) The potential energy per atom ϕ^α can be defined by partitioning the total potential energy to the atoms in any reasonable way, *e.g.*partitioning the energy of a bond equally to all its constituent atoms (refer to [200] for more details).

3.3.2 Displacement gradient

In order to define the displacement gradient $\mathbf{H}$ in terms of atomic quantities, we must first define the displacement $\mathbf{u}$. This is done in a mass-weighted fashion

$$\mathbf{u}(\mathbf{X},t) = \frac{\sum_\alpha (\mathbf{x}^\alpha(t) - \mathbf{X}^\alpha)\, m^\alpha \psi(\mathbf{X}^\alpha - \mathbf{X})}{\sum_\alpha m^\alpha \psi(\mathbf{X}^\alpha - \mathbf{X})}, \tag{3.14}$$

with m^α being the mass of atom α, in order to connect to the dynamical variable, momentum, which is given a primitive definition.[1] A direct differentiation of this kernel estimator leads to

$$\boldsymbol{\nabla}_{\mathbf{X}}\mathbf{u} = \frac{\sum_{\alpha=1}^{N} (\mathbf{u}^\alpha - \mathbf{u}) m^\alpha \otimes \boldsymbol{\nabla}_{\mathbf{X}} \psi(\mathbf{X}^\alpha - \mathbf{X})}{\sum_{\alpha=1}^{N} m^\alpha \psi(\mathbf{X}^\alpha - \mathbf{X})} \tag{3.15}$$

Since we need to efficiently represent continuous fields, we instead adopt partition of unity interpolation $N_I \,|\, \sum_I N_I = 1$, specifically finite element (FE) shape functions. This choice allows us to compute, for example, (3.14) on a grid of points $\mathbf{X}_I$ and then interpolate $\mathbf{u}$ as

$$\mathbf{u}(\mathbf{X},t) = \sum_I \mathbf{u}_I(t) N_I(\mathbf{X}) = \sum_{I,\alpha} N_I\, \psi_{I\alpha}\, \mathbf{u}^\alpha, \tag{3.16}$$

where $\mathbf{u}_I = \mathbf{u}(\mathbf{X}_I,t)$ and $\psi_{Ia} = \psi(\mathbf{X}^\alpha - \mathbf{X}_I)$. A differentiation of this interpolation leads directly to our definition of the displacement gradient

$$\mathbf{H} = \boldsymbol{\nabla}_{\mathbf{X}}\mathbf{u} = \sum_I \mathbf{u}_I(t) \boldsymbol{\nabla}_{\mathbf{X}} N_I(\mathbf{X}) \,. \tag{3.17}$$

3.3.3 Stress

Finally, the referential first Piola-Kirchhoff stress [224] for pair potentials can be defined in terms of the force $\mathbf{f}^{\alpha\beta}$ between atoms α and β and the difference between their positions in the reference configuration $\mathbf{X}^{\alpha\beta} = \mathbf{X}^\alpha - \mathbf{X}^\beta$. Instead of a simple average of the virial weighted by $\psi_{I\alpha}$, the so-called "bond" function $B^{\alpha\beta}$ is required for consistency with the continuum. The bond function

$$B^{\alpha\beta}(\mathbf{X}) = \int_0^1 \psi\left(\lambda(\mathbf{X}^\alpha - \mathbf{X}) + (1-\lambda)(\mathbf{X}^\beta - \mathbf{X})\right) d\lambda \tag{3.18}$$

is constructed directly from the localization function ψ in order to have the defining property that the difference in localization values at α and β is the directional derivative along the vector from α to β, *i.e.*

$$\psi(\mathbf{X}^\alpha - \mathbf{X}) - \psi(\mathbf{X}^\beta - \mathbf{X}) = \mathbf{X}^{\beta\alpha} \cdot \boldsymbol{\nabla}_{\mathbf{X}} B^{\alpha\beta} \,. \tag{3.19}$$

[1] In the Hardy formalism [71], momentum is defined as $\sum_\alpha m^\alpha \mathbf{v}^\alpha \psi(\mathbf{X}^\alpha - \mathbf{X})$ and velocity as the ratio of momentum and mass density $\mathbf{v} = \frac{\sum_\alpha m^\alpha \mathbf{v}^\alpha \psi(\mathbf{X}^\alpha - \mathbf{X})}{\sum_\alpha m^\alpha \psi(\mathbf{X}^\alpha - \mathbf{X})}$.

Our definition of the first PK stress [224] is derived by equating the stress divergence in the balance of momentum with the ψ-weighted average of the forces $\mathbf{f}^\alpha$ of Newton's law for the particles,[2]

$$\nabla_{\mathbf{X}} \cdot \mathbf{P} = \sum_\alpha \mathbf{f}^\alpha(t)\psi(\mathbf{X}^\alpha - \mathbf{X}) \; . \tag{3.20}$$

Subsequent manipulation produces the following expression for first PK stress:

$$\mathbf{P}(\mathbf{X},t) = -\sum_{\alpha<\beta} \mathbf{f}^{\alpha\beta}(t) \otimes \mathbf{X}^{\alpha\beta} B^{\alpha\beta}(\mathbf{X}) \tag{3.21}$$

for pair potentials where $\mathbf{f}^{\alpha\beta}$ is the force between atom α and β. The evaluation of the line integral in (3.18) will be discussed in Section 3.4.

3.4 Consistency of the atomic and continuum descriptions

A number of issues need to be addressed to get accurate estimates of the **J**-integral using atom-based data. In the following sections we discuss: (a) the convergence of the field estimates with grid and kernel size; (b) the consistency between the energy, stress and deformation fields; and (c) the intrinsic errors in the contour integrals used to evaluate the divergence of the relevant stress fields.

In order to examine these issues, we performed molecular static and dynamic simulations in well defined ensembles with regard to energy, stress, and temperature. These simulations were done using the LAMMPS molecular simulation code [168] together with the "user-atc" package developed in-part by the authors.[3] In the discussion that follows (and in Section 3.5), specific simulation details are provided for each case examined.

3.4.1 Convergence of stress estimate

The consistency of Hardy's stress measure and the virial has been explored in [222] and [224] for the Eulerian and Lagrangian descriptions, respectively. We will revisit this subject to (a) prove that the two measures are exactly consistent in one-dimension and (b) show why they are only approximately so in higher dimensions, for the practical reason of tuning our subsequent simulation.

For a homogeneous system, the virial stress in one dimension is simply

$$\sigma = \frac{1}{2V}\sum_{\alpha,\beta} \nu^{\alpha\beta} = \frac{N}{2V}\sum_{\beta} \nu^{\alpha\beta} = \frac{N}{V}\sum_{s=1}^{n_s} \nu^s \tag{3.22}$$

[2] At zero temperature, the only difference between this definition of the first PK stress and that of the Cauchy stress is the replacement of $\mathbf{X}$ with $\mathbf{x}$ in the second leg of the dyad $\mathbf{f}^{\alpha\beta}(t) \otimes \mathbf{X}^{\alpha\beta}$ and in the function $B(\mathbf{X})$.

[3] More information can be found at the URL: http://lammps.sandia.gov/doc/fix_atc.html.

where $\nu^{\alpha\beta} = -f^{\alpha\beta} \otimes x^{\alpha\beta} = \nu^{\beta\alpha}$ is the virial contribution of pair $\alpha\beta$, and $\nu^s = f^{\alpha\beta_s} \otimes x^{\alpha\beta_s}$ is the virial contribution of the s-th shell. Here, $\beta_s = \alpha + s$ and n_s is the number of shells. The corresponding Hardy estimate of the Cauchy stress at a point $\mathbf{x}_I$ is

$$\sigma_I = \frac{1}{2} \sum_{\alpha,\beta} \nu^{\alpha\beta} B_I^{\alpha\beta} = \sum_{s=1}^{n_s} \nu^s \sum_{\alpha} B_I^{\alpha\beta_s} \tag{3.23}$$

So in order for this estimate to be consistent with the virial value, and in this case also with the Cauchy-Born stress, $\sum_\alpha B_I^{\alpha\beta_s}$ must be equal to $\frac{N}{V}$. Now re-examine (3.18) in this context

$$\sum_{\alpha} B_I^{\alpha\beta_s} = \sum_{\alpha} \int_0^1 \psi(\lambda x^{\alpha\beta_s} + x^{\beta_s} - x_I)\, d\lambda = \sum_{\alpha} \int_{x^\alpha}^{x^{\alpha+s}} \psi(x - x_I)\, dx \frac{1}{sa} \tag{3.24}$$

which is simplified via $x = \lambda x^{\alpha\beta_s} + x_s^\beta = \lambda(sa) + x^\alpha + (sa)$ where a is the lattice constant in the current configuration. Finally, realize that for the s-th version of this expression $\sum_\alpha \int_{x^\alpha}^{x^{\alpha+s}}$ gives us s copies of the domain (*i.e.* $\Omega = \mathbb{R}$, the real line)[4] so that

$$\sum_{\alpha} B_I^{\alpha\beta} = \sum_{\alpha} \int_{x^\alpha}^{x^{\alpha+s}} \psi(x - x_I)\, dx \frac{1}{sa} = s \int_{\Omega} \psi(x - x_I)\, dx \frac{1}{sa} = \frac{1}{a} \tag{3.25}$$

Since $\frac{N}{V} = \frac{1}{a}$ in one dimension, we have proved consistency for all admissible localization functions ψ and node locations x_I in one dimension. An analogous result holds for the first Piola-Kirchhoff stress, with a being the lattice constant in the reference configuration. This proof relies directly on the fact that the line integral in the definition for $B_I^{\alpha\beta}$ is also a volume integral equivalent, in one dimension, to the normalization condition (3.12). Hence, we can not expect this same result in three dimensions.

In fact, direct simulation shows, see Figure 3.1, that even for a homogeneous stress state the Hardy estimate is sensitive to alignment of the kernel support and the lattice. Here, Hardy estimates of the first PK stress using two types of kernels were compared to the Piola transformed virial stress. The results labeled "spline" employed a quartic spline with a cylindrical support aligned with the x_3 direction, and the results labeled "FE" used the bilinear shape function on the rectangular domain typically employed in finite elements. Note that these kernels are centered on an atom since typically centering the kernel at off-lattice sites leads to higher errors. For small values of stress the errors relative to the virial stress can be excessive, see Figure 3.1a, but fortunately these errors decreases with magnitude of stress, see Figure 3.1b. This error seems to be a fictitious residual stress induced by a bias in the method that becomes insignificant as stress levels increase.

An interesting and useful feature of the FE-based kernel is that it is exact relative to virial at radius equal to $\{1, 2, 4, \ldots\}a$. It also appears to be a biased estimator since it typically underpredicts stress. For both types of kernel the actual integration of the bond function (3.18) was performed using a 10 point Gauss quadrature.[5] For the non-FE kernel the domain of integration

[4] To see this, draw the lattice and skip every other atom, first for the even atoms and second for the odds. This constructs two copies of the real line for second nearest neighbors.

[5] The integration ψ can be accomplished analytically for a step function on any support since it involves only the difference in the intersection points; however, these type of kernels have lower accuracy in practice.

was the intersection of the line segment $\mathbf{X}^\alpha$ to $\mathbf{X}^\beta$ with the compact support of the kernel.[6] For the FE kernel, on the other hand, the quadrature points were placed on the line segment, without any regard to intersection of the support of the kernel and the segment delineating the bond, and the partition of unity property was used to assign contributions to the nodes whose support overlaps the bond. This was done for efficiency but also plays a role in the convergence of estimates with FE-based kernels. Put succinctly, the FE-based kernels can be tuned easily but the spline kernels allow the freedom of picking their support independent of mesh size.

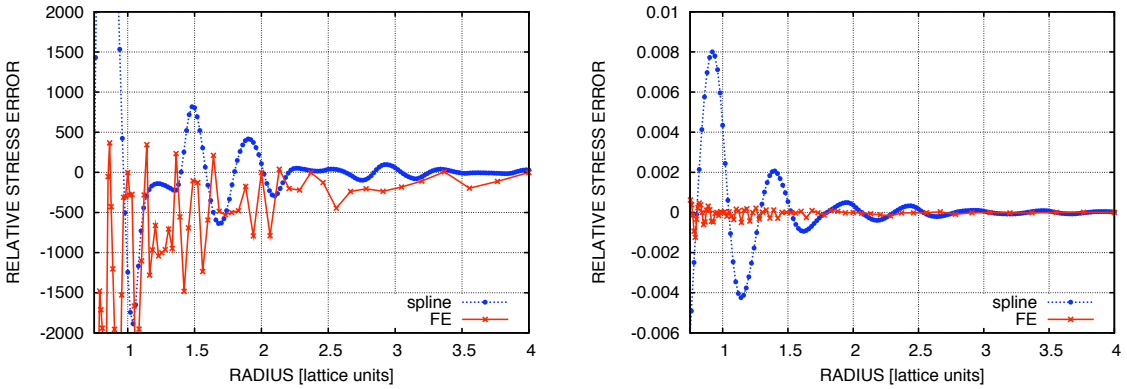

(a) low stress **(b)** high stress

Figure 3.1. Kernel and mesh convergence for support centered on an atom. Error in the 11 stress is computed relative to the virial which is $0.022\,bar$ in the left graph (a) and $2.06\times10^5\,bars$ in the right graph (b).

3.4.2 Work conjugacy

The work conjugacy of the stress and strain measures is crucial towards ensuring that these measures are physically meaningful, and to calculating an accurate energy release rate (3.8) which is at the core of the **J**-integral. The momentum balance in equilibrium is given by (3.4) and the energy balance is simply

$$\dot{W}(\mathbf{F}) = \frac{\partial W}{\partial \mathbf{F}} \cdot \dot{\mathbf{F}} = \mathbf{P} \cdot \dot{\mathbf{F}} \tag{3.27}$$

[6] A bond fully in support of a step kernel, or approximately for a general kernel in a region where B is nearly constant, does not contribute to the stress

$$B\sum_{\alpha,\beta}\mathbf{f}^{\alpha\beta}\otimes\mathbf{X}^{\alpha\beta} = B\sum_{\alpha,\beta}\mathbf{f}^{\alpha\beta}\otimes(\mathbf{X}^\beta-\mathbf{X}^\alpha) = B\left(\sum_\beta\mathbf{f}^\beta\otimes\mathbf{X}^\beta-\sum_\alpha\mathbf{f}^\alpha\otimes\mathbf{X}^\alpha\right)=\mathbf{0} \tag{3.26}$$

So it appears that accurate integration of $\mathbf{P}$ in regions where B has relatively high gradients is crucial.

in the absence of heat flow and heat generation, defect evolution or any other type of dissipation. For a quasi-static, constant temperature process, where time is merely a parameter, the energy balance (3.27) is exactly the rate of change of mechanical energy and a statement of work conjugacy between $\mathbf{P}$ and $\mathbf{F}$.

Using a undefected bulk system loaded by stretching the periodic box in one direction, we see in Figure 3.2 that the Hardy estimate of the referential stress (3.21) is consistent with the Hardy measures of energy (3.13) and deformation (3.17) through the usual first Piola-Kirchhoff formula (3.6). A central difference scheme with small load increments was used to evaluate the derivative $\frac{\partial W}{\partial \mathbf{H}} = \frac{\partial W}{\partial \mathbf{F}}$.

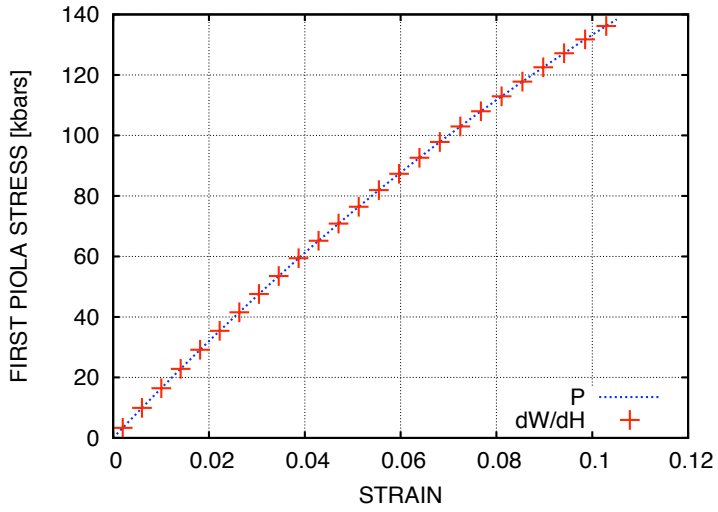

Figure 3.2. Consistency of the Hardy estimates of stress $\mathbf{P}$, energy W and strain $\boldsymbol{\varepsilon} = \mathbf{H}$ for a constrained, uniaxial tension simulation of EAM Cu. Only the along-axis, normal 11 components of $\mathbf{P}$ and $\boldsymbol{\varepsilon}$ are plotted.

3.4.3 Convergence of contour integration

There are intrinsic errors in calculating the continuum fields, as we have seen in Section 3.4.1. Additional errors affect our $\mathbf{J}$-integral results, specifically the errors due to the contour integration.[7] Although these errors affect the estimate of the contour integration of the Eshelby stress $\mathcal{S}$ (3.2), they are most clearly seen in the integration of the stress $\mathbf{P}$ since the expected value is known to be

[7] We have chosen contour integration over domain integration of the $\mathbf{J}$-integral mainly due to the fact that our data is at nodes, whereas in a finite element simulation the relevant data is a integration points interior to the interpolation cells.

zero for a system in equilibrium (3.4).[8]

The divergence theorem connects the boundary integral used to simplify (3.3) to the momentum balance (3.4)

$$\int_{\partial\Omega} \mathbf{P}\cdot\mathbf{N}\,dA = \int_{\Omega} \boldsymbol{\nabla}_{\mathbf{X}}\cdot\mathbf{P}\,dV \tag{3.28}$$

if $\mathbf{P}$ is differentiable and $\partial\Omega$ is piece-wise smooth. If we are using a non-interpolated version of Hardy and $\Psi(r)\to 0$ as $r\to\infty$ smoothly so that the fields are smooth and continuous, then the divergence theorem is applicable, *i.e.*

$$\int_{\partial\Omega} \mathbf{P}\cdot\mathbf{N}\,dA = \int_{\Omega} \boldsymbol{\nabla}\cdot\mathbf{P}\,dV = \sum_{\alpha}\mathbf{f}^{\alpha}\int_{\Omega}\Psi(\mathbf{X}^{\alpha}-\mathbf{X})\,dV = \mathbf{0} \tag{3.29}$$

by virtue of (3.20) since $\mathbf{f}^{\alpha}=\mathbf{0}$. On the other hand, if we are using a FE interpolation , we have

$$\int_{\square} \boldsymbol{\nabla}\cdot\mathbf{P}\,dV = \sum_{I}\mathbf{P}_I\cdot\int_{\square}\boldsymbol{\nabla}N_I\,dV \tag{3.30}$$

$$\int_{\partial\square} \mathbf{P}\cdot\mathbf{N}\,dA = \sum_{I}\mathbf{P}_I\cdot\int_{\partial\square} N_I\mathbf{N}\,dA \tag{3.31}$$

over every element region, with $\square$ being the domain of a single element and $\mathbf{P}_I = -\sum_{\alpha<\beta}\mathbf{f}^{\alpha\beta}\otimes\mathbf{X}^{\alpha\beta}B(\mathbf{X}^{\alpha I},\mathbf{X}^{\beta I})$. Note that within an element N_I is smooth enough for $\int_{\square}\boldsymbol{\nabla}N_I\,dV = \int_{\partial\square}N_I\mathbf{N}\,dA$. From this observation and the fact that the interpolated field is continuous we see that we can extend this result to any region that is an assembly of element volumes. Apparently, unlike the non-interpolated case where we have estimated divergence-free values at all points, the FE interpolated version has an inherent error at the interpolated points, *i.e.* $\mathbf{X}\neq\mathbf{X}_I$, that can be mitigated by taking finer meshes. This process, of course, reaches the non-interpolated case in the limit if the radius of the kernel is held fixed.

Figure 3.3 shows the rate of decrease in the integration error with decreasing mesh size for a simulation with a inhomogeneous stress field created by displacing a subset of atoms. By plotting the convergence of a spline kernel with a fixed radius in addition to a mesh kernel tied to the size of the mesh elements we have tried to separate the the field estimation error discussed in Section 3.4.1 from the error directly attributable to the contour quadrature. Given that the two curves are comparable, Figure 3.3 implies that the contour integration error is dominant, at least in this particular example of the compression of a hard inclusion in a quasi-two-dimensional periodic domain.[9]

[8] Note that errors in stress that are constant over the region of integration do not affect the accuracy of the contour integration.

[9] Note that a kernel with a very small support is not ideal in a thermalized system since it reduces the number of atoms to average over; we will revisit this issue in future work.

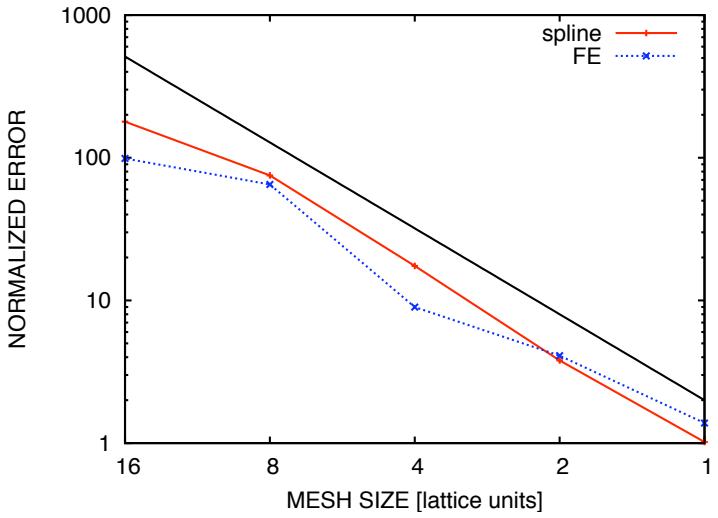

Figure 3.3. Error in the contour integration of stress in equilibrium as a function of mesh size (in lattice units) for a kernel of fixed radius (with cylindrical support with radius $R = 2.5$ lattice units) and a finite element kernel whose support scales with mesh size. The black trend line has an exponent of 2.

3.5 Simulations

In this section, we demonstrate the utility of our approach by estimating **J** for two common defects, an isolated crack and an isolated edge dislocation, and examining the properties of the atomistic **J** relative to its continuum counterpart. The configurations employed are meant to be simple enough to be relatively easy to interpret and compare to classical theory. The quasi-two-dimensional semi-infinite crack and dislocation have some common features since they are both treated as line defects in Eshelby's work [48] and their dissipation is due to a change in area swept by the line singularity; however, they also have some fundamental differences that make them canonical test problems for the atomistic **J**-integral.

In order to obtain accurate estimates of the **J**-integral we must choose the reference configuration and reference energy rationally. To obtain, for example, the correct Burgers vector for a dislocation, we must take the undeformed, perfect lattice sites as the reference configuration. This reference configuration is also appropriate for the crack. This choice can lead to non-zero stress in an unloaded initial state, at least in the case of a dislocation whereas for a crack the initial state is relatively stress-free. In addition to setting the reference configuration, we also choose to cut the interpolation mesh in order to allow for jumps in the fields. This is particularly crucial for estimating Burgers vector from the displacement field but makes no significant difference in the **J**-integral in the crack or the dislocation, as we will see. We also have some freedom in assigning the reference energy density (3.13). For the crack configuration, we set it to the energy density of

the undeformed, unrelaxed bulk after the bonds that form the crack have been deleted. This has the effect of negating the surface energy present in the initial configuration. For the dislocation case, we set the reference energy density equal to a value corresponding to an unloaded bulk crystal.

In all the following simulations we used a FE-based kernel and a mesh spacing set to the lattice size for efficiency and accuracy. Periodic boundary conditions were used in the third dimension to effect plane strain. In all the examples, we use energy minimization to create a sequence of zero temperature lattice configurations parametrized by the loading. As already mentioned, simulations were performed using the LAMMPS molecular simulation code [168]. Units given in this paper are the same as the 'metal' units designated within LAMMPS, *e.g.*distance in units of Angstroms ($1\mathring{A} = 0.1\,nm$), stress in units of *bars* ($1\,bar = 0.1\,MPa$), energy in units of *eV* ($1\,eV = 1.602 \times 10^{-19}\,J$).

3.5.1 Planar crack

In this example we examine a quasi-two dimensional, non-branching idealized crack propagating in the $\mathbf{e}_1$ direction with the crack front aligned with $\mathbf{e}_3$. As mentioned in Section 3.2, the **J**-integral is work conjugate to the change in reference configuration, specifically the area of an idealized crack with a single crack front $A_c = L_3\ell$. Here the length of the crack is ℓ and the depth of the system is L_3. The potential energy of such a system $\Pi(\boldsymbol{\xi}, \mathbf{F})$ is explicitly a function of the location of the crack tip $\boldsymbol{\xi}(t)$ in the reference configuration so that

$$\dot{\Pi} = \mathbf{J} \cdot \dot{\boldsymbol{\xi}} L_3 = J_1 L_3 \dot{\ell} \tag{3.32}$$

Semi-infinite crack

In order to directly compare an atomic system with this theory, we form a crack in an Au FCC system by deleting interactions crossing the $(-x_1)$-x_3 half plane in a cylindrical region of $22a$ in radius, see Figure 3.4, where the lattice spacing is $a = 4.08\mathring{A}$, $\mathbf{e}_1$ is aligned with $\langle 100 \rangle$, and $\mathbf{e}_2$ is aligned with $\langle 010 \rangle$. The displacement of the outer annulus of atoms, approximately $2a$ thick to avoid spurious free surface effects, was prescribed from the linear elastic fracture mechanics (LEFM) solution [107, Chapter 2] to this boundary value problem:

$$\begin{aligned} u_1 &= \frac{K_I}{2\mu}\sqrt{\frac{r}{2\pi}}\cos\left(\frac{\theta}{2}\right)\left[\kappa - 1 + 2\sin^2\left(\frac{\theta}{2}\right)\right] \\ u_2 &= \frac{K_I}{2\mu}\sqrt{\frac{r}{2\pi}}\sin\left(\frac{\theta}{2}\right)\left[\kappa + 1 - 2\cos^2\left(\frac{\theta}{2}\right)\right] \end{aligned} \tag{3.33}$$

where K_I is the stress intensity factor parametrizing the solution, (r, θ) are the usual polar coordinates and $u_3 = 0$ in plane strain. Note that the origin of coordinates was not updated to follow the crack tip. Periodic boundary conditions were used in the out-of-plane direction $\mathbf{e}_3$ which was $3a$ deep. Before loading, the reference configuration is set to the perfect lattice sites and the reference energy is such that it negates the surface stress induced by the initial cut. Our configuration and

methodology are similar to that used by Farkas and coworkers [53, 54, 145], who verified that this technique shows good correspondence with expectations from LEFM regarding predicting the onset of brittle cleavage.

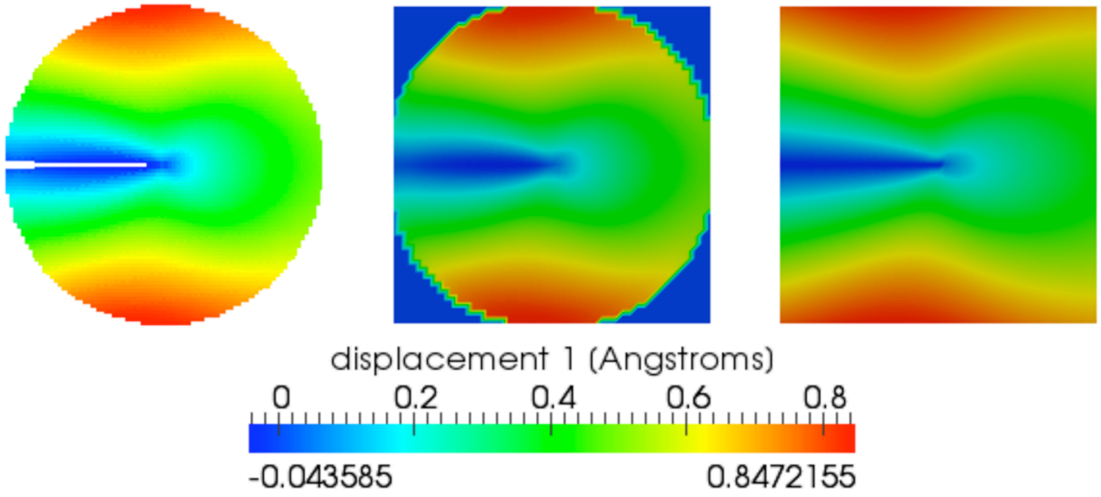

Figure 3.4. The configuration of single crack showing the u_1 displacement of the underlying MD lattice (left), Hardy estimate of the continuum fields (middle), and the prediction of LEFM (right)

Although the atomic system is not exactly the idealization of the continuum LEFM solution, it is clear from Figure 3.4 that the two displacement solutions compare well. This is despite the fact that the atomic system is anisotropic, non-linear, and does not have a sharp crack with parallel faces. In order to distinguish non-linear geometrical effects from the non-linearity of the typical potential we simulated the cracking process with a third nearest neighbor Lennard-Jones (LJ) potential and also with a purely harmonic one. The LJ potential used is a shifted and truncated version of original Lennard-Jones function, shown in equation (121) of [100], with parameter values $\varepsilon = 0.72427860$ eV, $\sigma = 2.59814680$ Å, and $r^c = 2.1\sigma = 5.45610827$ Å. The harmonic potential is a pair potential with the energy per pair equal to $\frac{1}{2}k(r - r_o)^2$, with parameters $k = 6.33422$ eV/Å^2 and $r_o = 2.88499567$ Å. An atomic interaction cutoff distance of 3.60624 Å was used to include only nearest neighbor interactions, and neighbor assignment was only done once, during the simulation setup (please note that this freezing of the neighbor lists was only done for the harmonic potential). The values of r_o and k were specifically chosen such that the LJ and harmonic materials possessed the same values of lattice parameter and elastic modulus C_{11} at zero temperature. The choice of fitting C_{11}, while arbitrary, is reasonable given the nature of Mode I loading and the cubic structure of the modeled crystal. Parameters of potentials are usually tuned using cohesive energy (the energy per atom for a crystal's bulk, equilibrium configuration), surface energy, or work of decohesion (the amount of energy per unit area expended to create free surfaces). For the harmonic model, both cohesive energy and surface energy are zero, while the work of decohesion is effectively in-

finite and thus not well-defined. Hence, the choice was made to match C_{11} between the LJ and harmonic potentials. Figure 3.4 and Figure 3.5 show the results for the harmonic system where the only non-linearities are of a geometric nature. Note that these results are shown for a mesh without any cuts to allow discontinuities in the field across the crack. We performed analogous simulations with such a cut and the results were comparable. Also, it should be clear that using perfect lattice sites and a Lagrangian formulation effectively gives a conformal map between the lattice and the mesh throughout the deformation process. Lastly, it should be noted that a **J**-integral based on a coarse-grained atomic virial transformed to a 1st PK stress using the estimated displacement gradient also achieved path-independence commensurate with our proposed method. This demonstrates that the particular stress measure may not be crucial for some simulations; however, the use of an averaged virial would have to be evaluated on a case-by-case basis whereas the Hardy measure's property of consistency with the continuum momentum balance gives us confidence that it is universally applicable as an accurate measure of stress in an inhomogeneous environment.

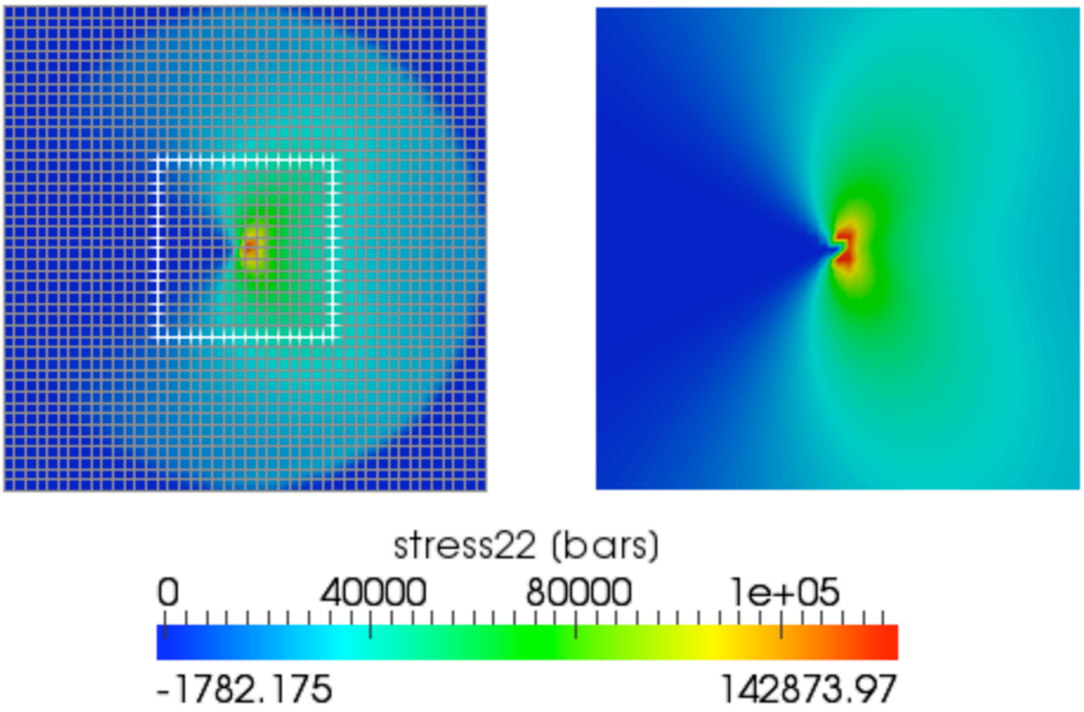

Figure 3.5. The P_{22} stress from the Hardy estimate (left) and from LEFM theory (right). A mid-size contour loop ("loop 2") and the FE interpolation grid are also shown on the left. Note that the apparent asymmetry of the LEFM solution at the crack tip is an artifact of the graphical tool used to produce the figure.

We also note that Figure 3.5 shows satisfaction of the traction-free condition on the crack faces, as the value of P_{22} is nominally close to zero for the Hardy estimate. The existence of a traction free

surface near the boundary of a lattice was established by Zimmerman *et al.* [222] for the original Hardy formulation, and is confirmed here for the material frame formulation [224].

In Figure 3.5, we compare the stress fields with those of LEFM [107, Chapter 2]

$$\begin{aligned}
\sigma_{11} &= \frac{K_I}{\sqrt{2\mu r}}\cos\left(\frac{\theta}{2}\right)\left[1-\sin\left(\frac{\theta}{2}\right)\sin\left(\frac{3\theta}{2}\right)\right] \\
\sigma_{22} &= \frac{K_I}{\sqrt{2\mu r}}\cos\left(\frac{\theta}{2}\right)\left[1+\sin\left(\frac{\theta}{2}\right)\sin\left(\frac{3\theta}{2}\right)\right] \\
\sigma_{12} &= \frac{K_I}{\sqrt{2\mu r}}\cos\left(\frac{\theta}{2}\right)\sin\left(\frac{\theta}{2}\right)\cos\left(\frac{3\theta}{2}\right)
\end{aligned} \tag{3.34}$$

To evaluate the **J**-integral, we use four square loops centered on the crack tip with side lengths of $8a$ (loop 1), $16a$ (loop 2), $20a$ (loop 3) and $24a$ (loop 4), where a is the lattice constant of the atomic crystal. For example, Figure 3.5 shows loop 2 superimposed on the estimated P_{22} stress field. Note that we set the spacing of the interpolation mesh to a in this and all subsequent simulations to reduce contour integration errors.

Using the fundamental crack tip solution (3.33) and superposition, LEFM predicts the value of **J** to be quadratically dependent on the stress intensity factor K_I and inversely proportional to the appropriate modulus E^*:

$$J_1 = \frac{K_I^2}{E^*} \quad J_2 = J_3 = 0 \tag{3.35}$$

For our case of normal (mode I) loading, and given the cubic symmetry of the lattice, the modulus E^* is

$$E^* = \frac{E}{1-\nu^2} = \frac{C_{11}-2C_{12}^2/(C_{11}+C_{12})}{1-(C_{12}/(C_{11}+C_{12}))^2}. \tag{3.36}$$

For the LJ potential, $C_{11} = 4.97478 \times 10^6$ bars, $C_{12} = 2.8158 \times 10^6$ bars, and $E^* = 3.38099 \times 10^6$ bars. It has a surface energy of 0.1599 eV/Å^2. For the harmonic potential, $C_{11} = 4.97478 \times 10^6$ bars, $C_{12} = 2.48739 \times 10^6$ bars, and $E^* = 3.73108 \times 10^6$ bars. No well-defined surface energy exists for the harmonic potential.

Figure 3.6 clearly establishes path independence of the atomistic **J**-integral even at this extremely small length-scale and also shows that a loop (loop 0) not around the defect generates an insignificant $J_1 < 0.001$ in reduced units. The fact that $J_2 < 10^{-7}$ in reduced units is another indication that we obtain accurate results.

Figure 3.7 shows the nearly perfect quadratic dependence of J_1 on loading K_I of the harmonic potential and a slight deviation due to strain softening apparent at higher loads in the Lennard-Jones system. Both systems correspond very well to the LEFM result at low loads (and correspondingly small strains). The deviation at higher strains could well be due to the growth of the non-linear region with loading which would invalidate our use of (3.33) as "far-field" loading.

As the loading increases, the LJ crack propagates. Griffith's criterion states that a reversible crack in equilibrium will be in incipient propagation if the available mechanical energy J_1 is equal

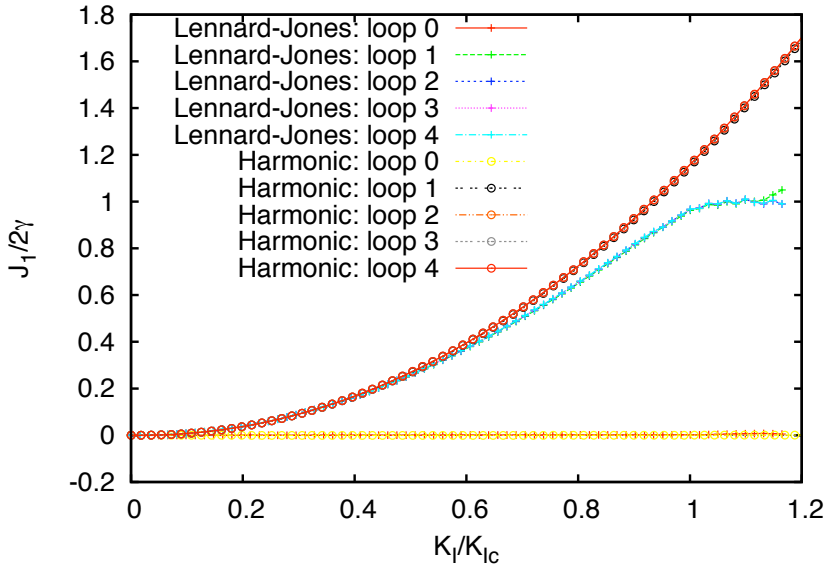

Figure 3.6. The calculated **J**-integral for the single crack configuration showing path independence. The **J**-integral values were normalized by twice the surface energy of the Lennard-Jones system and the loading parameter K_I by the corresponding critical value K_{Ic} for the Lennard-Jones system. Note that J_2 components of all loops were negligible and not plotted.

to the resistance to propagation R

$$J_1 = -\frac{\partial \Pi}{\partial A_c} \leq R \tag{3.37}$$

For an ideal brittle crack the resistance R is equal to the energy of the two new surfaces created by the crack, *i.e.* $R = 2\gamma$ where γ is surface energy. Consequently, the critical load K_{Ic} can be calculated as $K_{Ic} = \sqrt{2\gamma E^*}$. Figures 3.6 and 3.7 demonstrate that the LJ system attains its ideal crack resistance limit upon crack propagation, which initiates at the appropriate load K_{Ic} and is stable and incremental with subsequent loading.

Note that simulations discussed in this section show no evidence of lattice trapping, a phenomenon first identified by Thomson *et al.* [184] for discrete models of fracture in which a crack is stable for applied loadings that exceed the amount predicted by the classical Griffith criterion to induce crack growth. The magnitude of this effect is influenced by the type and range of the inter-atomic potential used and the orientation of the crystal relative to the crack front and crack plane. In some cases, this effect has been shown to be negligible [55, 67, 148], while in others it is quite significant [55, 173, 184]. Since most of the potentials we use are long-ranged, the absence of noticeable lattice trapping in our simulations is consistent with expectations developed in [148] and [67].

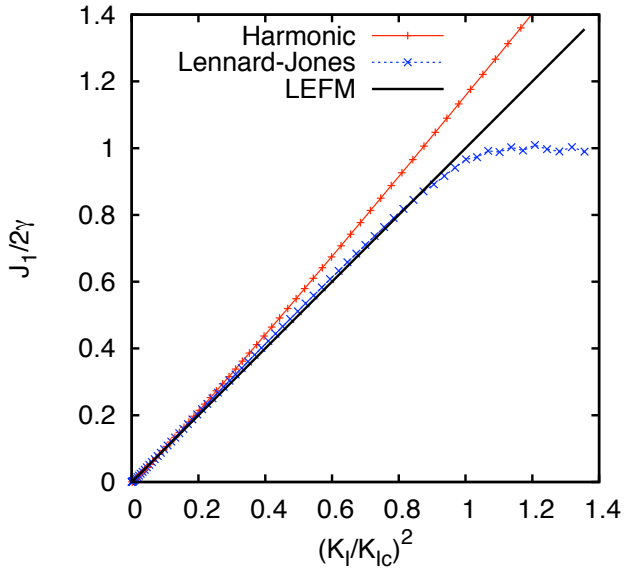

Figure 3.7. The J_1 integral scaled by 2γ plotted versus the load factor $(K_I/K_{Ic})^2$ which shows the nearly quadratic dependence on loading for the harmonic and Lennard-Jones potentials.

In Figure 3.8 we compare the components that comprise J_1, namely the divergence of the stored energy

$$\int_{\partial\Omega} W\mathbf{N}\,dA = \frac{1-2\nu}{4(1-\nu)}\frac{K_I^2}{E^*} = \frac{1-2\nu}{4(1-\nu)}J_1 \tag{3.38}$$

in plane strain and the work term $-\int_{\partial\Omega}\mathbf{H}^T\mathbf{P}\mathbf{N}\,dA$, which can be calculated using the definition (3.3) and (3.38). We see very good correspondence for both potentials (at least up to fracture for LJ). We have also plotted the contour integral measuring the stress divergence to demonstrate that it is insignificant relative to our $\mathbf{J}$ values.

Finite width crack

Using the same LJ potential as well as a corresponding Embedded Atom Method (EAM) Au potential formulated by Foiles *et al.* [57], we performed simulations with a center crack configuration by deleting interactions for a cut $\ell = 4a$ wide in the x_1-x_3 plane, see Figure 3.9. The overall dimensions of this quasi-two-dimensional, fully periodic system was $L_1 = L_2 = 20a$ square and $L_3 = 3a$ deep. As before, the reference configuration is set to the perfect lattice sites and the reference energy is such that it negates the surface energy induced by the initial deletion of bonds (refer to Figure 3.9a). Loading strain is effected by stretching the periodic simulation box so that at the boundary the displacement gradient is $\bar{\mathbf{H}}(\lambda) = (\lambda-1)\mathbf{e}_2 \otimes \mathbf{E}_2$.

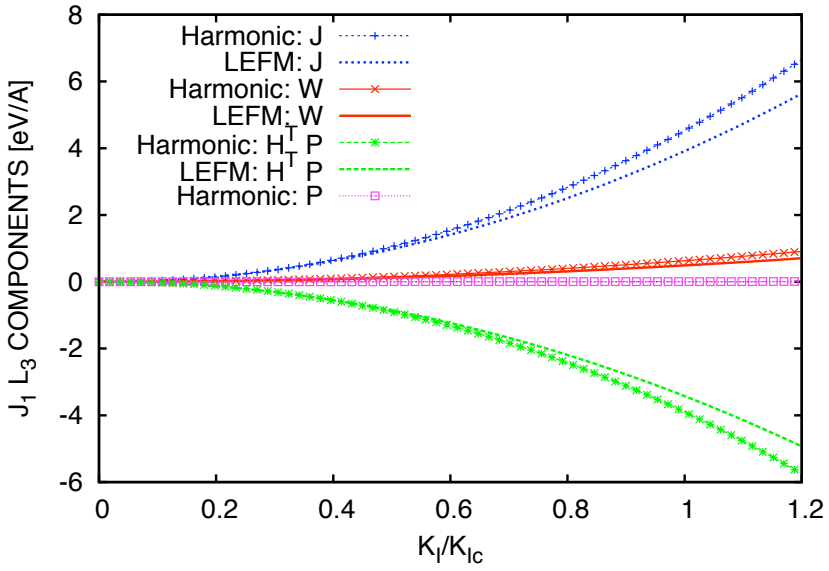

(a) Harmonic

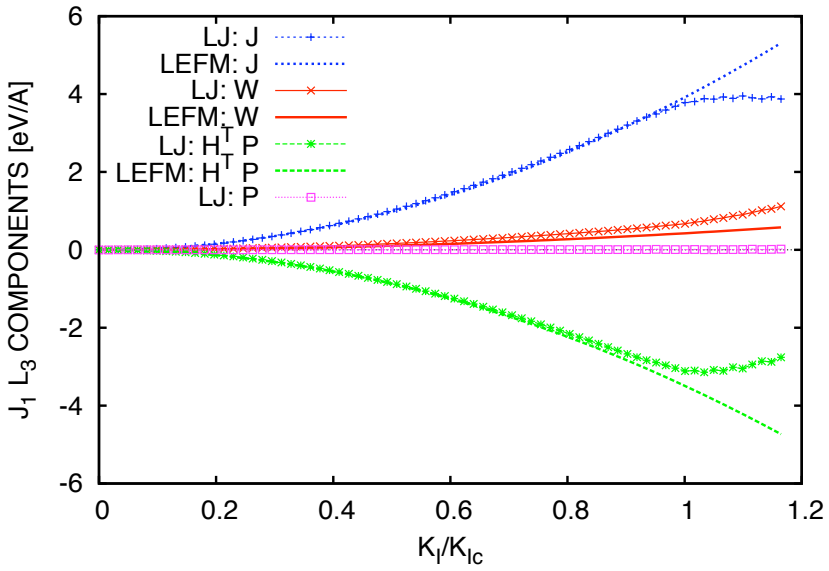

(b) Lennnard-Jones

Figure 3.8. The constituent components of the J_1 integral compared to the predictions of LEFM for the single crack, (a) harmonic potential on the top and (b) Lennard-Jones on the bottom. Both horizontal axes have been normalized by K_{Ic} from the Lennard-Jones system.

From Figure 3.9, we can see that the Eshelby stress is smooth and localized appropriately. Figure 3.10 shows that the **J** estimates are still path independent. For this configuration, the crack tips are too close to one another to be treated accurately using LEFM (which significantly overestimates J_1). This observation agrees with work done by Shastry and Farkas [171], who noted that for a short crack similar to ours the two tips exhibit an antishielding interaction that results in an increase of the critical stress intensity over the Griffith value. Figure 3.10 also shows that there are significant differences in potentials due to their respective surface energies, which is manifest in the balance between stored energy accumulated during loading versus work done. Nevertheless, both attain their surface energy limits. In addition to being quantitatively different, EAM has the qualitative difference that, for this system size and loading step size, the crack propagated and arrested before fully rupturing. This is manifest by the slight increase in the J_1 curves over the ultimate resistance limit near complete fracture. Figure 3.10b also shows that almost all the energy attributed to J_1 comes from W and the energy associated with the new surfaces created after rupture, while the stress component $\int \mathbf{H}^T \mathbf{P}\mathbf{N}\, dA$ goes nearly to zero as the system relaxes. The J_1 vs. strain squared curve in Figure 3.10 also has a pronounced change in slope right before rupture, especially for the LJ system, that we attribute to the coarseness of the loading since it was not observed in the semi-infinite crack case.

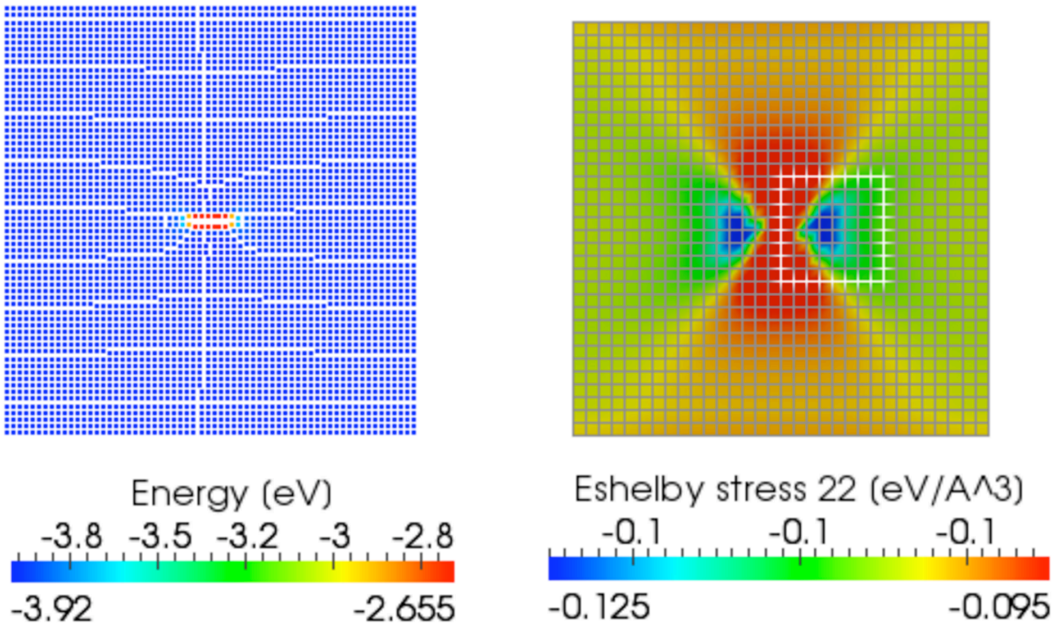

Figure 3.9. The atomic configuration of the LJ system colored by potential energy (in eV and relative to potential energy of a free atom) showing surface energy (left) and 11 component of the Eshelby stress $\mathcal{S}$ (in $eV/\mathring{A}^3$, right) for an applied strain of 4%.

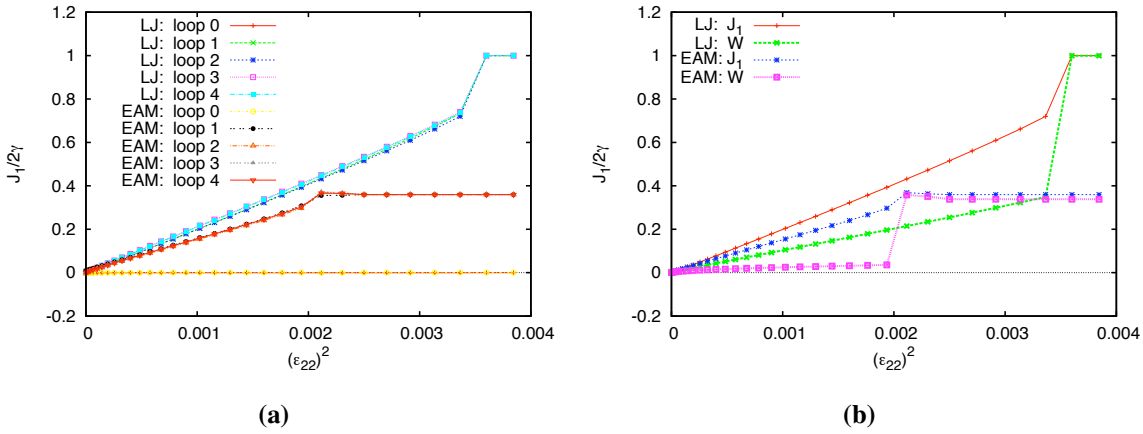

Figure 3.10. **J**-integral curves for Lennard-Jones and Embedded Atom Method Au normalized by the surface energy of the Lennard-Jones system. Left (a) path independence and right (b) components. Note $\varepsilon_{22} \equiv H_{22}$.

3.5.2 Edge dislocation

In this example, an edge dislocation is created in a FCC crystal of Pd (lattice parameter a = 3.89 Å) through the removal of a partial plane of atoms. The crystal is oriented such that $\mathbf{e}_1 = [110]$, $\mathbf{e}_2 = [\bar{1}11]$, and $\mathbf{e}_3 = [1\bar{1}2]$, and the Burgers vector of the created dislocation is $\mathbf{b} = \frac{a}{2}[110]$. Consistent with the treatment of the crack, the reference configuration is set to the perfect lattice sites and the reference potential energy is also defined by this configuration. Subsequent to the deletion, the whole system (approximate dimensions of 325 Å × 322 Å × 14.3 Å) is relaxed by applying the continuum displacement field associated with a unloaded edge dislocation,

$$\begin{aligned} u_1^{\perp} &= \frac{b}{2\pi}\left[\tan^{-1}\left(\frac{x_2}{x_1}\right) + \frac{x_1 x_2}{2(1-\nu)(x_1^2+x_2^2)}\right] \\ u_2^{\perp} &= -\frac{b}{2\pi}\left[\frac{1-2\nu}{4(1-\nu)}\ln\left(x_1^2+x_2^2\right) + \frac{x_1^2-x_2^2}{4(1-\nu)(x_1^2+x_2^2)}\right], \end{aligned} \tag{3.39}$$

where b is the magnitude of the Burgers vector in the the $\mathbf{e}_1$ direction. Note that these displacement fields decay faster than r^{-1}, where $r = \sqrt{x_1^2+x_2^2}$. Poisson's ratio

$$\nu = \frac{2(C_{11}-C_{12})(C_{11}+2C_{12}-2C_{44})}{3(C_{11}^2-2C_{12}^2+C_{11}(C_{12}+2C_{44}))} \tag{3.40}$$

and the shear modulus

$$\mu = \frac{1}{3}(C_{11}-C_{12}+C_{44}) \tag{3.41}$$

are estimated via application of the Cauchy-Born formalism to the potential for this crystal orientation. The interatomic potential used was an EAM model developed by Foiles and Hoyt [58] and

specially fitted to accurately predict the high value of intrinsic stacking fault energy for Pd. The cubic elastic constants of this simulated material are $C_{11} = 2.392 \times 10^6\, bars$, $C_{12} = 1.735 \times 10^6\, bars$, and $C_{44} = 0.656 \times 10^6\, bars$, and Youngs' modulus in the 1 direction is $2.7195 \times 10^6\, bars$. Climb loading is effected by prescribing motion in the $\mathbf{e}_1$ direction of a bounding layer of atoms 7.78 Å thick, so that

$$\begin{aligned} \mathbf{u} &= \mathbf{u}^{\perp} + \mathbf{u}^{\infty} \\ \boldsymbol{\sigma} &= \boldsymbol{\sigma}^{\perp} + \boldsymbol{\sigma}^{\infty} \end{aligned} \tag{3.42}$$

in the linear regime. Here the linear field $\mathbf{u}^{\infty}$ and homogeneous Cauchy stress $\boldsymbol{\sigma}^{\infty}$ are due solely to the far-field loading. The stress fields due to the edge dislocation are

$$\begin{aligned} \sigma_{11}^{\perp} &= -\frac{\mu b}{2\pi(1-\nu)} \frac{y(3x^2+y^2)}{(x^2+y^2)^2} \\ \sigma_{22}^{\perp} &= \frac{\mu b}{2\pi(1-\nu)} \frac{y(x^2-y^2)}{(x^2+y^2)^2} \\ \sigma_{12}^{\perp} &= \frac{\mu b}{2\pi(1-\nu)} \frac{x(x^2-y^2)}{(x^2+y^2)^2} \end{aligned} \tag{3.43}$$

from linear elasticity [76].

Figure 3.11 shows the characteristic stress field of an edge dislocation for the initial state. In this figure, the P_{11} and P_{22} fields are calculated via the material frame Hardy formulation, and are compared with Cauchy stress fields as given by the analytical formula (3.43). These fields also show some artifacts of the Hardy estimation, as in [200], and the cut in the mesh which follows the deleted plane of atoms. Nevertheless, there is good qualitative agreement between the pictured fields, and decent quantitative agreement given expected differences due to anisotropy, a nonlocal interatomic potential, and large-strain deviations from linear elasticity.

For an edge dislocation, the **J**-integral is related to the Peach-Koehler force [149] as shown by [48]. Here the total potential energy (3.7) reduces to [123, Chapter 2]

$$\Pi = -\mathbf{b} \cdot \int_{\partial\Omega} \mathbf{P}\mathbf{N}\, dA \tag{3.44}$$

where the Burgers vector $\mathbf{b}$ is defined

$$\mathbf{b} = \oint d\mathbf{u} = \oint \nabla_{\mathbf{X}} \mathbf{u} \cdot d\mathbf{s} \tag{3.45}$$

and $d\mathbf{s} = \frac{\partial \mathbf{x}}{\partial s} ds$ is the tangent to the loop encircling the dislocation core. Here, we have assumed small strains, where $\mathbf{P} \approx \boldsymbol{\sigma}$. The change in potential energy with motion of the core is

$$\dot{\Pi} = -\int (\mathbf{P}\mathbf{b}) \times (L_3 \mathbf{e}_3) \cdot \dot{\boldsymbol{\xi}}\, ds = \mathbf{J} \cdot \dot{\boldsymbol{\xi}} \tag{3.46}$$

where $\mathbf{N}\, dA = d\mathbf{s} \times L_3 \mathbf{e}_3$ and $L_3 \mathbf{e}_3 \times \dot{\boldsymbol{\xi}}$ is rate of change in area swept by dislocation. This result is consistent with the direct application of the Eshelby tensor

$$\begin{aligned} \mathbf{J} &= \int W\mathbf{N} - \mathbf{H}^T \mathbf{P}\mathbf{N}\, dA = \int \mathbf{P}^{\infty} \cdot \nabla_{\mathbf{X}} \mathbf{u}^{\perp} \mathbf{N} - \nabla_{\mathbf{X}} \mathbf{u}^{\perp} \mathbf{P}^{\infty} \mathbf{N}\, dA \\ &= \left(\mathbf{P}^{\infty} \oint \nabla_{\mathbf{X}} \mathbf{u}^{\perp} d\mathbf{s} \right) \times L_3 \mathbf{e}_3 = (\mathbf{P}^{\infty} \mathbf{b}) \times L_3 \mathbf{e}_3 \end{aligned} \tag{3.47}$$

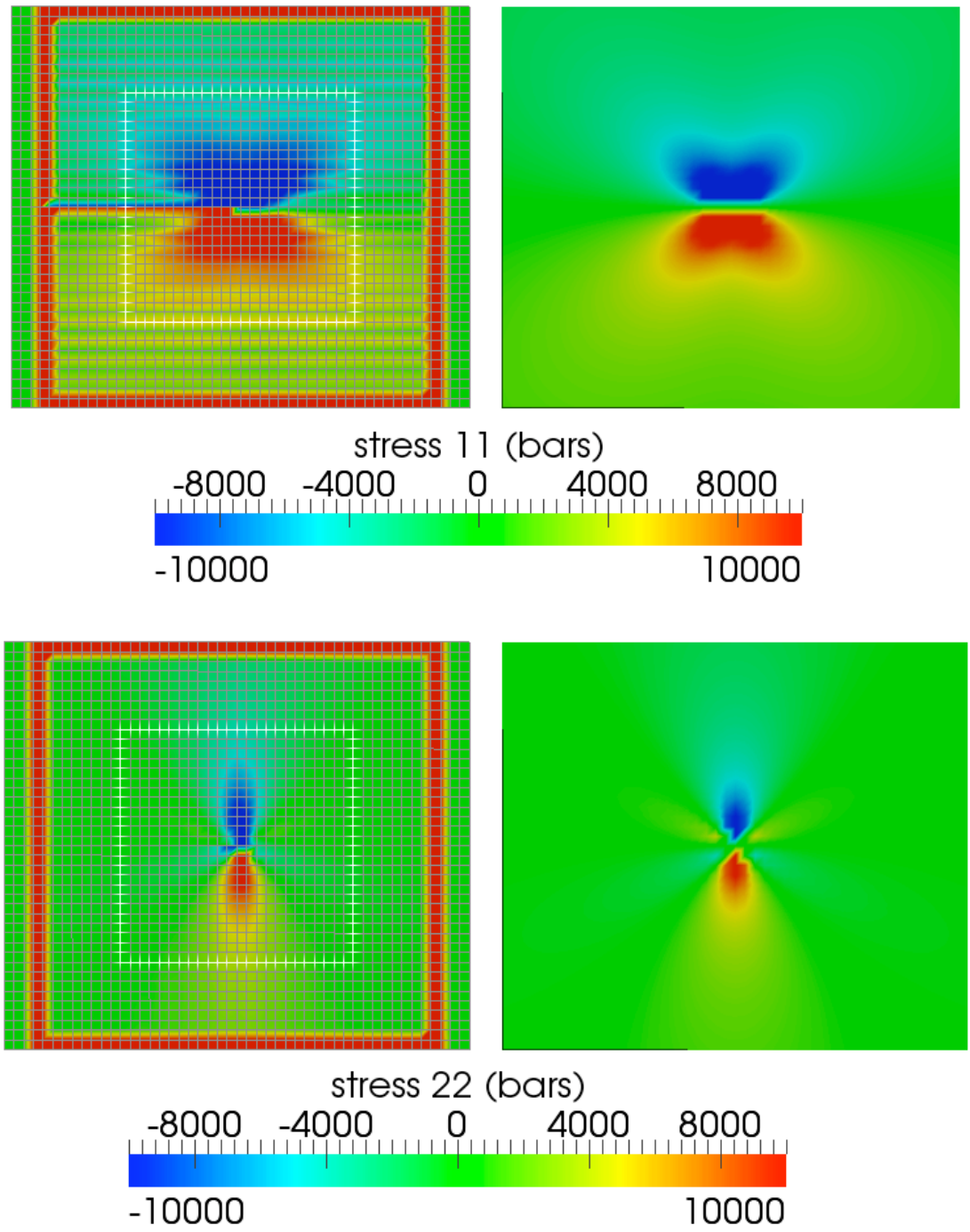

Figure 3.11. The 11 stress (top) and 22 stress (bottom) of the edge dislocation in the initial configuration. Hardy field with a mid-size contour (loop 2) on the left and linear elasticity on the right.

given the decomposition (3.42). The expression shown in (3.47) is a direct consequence of the known property that in order for $\mathbf{J}$ to possess path independence, the integration of terms W and $\mathbf{H}^T\mathbf{P}$ must produce a finite, non-zero value in the limits of very small and very large contours. As such, the only terms contributing to $\mathbf{J}$ must be of order $O(r^{-1})$, where r is the distance from the defect to a point on the contour. For the case of a crack under Mode I loading, the induced stress fields (3.34) are of the order $O(r^{-\frac{1}{2}})$ and thus satisfy this requirement. For the case of a dislocation subjected to far-field loading, as the self-stress fields (3.43) are of the order $O(r^{-1})$, only the cross-terms between the self-induced fields $\{\mathbf{u}^{\perp},\mathbf{P}^{\perp}\}$ and remote fields $\{\mathbf{u}^{\infty},\mathbf{P}^{\infty}\}$ yield a non-zero contribution to $\mathbf{J}$.

As mentioned previously, the reference configuration must be the undistorted bulk to obtain an accurate Burgers vector. As mentioned previously, we also inserted a horizontal cut in the mesh extending from the left boundary to the center of the system. Figure 3.12 shows that we do an excellent job of estimating the theoretical Burgers vector, which clearly has a tendency to increase with stretch. This figure also shows convergence of this estimate with increasing loop size, *i.e.* loop 1 is $12a$ on a side, loop 2 is $24a$ on a side and loop 3 is $36a$ on a side.

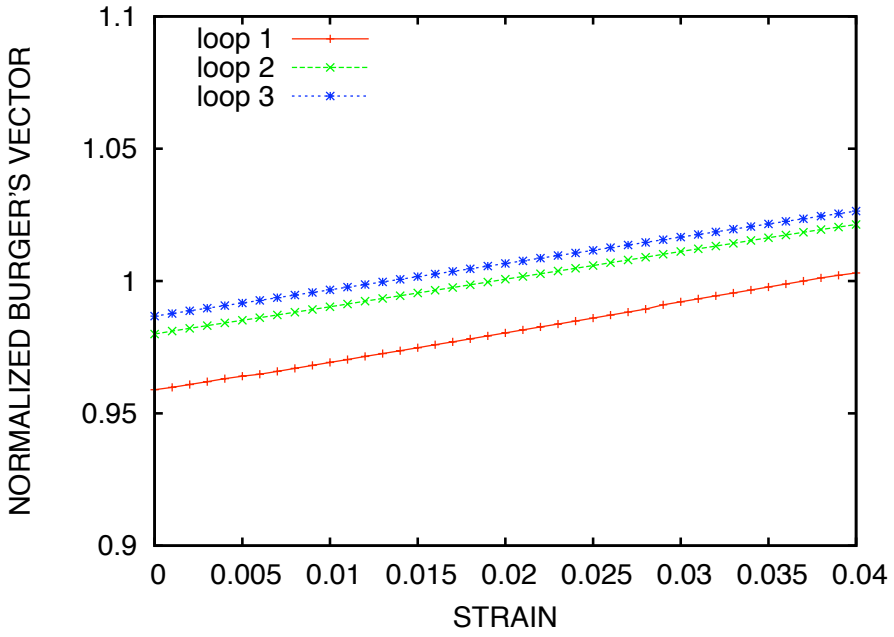

Figure 3.12. Burgers vector for loops of increasing size showing convergence and also increase of the effective Burgers vector with stretch. Values of Burgers vector are normalized with respect to the theoretical value of $a/\sqrt{2} \approx 2.751$ Å.

To estimate the far field stress $\mathbf{P}^{\infty}$, we used the average normal stress on the right boundary

$$\bar{P}_{11} = \frac{1}{L_2 L_3} \int \mathbf{n} \cdot \mathbf{P}\mathbf{N} \, dA \tag{3.48}$$

Although our "far-field" stress is not constant, it is nearly so, with P_{11} deviating only 2 % from its mean. This also gives us confidence that the boundaries are far enough away from the dislocation core. Figure 3.13 shows an excellent correspondence with linear elasticity, *i.e.* $J_2 \sim \varepsilon_{11}$ in the low strain regime where $\widetilde{C}_{11}\varepsilon_{11}$ is a good estimate of the stress and $\widetilde{C}_{11} = \frac{1}{2}(C_{11} + C_{12} + 2C_{44})$. As strain increases, the atomic estimates of J_2 track the applied stress $\bar{P}_{11}$ times the theoretical Burgers vector value $b = \frac{a}{\sqrt{2}}$ remarkably well. Figure 3.13 (inset) also shows that there is convergence to the expected value with increasing loop size.

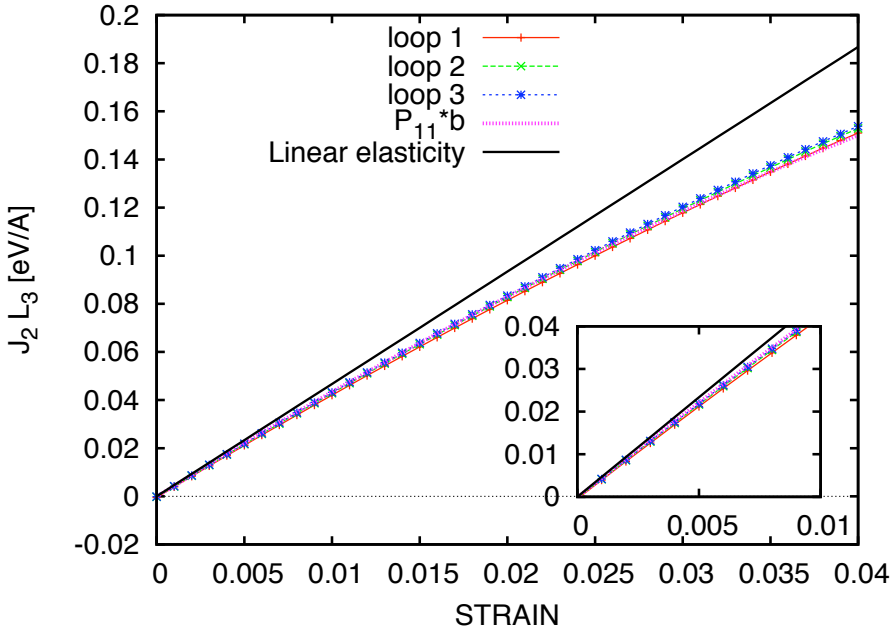

Figure 3.13. Variation of the J_2-integral with applied normal strain in the 1 direction showing convergence to the linear elastic values with increasing loop size. The J_1 components were all negligible and not plotted.

With this loading our particular edge dislocation does not propagate due to a high energy barrier for climb. However, for shear loading in the $\mathbf{e}_2$ direction, the dislocation slips readily. We performed such a simulation using additional concentric loops of sizes $12a$ (loop 1), $16a$ (loop 2), $20a$ (loop 3), $24a$ (loop 4), $28a$ (loop 5), $32a$ (loop 6), and $36a$ (loop 7) on a side. Figure 3.14 shows that the Burgers vector is nearly the theoretical value and follows a similar loading trend as in the climb case. Unlike the climb case, as the core moves away from the left boundary with the cut all contours converge. On the other hand, the **J**-integral, shown in Figure 3.15, does not follow

the analytical solution as the dislocation slips from its original position, nor is it path independent. However, detailed examination reveals that the initial loading follows the analytical solution, at least for the smallest loop. Also, the **J** value for each loop reaches a common limiting value before decaying as the core moves out of the loop, and overall, the curves are similar in shape implying a scaling relation between them.[10]

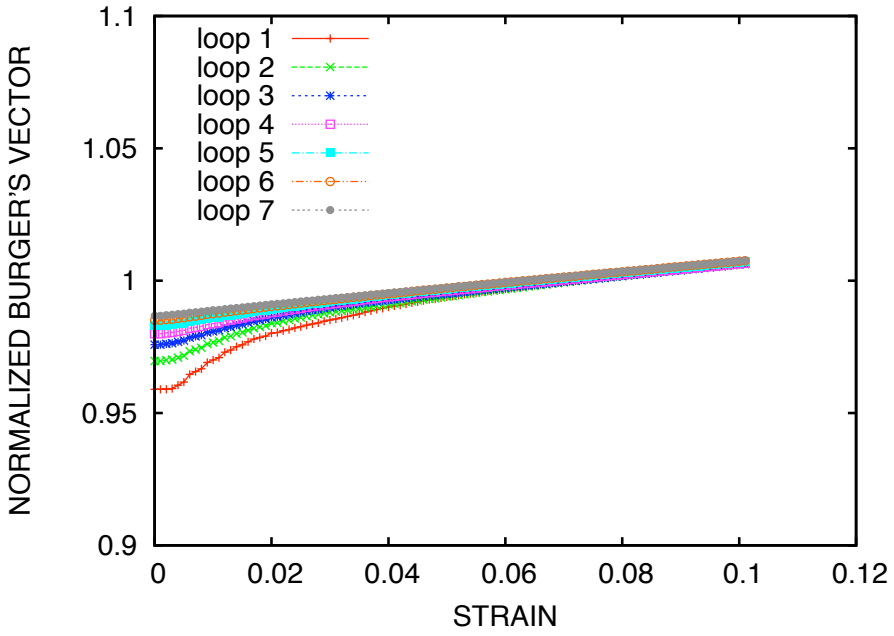

Figure 3.14. Burgers vector for loops of increasing size showing convergence and also increase of the effective Burgers vector with stretch.

At least one possible explanation exists for why path independence is lost once the defect has slipped from its original position. Our system is not infinite in its extent but rather is constrained by controlled boundary regions. As such, our dislocation may be subject to additional stress fields caused by image dislocations. Arguments of symmetry and functional dependence of the dislocation stress fields can be used to reason that while these fields negligibly contribute to the tensile loading considered in the climb scenario, they may be considerable with regard to the shear loading for the slip case. And, as the dislocation moves to new equilibrium positions upon increase of the far-field shear loading, this excess contribution becomes increasingly significant. It is important to realize, of course, that path independence is only expected until the dislocation intersects each contour. For a given contour, it is reasonable that the estimate of **J** drops to zero once the dislocation no longer resides within its interior region.

[10] In fact by rescaling strain for each loop all the curves can be made to lie on top of each other.

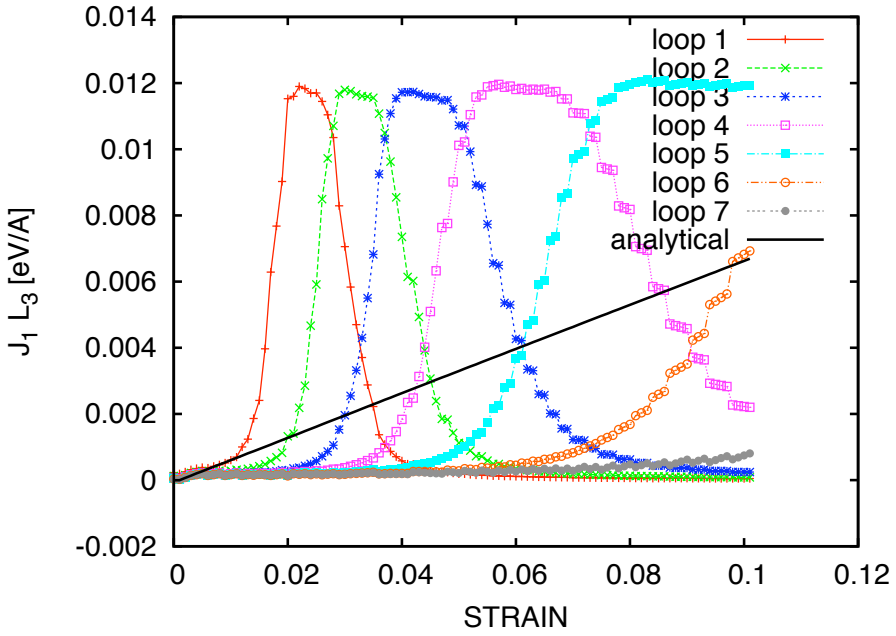

Figure 3.15. Variation of the J_2-integral with applied normal strain in the 1 direction.

3.6 Conclusion

In this article, we have presented an innovative method for estimating the **J**-integral in nanoscale systems using molecular simulation results. Our method represents a distinct departure from the traditional attempt to use atomic energies and contributions to the virial directly with "atomistic" versions of the **J**-integral. Instead we employ a material frame version of the well-regarded Hardy formulation to calculate continuum mechanical field variables and use these calculations within the traditional contour/surface integral expressions to estimate the **J**-integral. The Hardy formulation is marginally more expensive than a coarse-grained virial and has been shown to give superior results even for cases where simple linear elastic solutions do not exist. Using several numerical examples including cracks and dislocations, we have shown that our method of **J**-integral calculation:

- displays the path independence (independent of load) consistent with continuum mechanics theory. Without this property any **J** estimate is questionable. Also this property leads to straightforward localization of estimates for individual defects in complex environments;

- is in agreement with predictions of linear elasticity theory in the appropriate small strain regime, predicting the correct limiting values for **J** and K_I in fracture and the correct dependence on loading for both isolated cracks and dislocations.

None of the existing methods have achieved this. Arguably the best contour/domain integral-based method to-date [140, 141] displays greater variability in its **J** estimates, questionable path-independence at low loads, and greatly degraded path-independence with increasing load. Also in contrast with existing methods, the proposed method:

- gives pre-propagation information, without any issues with measuring crack length or crack stability, unlike Griffith's criteria methods based directly on estimates of energy release rate;
- can be more efficient than domain integral-based methods since fields need to be computed in only a thin annulus of the lattice around defect.

The superior results that we have obtained are due to: the use of coarse grained stress and displacement fields consistent with the continuum momentum balance and the work conjugacy relation (3.27), and an appropriate choice of reference configuration and state. Moreover, this rational development leads to an elegant, direct of application of continuum configurational mechanics to atomistic systems without the specialized, *ad hoc* treatments found in many other methods.

The potential of our new method is easily grasped. First, it can be used within coupled atomistic-continuum simulation frameworks, *e.g.*[100], to establish a consistent metric for predicting the onset of defect propagation that is well-defined in both types of simulation regions. Second, it can provide an accurate measure of the resistance to defect propagation at the nanoscale, which can in-turn be used to construct traction-separation laws used in the continuum-scale cohesive zone simulation. Finally, for problems where molecular simulation is exclusively used (such as the analysis of nanoscale structures, *e.g.*nanowires, and nanostructured materials), it extends proven concepts of traditional fracture mechanics down to this regime, providing a possibility for their usefulness in the engineering of nanotechnology.

While this effort promotes a powerful new technique, clear paths are evident that warrant further investigation. Our example of a dislocation subjected to shear loading shows that issues need to be resolved to determine if our **J**-integral calculation method has the potential for path independence when the defect is undergoing quasi-static motion during transitions in applied loading. More generally, our method needs to be extended to the case of mobile defects to determine if its consistency with the continuum measure of **J** is retained when kinetic fields are present. Likewise, expansion of method is required to analyze systems subject to finite, non-zero temperature. In such situations, we anticipate that calculation of a free energy (rather than strain energy) density will be required, and we have begun to pursue this path. In addition, the stress measure employed in the **J**-integral would need to include temperature effects. This can be done explicitly in the case of the Cauchy stress by the inclusion of a kinetic term [178], or implicitly, using the Lagrangian, first Piola-Kirchhofff stress [115, 224] employed in this work. Finally, while we have not performed a comprehensive study of multiple, interacting defects, the results of Section 3.5.1 give us confidence that our method will retain the properties of path independence and correct predictions of defect propagation resistance in complex environments.

Chapter 4

Continuum constitutive models from analytic free energies

Principal Authors: Christopher J. Kimmer and Reese E. Jones

In this chapter, we present a critical investigation of the validity of the harmonic approximation for developing constitutive models for multiscale simulations. We examine models using the Cauchy-Born hypothesis within the quasiharmonic, local harmonic, and modified local harmonic approximations in order to characterize the strain and temperature dependence of the Cauchy stress for uniaxial, equibiaxial and equitriaxial deformations. We compare these predictions with molecular dynamics simulations to evaluate each harmonic model's suitability over a wide range of strains and temperatures. The various harmonic approximations are found to be very robust over a large temperature range. All the approximations make very similar predictions at small strains and temperatures. At larger strains and temperatures, the quasiharmonic model is the most accurate but also the most computationally expensive. The modified local harmonic model is seen to provide an accurate alternative to the full quasiharmonic model over a wide range of strains while being much less computationally expensive. The local harmonic model is similar in absolute accuracy to the modified local harmonic model, but the modified harmonic model is seen to more accurately predict the elastic moduli.

4.1 Introduction

Knowledge of the free energy of a system is crucial for understanding its properties as a function of temperature, stress, or strain. Although quite general numerical methods exist for computing the free energy of a system, many important problems only benefit from having analytic expressions for the free energy. For a crystalline solid, exact analytic expressions are available only if the interatomic interactions are linear so that the solid is harmonic. At low temperatures in a nonlinear solid, anharmonic effects may be small and, consequently, the harmonic free energy can be an accurate and useful analytic approximation. Since anharmonic effects in a strained lattice can render the harmonic approximation invalid even at low temperatures, a variety of approximations based on expanding the potential energy about the strained state have been developed.

The quasiharmonic (QH) approximation [12] is based on a second-order expansion about a homogeneously deformed reference state. The dynamics of the solid are approximated as harmonic oscillations around strained atomic positions which are expected to coincide with the average sys-

tem configuration. The QH vibrational frequencies are found from the eigenvalues of the $3N \times 3N$ dynamical matrix. In contrast, the local harmonic (LH) approximation [111] neglects the vibrational coupling between atoms, and the vibrational frequencies are found from an approximate dynamical matrix that is only 3×3. A third approach, the so-called modified local harmonic model (MLH) [157] adds correction terms to the LH free energy in order to more closely approximate the QH free energy. The MLH approach yields a power series that is in principle exact for systems and strains that are sufficiently symmetric, but approximations are required in order to develop expressions for more general systems or strain states. In this paper, we present one such approximation developed in terms of an average local harmonic frequency which is suitable for anisotropic strain states and general crystal symmetries. The LH and MLH methods are less accurate than the QH model, but they have tremendous advantages in computational time even for moderately-sized systems, due to the smaller dynamical matrices required.

Numerous studies have compared the accuracy of the various harmonic approximations for perfect crystals [56, 104, 111, 139] as well as systems containing grain boundaries and vacancies [56] or point defects [39]. Likewise, the QH models alone have been compared directly with molecular dynamics (MD) simulations for systems in an isotropic stress state [191]. Most of these studies focus on the accuracy of the free-energy function itself or the ability to predict the free energy associated with system inhomogeneities. Little attention has been paid to the validity of these harmonic models for systems in anisotropic stress or strain states. Likewise, while the pressure versus density or temperature has been extensively characterized, less attention has been paid to the accuracy of individual components of the stress tensor predicted by these models for more general stress or strain states.

A class of problems where the model's performance in general stress or strain states must be well-understood is exemplified by current efforts to seamlessly couple MD and the finite element method (FEM) in a single, concurrent multiscale simulation. These simulations are expected to be accurate, efficient alternatives to current direct approaches for problems involving coupled physics with widely different characteristic length and time scales. A canonical example is brittle fracture and subsequent crack propagation. The fracture process ultimately depends on the rupture of individual bonds at or near the crack tip, while the motion of atoms far from the crack tip are well characterized by the smooth continuum strain field of linear elasticity. Consequently, the region near the crack tip is modeled with MD while the longer-scale physics are modeled with FEM further from the crack. Among the currently-proposed multiscale methods are the quasicontinuum method [42], the bridging-scale method [196], and coarse-grained molecular dynamics [164].

All these methods can at best match, in a locally averaged sense, the "exact" solution obtained with a single MD simulation modeling the entire system. This constraint typically leads to an interpretation of the FEM region as a coarse-scaled atomic region with all atoms locally experiencing the same homogeneous deformation described by the continuum strain field. This interpretation, known as the Cauchy–Born (CB) hypothesis [17], allows the energetics of the continuum to be derived from the energy per unit volume of the homogeneously-deforming atomic system. At nonzero temperature, the effects of thermal vibrations about the mean position are neglected in the continuum by the CB hypothesis. To include thermal effects in the coarse-scale constitutive model and to correctly couple to an MD region at nonzero temperature, the CB hypothesis is ex-

tended so that only the ensemble-averaged deformation is homogeneous. Although not explicitly modeled, fluctuations about the average deformation contribute to the average stress tensor [179], so the long-time, large-scale dynamics modeled by the FEM region must correctly reproduce this average stress. Consequently, the continuum energetics and dynamics are obtained from the free energy, as in the finite-temperature Cauchy–Born methods [85, 202].

As mentioned earlier, most work has focused on the accuracy of the free energy function itself, while the MD-FEM coupling problem requires that the derivatives of the free energy with respect to the strain measure be accurate. Moreover, this accuracy must hold over a wide range of strains and deformations. The accuracy of these harmonic approximations has been previously examined as a function of volumetric strain [111, 139, 191], but such deformation represents only a small part of the full deformation space expected in a multiscale simulation. The reliability of these models for anisotropic deformation states has received much less attention.

Another issue that has received scant attention as it pertains to multiscale modeling is stability. A partial explanation for this lack of attention is because it is still not completely clear within the continuum community what the basic stability criteria for a stressed solid should be, see, e.g., [13], and the references therein. This ambiguity arises, in part, because the criteria depend on the geometric description of the stressed state's deformation [75] as well as on the thermodynamic mechanism maintaining the system in a constant stress ensemble [135]. For the multiscale problem, stability issues become important from the continuum viewpoint because the vanishing elastic moduli are equivalent to the loss of ellipticity of the equations of equilibrium. Moreover, implicit solution methods in FEM codes rely on the elastic moduli or their approximants in order to determine the continuum strain field. Stability analysis can consequently be seen as providing a bounds on the strains and temperatures for which a coarse-scale stress model is valid.

We present a critical evaluation of the QH, LH, and MLH models for the specific purpose of deriving a temperature-dependent continuum constitutive model for a coupled MD/FEM simulation. We examine the effects of temperature as well as the type and amount of deformation on the average value of the stress tensor calculated from MD simulation. With this data, we investigate whether any of the existing harmonic approximations are valid over the range of temperatures and strains by comparing the data with predicted stress tensors of the various harmonic models. Finally, we point out that the differences observed between the various approximations have rather profound effects on stability estimates which may be important to the FEM application of the constitutive models. We find that the LH and QH models agree qualitatively only for the case of isotropic deformations. The QH and MLH models better capture the deformation dependence for all the anisotropic strain states considered here. Even though less accurate, the LH and MLH approaches may be preferred in practice because they are computationally inexpensive. For anisotropic models, the LH model performs worse than the MLH model. We show that this has implications for stability predictions using the LH model, so that the MLH model should be preferred over the LH model for multiscale methods as an reasonably accurate but less expensive alternative to the QH method.

The outline of the paper is as follows. In Section 4.2 we present an overview of continuum stress tensors derived from the Helmholtz free energy using the harmonic approximations. In Section 2, we also present a general version of the MLH model suitable for anisotropic strains and

any crystallographic symmetry. In Section 4.3, we compare the harmonic predictions with MD simulation, and we conclude in Section 4.4. In the Appendix, we present useful expressions for implementing the various harmonic models and performing stability calculations.

4.2 Methodology

We consider a monatomic crystal in its reference state with atoms located at $\mathbf{R}^\alpha$ and labeled by their unit cell α. In particular, for an N-atom crystal we have $\sum_\alpha 1 = N$. A homogeneous deformation of the crystal maps any point $\mathbf{X}$ in the reference configuration to a point $\mathbf{x}$ in the strained configuration; and, consequently, atoms at $\mathbf{R}^\alpha$ map to $\mathbf{r}^\alpha = \mathsf{F}.\mathbf{R}^\alpha$. Here F is the deformation gradient

$$\mathsf{F} \equiv \frac{\partial \mathbf{x}(\mathbf{X})}{\partial \mathbf{X}}. \tag{4.1}$$

The homogeneous deformation is viewed as describing the thermally-averaged atomic positions so that the appropriate dynamic variables are the displacements $\mathbf{u}^\alpha$ measured *relative to the homogeneously deformed crystal*, i.e. the configuration represented by $\mathbf{r}^\alpha$. In an MD-FEM multiscale simulation, the displacements $\mathbf{u}^\alpha$ would be resolved at the FEM scale only in a thermally-averaged sense while the longer wavelength degrees of freedom $\mathbf{r}^\alpha$ would be resolved fully. For simplicity, we restrict attention to interatomic potential energies Φ that are sums over pair potentials $\phi(r)$, but the treatment of more general cases is straightforward. In this case, the potential energy is given by

$$\Phi(\{\mathbf{u}^\alpha\};\mathsf{F}) = \sum_{\alpha<\beta} \phi(\mathbf{r}^{\alpha\beta} + \mathbf{u}^{\alpha\beta}) \tag{4.2}$$

with $\mathbf{r}^{\alpha\beta} = \mathbf{r}^\alpha - \mathbf{r}^\beta$ and a similar definition for $\mathbf{u}^{\alpha\beta}$. At constant energy, the dynamics are derived from the Hamiltonian $\mathcal{H}$. At constant temperature T, the Helmholtz free energy $\mathcal{F}$ provides information about the system's static and dynamic properties. $\mathcal{F}$ is a function of F and T and a functional of Φ over the configurational space $\{\mathbf{u}^\alpha\}$. The 1st Piola–Kirchoff stress P is work–conjugate to F, namely

$$\mathsf{P} = V_0^{-1} \left.\frac{\partial \mathcal{F}}{\partial \mathsf{F}}\right|_T \tag{4.3}$$

where V_0 is the volume of the undeformed system. For comparison with MD simulation, the Cauchy stress, σ may be equated with the time-averaged virial stress tensor [221] and the stress controlled by typical MD barostats [5]. The Cauchy stress is found from P

$$\sigma = J^{-1}\mathsf{P}\mathsf{F}^T \tag{4.4}$$

where $J = \det \mathsf{F} = V/V_0$.

All the harmonic approximations studied here may be viewed as arising from an approximate Hamiltonian that depends on the deformation F but is quadratic in the atomic displacements. Within this approximation, $\mathcal{F}$ becomes the sum of the potential energy due to the average homogeneous deformation and a harmonic vibrational energy term. Omission of the vibrational energy

term yields the familiar Cauchy-Born energetics and constitutive model for the averaged kinematics $\mathbf{r}^\alpha$. The vibrational terms describe uncoupled harmonic oscillators with frequencies $\{\omega_\gamma\}$. The actual values of the frequencies depend on the exact nature of the approximation used and will be treated shortly. To compare with MD, which is a classical simulation technique, we restrict attention to the classical or high–temperature limit ($\hbar\omega_\gamma \ll k_B T$) where the distribution function obeys Boltzmann statistics. The free energy in the various harmonic models is then completely determined by the Cauchy-Born energy and the vibrational spectrum of the model [198]

$$\mathcal{F}(\mathsf{F},T) = \Phi(\mathsf{F}) + k_B T \sum_\gamma \ln\left(\frac{\hbar\omega_\gamma(\mathsf{F})}{k_B T}\right). \tag{4.5}$$

The first term on the right hand side is independent of temperature and is the energy of the Cauchy-Born system, $\mathcal{F}_{CB} \equiv \Phi(\mathsf{F})$. The temperature dependence is determined by the vibrational spectrum in the second term above which we denote $\mathcal{F}_\omega$. Using (4.3), the 1st Piola–Kirchoff stress follows

$$V_0\mathsf{P} = \frac{\partial\Phi}{\partial\mathsf{F}} + k_B T \sum_\gamma \omega_\gamma^{-1}\frac{\partial\omega_\gamma}{\partial\mathsf{F}} \tag{4.6}$$

where we have suppressed the dependence of the stress tensor on F and T for brevity. The first term on the right hand side is the stress determined from the Cauchy–Born model, $V_0\mathsf{P}_{\rm CB} = \frac{\partial}{\partial\mathsf{F}}\mathcal{F}_{CB}$. The temperature dependence of the constitutive model is solely due to the change in frequency with deformation which is a consequence of the anharmonicity of the potential. We denote these temperature dependent terms P_ω. Thus, we have

$$\mathsf{P} = \mathsf{P}_{\rm CB} + \mathsf{P}_\omega \tag{4.7}$$

and may use an analogous decomposition and notation for the Cauchy stress tensor. This decomposition is advantageous since we consider the QH, LH, and MLH harmonic approximations which share the same Cauchy-Born term but differ in their treatment of the vibrational free energy and P_ω. Consequently, we use $\mathcal{F}_\omega$ only for the generic vibrational free energy term computed using any approximation and use $\mathcal{F}_{QH}, \mathcal{F}_{LH}$, and $\mathcal{F}_{MLH}$ to refer to the vibrational free energy using one of the three specific harmonic approximations. A similar notation may be employed for the vibrational contributions to the stress calculated with each specific model. Finally, as seen from Eq. 4.6, P_ω is linear in temperature. This linearity is important in providing a means to ascertain whether *any* harmonic approximation is accurate in describing the thermally-averaged dynamics over a given range.

Although each of the three different harmonic approximations differ in their treatment of the vibrational spectrum, they all depend fundamentally on the force constant matrix $D^{\alpha\beta} \equiv \frac{\partial^2}{\partial\mathbf{u}^\alpha\partial\mathbf{u}^\beta}\Phi$ describing the linear interaction of atom α with atom β. For defect-free crystals, translational invariance allows us to restrict attention to a subset of force-constant matrices $D^\alpha \equiv \frac{\partial^2}{\partial\mathbf{u}^\alpha\partial\mathbf{u}^0}\Phi$ for the bond between two atoms separated by $\mathbf{r}^\alpha$. The vibrational frequencies $\{\omega_\gamma\}$ in the QH approximation are determined from the eigenvalues $\omega^2_{\mathbf{K}\lambda}$ of the Fourier-transformed force constant matrix $D_{\rm QH}(\mathbf{K})$. This *dynamical matrix* is given by

$$D_{\rm QH}(\mathbf{K}) = \sum_\alpha D^\alpha \exp\left(-i\mathbf{K}\cdot\mathbf{R}^\alpha\right). \tag{4.8}$$

The N wave-vectors $\{\mathbf{K}\}$ span the lattice reciprocal to the *reference configuration*. The deformation of the reciprocal lattice need not be considered since $\mathbf{k}\cdot\mathbf{r}^{\alpha} = \mathbf{K}\cdot\mathbf{R}^{\alpha}$ is invariant under homogeneous deformation. The deformation dependence is contained in the force constant matrices and enters only through the derivatives of the potential evaluated in the strained configuration. The QH model for an N-atom monatomic crystal yields a maximum of N distinct wave-vectors $\mathbf{K}$ each corresponding to three frequency branches labeled by λ. The QH approximation thus models acoustic and optical branches as well as the dispersion relation for longitudinal and transverse normal modes.

In contrast to the QH model, the LH approximation neglects the coupling between interacting atoms. Each branch of the QH spectrum is then approximated by a single LH frequency. For a homogeneous monatomic system, the LH simplification of the QH model yields the single 3×3 dynamical matrix

$$D_{\mathrm{LH}} = \sum_{\alpha} D^{\alpha} \tag{4.9}$$

with three possibly degenerate eigenvalues $\omega_{\gamma}^{2}, \gamma = 1,2,3$. Because of the drastic reduction in size of the dynamical matrices, the LH model is much less computationally expensive than the QH model. The MLH model is likewise less expensive than the QH model, and it takes the form of a correction to the LH vibrational free energy. This correction is derived from the construction of an analytic expression for the difference between the QH free energy and the LH free energy [157]. For certain deformations where the local harmonic frequency is triply degenerate, this difference may be written exactly as a power series in the complete $3N\times 3N$ QH dynamical matrix. For more general deformations, we develop the MLH approximation in terms of an average frequency $\omega_{MLH}^{6} \equiv \det D_{\mathrm{LH}}$, recovering the original method for isotropic deformations of cubic systems. The vibrational free energy within the MLH model is then given by:

$$\mathcal{F}_{MLH} = \mathcal{F}_{LH} - \frac{3Nk_BT}{\omega_{MLH}^{4}} \sum_{\alpha} \mathrm{Tr}\,(\mathbf{D}^{\alpha})^{2} + \mathrm{O}(\mathbf{D}^{3}). \tag{4.10}$$

For this version of the MLH model, we retain only this first correction term before truncating the expression. The leading term in this power series is a second-order term proportional to the square of the QH dynamical matrix. For the homogeneous systems studied here, the correction term can be written as a sum of the elements of the force constant matrices. We defer further details of the exact computation of the MLH correction term and the various harmonic stress-tensor calculations to the Appendix.

4.3 Results

The analytic expressions for the Helmholtz free energy and its strain derivatives presented in the previous section can provide predictions for several averaged quantities which may be obtained from MD simulation. Here we compare the various harmonic models' predictions for the pressure and the diagonal components of the Cauchy stress tensor with MD data. Herein, we consider only deformations in which the off-diagonal stress components are zero.

The MD simulation method has been described in detail elsewhere [5], but we briefly describe our technical approach. We integrate Hamilton's equations of motion with the velocity Verlet algorithm and thermostat our system with a Nose-Hoover thermostat. We use a smooth Lennard-Jones interatomic potential cutoff after 2nd nearest neighbors. The specific cutoff distance as a function of deformation depends on the strain state, since the number of neighbors within a cutoff distance can change as the stretch is increased or decreased. The interatomic pair potential is

$$\phi(r) = 4\varepsilon \left[\left(\frac{\sigma}{r}\right)^{12} - \left(\frac{\sigma}{r}\right)^{6} \right]. \tag{4.11}$$

We use reduced units where mass m is 1, energy is in units of ε, length is units of σ, and stress is units of ε/σ^3. We use a timestep of $\Delta t = 10^{-3}\sqrt{m\sigma^2/\varepsilon}$ for all MD simulations. For each strain state and temperature, we apply the homogeneous deformation to the unstrained crystal and to the periodic simulation box. Initial velocities are chosen for each prescribed temperature from a Gaussian distribution with zero center of mass momentum and the correct temperature achieved by scaling. The system is equilibrated in the initial state for 40,000 time steps and then spatial and temporal averages are calculated for the next 160,000 time steps. The NVT ensemble is sampled using a Nose'-Hoover thermostat with a characteristic period of 400 timesteps. We have verified that our ensemble averages and results are independent of the particular sampling scheme used and the specific value chosen for the thermostat mass.

We simulate an FCC crystal in a cubic periodic simulation cell with 8 cubic unit cells on each side, yielding N = 2048 atoms. We investigate three different deformation states: uniaxial deformation (straining the (100) direction), equibiaxial deformation (straining (100) and (010) equally), and isotropic deformation (a volumetric strain) as a function of temperature and strain. In other words, each type of deformation is characterized by a single parameter, i.e. uniaxial deformation by F_{11}, equibiaxial deformation by $F_{11} = F_{22}$, and isotropic deformation by $F_{11} = F_{22} = F_{33}$. We consider stretches from -5% to +10% ($F_{11} = 0.95$ to 1.1), investigating both tension and compression over a wide range. For each strain state, we model temperatures $k_{\mathrm{B}}T$ ranging from 0 to a maximum of 1.2 ε. For many strain states, this maximum temperature is above the melt temperature, and the solid becomes unstable well before this maximum temperature is reached. We show only data for stable solids at each strain state and temperature. We choose the zero-temperature stress-free lattice as our reference configuration.

Stress-strain curves at constant temperature for this system computed from the various harmonic models in uniaxial tension are shown in Fig. 4.1. Up to strains of about 3%, the approximations are seen to be indistinguishable. At higher strains, they show markedly different behaviors with the QH model in between the extremes suggested by the LH and MLH models. The MLH correction term added to the LH model is thus seen as an over–correction to the actual QH stress-strain curve, but both the LH and MLH approximations have roughly the same absolute error with respect to the QH values. One can ignore the complex frequency- and deformation-dependence of each model and characterize the differences in each stress strain curve by the derivatives of the stress tensor with respect to deformation and with respect to temperature. From this viewpoint, the LH provides an over estimation of the deformation derivative while the MLH and QH models are qualitatively similar. Because of the simple dependence on temperature within the harmonic approximations, the derivative of stress with respect to temperature is constant.

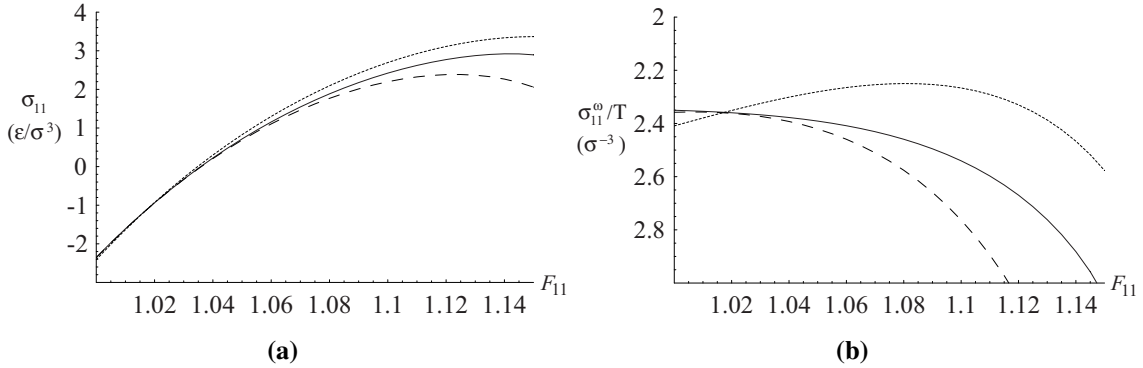

Figure 4.1. (a) Isothermal Cauchy stress-strain curves for $k_BT = \varepsilon/4$ showing the harmonic models' predictions for uniaxial tension. Shown is σ_{11} as predicted by the QH model (solid), the LH model (short dashes), and the MLH model (long dashes). The MLH model is seen to be an over-correction from the LH to the QH predictions. All models are virtually indistinguishable at small strains. (b) The frequency-dependent part of the stress scaled by temperature for the QH (solid), LH (long dashes), and MLH (short dashes) models.

For the temperature range studied here, we observe a linear variation of pressure with temperature as shown in Fig. 4.2 for equibiaxial deformation. This data is representative of similar results seen for isotropic and uniaxial deformations. At small strains, the data agree well with the harmonic approximations throughout the large temperature range. The melt temperature of the LJ FCC crystal at zero-pressure is $0.65\varepsilon - 0.68\varepsilon$, depending on the range of the potential [134]. Consequently, the suppression of surface effects by the periodic boundary conditions leads to some MD simulations being run for superheated LJ crystals [63, 87]. Although the physical relevance of these simulations is scant, this large temperature range reveals that the predictions are reasonably close to the data even beyond the melt temperature. The harmonic approximations can be considered extremely robust even under the anisotropic deformations considered here. At higher stretches, the melting temperature is reduced. So, although the LH model performs more poorly at large temperatures and strains, it still performs well between zero temperature and the reduced melt temperature for each corresponding strain. It is also apparent that the LH approximation overestimates derivatives with respect to temperature. In fact, all three harmonic approximations are similar in this sense. The case of uniaxial deformation leads to the best agreement between simulation and the analytic models, yet all three deformations studied clearly show deviations from the expected linear dependence. These deviations are small relative to the value of the pressure itself, so these harmonic approximations are indeed suitable over the temperature and strain ranges studied here.

The MD data displays smooth variations in the energy or stress as a function of temperature and deformation up until critical strains or temperatures are reached. We associate the onset of

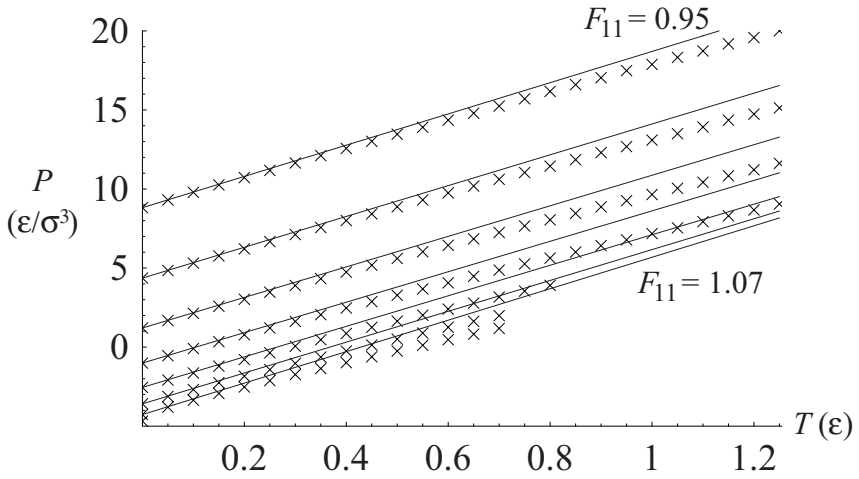

Figure 4.2. Comparison of the predicted LH pressure at constant deformation (solid lines) with the MD results (crosses) vs. T for equibiaxial deformation over a range of strains and temperatures. The strain increases from top to bottom, and the LH approximation is seen to perform well at low temperatures and more poorly at high temperatures.

instability as a function of strain and temperature with these critical values where discontinuities in the stress tensor are first observed. The initial instabilities correspond to localized defects in the solid and are dependent on the initial conditions of the simulation. At slightly larger critical strains or temperatures, we find that no initial conditions produce a stable solid. The critical strains and temperatures may be compared with predictions using any of the various stability criteria for a stressed solid. An upper bound on these critical values is found using the commonly employed Legendre-Hadamard condition [187], a long-wavelength elastic measure of the stability. We also may equate a short-wavelength, or phonon instability, with the strain and temperature at which the QH or LH dynamical matrices no longer have real eigenvalues. A zero or imaginary eigenvalue corresponds to a localized deformation whose amplitude grows without without energy penalty or without bound, respectively. This failure of the harmonic models is sensitively dependent on the model and range of potential, and it has not been previously pointed out as a limitation of the harmonic models.

In Fig. 4.3a we compare the MD data for a variety of temperatures with the harmonic predictions for the 11 component of the temperature-dependent part of the Cauchy stress σ_ω. We have subtracted the Cauchy-Born stress tensor from the measured MD virial stress in order to compare with the predicted temperature-dependent contribution to the stress tensor, σ_ω. We then scale this tensor by temperature so that the data at different temperatures would fall on the same curve if the harmonic approximation were exact. That collapse to a single curve is not observed is indicative of the degree of anharmonicity in the system increasing with temperature and strain. Interestingly, none of the harmonic models reproduces the simulation data well even at low temperatures us-

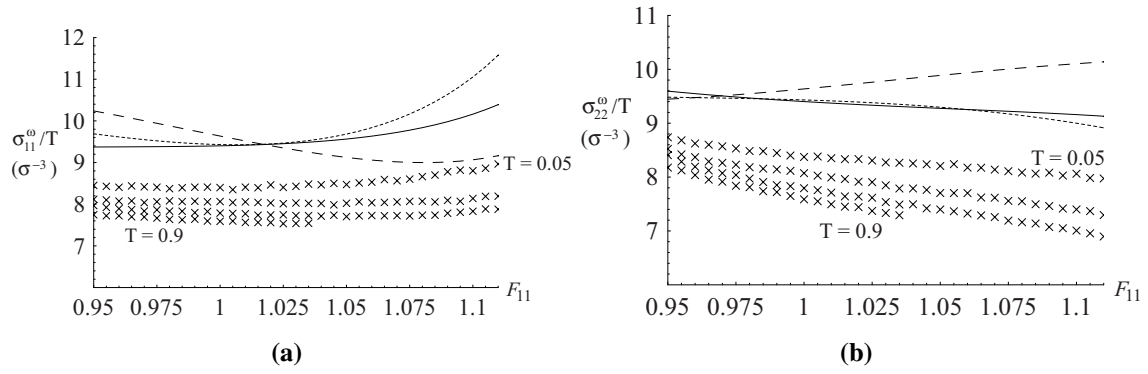

Figure 4.3. Comparison of the temperature-dependent (a) on-axis component $(\sigma_\omega)_{11}$ and (b) off-axis components $(\sigma_\omega)_{22} = (\sigma_\omega)_{33}$ of the Cauchy stress tensor for uniaxial deformation vs. the stretch F_{11}. Shown are predictions from the QH (solid line), MLH (short dashes), and LH (long dashes) models vs. the MD (crosses) results.

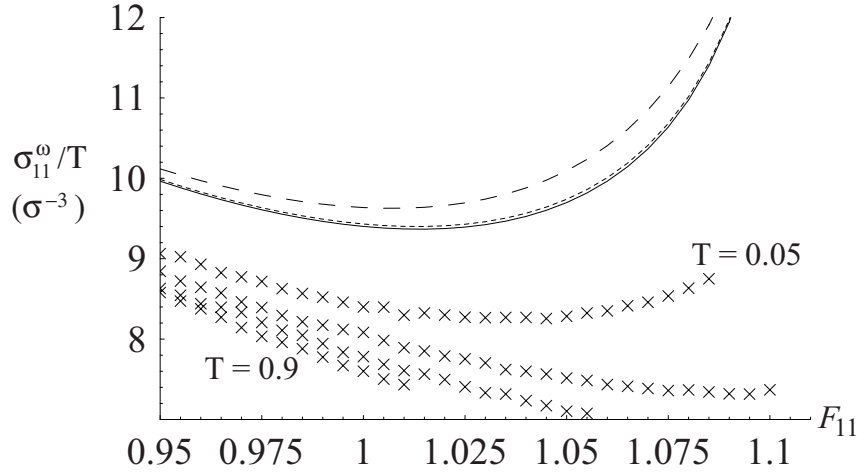

Figure 4.4. Comparison of the temperature-dependent diagonal component of the Cauchy stress $(\sigma_\omega)_{11} = (\sigma_\omega)_{22} = (\sigma_\omega)_{33}$ for isotropic stretch. Shown are predictions from the QH (solid line), MLH (short dashes), and LH (long dashes) models vs. the MD (crosses) results.

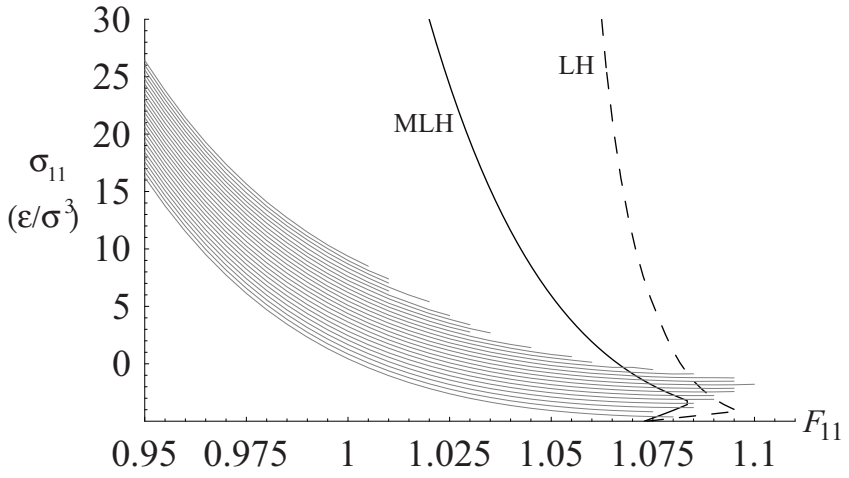

Figure 4.5. Comparison of the locus of instabilities seen in MD simulation against the long-wavelength elastic predictions for the onset of instability using the LH (long dashes) and MLH (solid) models for isotropic deformation.

ing this criterion. However, the scaling by temperature effectively reduces this contribution to the stress tensor at small temperatures so that the overall error between simulation and prediction remains small. The error between the data and the harmonic predictions is roughly similar for all three models, but the QH and MLH models clearly match the first derivative of the data more accurately than the LH model does. We see similar results for the off-axis stress in the uniaxial case (Fig. 4.3b) and for the equibiaxial case. Interestingly, all three harmonic models perform more or less equally well for isotropic deformation, as seen in Fig. 4.4. Overall, it is seen that one must consider the models' performance under anisotropic deformation in order to completely describe the relative strengths of each approximation.

To further characterize the accuracy of the LH and MLH approximations, we consider each models' predictions for the elastic stability limits of the solid. We employ a Legendre-Hadamard condition [187] to ascertain the large-scale incremental stability of the lattice, namely

$$\mathbb{B}_{iJkL} a_i N_J a_k N_L > 0 \quad \forall\, a_i, N_J \,. \tag{4.12}$$

Here $\mathbb{B}$ is the so-called 1st elasticity tensor

$$\mathbb{B} = \frac{\partial \mathsf{P}}{\partial \mathsf{F}} = \frac{\partial^2 \mathcal{F}}{\partial \mathsf{F} \partial \mathsf{F}}. \tag{4.13}$$

Physically speaking, condition (4.12) can be interpreted as a requirement that small-amplitude plane waves solutions to the equation of motion linearized about the deformed configuration have positive, real frequencies; or in other terms, it requires that the deformed configuration is such that the equilibrium equation $\frac{\partial}{\partial \mathbf{X}} \cdot \mathsf{P} = \mathbf{0}$ is still elliptic [51, 74]. In the former interpretation, $\mathbf{N}$ is

the propagation direction and **a** is the polarization vector. We find the eigenvalues of the acoustic tensor

$$\mathbf{A}_{ik}(\mathbf{N}) = \mathbb{B}_{iJkL} N_J N_L \tag{4.14}$$

for all **N** for a given deformation and temperature. If the minimum eigenvalue is non-positive the state is considered unstable. To follow the locus of stability points in (F, T) we start by finding the critical deformation F along the zero temperature curve, i.e. for $\mathbb{B} = \mathbb{B}_{CB}$, and then index the one-parameter deformation gradient F and find the critical temperature for this deformation.

In Fig. 4.5 we show the LH and MLH models' predictions of the long-wavelength elastic stability limits. Both models predict the same trends as the MD data, but the MLH model's estimations of the maximum stable stretch at a given temperature are considerably smaller than those of the LH model. For each model, the failure mode is shear at low temperatures while at higher temperatures the stability limit is governed by tensile failure. The critical strain for shear failure increases with increasing temperature while the tensile failure modes have a decreasing critical strain with increasing temperature. The shear failure regime is in essence the Born stability criterium for the vanishing shear modulus $C_{1212} = 0$ [19] except that additional finite-strain and temperature-dependent effects on the elastic moduli are included in the calculations. As temperature increases, the harmonic models' vibrational contribution to the elastic moduli increases and eventually becomes the dominant factor in determing the stability locus. The transition temperature or strain from shear to tensile failure is consequently different for each of the harmonic approximations. The MLH model more accurately models the elastic moduli as a function of temperature and strain, and this accuracy is seen here to produce a better estimate of the onset of instability in the crystal, at least at low T. Neither estimate is very accurate at high T however, indicating that a more localized measure for the onset of stability may be appropriate. This is not completely surprising since the short-wavelength modes become unstable at smaller strains than the longer wavelength modes in general. This data indicates that the most accurate stability measure may need to be based on the complete vibrational spectrum and not just the long-wavelength elastic properties. However, the MLH model is clearly seen to provide a better estimate than the LH model.

4.4 Discussion

It has been shown that all three harmonic models can be used to provide a reasonably-accurate constitutive model for the multiscale modeling of Lennard-Jones crystals using coupled MD-FEM simulations. Indeed, up to temperatures approaching the melt temperature, all three harmonic models can be said to be sufficiently accurate over a wide range of strains to closely follow the Cauchy stress tensor as determined from the MD simulation data. A critical examination of the temperature-dependent terms in the Cauchy stress tensor reveals that all three harmonic approximations have similar absolute errors between their predictions and the actual values seen from the MD simulations. At low temperatures, this error is small relative to the Cauchy Born contribution to the stress, and at high temperatures, the differences in the various harmonic approximations lead to different over- and under-estimations relative to the MD data. From this point of view, the LH model is insufficient to capture trends that depend on the elastic moduli or the strain derivatives of

the stress tensor. The MLH and QH models do capture these trends, and the MLH is considerably less computationally expensive than the QH model. Of the deformation states studied, the LH model performs worst for uniaxial deformation and best for isotropic deformation. On the other hand, the MLH and QH models perform similarly for all the deformation states investigated. The more accurate approximation of the elastic moduli is also reflected in the MLH model's ability to predict the onset of instability more accurately than the LH model.

The tremendous decrease in computer time gained with the LH and MLH models strongly argue against using the QH model in a multiscale simulation where the stress tensor is evaluated repeatedly for different local deformation states. Similarly, the MLH model is seen to be more accurate than the LH model, yet the first-order correction incurs only a modest additional computation cost. Consequently, the results shown here suggest that adoption of the MLH model would lead to some increase in the accuracy of current multiscale methods that currently use the LH model.

Finally, we note that investigations similar to those described here should be carried out for additional potentials, such as the embedded atom method (EAM) potentials. The LJ potential used here is known to have smaller anharmonic effects than the EAM potentials. Similar critical investigations of the stress tensor's detailed dependence on the deformation state for more anharmonic potentials can provide important indications of the robustness of these results and their general applicability to current multiscale efforts.

4.5 Appendix B: Analytical formulation of traction-displacement-mixity relation

Following Sec. 4.2, we consider a static homogeneous deformation F with dynamic displacements $\{\mathbf{u}^\alpha\}$ about the deformed configuration. We use Greek indices to label atoms, dynamical matrices, or frequencies and reserve Arabic indices to label components (lowercase for current quantities and uppercase for referential). In component notation, the deformation gradient is

$$\mathsf{F}_{iJ} = \frac{\partial x_i}{\partial X_J} \tag{B.1}$$

where $\mathbf{e}_k$ and $\mathbf{E}_L$ are Euclidean basis vectors. Given

$$(r^\alpha)^2 = \mathbf{R}^\alpha \mathbf{C} \mathbf{R}^\alpha, \quad \mathbf{C} \equiv \mathsf{F}^T \mathsf{F} \tag{B.2}$$

and the pair potential ϕ, the derivatives of the frequencies with respect to the deformation can be calculated in a straightforward but tedious fashion.

With the restriction to pair potentials $\phi(r)$, the force constant matrix $\mathbf{D}^\alpha$ becomes

$$\mathbf{D}^\alpha = \delta^{\alpha 0} \sum_\gamma \frac{\partial^2 \phi}{\partial \mathbf{u}^\gamma \partial \mathbf{u}^0} - \frac{\partial^2 \phi}{\partial \mathbf{u}^\alpha \partial \mathbf{u}^0} \tag{B.3}$$

The second derivatives in component notation are

$$\left.\frac{\partial^2\phi}{\partial u_i^\alpha \partial u_j^0}\right|_{\mathbf{u}=0} = g(r^\alpha)\delta_{ij} + 2f(r^\alpha) r_i^\alpha r_j^\alpha. \tag{B.4}$$

where $g(r) = r^{-1}\phi'(r)$ and $f(r) = r^{-2}\left(\phi''(r) - r^{-1}\phi'(r)\right)$. In the QH model, we note that

$$\prod_\lambda \omega_{\mathbf{K}\lambda}^2 = \det D_{\mathrm{QH}}(\mathbf{K}). \tag{B.5}$$

Consequently, $\mathcal{F}$ can be written as a sum of determinants of the N dynamical matrices

$$\mathcal{F} = \Phi(\mathsf{F}) + \frac{k_B T}{2}\sum_{\mathbf{K}} \ln\det D_{\mathrm{QH}}(\mathbf{K}). \tag{B.6}$$

Likewise, within the LH model one has that

$$\prod_\gamma \omega_\gamma^2 = \det D_{\mathrm{LH}}. \tag{B.7}$$

The free energy becomes

$$\mathcal{F} = \Phi(\mathsf{F}) + \frac{k_B T}{2}\sum_{\alpha} \ln\det D_{\mathrm{LH}}. \tag{B.8}$$

which may also be used to write down $\mathcal{F}$. Returning to the generic label γ for the different dynamical matrices, both models yield a free energy of the form

$$\mathcal{F} = \Phi(\mathsf{F}) + \frac{k_B T}{2}\sum_{\gamma} \ln\det D^\gamma. \tag{B.9}$$

As described in Sect. 4.2, the MLH model is implemented as a single correction term applied to the Helmholtz free energy obtained within the LH approximation.

The determination of the temperature-dependent terms in the 1st Piola-Kirchoff stress in the QH or LH models thus reduces to determining the derivatives of the determinant with respect to the deformation gradient. For the MLH model, one supplements this with the derivatives of the force constants with respect to the strain. We note here that first order perturbation theory may be used to write these eigenvalue derivatives in terms of the eigenvectors and the derivative of the dynamical matrix with respect to F. We prefer to calculate the derivatives directly from determinants of the dynamical matrices. Our approach offers considerable ease in implementing the second derivatives using symbolic algebra on the computer, and perhaps more importantly, subtleties about the treatment of degenerate frequencies do not arise. We calculate the derivatives of the determinant using the chain rule. In coordinate notation,

$$\det D^\gamma = D^\gamma_{1j}\mathsf{c}_{1j} = D^\gamma_{2j}\mathsf{c}_{2j} = D^\gamma_{1j}\mathsf{c}_{3j} \tag{B.10}$$

where summation over repeated variable indices is implied and c_{ij} is the the ij component of the adjugate of D^γ, i.e the cofactor of D^γ_{ij}. With this result, Jacobi's Formula gives us the necessary derivative

$$\frac{\partial \det D^\gamma}{\partial F_{kL}} = \frac{\partial D^\gamma_{ij}}{\partial F_{kL}}\mathsf{c}_{ij}. \tag{B.11}$$

The derivative of the QH dynamical matrix is given by

$$\frac{\partial D_{\mathrm{QH}}(\mathbf{K})}{\partial \mathsf{F}} = \sum_{\alpha} \frac{\partial D^{\alpha}}{\partial \mathsf{F}} \mathrm{e}^{-i\mathbf{K}\cdot\mathbf{R}^{\alpha}}. \tag{B.12}$$

The derivatives of the LH dynamical matrix follow simply from Eq. 4.9 and the chain rule. When specialized to pair potentials, the derivative of D^{γ} is calculated from Eqs. B.3 and B.4

$$\frac{\partial D^{\alpha}_{ij}}{\partial F_{kL}} = \left(\frac{g'(r)}{2r}\delta_{ij} + \frac{f'(r)}{r} r_i r_j \right) R_P R_Q \frac{\partial C_{PQ}}{\partial F_{kL}} + f(r)\left(\delta_{ik} r_j R_L + \delta_{jk} r_i R_L\right). \tag{B.13}$$

The remaining required derivative above is given by

$$\frac{\partial C_{PQ}}{\partial F_{kL}} = (\delta_{PL} F_{kQ} + F_{kP}\delta_{QL}) \tag{B.14}$$

The temperature-dependent terms of the 1st Piola-Kirchoff stress become

$$V_0 \, \mathsf{P}_{\omega} = \frac{k_B T}{2} \sum_{\gamma} \left(\det D^{\gamma}\right)^{-1} \frac{\partial \det D^{\gamma}}{\partial \mathsf{F}}. \tag{B.15}$$

With this expression, the required components of the Cauchy stress tensor may be evaluated, too.

The elastic moduli are also now obtainable, although they involve considerably more computation in the QH approximation. Given the additive decomposition of the free energy $\mathcal{F}$, we obtain a similar one for the moduli

$$\mathbb{B} \equiv \frac{\partial \mathsf{P}}{\partial \mathsf{F}} = \mathbb{B}_{CB} + \mathbb{B}_{\omega}. \tag{B.16}$$

We compute the Cauchy-Born contribution to the modulus

$$V_0 \, (\mathbb{B}_{CB})_{iJkL} = \delta_{ik} \left.\frac{\partial \Phi}{\partial C_{JL}}\right|_{\mathbf{r}^{\alpha}} + 4 \sum_{\alpha} \left.\frac{\partial^2 \Phi}{\partial r^2 \partial r^2}\right|_{\mathbf{r}^{\alpha}} r_i R_J \, r_k R_L \tag{B.17}$$

by employing the fact that we are examining only pair potentials. The temperature-dependent tangent modulus is given by

$$V_0 \, \mathbb{B}_{\omega} = \frac{k_B T}{2} \sum_{\gamma} \left[-\left(\det D^{\gamma}\right)^{-2} \frac{\partial \det D^{\gamma}}{\partial \mathsf{F}} \otimes \frac{\partial \det D^{\gamma}}{\partial \mathsf{F}} + \left(\det D^{\gamma}\right)^{-1} \frac{\partial^2 \det D^{\gamma}}{\partial \mathsf{F} \partial \mathsf{F}} \right]. \tag{B.18}$$

The second derivative of the determinant is

$$\frac{\partial^2 \det D^{\gamma}}{\partial F_{lM} \partial F_{pQ}} = \frac{\partial D^{\gamma}_{ik}}{\partial F_{lM} \partial F_{pQ}} \mathsf{c}_{ik} + \frac{\partial D^{\gamma}_{ik}}{\partial F_{lM}} \frac{\partial \mathsf{c}_{ik}}{\partial F_{pQ}}, \tag{B.19}$$

which contains terms proportional to the second derivative of the dynamical matrices as well as terms containing the product of two first derivatives. The second derivative of the dynamical matrix

is

$$\frac{\partial^2 D_{ij}^{\gamma}}{\partial F_{kL}\partial F_{mN}} = (4r)^{-1}\left[\frac{\partial}{\partial r}\left(\frac{g'(r)}{r}\right)\delta_{ij} + \frac{\partial}{\partial r}\left(\frac{f'(r)}{r}\right) r_i r_j\right] R_P R_Q \frac{\partial C_{PQ}}{\partial F_{kL}} R_S R_T \frac{\partial C_{ST}}{\partial F_{mN}} + \left[\frac{g'(r)}{r}\delta_{ij} + \frac{f'(r)}{r} r_i r_j\right] R_L R_N \delta_{km} + \frac{f'(r)}{2r}\left(r_j R_N \delta_{im} + r_i R_N \delta_{jm}\right)\frac{\partial r}{\partial F_{kL}} + \frac{f'(r)}{2r}\left(r_j R_L \delta_{ik} + r_i R_L \delta_{jk}\right)\frac{\partial r}{\partial F_{mN}} + f(r)\left(R_L R_N \delta_{ik}\delta_{jm} + R_L R_M \delta_{jk}\delta_{im}\right). \tag{B.20}$$

Within the QH approximation for a moderately-sized system, this term is prohibitively expensive to evaluate using symbolic algebra programs.

Chapter 5

An atomistic J-integral at finite temperature based on Hardy estimates of continuum fields

Principal Authors: Reese E. Jones, Jonathan A. Zimmerman, Jay Oswald, and Ted Belytschko

In this chapter, we apply a material-frame, kernel-based estimator of continuum fields to atomic data in order to estimate the **J**-integral for the analysis of an atomically sharp crack at finite temperatures. Instead of the potential energy appropriate for zero temperature calculations, we employ the quasi-harmonic free energy as an estimator of the Helmholtz free energy required by the Eshelby stress in isothermal conditions. We employ the simplest of the quasi-harmonic models, the local harmonic model of LeSar *et al.* , and verify that it is adequate for correction of the zero temperature **J**-integral expression at various deformation states for our Lennard-Jones test material. We show that this method has the properties of: consistency between the energy, stress and deformation fields; path independence of the contour integrals of the Eshelby stress; and excellent correlation with linear elastic fracture mechanics theory.

5.1 Introduction

Configurational forces [69, 123] based on the Eshelby stress [48, 49] are typically used to describe the mechanics of extended defects such as dislocations and cracks. In fracture mechanics, the **J**-integral [152] (the divergence of the Eshelby stress calculated via a contour integral) was developed to quantify the driving force for propagation of a crack due to mechanical energy available from external loading and other material inhomogeneities. It has been widely employed in macroscale experimental mechanics to measure materials inherent resistance to crack propagation. In nanoscience and nanotechnology, there is strong motivation to extend the application of **J** to the nanoscale given the influence of defects on performance and reliability of devices and materials. In a recent article [88], we developed a methodology for predicting the **J**-integral in nanostructures through the construction of continuum fields from atomic data, and using these fields in the traditional contour-integral expression for **J**. While we were able to show good agreement between our metric and expectations from continuum linear elastic fracture mechanics (LEFM), our method was only applied to quasi-static calculations performed at zero temperature where the atomic configurations were determined via energy minimization and the atomic potential energies

were employed in the potential for stress [1] .

Eshelby's tensor relies on the energy, stress and deformation measure be related such that the stress and the deformation measure are conjugate through the chosen energy. At finite temperatures, the stress potential depends on the process or ensemble. It is well known that the Helmholtz free energy is the potential for stress given a constant temperature process, whereas the internal energy is the appropriate potential for an isentropic process, see *e.g.*[119, Chapter 4] [23, Chapters 6 & 7]. We limit our present investigation to quasi-static loading at finite temperatures in thermal equilibrium using the Nosé-Hoover [77] realization of the constant temperature ensemble (NVT) in molecular dynamics (MD), where the appropriate energy is the Helmholtz free energy. For the case of non-equilibrium dynamic propagation, where the fracture process may be effectively adiabatic, the internal energy is the more appropriate quantity to include in the **J** expression. However, the standard expression for **J** would need to be amended with additional inertial and possibly temperature gradient terms to be valid. The estimated energy release rate will depend on which potential is employed as the theory of Nikolaevskii [142] shows in in isothermal and adiabatic limits. More discussion of this point of departure will be given in the concluding section.

The existing MD literature devoted to fracture mechanics that we are aware of has not taken the approach we are proposing. First of all, many efforts to estimate an atomic **J** using molecular dynamics are done so at near zero temperatures, *e.g.*Inoue *et al.* [81], where differences between internal energy and free energy are not significant. Nakatani *et al.* [141] estimate a strain energy density through changes in potential energy density (*i.e.* atomic potential energies divided by an atomic volume). Although they apply mechanical loading to a system equilibrated to a temperature of 300 K, it is not clear whether temperature controls are used during the loading process. While the imposed strain rate is very high ($\sim 10^{10}$ sec^{-1}), an unloading-relaxation-reloading process is used to evaluate mechanical properties. As such, the system cannot be considered to be either isothermal or adiabatic and, consequently, the relevant energy metric is unclear. Xu *et al.* [205] used a system energy release rate approach to estimate the critical value of **J** for the ductile fracture of a nano-sized crystal of nickel. Their analysis calculates **J** using changes in potential energy due to crack advance; however, their simulation is run at a temperature of 300 K using a specialized algorithm to scale atomic velocities at every step such that this temperature is maintained, *i.e.* isothermally. In another Griffith's-criteria [107, Chapter 1] based method, Latapie and Farkas [106] used MD to examine the ductile fracture behavior of nanocrystalline α-Fe at temperatures of 100 K, 300 K, and 600 K. While these authors do not attempt to quantify **J**, they do estimate the excess potential energy of the system as a function of average crack tip position. The slope of these calculated curves is equated to an estimate of fracture toughness which they observe to increase with increasing temperature. They associate this trend with an increase in observed plasticity in their simulations at higher temperatures. None of these past attempts to quantify the fracture process at finite temperature systems have made use of the free energy.

Free energy is complex to measure directly since it inherently involves an estimation of entropy density. We seek to construct a free energy density field in the same way that our formulation constructs stress, temperature and deformation gradient fields using weighted spatial average of atomic data over a region of compact support in the manner of Irving and Kirkwood [83] and Hardy [71].

[1] The potential for stress is sometimes called the "strain energy" density in the context of theory of elasticity.

One viable method for local estimates of free energy is the quasi-harmonic (QH) approximation [12, 18]. The QH method has known limits of applicability: the material has to behave classically [2], and the temperature must be low enough such that the approximation of harmonic motion superposed on large strain is valid. The full QH approximation, which is quite expensive to compute, has been followed by simplifications known as the local harmonic (LH) [111] and modified local harmonic (MLH) [155] approximations. The LH approximation is essentially an Einstein model of the vibrational frequencies and has been used extensively in MD-finite element coupling [16, 42, 90, 121, 186].

The QH model and its variants have been applied to the analysis of the free energy of vacancies, *e.g.*[56, 212], other point defects, *e.g.*[39, 131] and bulk mixtures, *e.g.*[84], using pair and many-body potentials. A number of authors have also used the QH method to examine extended defects. Foiles [56] performed simulations to calculate the free energy of a $\Sigma 5$ symmetric tilt grain boundary in copper as modeled with the embedded-atom method (EAM) [57]. The article compares free energy calculated via thermodynamic integration (TI), see *e.g.*[154], using data from Monte Carlo simulations with estimates made using the QH and LH approximations. Foiles notes that QH and LH are adequate for non-defected bulk crystals at low-to-moderate temperatures, but their underlying assumptions can break-down at high temperatures and around defects. As Foiles explains, the presence of defects can result in large amplitude vibrations that invalidate the assumption of a quadratic form of the potential energy. This, along with a loss of structural symmetry of the crystal around defects, results in third- and fourth-order terms contributing significantly to the potential energy expansion. Upon applying his method to the $\Sigma 5$ grain boundary, he observes that both QH and LH over-predict the interfacial free energy, with QH slightly better than LH. However, Foiles also remarks that his QH and LH estimates do not reflect systems that have been fully energy-minimized, *i.e.* atomic positions have not been relaxed to minimize the total free energy, which is likely the cause of at least some of the over-estimation. Even with this issue, the estimates appear to be acceptable for temperatures below half the melt temperature. Lebouvier *et al.* [108] used QH to model a $\Sigma 13$ grain boundary in silicon. They observed that variations in the grain boundary structure have only a small effect on the free energy calculated over a large variation in temperature (from 300 K to 1500 K). Najafabadi and Srolovitz [139] compared TI of Monte Carlo data with QH and their free-energy minimization method by analyzing bulk and defected structures in copper as modeled by both EAM and pair potentials (Lennard-Jones and Morse). Defected structures examined include the (001) free surface and single vacancy formation. Their results show very good agreement between the three methods for bulk crystals at various temperatures, particularly between QH and TI. For free surfaces, calculation of surface energy shows good agreement between QH and TI for the Lennard-Jones potential, while QH overestimates surface energy for Morse and even more-so for EAM. This difference between QH and TI is near zero at room temperature, but increases at higher temperatures. For example, at 1200 K the QH overestimates the TI estimate for surface energy by approximately 13.1%, 2.2%, and 0.5% for EAM, Morse, and Lennard-Jones, respectively. These same trends are also observed for vacancy formation energy.

In this chapter, we first develop the basic theory of the **J**-integral and the LH approximation specific to our goal of characterizing atomic-scale cracks at finite temperature. Next, we discuss

[2] An actual material would have to be above its Debye temperature, but for MD simulation this classical behavior exists at any temperature

our material frame formulation for constructing fields from MD data. Motivated by the results of Najafabadi and Srolovitz [139], we chose a Lennard-Jones test material and we show that that LH is sufficiently accurate for bulk states using a comparison with TI. Also, taking into account findings of Foiles [56], we measure the free energy in contours away from the crack tip and minimize the effects of the free surface that the contours cross by taking the free energy relative to a zero temperature reference configuration. Relying on these results, we subsequently show that our **J**-integral estimate based on free energy provides a significant correction to an estimate based on internal energy for an atomically sharp and smooth-sided single crack.

5.2 The J-integral

The Eshelby energy-momentum tensor $\mathcal{S}$ [48, 49] quantifies the configurational forces that drive the evolution of defects. It is defined in terms of the (Helmholtz) free energy density $\Psi = \Psi(\mathbf{F}, T)$, the deformation gradient $\mathbf{F}$ and the first Piola-Kirchhoff (PK) stress

$$\mathbf{P} = \partial_{\mathbf{F}}|_T \, \Psi \tag{5.1}$$

as

$$\mathcal{S} = \Psi \mathbf{I} - \mathbf{F}^T \mathbf{P} \, . \tag{5.2}$$

where T is the temperature. The deformation gradient $\mathbf{F} = \boldsymbol{\nabla}_{\mathbf{X}} \boldsymbol{\chi}$ is a kinematic measure defined in terms of the motion $\mathbf{x} = \boldsymbol{\chi}(\mathbf{X}, t)$ of material, with $\mathbf{X}$ being the position vector in the reference configuration. The Eshelby tensor has many applications to the mechanics of defects, specifically in characterizing the evolution and propagation of cracks and dislocations, see, *e.g.*[69, 123]. Rice's **J**-integral [152] is defined as a boundary integral of $\mathcal{S}$

$$\mathbf{J} = \int_{\partial\Omega} \mathcal{S}\,\mathbf{N}\, dA = \int_{\partial\Omega} \Psi \mathbf{N} - \mathbf{F}^T \mathbf{P}\mathbf{N}\, dA \tag{5.3}$$

where the Eshelby stress acts on $\mathbf{N}$, the outward normal to the surface $\partial\Omega$ enclosing the region Ω in the reference configuration. Consequently, $\mathbf{J}$ is directly related to the divergence of $\mathcal{S}$. Specifically, the **J**-integral can be employed to quantify the driving force for crack propagation.

5.3 Quasi-harmonic Cauchy-Born model

The basic thermodynamic quantities embedded in (5.2) can be related to the partition function Z [127, Chapter 7] of the lattice of atoms comprising the body occupying the region Ω. The free energy density

$$\Psi = U - TS = -\frac{k_B T}{V} \log Z \tag{5.4}$$

is a Legendre transform of the internal energy density

$$U = -\frac{1}{V} \frac{\partial}{\partial \bar{\beta}} \log Z \tag{5.5}$$

via the entropy density

$$S = \frac{k_B}{V}\left(\log Z - \bar{\beta}\frac{\partial}{\partial\bar{\beta}}\log Z\right) \tag{5.6}$$

where $\bar{\beta} = (k_B T)^{-1}$, k_B is Boltzmann's constant and V is a reference volume for the system. Note that we are using densities as opposed to the extensive versions that are more traditional in the literature, see, e.g. [98]. We define a tributary volume for an atom as $V_\alpha = V/N$ where N is the number of atoms in the system volume V.

The classical harmonic partition function [201, Section 4.5] for a quasi-harmonic (QH) system is based on the harmonic approximation of the Hamiltonian H

$$H \approx H_{QH} = \Phi_0(\mathbf{F}) + \frac{1}{2}\sum_{i=1}^{n}\left(\omega_i^2 m_i q_i^2 + \frac{1}{m_i}p_i^2\right) \tag{5.7}$$

with the atomic positions $\mathbf{x}_\alpha$ in the current configuration following the decomposition $\mathbf{x}_\alpha = \mathbf{F}\mathbf{X}_\alpha + \mathbf{q}_\alpha$, and the momenta $\mathbf{p}_\alpha$ begin given their usual definition. Here, and throughout this section, we will use a Greek subscript to refer to an enumeration of atomic quantities, e.g. $\mathbf{x}_\alpha$, and a Latin one for enumeration based on degrees of freedom, e.q. q_i, where i runs 1 to $n \approx 3N$. The resulting partition function Z is

$$\begin{aligned} Z_{QH} = Z_{QH}(\mathbf{F},T) &= h^{-n}\int_\Gamma \exp\left(-\bar{\beta}H(\mathbf{q},\mathbf{p};\mathbf{F})\right)\, d\mathbf{q}\, d\mathbf{p} = h^{-n} Z_{\mathbf{q}} Z_{\mathbf{p}} \\ &= \exp(-\bar{\beta}\Phi_0) h^{-n}\prod_{i=1}^{n}\int_{-\infty}^{\infty}\exp\left(-\frac{1}{2}\bar{\beta}\frac{1}{m_i}p_i^2\right) dp_i \int_{-\infty}^{\infty}\exp\left(-\frac{1}{2}\omega_i^2\bar{\beta}m_i q_i^2\right) dq_i \\ &= \exp(-\bar{\beta}\Phi_0) h^{-n}\prod_{i=1}^{n}\frac{2\pi}{\bar{\beta}\omega_i} = \exp(-\bar{\beta}\Phi_0)\prod_{i=1}^{n}\frac{k_B T}{\hbar\omega_i} \end{aligned} \tag{5.8}$$

We have non-dimensionalized Z by a factor of Planck's constant h (raised to the power $-n$) to connect with the quantum partition function, see *e.g.*[127, Chapter 7], in the the classical high temperature limit ($\hbar\omega_i \ll k_B T$)[3] . Hence, the Helmholtz free energy density, Ψ, of a crystalline solid is determined from the potential energy density, Φ_0, of the atoms in their average positions $\mathbf{F}\mathbf{X}_\alpha$ and the vibrational spectrum of frequencies, ω_i, [18, Section 16] as

$$\Psi_{QH} = \Phi_0 + \frac{k_B T}{V}\log\prod_{i=1}^{n}\frac{\hbar\omega_i}{k_B T} \tag{5.9}$$

The term in Eq. (5.9) depending on the vibrational modes of the lattice can be connected to eigenvalues of the dynamical matrix. The dynamical matrix, $\mathbb{D}_{\alpha\beta} = \mathbb{D}_{\alpha\beta}(\mathbf{F})$, is simply

$$\mathbb{D}_{\alpha\beta} \equiv \frac{V}{\sqrt{m_\alpha m_\beta}}\frac{\partial^2\Phi}{\partial\mathbf{q}_\alpha\partial\mathbf{q}_\beta}, \tag{5.10}$$

[3]Note $\int_{-\infty}^{\infty}\exp(-\frac{1}{2}\bar{\beta}x^2)\,dx = \sqrt{\frac{2\pi}{\bar{\beta}}}$. Also, it is necessary for the potential energy $\Phi_0 = \Phi(\mathbf{F})$ to be independent of q_i, and for the system to be in equilibrium $\frac{\partial\Phi}{\partial\mathbf{x}_\alpha} = \mathbf{0}$ to obtain this form.

where $V\Phi$ is the total potential energy of the crystal, and $\mathbf{q}_\alpha = \mathbf{x}_\alpha - \mathbf{F}\mathbf{X}_\alpha$ is the displacement of atom α from the (homogeneously) deformed state $\mathbf{F}\mathbf{X}_\alpha$. It is important to realize that Φ is distinct from Φ_0 as the former represents the true potential energy density while the latter is an approximation based on the assumption of homogeneous deformation.

Clearly, the vibrational frequencies ω_i are the eigenvalues of the dynamical matrix, and their product is related to the determinant of the dynamical matrix by

$$\prod_{i=1}^{n} \omega_i = \sqrt{\det \mathbb{D}} \tag{5.11}$$

where $\mathbb{D}$ is the system dynamical matrix assembled from the constituent $\mathbb{D}_{\alpha\beta}$ matrices. If the deformation gradient is uniform and the crystal is free of defects, infinite, and composed of a single element (so that $m_\alpha = m$), then each $\mathbb{D}_{\alpha\beta}$ is identical and, by translational invariance, the row of the dynamical matrix associated with any atom is identical (given an appropriate rotation of the indices). In this case, we can restrict our attention to interactions between a representative atom, denoted as $\beta = 0$, and all other atoms in the lattice

$$\mathbb{D}_\alpha \equiv \frac{V}{m} \frac{\partial^2 \Phi}{\partial \mathbf{q}_0 \partial \mathbf{q}_\alpha} \tag{5.12}$$

The local harmonic (LH) approximation [156] neglects the coupling between interacting atoms. For a homogeneous system, the LH simplification reduces the QH dynamical matrix to a single 3×3 matrix by dropping all the elements of the dynamical matrix except for $\alpha = \beta = 0$.

$$\mathbb{D}_{LH} \equiv \mathbb{D}_0 = m^{-1} \frac{\partial^2 \Phi}{\partial \mathbf{q}_0 \partial \mathbf{q}_0} \tag{5.13}$$

It will be shown in Section 5.5 that this drastic approximation is sufficient to accurately describe the behavior of our test material. In this case, the free energy density is:

$$\Psi_{LH} = \Phi_0 + \Theta_{LH} \tag{5.14}$$

where

$$\Theta_{LH} = \frac{k_B T}{V_\alpha} \log \left(\left(\frac{\hbar}{k_B T} \right)^3 \sqrt{\det \mathbb{D}_{LH}} \right) . \tag{5.15}$$

See Appendix 5.7 for details specific to pair potentials.

The internal energy density in this approximation is

$$U = \Phi_0 + \frac{n}{V} k_B T = \Phi_0 + c_v T \tag{5.16}$$

via (5.5), where nk_BT is the equilibrium total energy above the ground state $\Phi_0(\mathbf{F})$ and c_v is the heat capacity per volume at constant volume. For a classical system, the law of Dulong and Petit [10, Chapter 21] identifies the heat capacity c_v with

$$c_v = \frac{nk_B}{V} = \frac{3k_B}{V_\alpha} \tag{5.17}$$

5.4 J-integral estimates

The results in the previous section were for full system averages. Hardy's methodology allows for the local averaging needed to obtain fields and ultimately the divergences of fields necessary to evaluate the **J**-integral. Briefly, Hardy's methodology [71, 159] generalizes Irving and Kirkwood's well-known results [83] on relating atomic quantities to the continuous fields in the Euler balance laws to extended, continuous kernels.

If the system is in mechanical equilibrium, $\nabla_{\mathbf{X}} \cdot \mathbf{P} = \mathbf{0}$, the expression (5.3) can be simplified to

$$\mathbf{J} = \int_{\partial\Omega} \langle \Psi \rangle \mathbf{N} - \langle \mathbf{F}^T \mathbf{P} \rangle \mathbf{N} \, dA = \int_{\partial\Omega} \langle \Psi \rangle \mathbf{N} - \langle \mathbf{H}^T \mathbf{P} \rangle \mathbf{N} \, dA \tag{5.18}$$

where $\mathbf{H} = \mathbf{F} - \mathbf{I}$ is the displacement gradient. We use the zero temperature, perfect lattice as the reference configuration $\{\mathbf{X}_\alpha\}$, see our previous work [88, 224] and [201, Chapter 4] for a full justification. Assuming thermal equilibrium, $\nabla_{\mathbf{X}} T = \mathbf{0}$, or equivalently $\int_{\partial\Omega} T\mathbf{N} \, dA = \mathbf{0}$, allows us to drop directly related terms, *e.g.*the kinetic energy, in the boundary integral. This assumption leads specifically to

$$\int_{\partial\Omega} U\mathbf{N} \, dA = \int_{\partial\Omega} \Phi\mathbf{N} \, dA = \int_{\partial\Omega} \Phi_0 \mathbf{N} \, dA \tag{5.19}$$

via (5.16). In this case, another (equivalent) expression for **J** arises in the form of a correction to the **J**-integral calculated based on either: the zero-temperature potential energy $\mathbf{J}_0 = \mathbf{J}(\mathbf{F}, T = 0)$ or internal energy $\mathbf{J}_U$,

$$\begin{aligned} \mathbf{J}_T &= \int_{\partial\Omega} \Phi_0 \mathbf{N} - \langle \mathbf{H}^T \mathbf{P} \rangle \mathbf{N} - \langle \Theta \rangle \mathbf{N} \, dA = \mathbf{J}_0 - \int_{\partial\Omega} \langle \Theta \rangle \mathbf{N} \, dA \\ &= \int_{\partial\Omega} \langle U \rangle \mathbf{N} - \langle \mathbf{H}^T \mathbf{P} \rangle \mathbf{N} \, dA - \int_{\partial\Omega} \langle \Theta \rangle \mathbf{N} \, dA = \mathbf{J}_U - \int_{\partial\Omega} \langle \Theta \rangle \mathbf{N} \, dA \end{aligned} \tag{5.20}$$

given the definition (5.14). It is noteworthy that $\mathbf{J}_U$ can be estimated by the usual formula based on Hardy estimates alone, *i.e.* without resorting to the QH model. We will assume that ensemble average $\langle \bullet \rangle$ is approximated by the long time average under constant temperature dynamics. Specifically, the quantities in angle brackets are functions of $\mathbf{H}$ and T which are estimated from the atomic positions relative to a reference configuration and atomic velocities in a manner that will be described shortly. Lastly, as in our previous work [88], we employ a free energy relative to the reference configuration by shifting Ψ by the potential energy density field of the zero-temperature, reference configuration.

For a uniform temperature field

$$\begin{aligned} \int_{\partial\Omega} \langle \Theta \rangle \mathbf{N} \, dA &= \int_{\partial\Omega} \left\langle \frac{k_B T}{V_\alpha} \log \left(\left(\frac{\hbar}{k_B T} \right)^3 \sqrt{\det \mathbb{D}_{LH}} \right) \right\rangle \mathbf{N} \, dA \\ &= \int_{\partial\Omega} \left\langle \frac{k_B T}{V_\alpha} \log \left(\sqrt{\det \mathbb{D}_{LH}} \right) \right\rangle \mathbf{N} + \left\langle \frac{k_B T}{V_\alpha} \log \left(\frac{\hbar}{k_B T} \right)^3 \right\rangle \mathbf{N} \, dA \\ &= \frac{k_B T}{V_\alpha} \int_\Omega \nabla_{\mathbf{X}} \left\langle \log \sqrt{\det \mathbb{D}_{LH}} \right\rangle dV = \frac{k_B T}{V_\alpha} \int_\Omega \left\langle \frac{\nabla_{\mathbf{X}} \det \mathbb{D}_{LH}}{2 \det \mathbb{D}_{LH}} \right\rangle dV \end{aligned} \tag{5.21}$$

is clearly nearly linear in T, given a weak dependence of $\mathbb{D}_{LH}$ on T. Furthermore, using linearization based on Jacobi's formula : $\det\mathbb{D}(\mathbf{x}_\alpha) = \det\mathbb{D}(\mathbf{X}_\alpha)(1+\mathrm{tr}(\mathbb{D}^{-1}(\mathbf{X}_\alpha)\Delta\mathbb{D})) + O(\|\Delta\mathbb{D}\|^2)$, we see that this same correction to Ψ is linear in the change in $\mathbb{D}$ due to deformation, $\Delta\mathbb{D}$,

$$\begin{aligned}\int_{\partial\Omega}\langle\Theta\rangle\mathbf{N}\,dA &\approx \frac{k_BT}{V_\alpha}\int_\Omega\left\langle\frac{\det\mathbb{D}(\mathbf{X}_\alpha)\boldsymbol{\nabla}_\mathbf{X}\,\mathrm{tr}\left(\mathbb{D}^{-1}(\mathbf{X}_\alpha)\Delta\mathbb{D}\right)}{2\left(\det\mathbb{D}(\mathbf{X}_\alpha)+\det\mathbb{D}(\mathbf{X}_\alpha)\,\mathrm{tr}\left(\mathbb{D}^{-1}(\mathbf{X}_\alpha)\Delta\mathbb{D}\right)\right)}\right\rangle dV \\ &\approx \frac{k_BT}{2V_\alpha}\int_\Omega\left\langle\boldsymbol{\nabla}_\mathbf{X}\left(\mathrm{tr}\left(\mathbb{D}^{-1}(\mathbf{X}_\alpha)\Delta\mathbb{D}\right)\right)\right\rangle dV\end{aligned} \tag{5.22}$$

for a small perturbation $\Delta\mathbb{D}$ from an undeformed, perfect lattice reference configuration $\mathbf{X}_\alpha$, *i.e.* $\boldsymbol{\nabla}_\mathbf{X}\mathbb{D}(\mathbf{X}_\alpha) = \mathbf{0}$. Here we have dropped the subscript *LH* for clarity.

Given the expressions (5.18) and (5.20), we need estimates for $\mathbf{H}$, $\mathbf{P}$, and T given the explicit dependencies and the arguments of Ψ and Θ. As in our previous work [88, 224], we employ a Lagrangian formulation of Hardy estimation based on a normalized localization function $\psi(\mathbf{X}) \mid \int_\Omega \psi\,dV = 1$. Many suitable choices for the particular form of ψ are available; in this work we adopt the piece-wise linear finite element basis functions first introduced in [224].

In order to define the displacement gradient $\mathbf{H}$ in terms of atomic quantities, we must first define the displacement $\mathbf{u} = \mathbf{x} - \mathbf{X}$. This is done in a mass-weighted fashion

$$\mathbf{u}(\mathbf{X},t) = \frac{\sum_\alpha(\mathbf{x}_\alpha(t)-\mathbf{X}_\alpha)\,m_\alpha\psi(\mathbf{X}_\alpha-\mathbf{X})}{\sum_\alpha m_\alpha\psi(\mathbf{X}_\alpha-\mathbf{X})}, \tag{5.23}$$

with m_α being the mass of atom α, in order to connect to the dynamical variable, momentum, which is given a primitive definition in the Hardy formalism [71]. To obtain the gradient $\mathbf{H} = \boldsymbol{\nabla}_\mathbf{X}\mathbf{u}$, we compute (5.23) on a grid of points $\mathbf{X}_I$ and then interpolate $\mathbf{u}$ as

$$\mathbf{u}(\mathbf{X},t) = \sum_I \mathbf{u}_I(t)N_I(\mathbf{X}) = \sum_{I,\alpha} N_I\,\psi_{I\alpha}\,\mathbf{u}_\alpha, \tag{5.24}$$

using a partition of unity[4] basis N_I, where $\mathbf{u}_I = \mathbf{u}(\mathbf{X}_I,t)$ and $\psi_{Ia} = \psi(\mathbf{X}_\alpha - \mathbf{X}_I)$. A differentiation of this interpolation leads directly to our definition of the displacement gradient

$$\mathbf{H} = \boldsymbol{\nabla}_\mathbf{X}\mathbf{u} = \sum_I \mathbf{u}_I(t)\boldsymbol{\nabla}_\mathbf{X}N_I(\mathbf{X})\ . \tag{5.25}$$

The temperature field is simply given a kinetic definition

$$T(\mathbf{X},t) = \frac{1}{3k_B}\frac{\sum_\alpha m_\alpha\mathbf{v}_\alpha(t)\cdot\mathbf{v}_\alpha(t)\,\psi(\mathbf{X}_\alpha-\mathbf{X})}{\sum_\alpha\psi(\mathbf{X}_\alpha-\mathbf{X})} \tag{5.26}$$

The referential first Piola-Kirchhoff stress [224] for pair potentials[5] can be defined in terms of the force $\mathbf{f}_{\alpha\beta}$ between atoms α and β and the difference between their positions in the reference

[4] A partition of unity interpolation has the property $\sum_I N_I = 1$ and examples include the usual finite element interpolations.

[5] Additional details on the form of $\mathbf{P}$ for pair and central force potentials can be found in [224]. This reference also discusses the definition of $\mathbf{f}_{\alpha\beta}$ in the case of more general potentials, *e.g.*, Stillinger-Weber.

configuration $\mathbf{X}_{\alpha\beta} = \mathbf{X}_\alpha - \mathbf{X}_\beta$. Instead of a simple average of the virial weighted by $\psi_{I\alpha}$, the so-called "bond" function $B_{\alpha\beta}$ is required for consistency with the continuum [71, 159, 224]

$$B_{\alpha\beta}(\mathbf{X}) = \int_0^1 \psi\left(\lambda(\mathbf{X}_\alpha - \mathbf{X}) + (1-\lambda)(\mathbf{X}_\beta - \mathbf{X})\right) d\lambda \tag{5.27}$$

and is constructed directly from the localization function ψ. The resulting expression for the first PK stress is

$$\mathbf{P}(\mathbf{X},t) = -\sum_{\alpha<\beta} \mathbf{f}_{\alpha\beta}(t) \otimes \mathbf{X}_{\alpha\beta} B_{\alpha\beta}(\mathbf{X}) \tag{5.28}$$

Lastly, we can estimate the potential energy density as

$$\Phi = \frac{1}{2}\sum_\alpha \phi_\alpha \psi_{I\alpha} \tag{5.29}$$

and the internal energy density in a manner consistent with (5.16). For further details the construction of fields via the Lagrangian Hardy formalism consult [88, 224].

5.5 Results

For this study we use a Lennard-Jones (LJ) model of Au with lattice constant $a = 4.08$ Å and parameter values $\varepsilon = 0.72427860$ eV, $\sigma = 2.59814680$ Å, as representative of a well-behaved atomic solid. This inter-atomic potential is truncated at a separation of $r_c = 2.1\sigma = 5.45610827$ Å, and smoothed such that pair energy and forces are zero at this distance, see [100, equation (121)]. This parametrization leads to elastic constants , $C_{11} = 497.478$ GPa, $C_{12} = C_{44} = 281.58$ GPa [6] , and a surface energy of 0.1599 eV/Å^2. For reference, the experimentally measured Debye temperature for Au is $170\,K$ and its melt temperature is $1337\,K$. Since the LJ model over-estimates the elastic constants of Au ($C_{11} = 186$ GPa, $C_{12} = 157$ GPa, $C_{44} = 42$ GPa), the approximate effective Debye and melt temperatures are $280\,K$ and $5200\,K$, respectively [7] .

In the following, we first validate the free-energy model and then employ it in the estimation of the **J**-integral of a finite temperature, quasi-static crack. The validation is necessary to give confidence in the **J**-integral and the conclusions we draw from it. All simulations were performed with the publicly available LAMMPS MD code (see http://lammps.sandia.gov).

5.5.1 Free energy

To validate the use of a LH model of free energy, we compare Ψ_{LH} to estimates of Ψ from thermodynamic integration (TI) for four (one-parameter) deformations: (a) uniaxial stretch $\mathbf{F} = \lambda \mathbf{e}_1 \otimes \mathbf{E}_1$,

[6] These elastic constants were determined analytically and verified empirically.

[7] The Debye temperature T_{Debye} is estimated using the fact that it is proportional to the speed of sound in the material so that $T_{Debye} \sim \sqrt{C_{11}}$. The melt temperature T_{melt} is proportional to the depth of the potential well and can be approximated by $k_B T_{melt} \approx 0.62\varepsilon$ where k_B is the Boltzmann constant.

(b) simple shear $\mathbf{F} = \lambda \mathbf{e}_1 \otimes \mathbf{E}_2$, (c) biaxial stretch / pure shear $\mathbf{F} = \lambda \mathbf{e}_1 \otimes \mathbf{E}_1 + 1/\lambda \mathbf{e}_2 \otimes \mathbf{E}_2$, and (d) volumetric dilation $\mathbf{F} = \lambda \mathbf{I}$, through $\{\mathbf{F}, T\}$ space, where $\mathbf{F} = \mathbf{I} + \mathbf{H}$. The Cartesian bases $\mathbf{e}_i$ and $\mathbf{E}_i$, in the current and reference configurations respectively, are aligned with the lattice basis in the reference configuration. To perform TI we fitted the $\mathbf{P}$ vs $\mathbf{F}$ and U vs T trends (for small values of λ and T) from NVT MD data using the Nosé-Hoover thermostat (NH) and integrated these fits to obtain Ψ_{TI}. It was also necessary to take a single temperature close to zero where we assumed $\Psi_{TI} \equiv \Psi_{LH}$ for all deformations. The correspondence of Ψ_{LH} and Ψ_{TI} at higher temperatures justifies the somewhat arbitrary choice of 1 K for this reference temperature. See Appendix 5.8 for more details of the procedure.

To realize the various deformation-temperature states we : (a) obtained a sequence of zero temperature, deformed configurations through energy minimization and displacement boundary conditions on a periodic system, (b) from each of these states we thermalized the system to a steady, equilibrium state using NH dynamics, and then (c) took long time averages of the necessary quantities under the same dynamics. Since these are equilibrium states, the path to arrive at them is immaterial and consequently the procedure was chosen based on expediency. The states were verified to be at equilibrium by reversing the temperature loading and checking that the same averages where obtained to within error.

First, we take a temperature excursion from $1K$ to $600K$ for: a uniaxial stretch (a) $F_{11} = 1.015$ and a volumetric dilation (d) $F_{11} = F_{22} = F_{33} = 1.045$. Figure 5.1 shows the excellent comparison of Ψ_{LH} and Ψ_{TI} for the uniaxial case and, likewise, Figure 5.2 shows similar results for the volumetric case. Both Figure 5.1a and Figure 5.2a exhibit similar slopes, 1.52163×10^{-5} and 1.52176×10^{-5} eV/(K-Å)^3, respectively corresponding to the heat capacity $c_v = 1.52256 \times 10^{-5}$ eV/(K-Å)^3 based on the reference V_α in (5.17). The intercepts, -0.23112 and -0.22945 eV/Å^3 respectively, depend on deformation as Eq. (5.16) indicates. The temperatures at which U crosses Ψ and is henceforth strictly greater than Ψ are 12.2 K and 14.1 K respectively as can be seen in the insets of Figures 5.1(b) and 5.2(b).

Second, we deform for simple shear (b) and biaxial stretch (c) at a sequence of constant temperatures $T = 30, 100, 300$ K. The reader should note that biaxial stretch effects a "pure" shear state with respect to a coordinate system rotated by $\pi/4$ about the $\mathbf{E}_3$ axis and that $F_{12} \equiv H_{12}$. These shear deformation modes are particularly rigorous tests of the LH model. Figure 5.3 shows reasonable correlation between the LH and TI estimates of free energy for simple shear (b) and Figure 5.4 shows similar results for biaxial stretch. It is apparent that the behavior of the LH estimate is less noisy for a temperature process than for a deformation process, perhaps due to the differencing of atomic positions required in the Hardy based estimate of $\mathbf{F}$. The discrepancies are clearly temperature dependent and are not noticeable at the lowest temperature. These tests demonstrate that there is thermodynamic consistency between the derivative of the free energy and the stress measure *i.e.* (5.1). As expected, the respective moduli are relatively insensitive to temperature. For our material, the modulus for simple shear is C_{12} = 281.58 GPa which is slightly higher than the modulus for pure shear $(C_{11} - C_{12})$ = 215.898 GPa.

The results displayed in this section are typical for temperatures below half melt and strains below 10 %. Although not completely verified, it appears that our test system is behaving in

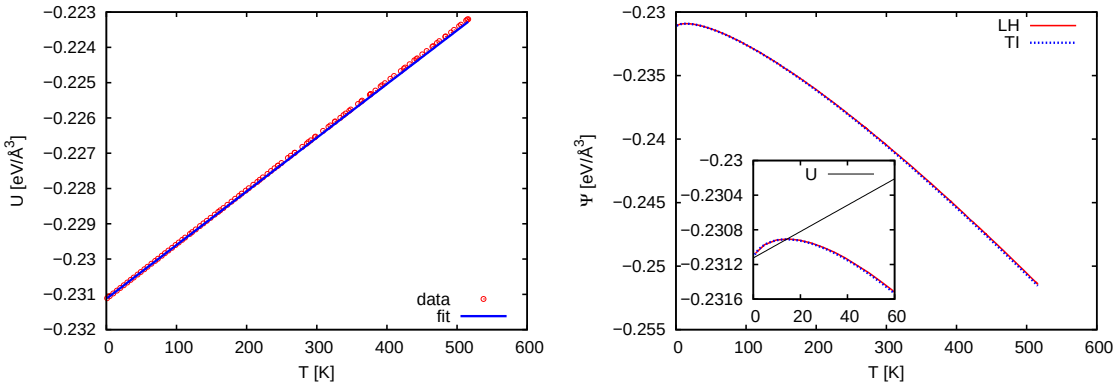

(a) **(b)**

Figure 5.1. (a) Internal, and (b) Free energy density variation with temperature for the LJ-gold system at a uniaxial stretch of 1.015 and T_{ref} = 1 K.

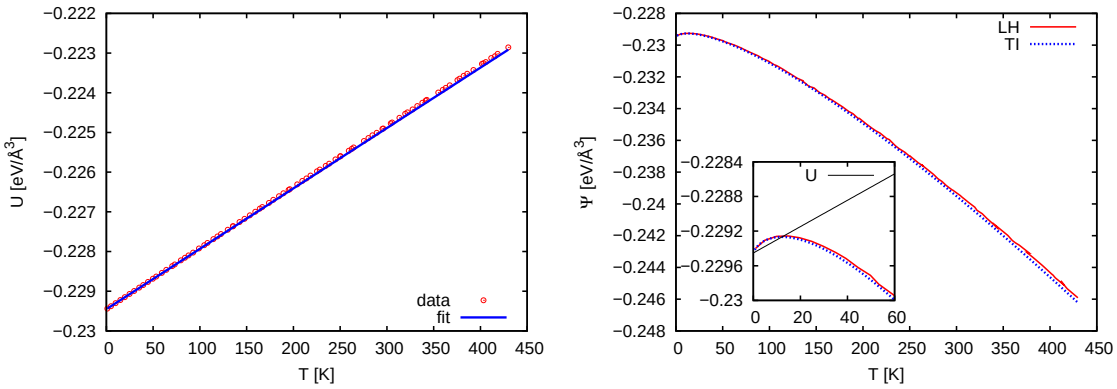

(a) **(b)**

Figure 5.2. (a) Internal, and (b) Free energy density variation with temperature for the LJ-gold system at a volumetric stretch of 1.045 and T_{ref} = 1 K.

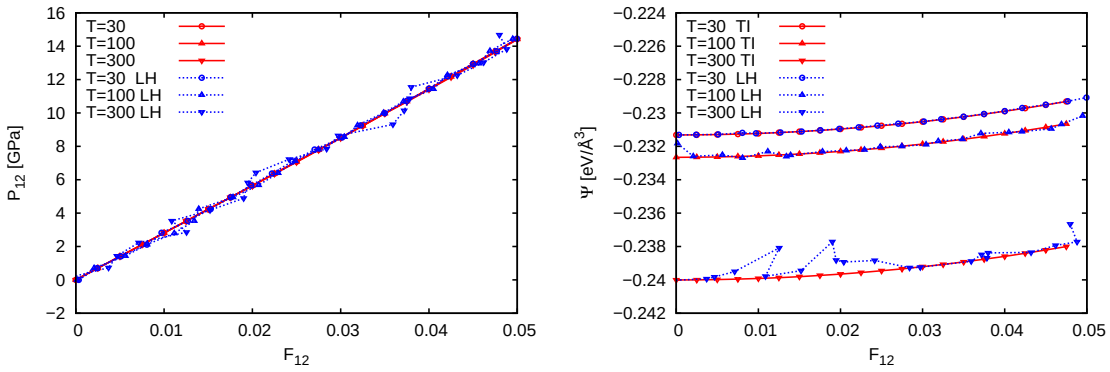

(a) **(b)**

Figure 5.3. Simple shear at $T = 30, 100, 300\,K$. (a) P_{12} vs. F_{12} and (b) U, Ψ_{LH} and Ψ_{TI} vs. F_{12}.

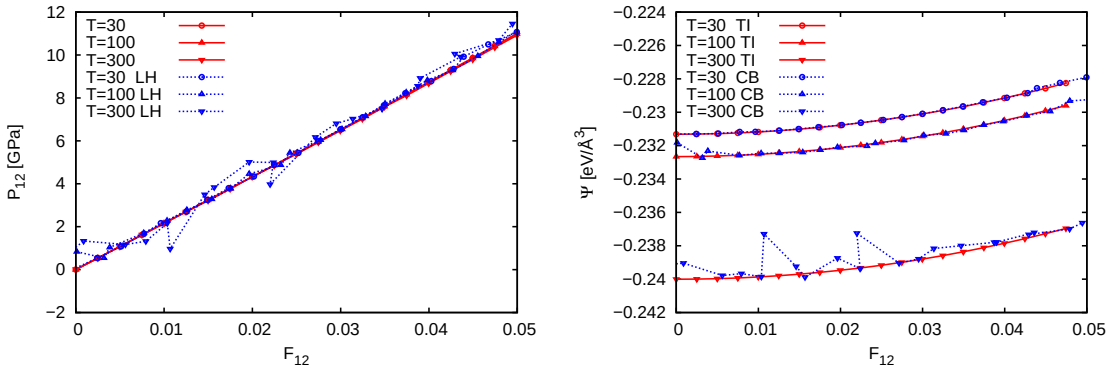

(a) **(b)**

Figure 5.4. Biaxial stretch at $T = 30, 100, 300\,K$. (a) P_{12} vs. F_{12} and (b) U, Ψ_{LH} and Ψ_{TI} vs. F_{12}.

manner consistent with a linear thermo-elastic material with a free energy of the form [9]:

$$\Psi = \frac{1}{2}\mathbf{H}\cdot\mathbb{C}\mathbf{H} - T\boldsymbol{\alpha}\cdot\mathbf{H} - \frac{1}{2}c_v T^2 \tag{5.30}$$

where $\mathbb{C} = \frac{\partial^2\Psi}{\partial\mathbf{H}\partial\mathbf{H}}$ is a (fourth-order) elastic modulus tensor and $\boldsymbol{\alpha} = \frac{\partial^2\Psi}{\partial\mathbf{H}\partial T}$ is a thermal expansion tensor. These results give confidence that the thermodynamic consistency necessary establish Eq. (5.1) with Hardy measures of the fields is satisfied. It should also be noted that $\boldsymbol{\alpha}$ can be related to a Grüneisen-like tensor $\boldsymbol{\gamma} = -\frac{1}{c_v}\boldsymbol{\alpha}$, which is a well-known measure of the sensitivity of entropy to deformation as well as stress to changes in temperature and therefore related to how the vibrational modes ω_i are affected by these changes.

5.5.2 J-integral of a single crack at finite temperature

The fundamental crack tip solution [107, Chapter 2] in polar coordinates r, θ is

$$\begin{aligned} u_1 &= \frac{K_I}{2\mu}\sqrt{\frac{r}{2\pi}}\cos\left(\frac{\theta}{2}\right)\left[\kappa - 1 + 2\sin^2\left(\frac{\theta}{2}\right)\right] \\ u_2 &= \frac{K_I}{2\mu}\sqrt{\frac{r}{2\pi}}\sin\left(\frac{\theta}{2}\right)\left[\kappa + 1 - 2\cos^2\left(\frac{\theta}{2}\right)\right] \end{aligned} \tag{5.31}$$

for a two-dimensional crack aligned with $\mathbf{e}_1$. Here μ is the elastic shear modulus, $\kappa = 3 - 4\nu$ and ν is Poisson's ratio. Linear elastic fracture mechanics (LEFM) predicts the value of $\mathbf{J}$ to be quadratically dependent on the stress intensity factor K_I and inversely proportional to the appropriate modulus E^*

$$\mathbf{J} = \frac{K_I^2}{E^*}\mathbf{E}_1 \tag{5.32}$$

For normal (mode I) loading, the modulus E^* is

$$E^* = \frac{E}{1-\nu^2} = \frac{C_{11} - 2C_{12}^2/(C_{11}+C_{12})}{1-(C_{12}/(C_{11}+C_{12}))^2} = 338.099\,\text{GPa} \tag{5.33}$$

for a material with cubic symmetry.

To realize a system similar to the LEFM idealization of a crack, we created a perfect lattice in a cylindrical region of radius $20a$ and $3a$ in depth (consisting of 18276 atoms). Periodic boundary conditions were applied in the $\mathbf{e}_3$ direction. We created a crack by deleting interactions on a slit extending to the center of the cylindrical region and boundary conditions in the $\mathbf{e}_1$ and $\mathbf{e}_2$ directions corresponding to (5.31) were effected on an annular layer of zero temperature atoms away from the crack tip, see Figure 5.5. Using a loading procedure similar to that used in the previous section, *i.e.* zero temperature minimization of a sequence of deformed states indexed by K_I and then thermalized using a NH thermostat, we obtain the necessary time averaged fields taken over 10^5 samples at sampling frequency $40\,fs$ (variances were computed from 10 independent averages of same data). The support of the localization function ψ is twice the size of the mesh elements which are square and one lattice unit in width. The four loops that were used to compute

(5.18) were taken outside the central crack tip region where Ψ_{LJ} is expected to be a good estimator of free energy (loop 3 is shown in Figure 5.5b). As mentioned in Section 5.2 the free energy density field is computed relative to that of a zero temperature reference configuration, which has the effect of negating the perturbation due to the free energy of the existing surfaces.

As in our zero temperature work [88], Figure 5.6 shows remarkable path independence for T=100, 300 K (with similar results for other temperatures). All loops display equivalent values to within error based on thermal fluctuations for a given T. Loop 0, which does not encompass the crack, displays an insignificant J_1 value relative to the other loops, as expected.

Figure 5.7 shows the temperature dependence of $\mathbf{J}$ and $\mathbf{J}_U$ for $T = 10, 100, 300, 600, 900, 1200$ K. All J_1 curves at $T > 0$ are below the T=0 curve as a consequence of the reducing driving force which delays fracture propagation. It is notable that $(J_1)_U$ at T=10 K is actually above the T=0 curve and that at this temperature $U \approx \Psi$, so it seems that the divergence of Ψ is significantly different that that of U. The thermal expansion constrained by the boundary atoms used to stretch the system creates compressive stresses which are unloaded as the boundary atoms follow a motion given by (5.31). Near $K_I = 0$ we have identified some trends that are artifacts of the way in which we created the crack by deleting atomic interactions that would have supported the compressive stresses at low K_I. In the literature this is a common way to create a crack, but a non-healing crack under compression from thermal expansion leads to some fictitious relief of the compressive stresses. Once the boundary loading is sufficient to open the crack fully, these artifacts disappear. Without these artifacts we would expect that all the $\mathbf{J}$ curves for the various temperatures would approximately the same shape, even near the origin, and that the vertical shift of the $T = 0$ curve dependent on temperature seen at higher applied K_I would carry through to $K_I \rightarrow 0$. If this were achievable, it would clearly illustrate that the total K_I is the sum of the far-field, applied K_I and a component due to thermal effects. Also, it is apparent from Figure 5.7a that the strict ordering of the J_1 curves with temperature is broken in the neighborhood of $T \approx 1000$. This may be due solely to the larger variances in the observed quantities at higher temperature but it could also be due to the loss of accuracy of the LH model in a more anharmonic environment.

Figure 5.7c shows the difference in the internal energy and free energy-based J_1-integrals (the temperatures $T = 900, 1200$ have been omitted due to their large variances obscuring the other curves). The difference is clearly due to the divergence of Θ (5.21), since the difference for loop 0 that does not surround the crack is zero. The correction is apparently linear in K and T as Eqs. (5.21) and (5.22) would lead us to expect, and is approximately 10 % different at 300 K near K_{Ic}. The differences may not be strictly statistically significant given the calculated error estimates; however, we expect that the trends will remain if the time-averages were extended to the point that the variances in the averages become insignificant. It is well know the time averaging has a slow $N^{-1/2}$ convergence where N is the number of independent samples. An alternate method to overcome the errors is averaging over an ensemble of parallel replicates generated from the constant temperature Boltzmann distribution.

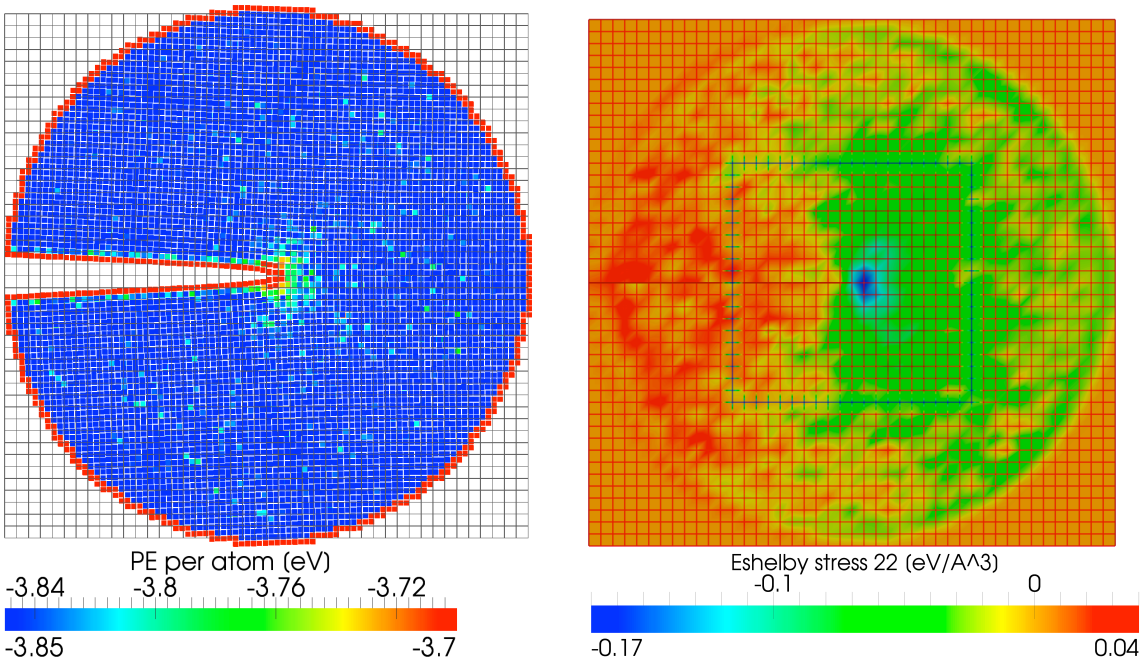

(a) Lattice colored by potential energy

(b) Eshelby stress component $\mathcal{S}_{22}$

Figure 5.5. Deformation and stress state at $K_I/K_{Ic} = 0.975$, $T = 300\,K$. (a) Lattice configuration showing overlaid mesh, only some of the boundary atoms used to control the deformation are show for clarity. (b) Eshelby stress component $\mathcal{S}_{22}$ showing concentration at crack tip in the center of the mesh (size $h = a$) and background thermal fluctuations. The third largest loop (loop 3) used to evaluate the **J**-integral is shown for size. Note in (a) the lattice is in its deformed configuration but the mesh is in its reference configuration.

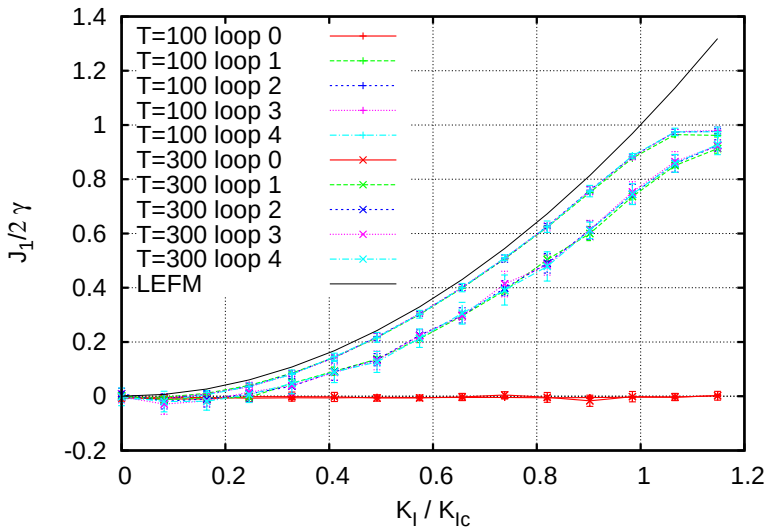

Figure 5.6. Path independence of the **J**-integral at T=100K and 300K. Loops of various sizes give the same J_1 values to within error. The four square loops centered on the crack tip with side lengths of $8a$, $16a$, $20a$ and $24a$ are labeled loop 1, 2, 3, 4, respectively. Note loop 0 does not encompass the crack tip and is used to give an estimate of the error in the evaluation of the contour integrals.

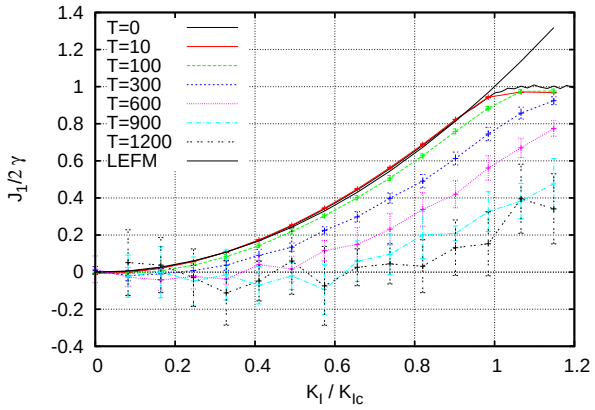

(a) **J**-integral based on LH free energy **J**

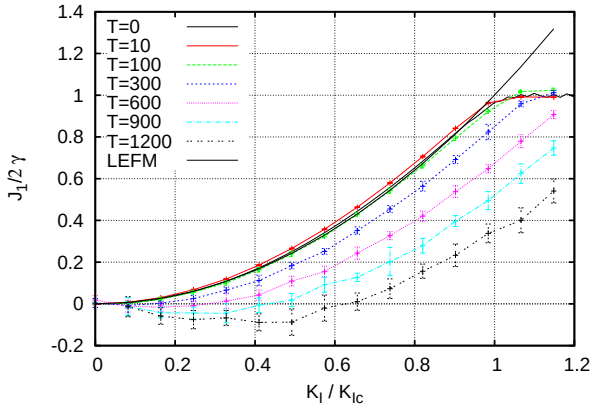

(b) **J**-integral based on internal energy $\mathbf{J}_U$

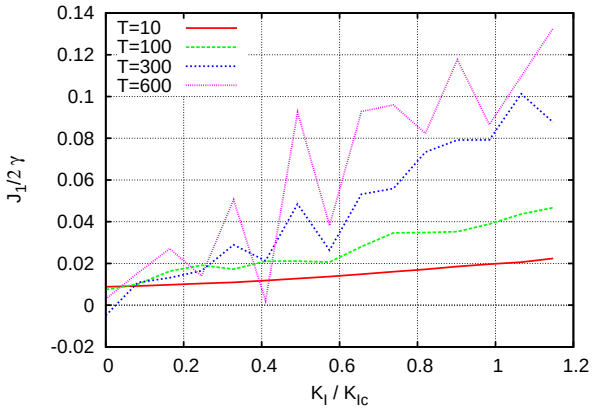

(c) Difference $\mathbf{J}_U - \mathbf{J}$

Figure 5.7. Temperature dependence of (a) **J** and (b) $\mathbf{J}_U$, (c) shows the small but significant overestimation of **J** by a estimator based on internal energy $\mathbf{J}_U$.

5.6 Discussion

This work shows the reduction of the **J** estimates due to fact that the free energy available for crack propagation is less that the internal energy at sufficiently high temperatures. Mechanically, this entropy increase is manifest in thermal expansion. We calculate that **J**-integrals at room temperature based on internal or potential energy can over-estimate **J** by approximately 10 %. In needs to be emphasized that both MD and QH require high enough temperatures $h\omega \gg k_B T$ for their classical behavior to correspond to real materials but QH has the additional restriction that the temperature needs to be sufficiently low so that harmonic approximation is still valid. Our results show that that behavior at temperatures at least as high as one-eighth of the effective melt temperature can be simulated sufficiently accurately with LH model. More accurate models like the MLH may extend this result to higher temperatures.

The present work is confined to crystalline solids; however, extension to amorphous solids is feasible. Since the Hardy methodology [71] using a kernel-based estimator of fields was originally developed for liquids, we have confidence that the means for determining the stress and displacement fields will be accurate for a dense, amorphous material without modification. On the other-hand, the Cauchy-Born formula that the free-energy estimates are based on would most likely need to be modified along the lines of the virtual internal bond [99] extension to the Cauchy-Born rule. Whether this would accurately represent the phonon modes needed to determine the dynamical matrix would need to be tested.

In future work, we intend to explore a wider range of materials that may warrant the accuracy of the MLH [94, 155] to produce physical results and significant corrections. To extend this work to a dynamically propagating crack, the issue of what constitutes the appropriate contour integral in this case would need to be revisited. A certain amount of previous work [103, 142] exists on the subject, most notably Maugin's [124]. The author noted that for general dynamic, thermo-mechanical problems the free energy density should be used, and a thermal material force dependent on the gradient of the temperature field should be included. For such an analysis, the resulting integral is not path-independent due to fact that a nonuniform temperature field can be viewed as a distributed source of material inhomogeneity.

5.7 Appendix C: Quasiharmonic model for pairwise potentials

In the case of pairwise potentials the potential energy density for the system is given by

$$\Phi = \frac{1}{2V} \sum_{\alpha}^{N} \sum_{\beta \neq \alpha}^{N} \phi(r_{\alpha\beta}), \tag{C.1}$$

where ϕ is the pairwise interaction which depends solely on the distance $r_{\alpha\beta}$ between two atoms and V is the volume of the undeformed crystal. The LH dynamical matrix for a monoatomic lattice

is

$$\begin{aligned}\mathbb{D}_{LH} &= \frac{1}{m}\frac{\partial^2\Phi}{\partial\mathbf{u}_0^2} = \frac{1}{m}\frac{\partial}{\partial\mathbf{u}_0}\sum_{\beta\neq 0}\phi'(r_{\beta 0})\frac{\mathbf{r}_{\beta 0}}{r_{\beta 0}} \\ &= \frac{1}{m}\sum_{\beta\neq 0}\left(\phi''(r_{\beta 0})\frac{\mathbf{r}_{\beta 0}}{r_{\beta 0}}\otimes\frac{\mathbf{r}_{\beta 0}}{r_{\beta 0}} + \phi'(r_{\beta 0})\frac{1}{r_{\beta 0}}\left[\mathbf{I} - \frac{\mathbf{r}_{\beta 0}}{r_{\beta 0}}\otimes\frac{\mathbf{r}_{\beta 0}}{r_{\beta 0}}\right]\right)\end{aligned} \tag{C.2}$$

given $\mathbf{I}$ being the identity tensor and

$$\begin{aligned}\frac{\partial r_{\beta 0}}{\partial\mathbf{u}_0} &= -\frac{\mathbf{r}_{\beta 0}}{r_{\beta 0}}, \\ \frac{\partial^2 r_{\beta 0}}{\partial\mathbf{u}_0^2} &= \frac{1}{r_{\beta 0}}\left(\mathbf{I} - \frac{\mathbf{r}_{\beta 0}}{r_{\beta 0}}\otimes\frac{\mathbf{r}_{\beta 0}}{r_{\beta 0}}\right),\end{aligned} \tag{C.3}$$

for $\beta \neq 0$.

5.8 Appendix D: Thermodynamic integration

Direct thermodynamic integration (TI) [95] can be used to calculate the free energy difference between two states connected by a reversible path. It is based on the differentials of the Helmholtz free energy state function $\Psi(\mathbf{F},T)$

$$d\Psi = d\Psi(V,T) = d(U-TS) = (TdS - \mathbf{P}\cdot d\mathbf{F}) - TdS - SdT = \mathbf{P}\cdot d\mathbf{F} - SdT \tag{D.1}$$

where $\left.\frac{\partial\Psi}{\partial T}\right|_{\mathbf{F}} = -S$, $\left.\frac{\partial\Psi}{\partial\mathbf{F}}\right|_{T} = \mathbf{P}$. Now, a path at constant temperature leads to

$$\Delta\Psi = \int\langle\mathbf{P}\rangle_{NVT}\cdot d\mathbf{F} \;\rightarrow\; \Psi_1 = \Psi_0 + \int\langle\mathbf{P}\rangle_{NVT}\cdot d\mathbf{F} \tag{D.2}$$

and likewise

$$\Delta\left(\frac{\Psi}{T}\right) = \int\langle U\rangle_{NVT}\,dT \;\rightarrow\; \Psi_1 = \Psi_0\frac{T_1}{T_0} + T_1\int_0^1\langle U\rangle_{NVT}\,d(1/T) \tag{D.3}$$

for a path at constant deformation. An example of the first formula for a uniaxial deformation $\mathbf{F} = \lambda\mathbf{e}_1\otimes\mathbf{E}_1 + \mathbf{e}_2\otimes\mathbf{E}_2 + \mathbf{e}_3\otimes\mathbf{E}_3$ is

$$\Psi_1 = \Psi_0 + \int_{\lambda_0}^{\lambda_1}\langle P_{11}\rangle_{NVT}\,d\lambda \tag{D.4}$$

The second statement (D.3) is a result of

$$\frac{\Psi}{T} = \frac{U}{T} - S \;\rightarrow\; d\left(\frac{\Psi}{T}\right) = Ud\left(\frac{1}{T}\right) + \frac{1}{T}dU - dS \;\rightarrow\; d\left(\frac{\Psi}{T}\right) = Ud\left(\frac{1}{T}\right) \tag{D.5}$$

which comes from the definition $dS = dS(V,T) = \frac{1}{T}dU$, the assumption that dU is equal to the differential of net heat absorbed, and the differential of the internal energy state function

$$dU = dU(\mathbf{F},S) = \left.\frac{\partial U}{\partial S}\right|_{\mathbf{F}} dS + \left.\frac{\partial U}{\partial \mathbf{F}}\right|_{S} d\mathbf{F} = T\,dS + \mathbf{P}\cdot d\mathbf{F} \tag{D.6}$$

restricted to constant deformation.

It is well-known that (D.3) is problematic starting from $T_0 = 0$. Even at small temperatures where the approximation

$$U|_{\mathbf{F}} = aT + b \tag{D.7}$$

(see Eq. (5.16)) is valid for a classical system and

$$\tilde{\Psi} = (\Psi_0 - b)\frac{T}{T_0} - aT_0\frac{T}{T_0}\log\left(\frac{T}{T_0}\right) + b \tag{D.8}$$

we see that the limit $\lim_{T_0\to 0}\tilde{\Psi}$ does not exist. Instead we define

$$\Psi_{TI} \approx (\Psi_{\text{ref}} - b)\frac{T}{T_{\text{ref}}} - aT_{\text{ref}}\frac{T}{T_{\text{ref}}}\log\left(\frac{T}{T_{\text{ref}}}\right) + b \tag{D.9}$$

with $\Psi_{\text{ref}} = \Psi_{LH}(\mathbf{F}, T_{\text{ref}})$ for $T_{\text{ref}} \ll T_{Debye}$. We use this approximation in TI for small temperatures above T_{ref} to avoid the cost of a logarithmic density of quadrature points (i.e. MD samples) needed to accurately evaluate (D.3) for temperatures near zero.

We observe that $\Psi = U$ at two temperatures. The first point is, of course, at $T = 0$ K. The second point is the the maximum of the $\Psi(T)$ curve at

$$T_{\max} = T_{\text{ref}}\exp\left(\frac{\Psi_{\text{ref}} - b}{aT_{\text{ref}}} - 1\right) \tag{D.10}$$

which results from solving $\frac{d\Psi}{dT} = 0$. Substituting equation (D.10) into (D.9), we verify

$$\begin{aligned}\Psi_{LH}(T_{\max}) &= (\Psi_{\text{ref}} - b)\frac{T_{\max}}{T_{\text{ref}}} - aT_{\text{ref}}\frac{T_{\max}}{T_{\text{ref}}}\log\left(\frac{T_{\max}}{T_{\text{ref}}}\right) + b \\ &= aT_{\text{ref}}\exp\left(\frac{\Psi_{\text{ref}} - b}{aT_{\text{ref}}} - 1\right) + b = aT_{\max} + b = U(T_{\max}).\end{aligned} \tag{D.11}$$

assuming $a = c_v$ and $b = \Phi_0$. This observation provides an independent check on the accuracy of our two methods of estimating the free energy (namely QH and TI).

Chapter 6

Prediction of instabilities at the atomic scale

Principal Authors: Terry J. Delph and Jonathan A. Zimmerman

Atomic scale instabilities, in which atomic bonds are broken and reform as the body shifts into a lower-energy configuration, are responsible for a wide range of material behaviours of interest. Building upon previous work, we outline here the construction of a criterion for the prediction of such instabilities. The criterion is implemented within the context of the well-known embedded atom (EAM) family of interatomic potentials. We present two examples of the application of this criterion: oriented cavitation in an FCC crystal due to uniform triaxial stretching, and dislocation nucleation due to nanoindentation of the (001) face of an FCC crystal.

6.1 Introduction

Numerous macroscale phenomena in the behaviour of solids, *e.g.*, plastic flow, fracture, and cavitation, are governed by the initiation of defects on the nanoscale. Various quite different continuum-based criteria have been proposed to separately describe each of these phenomena, but at the nanoscale it is possible to identify a few unifying features. In particular, each of these phenomena originates from a process in which a given atomic configuration, under the action of external loads or otherwise, becomes unstable and shifts into a stable, lower energy, configuration. This shift may involve the breaking and reforming of a relatively small number of interatomic bonds, as is the case in the nucleation of a single dislocation in a perfect crystal, or it may involve a large-scale change in atomic configuration, as with catastrophic brittle fracture. Viewed in this fashion, loss of stability of the atomic configuration becomes the general mechanism underlying a wide variety of macroscopic and microscopic features of great importance in the behaviour of materials.

Instability criteria that would predict atomic-scale defect initiation have accordingly been of considerable recent interest. Early work along these lines took the form of applications of continuum-scale criteria to the nanoscale. Work by Milstein and Huang [130] and Milstein and Hill [129] presented stability criterion based on the positive definiteness of atomic-scale elastic constants. Alber *et al.* [4] applied such a criterion to single atoms along a grain boundary to investigate grain boundary stability. Wang *et al.* [199] analyzed the stability of a homogeneous lattice under a constant uniform load, identifying several modes of instability: lattice decohesion by pure dilatation, tetragonal shear-induced bifurcation (Born instability), and simple shear-induced failure. This analysis was more rigorously probed by Morris and Krenn [135] in their effort to define the upper limits of mechanical strength. More recently, Van Vliet *et al.* [193] extended the strong ellipticity condition of Hill [74] downwards to the atomic scale, using atomic level elastic constants and stresses. As

with the work of Alber *et al.* , these quantities were calculated on an atom-by-atom basis. The resulting criterion was then applied to the prediction of dislocation nucleation in nanoindentation. Kolluri *et al.* [101] used the techniques by Wang *et al.* and Morris and Krenn in a molecular dynamics framework to evaluate the stability of biaxially strained thin films.

One notable weakness of these efforts is that they involve continuum-scale concepts, namely elastic constants and stress, which translate down to discrete atomic systems only with some difficulty, *e.g.* Delph [40]. In the articles cited above, the underlying assumption of homogeneous deformation is crucial towards defining these atomic-scale equivalents of continuum variables. Their validity for systems undergoing inhomogeneous deformations is questionable. In an effort to avoid this difficulty, Kitamura *et al.* [96, 97], Lu and Zhang [116] and Miller and Rodney [128] have independently proposed stability criteria that make no reference to continuum level quantities, but that depend only upon the interatomic potential. They have been applied by various researchers to predict thin film buckling and crack initiation [41, 96], the initiation of defects in carbon nanotubes [117], dislocation nucleation in nanoindentation [128], instability in shear [144] and in triaxial tension [41].

At least for the simple case of pair potentials, all of these criteria can be shown [41] to be equivalent to a stability criterion originally put forward by Wallace [198], but, to our knowledge, never systematically developed by him. This criterion, which we will subsequently call the Wallace criterion, states simply that a given atomic equilibrium configuration is stable if all admissible infinitesimal displacements of an atom, or of a group of atoms, result in an increase in the system energy. For an unstable state, in contrast, there exists a set of admissible atomic displacements that leads to a system energy lower than that of the initial state. Such a definition is very much in keeping with classical definitions of the stability of discrete systems. Wallace has, moreover, indicated that this criterion is completely equivalent to the requirement that small phonon disturbances decay with time. As we have noted, such a requirement is, at the continuum scale, the basis for the strong ellipticity requirement of Hill [74]. The Wallace criterion thus appears to be the equivalent of the strong ellipticity requirement at the atomic scale.

In principle at least, the Wallace stability criterion is easily implemented. The interatomic potential energy associated with a selected group of atoms is expanded in a Taylor series in the virtual atomic displacements and terms of up to quadratic order are retained. Because the system is assumed to be in initial equilibrium, the linear terms vanish, and the result is a quadratic form in the displacements. Instability is then signaled by the loss of positive definiteness of this quadratic form. Computationally, this implies that the lowest eigenvalue of the matrix associated with the quadratic form becomes negative. A valuable additional piece of information provided by the Wallace criterion is that the eigenvector associated with this lowest eigenvalue yields directly the magnitude and direction of the atomic motions associated with the instability mode, allowing ready identification of the type of instability. This information is not always easy to isolate in large-scale molecular static and dynamic simulations. For such calculations, the heterogeneity of the system geometry and applied loading may result in a cascade of defects produced following the initial instability that may obscure its nature. Thus, our method is useful in its ability to identify and characterize the deformation mode associated with that initial instability.

The purpose of the present paper is to extend the Wallace criterion to a realistic multibody in-

teratomic potential, the well-known embedded atom method (EAM) potential [57], of which there exist a number of variants. We give detailed computational formulas for the resulting stability criterion, and then apply the result to predict defect nucleation in several situations of interest. In addition to the usefulness already mentioned, the Wallace stability criterion has more general applicability as it can be used for any method that provides interatomic distances. Although atomistic simulation techniques are the most familiar means to generate these distances, alternative methods exist such as the Cauchy-Born rule and lattice Green's functions. This point will be elaborated on in the Discussion section of this paper.

6.2 Analysis

We consider an atomic assemblage consisting of N_A atoms, assumed to be in equilibrium and at a sufficiently low temperature so that thermal atomic fluctuations may be neglected. As we have noted above, the Wallace criterion involves the imposition of a set of arbitrary infinitesimal displacements on a relatively small group of N atoms contained within some region Ω interior to the ensemble, typically with $N \ll N_A$. To be more precise, suppose that we impose infinitesimal displacements $\mathbf{u}^\alpha$, $\alpha = 1,2,\cdots,N$, upon the atoms within Ω, so that these atoms move from an initial equilibrium position $\mathbf{R}^\alpha$ to position $\mathbf{r}^\alpha$, so that $\mathbf{r}^\alpha = \mathbf{R}^\alpha + \mathbf{u}^\alpha$. The set of positions $\{\mathbf{R}^\alpha\}$ does not necessarily constitute a reference configuration in the continuum mechanical sense. Rather, it is any configuration that represents a state of static equilibrium. This can include perfect single crystals, polycrystals, materials with a distribution of defects, or crystals possessing free and/or reconstructed surfaces. Here and subsequently, Greek letter superscripts denote atomic labels. If β likewise denotes a member of the group of N atoms, then the change in relative interatomic spacing between the two atoms is given by

$$\mathbf{r}^\alpha - \mathbf{r}^\beta \equiv \mathbf{r}^{\alpha\beta} = \mathbf{R}^{\alpha\beta} + \mathbf{u}^{\alpha\beta}. \tag{6.1}$$

Atoms exterior to this group of N atoms are assumed to be held fixed at their initial positions, so that if atom γ is a member of this exterior group, then $\mathbf{u}^\gamma = 0$ and $\mathbf{r}^{\alpha\gamma} = \mathbf{R}^{\alpha\gamma} + \mathbf{u}^\alpha$.

Using the EAM potential, the total potential energy of our atomic system, Ψ, is given as the sum of a two-body and an N-body term,

$$\Psi = \Psi_2 + \Psi_N. \tag{6.2}$$

The term Ψ_2 is a two-body potential having the standard form

$$\Psi_2 = \frac{1}{2}\sum_{\alpha=1}^{N_A}\sum_{\gamma=1,\gamma\neq\alpha}^{N_A}\psi_2\left(R^{\alpha\gamma^2}\right). \tag{6.3}$$

The N-body term is written in terms of a composite function $F\left(\rho^\delta\right)$, known as the "embedding function", so that

$$\Psi_N = \sum_{\delta=1}^{N_A} F\left(\rho^\delta\right), \tag{6.4}$$

where

$$\rho^{\delta} = \sum_{\varepsilon=1,\varepsilon\neq\delta}^{N_A} f\left(R^{\delta\varepsilon^2}\right). \tag{6.5}$$

It is worth noting that, following Martin [122], we have assumed that the potential functions depend upon the square of the relative interatomic spacings. Martin has shown that such a dependence guarantees translational and rotational invariance of the potential functions. Equivalently, as we will subsequently do when convenient, one could also consider a dependence upon $R^{\alpha\beta} = \sqrt{R^{\alpha\beta^2}}$, so that, for example, $f\left(R^{\alpha\beta^2}\right) = \hat{f}\left(R^{\alpha\beta}\right)$. However the use of $R^{\alpha\beta^2}$ makes it clear that the argument is always positive and moreover considerably simplifies the resulting algebra.

We now perturb our system from a state of static atomic force equilibrium, thereby altering our system's energy by the quantity $\Delta\Psi = \Psi(\{\mathbf{r}^{\alpha}\}) - \Psi(\{\mathbf{R}^{\alpha}\})$. We carry out a Taylor expansion of the interatomic potential in terms of $\Delta R^{\delta\varepsilon^2} \equiv r^{\delta\varepsilon^2} - R^{\delta\varepsilon^2} = 2R_i^{\delta\varepsilon} u_i^{\alpha\beta} + u_i^{\delta\varepsilon} u_i^{\delta\varepsilon}$ from equation (6.1), retaining terms of up to quadratic order in the displacement components. The details of this expansion for a two-body potential have been given by Delph *et al.* [41], and we focus here upon the expansion for the N-body term in equation (6.2). The composite nature of the embedding function renders the expansion somewhat algebraically complicated, and the details are given in Appendix E.

The linear term in the expansion vanishes from considerations of atomic equilibrium, and the result, including both two- and N-body terms, can be placed in the standard quadratic form

$$\Delta\Psi = \sum_{k=1}^{3N}\sum_{\ell=1}^{3N} A_{k\ell} v_k v_\ell, \tag{6.6}$$

where $u_i^{\alpha} = v_{3(\alpha-1)+i}$. Explicit expressions for the elements of the matrix $\mathbf{A}$ are given in Appendix E. This matrix is, in general, nonsymmetric. However it may be decomposed into the sum of symmetric and antisymmetric parts, $\mathbf{A} = \mathbf{B} + \mathbf{C}$, where $\mathbf{B} = (\mathbf{A} + \mathbf{A}^T)/2$ and $\mathbf{C} = (\mathbf{A} - \mathbf{A}^T)/2$. Then it is easy to see that the contribution to the quadratic form from the antisymmetric part vanishes identically, and we have

$$\Delta\Psi = \sum_{k=1}^{3N}\sum_{\ell=1}^{3N} B_{k\ell} v_k v_\ell. \tag{6.7}$$

We now seek a vector $\mathbf{v}$ so as to minimize $\Delta\Psi$. Minimization of a quadratic form is a well-known problem, *e.g.* [14], and we briefly sketch the procedure for the sake of clarity. Without loss of generality, we can assume the vector $\mathbf{v}$ to be normalized to unity, so that $\mathbf{v}\cdot\mathbf{v} = 1$. This normalization represents a constraint upon the minimization, and we enforce it through a Lagrange multiplier θ. Hence we seek to minimize

$$\Delta\Psi = \sum_{k=1}^{3N}\sum_{\ell=1}^{3N} B_{k\ell} v_k v_\ell - \theta\left(-1 + \sum_{k=1}^{3N} v_k v_k\right) \tag{6.8}$$

with respect to θ and $\mathbf{v}$. Minimization with respect to θ yields the constraint equation, and minimization with respect to $\mathbf{v}$ the symmetric eigenproblem

$$(\mathbf{B} - \theta\mathbf{I})\,\mathbf{v} = 0, \tag{6.9}$$

where $\mathbf{I}$ is the identity matrix. If now we take $\mathbf{v} = \mathbf{v}_{\min}$ to be the eigenvector corresponding to the lowest eigenvalue $\theta_{\min}$, then substitution into equation (6.7) gives the absolute minimum of the quadratic form as

$$\Delta\Psi_{\min} = \theta_{\min} \tag{6.10}$$

At this point, it is easy to see that $\Delta\Psi_{\min} = \theta_{\min} > 0$ represents the condition for stability, whereas $\theta_{\min} < 0$ signals an instability. By construction, the eigenvector corresponding to $\theta_{\min}$, $\mathbf{v}_{\min}$, represents the atomic displacement mode corresponding to the instability.

6.3 Implementation and examples

A number of variants of the EAM potential exist in the literature. The version that we have chosen to implement here is the one originated by Voter and Chen [195] and later parameterized to model gold [194]. This potential was recently modified by Foiles to improve its predicted values of surface energies and stacking fault energy, as reported by Park and Zimmerman [146]. It is this model that was used in the present study. In the Voter-Chen-Foiles potential, the two-body term is taken to be a Morse potential of the form

$$\hat{\psi}_2(R) = D\left(1 - \exp\left(\alpha_m\left(R - R_m\right)\right)\right)^2 - D, \tag{6.11}$$

where D, α_m, and R_m are constants. The values used in this study are $D = 0.6569397$ eV, $\alpha_m = 1.2031576$ Å^{-1}, and $R_m = 2.5471737$ Å. For the N-body term, we take the components of the atomic charge density function, the argument of the embedding function, to be

$$\hat{f}(R) = R^8\left(\exp\left(-\beta_m R\right) + 2^{11}\exp\left(-2\beta_m R\right)\right), \tag{6.12}$$

where $\beta_m = 3.18783126$ Å^{-1}.

Both $\hat{\psi}_2$ and $\hat{f}$ have cutoffs at $R_c = 5.6$ Å. In order to insure that the cutoff leads to no discontinuities either in the function or its first derivative, we replace $\hat{\psi}_2$ and $\hat{f}$ by a smoothed function $h_s(R)$, defined by

$$h_s(R) = h(R) - h(R_c) + \frac{R_c}{20}\left[1 - \left(\frac{R}{R_c}\right)^{20}\right]\left(\frac{dh}{dR}\right)_{R=R_c}, \tag{6.13}$$

where $h = \hat{\psi}_2$ or $h = \hat{f}$, as appropriate.

A distinguishing feature of the EAM potential is that the embedding function F, as well as its derivatives, is frequently unavailable in analytic form, but must be obtained by interpolation in lookup tables. We briefly outline in Appendix F how these lookup tables are constructed.

As a first example, we consider an FCC lattice subjected to uniform triaxial stretching along the principal crystallographic directions, using the EAM potential for gold described above. The atomic assemblage used here consisted of 8x8x8 unit cells, for a total of $N_A = 2048$ atoms, subjected to periodic boundary conditions on each of its sides. The values of critical stretch are determined through calculation of the lowest eigenvalue of the matrix **B** using a computer program developed by the lead author in which the expressions found in Appendices A and B have been hard-coded. Figure 6.1 shows the predicted stretch ratio λ at instability versus the number of atoms N contained in a spherical region Ω centered at the central atom in the 8x8x8 assemblage. It

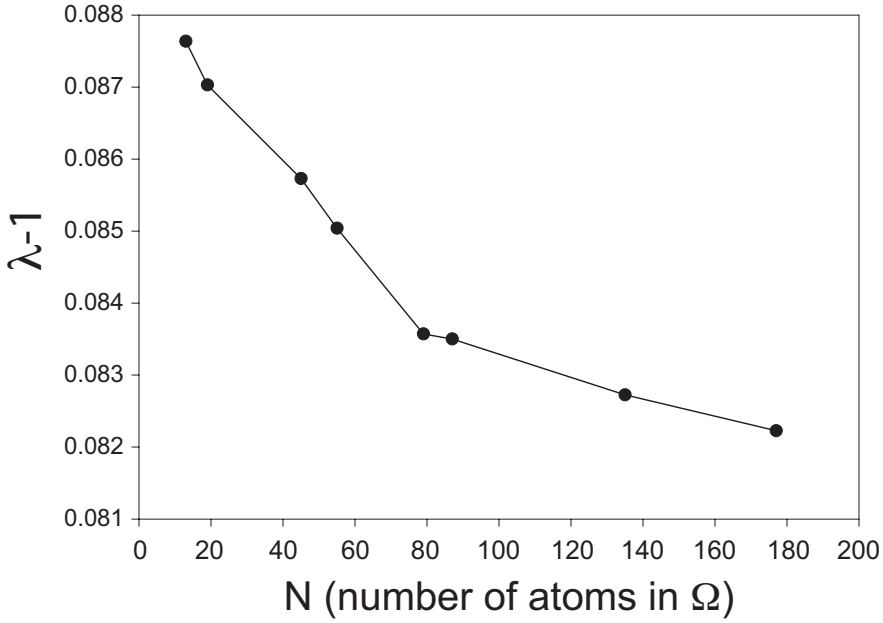

Figure 6.1. Predicted stretch ratio λ at instability versus the number of atoms N contained in a spherical region Ω centered at the central atom in the 2048 atom assemblage.

can be seen that the predicted stretch at instability decreases rather weakly with increasing N and appears to tend towards a value of about $\lambda = 1.081$ as N becomes large.

Of particular interest is the fact that the lowest eigenvalue in this situation, which becomes negative at the point of instability, is a triple root, and hence has three linearly independent associated eigenvectors. By construction, the eigenvectors are the infinitesimal displacements leading to a lower energy state, indicating that, at the point of instability, there exist at least three different neighboring states having lower energies than the initial equilibrium state. In principle, inspection of the eigenvectors allows a determination of the mode of instability, but in this case, the interpretation is complicated by the fact that any arbitrary linear combination of the three eigenvectors is likewise a valid eigenvector. Hence none of the eigenvectors is unique. With this in mind, Figure 6.2 show vector plots, plotted on the atomic lattice, of the eigenvectors obtained for the case N = 365 atoms, the largest value of N for which results were computed. The first two of these

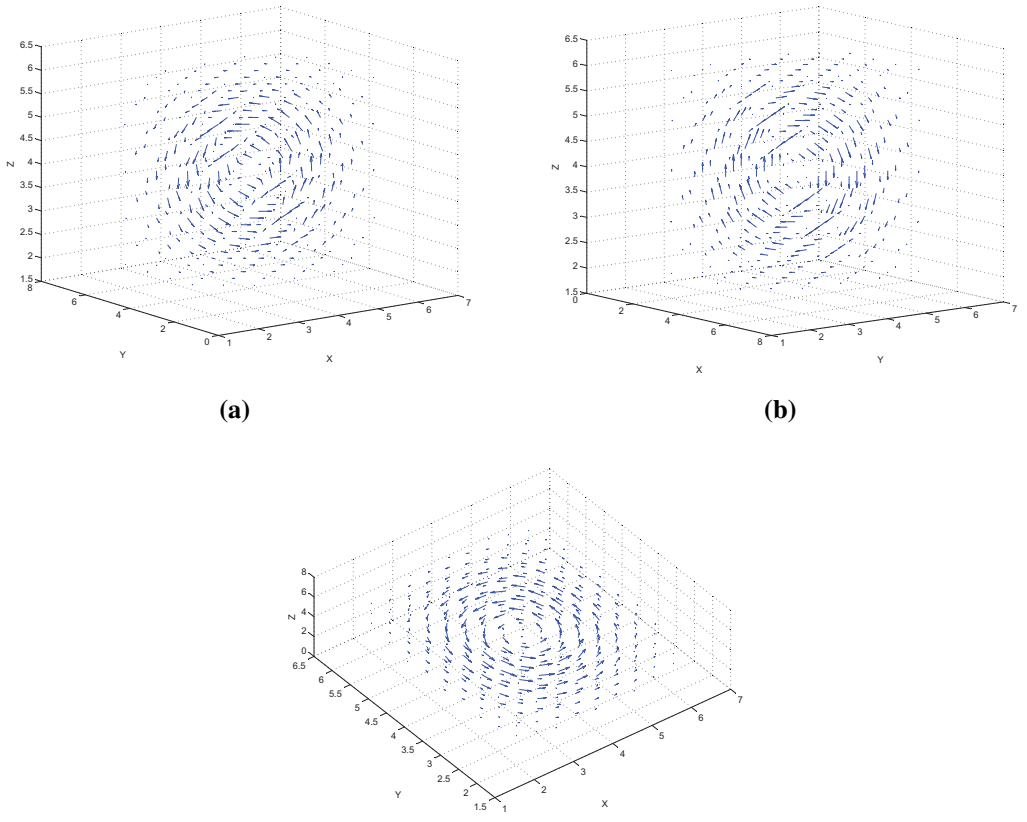

Figure 6.2. Vector plots of the eigenvectors corresponding with the lowest eigenvalue at the point of instability in the triaxial stretching calculation.

show a distinct circular pattern about the (110) axis, although in opposite directions, whereas the third shows much the same circular pattern about the (001) axis. Mutual orthogonality of all three eigenvectors was verified numerically.

A parallel molecular statics simulation of triaxial stretching using the same EAM potential was conducted with the widely-used LAMMPS molecular dynamics code [168], using the same assemblage of 2048 atoms. At a stretch level of $\lambda = 1.085$, the stretch value at instability for $N = 365$ atoms, the 365 atoms within Ω were perturbed in the direction indicated by the eigenvectors from the Wallace analysis. In all three cases, an adjacent lower-energy state was found to exist. The final equilibrium states corresponding to these lower-energy states are shown in Figures 6.3. It can be seen that these correspond roughly to an orientated cavitation pattern consisting of four cavities.

The next example is that of indentation of the (001) surface of an Au crystal by a rigid spherical

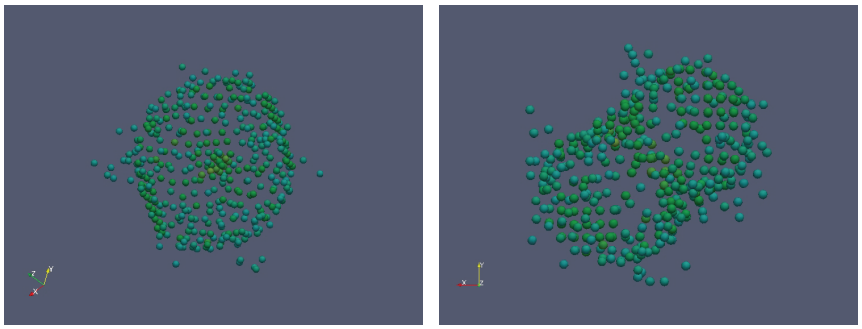

(a)

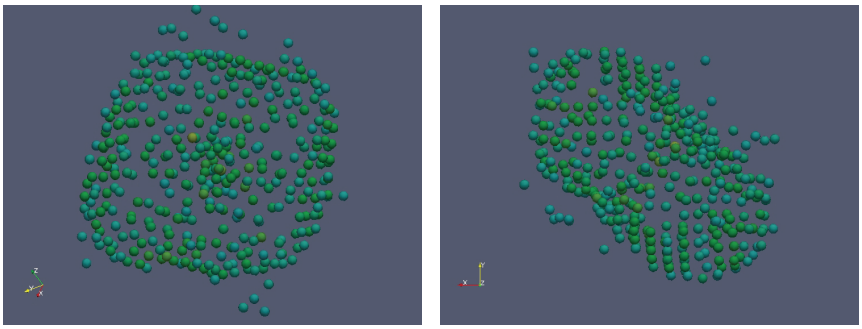

(b)

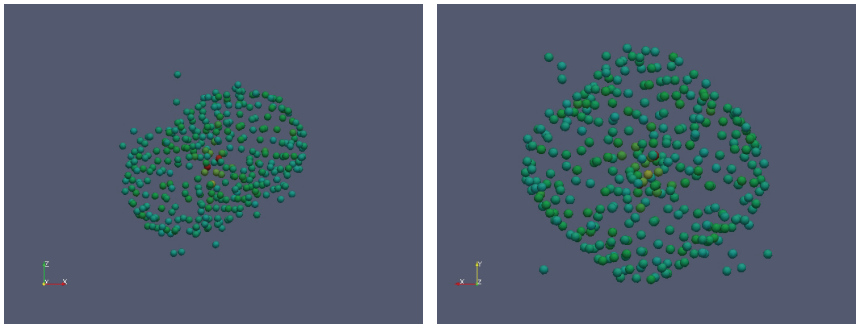

(c)

Figure 6.3. Atomic configurations for post-cavitated states produced from energy minimization of a perfect lattice perturbed by the three eigenvectors shown in Figure 6.2. For clarity, two views are shown for each state, and atoms are shown only if they possess a high value of centrosymmetry parameter [92].

indenter with a radius of 40 Å. An initial simulation of this situation was carried out with the LAMMPS code using an assemblage of 50x50x30 unit cells with 300,000 atoms. The assemblage was subjected to periodic boundary conditions along its sides, and was restrained against vertical (z-direction) motion along its bottom plane. The indentation was carried out in discrete steps of 0.5 Å, with the assemblage being allowed to equilibrate on each step before proceeding to the next. The results from the simulation indicate the nucleation of a dislocation at 5 atomic layers underneath the surface at an indenter penetration depth of 3.2 Å. The nucleation and its precursor instability event are shown in Figure 6.4. Subsequently, a V-type defect forms. The planes that

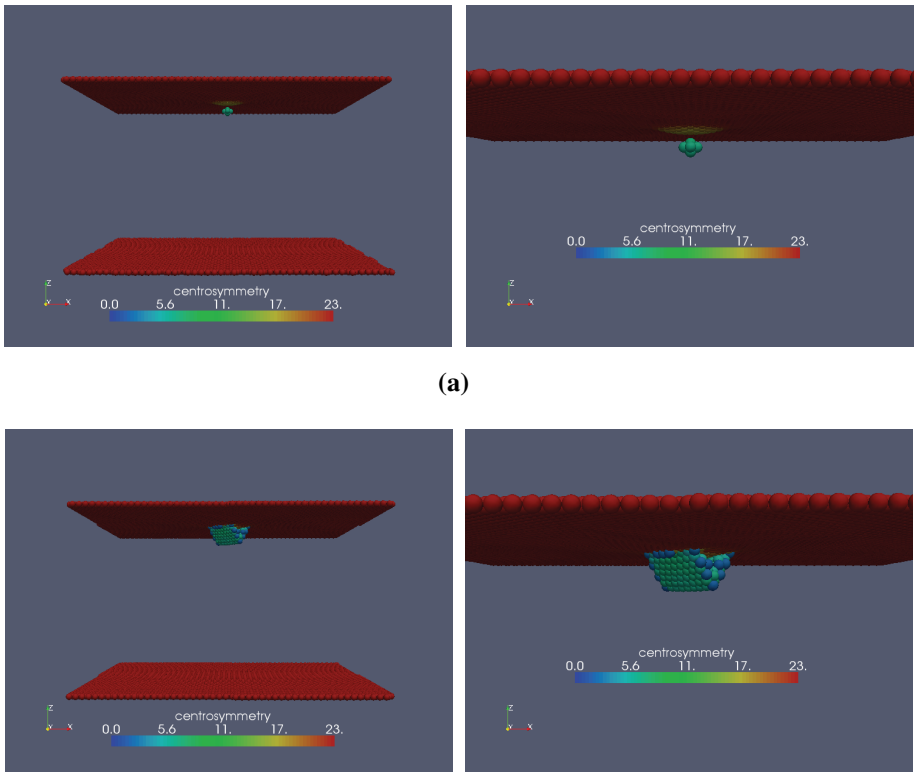

Figure 6.4. Dislocation nucleation below a nanoindented (001) gold surface. (a) shows a precursor instability event that occurs at an indentation depth of 3.2 Å. (b) shows a partial dislocation loop that is fully formed at an indentation depth of 3.7 Å. For clarity, atoms are shown only if they possess a high value of centrosymmetry parameter [92], and each subfigure shows both full-range (left) and close-up (right) views.

comprise the defect are (111) and (-1-11) planes, with the axis of the V oriented along [-1 1 0]. As the defect is small and the system is compressed, the slip vectors are somewhat distorted, but appear to be pointing in <112> directions. Specifically, these would be [-1-12] on the (111) plane

and [112] on the (-1-11) plane. The progression of defect growth is similar to that observed by Rodríguez de la Fuente *et al.* [158].

The atomic coordinates taken from this simulation after each increment of indenter displacement and subsequent equilibration were used as inputs to the stability analysis. Figure 6.5 shows the variation of the lowest eigenvalue with indenter depth, where Ω was taken to be a rectangular solid whose top surface was a square centered at the center of the indentation. It can be seen that,

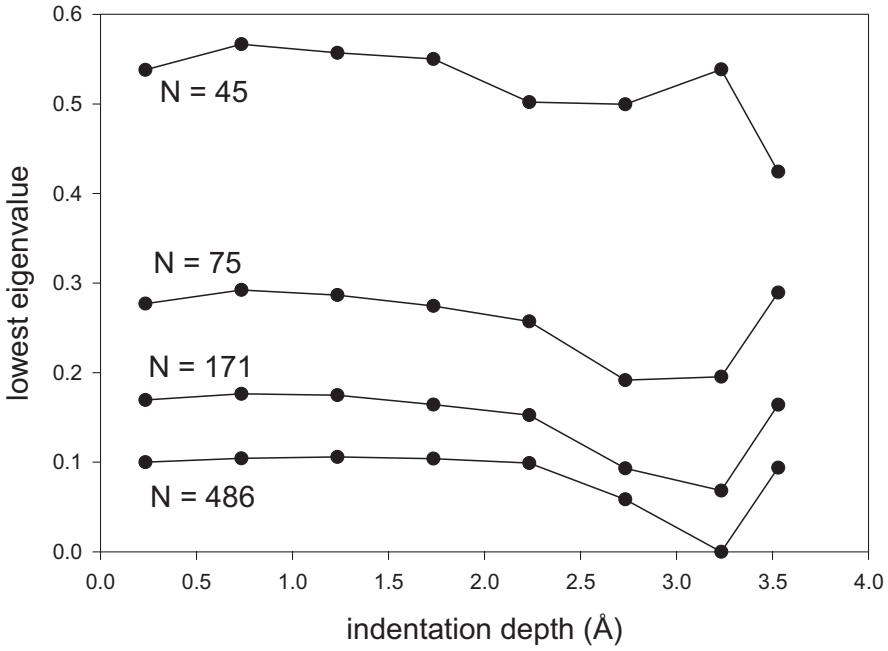

Figure 6.5. Lowest eigenvalue as a function of increasing load (step) for the nanoindentation simulation for analysis regions that contain N number of atoms and enclose the contact area. For systems where $N \geq 75$ the minimum of each curve is at an indentation depth of 3.2 Å, which corresponds with the precursor event shown in Figure 6.4(a).

at least for the larger values of N, the lowest eigenvalue remains constant until an indentation depth of approximately 1.5 Å, at which point it begins to decrease with increasing indentation. The minimum occurs at an indentation depth of 3.2 Å, a value that corresponds very well to the depth at which dislocation nucleation occurred in the LAMMPS simulation. Past this point, the lowest eigenvalue begins to increase.

Figure 6.6 shows a vector plot of the eigenvector corresponding to the lowest eigenvalue at the point of dislocation nucleation. The view is from the surface looking directly downwards into the crystal. A shearing motion is clearly visible in the center of the figure. This shearing motion occurs at a depth of 6.2 - 6.3 Å below the surface, at the fifth atomic layer. This location accords

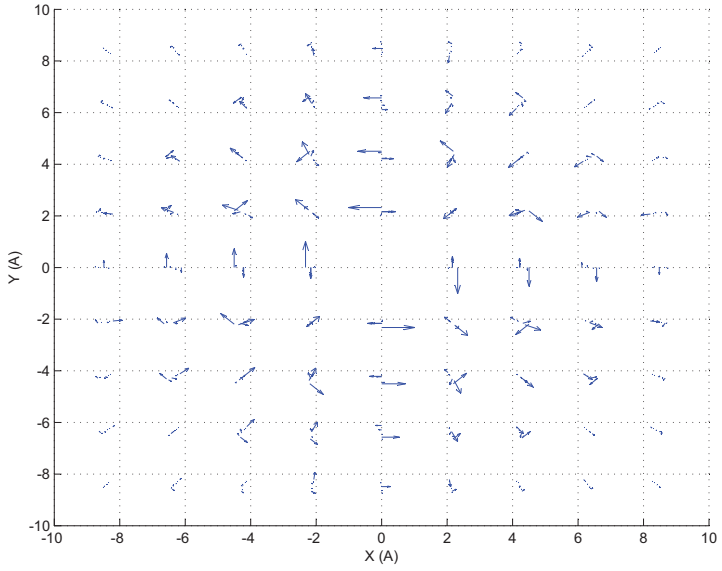

Figure 6.6. Eigenvectors corresponding to the minimum eigenvalue at the point of instability during the nanoindentation simulation. A shearing motion is clearly visible in the center of the figure.

well with the results of the simulation, which indicates that the dislocation nucleates at 6.3 Å below the surface.

6.4 Discussion

In this paper, we have extended the Wallace stability criterion to atomistic systems governed by the well-known EAM family of interatomic potentials. In essence, the Wallace criterion tests the stability of a relatively small number of atoms contained within a region Ω embedded within a larger atomic assembly. The measure of stability is whether or not arbitrary infinitessimal displacements of these atoms lead to a higher or a lower system energy. In the former case the system is stable; in the latter case, it is not. Computationally, this leads to an assessment of the lowest eigenvector of a symmetric matrix. If the lowest eigenvector is positive, then the system is stable; if it is negative, then instability is predicted.

One of the important ideas here is that accurate stability predictions can be obtained when the number of atoms N contained within Ω is considerably less than the total number of atoms contained within the assembly. In the examples considered both here and elsewhere, values of $N < 500$ have been found to suffice, even in rather complicated situations, *e.g.*, Mode I crack growth [41]. Values of N that are too small, on the other hand, can lead to inaccurate results. It is interesting to

note in this context that many of the prior results obtained using essentially similar stability criteria have focused upon the extreme limits of the possible values of N, that is, $N = 1$ [4, 116, 117, 193] and $N = N_A$, where N_A is the total number of atoms in the assemblage [96, 97, 144]. Apparently Miller and Rodney [128] were the first to realize that the use of intermediate values of N, comparatively small with respect to N_A, but not overly small, could lead to accurate and computationally efficient stability predictions, a finding that we have confirmed here and elsewhere.

We have presented two examples here of the use of the Wallace criterion in conjunction with the EAM potential, that of an FCC lattice subjected to equiaxed triaxial stretching and nanoindentation of an FCC crystal. The material constants in both cases were appropriate to the behaviour of gold [194]. In general, agreement between the Wallace stability analysis and the parallel LAMMPS simulations was excellent for both examples considered. Moreover both examples indicated that overly small values of N were likely to lead to inaccurate, or even erroneous, stability predictions.

The results from the triaxial stretching example were somewhat unexpected. A previous simulation of triaxial stretching of an FCC lattice described by a simple Lennard-Jones type of interatomic potential [41] indicated that the instability in this case took the form of spherical cavitation. Moreover the lowest eigenvalue for this case was a single root. In the present case, using the EAM potential with material constants appropriate to gold, we observed a triple root for the lowest eigenvalue. This indicates, in general, the formation of a defect with a specific orientation with respect to the principal crystallographic directions. Because the stretching is uniform in all directions, the defect can have any of three mutually orthogonal orientations. Unfortunately, because of lack of uniqueness, the three associated computed eigenvectors are not particularly helpful in describing the nature of the defect. However companion LAMMPS molecular statics simulations, when perturbed in the directions indicated by the eigenvectors, show the formation of a cellular type of cavitation having a definite orientation.

We tentatively interpret this instability in light of a continuum stability analysis due to Wang, Li, Yip, Phillpot, and Wolf [199]. These authors likewise considered the case of triaxial tensile stretching and showed that, in addition to spherical cavitation, an additional directionally oriented instability mode existed. The authors termed this instability "Born instability" and noted that it was associated, at least at the onset of instability, with isovolumetric deformation. This feature is in good agreement with the eigenvectors obtained from the Wallace analysis, for which the atomic motions seem to likewise indicate isovolumetric motion. To test their analysis, Wang *et al.* [199] carried out a series of molecular dynamics of an FCC lattice governed by the EAM potential using constants appropriate for Au, although their EAM potential took on a somewhat different form than that used here. They found that spherical cavitation was the dominant instability mode at temperatures up to about 1000K. At temperatures above this value, the Born instability became dominant. By contrast, we find that, at low temperatures, the Born instability is the dominant one. We ascribe the dissimilarities in predicted cavitation modes to differences in the EAM interatomic potential for Au used in the two studies.

In contrast to the triaxial stretching example, the Wallace stability analysis for dislocation nucleation underneath an indenter and the accompanying LAMMPS simulation were not completely independent, because the atomic coordinates required by the Wallace stability analysis were taken from the LAMMPS simulation on each step. The LAMMPS code, by construction, will not con-

verge to an unstable state, and hence the Wallace criterion will not yield negative values for the lowest eigenvalue. However the rapid drop in the lowest eigenvalue for the larger values of N, falling essentially to zero at a value of $N = 486$, clearly signals the onset of dislocation nucleation. On the other hand, smaller values of N, *e.g.*, $N = 45$, predict nucleation either poorly or not at all. This is in agreement with the results of Miller and Rodney [128], who noted a similar finding. By selecting the region Ω to be discs containing the planes of shearing, these authors were able to obtain good results with relatively small values of N. We have not attempted any such degree of sophistication here, but have, somewhat less efficiently, simply taken Ω to be a rectangular volume beneath the indenter.

In closing, we want to point out that the Wallace stability criterion and other stability criteria such as that of Miller and Rodney [128] depend crucially upon the equilibrium interatomic spacings that serve as an input to the analysis. In the present case, these were obtained either from simple geometric considerations or from a parallel molecular statics simulation. In cases other than homogeneous deformation of a centrosymmetric crystal, geometric considerations will in general not suffice to yield the equilibrium interatomic spacings. These may, of course, always be obtained from large-scale molecular statics simulations, as we have done here and elsewhere. In such cases, our instability analysis supplies additional information on the nature and characteristics of the underlying mechanism leading to a loss of stability.

In order to be more generally useful, atomic stability criteria such as the Wallace criterion require a relatively simple means of generating the required interatomic spacings. There are several possibilities for achieving this goal, most notably through the use of the Cauchy-Born rule and lattice Green's functions. The Cauchy-Born rule assumes simply that the atomic displacements are given by the continuum displacement field. For homogeneous deformation of centrosymmetric crystals, the Cauchy-Born rule is exact from simple geometric considerations. However it is of uncertain applicability in situations involving inhomogeneous deformation, and is moreover likely to break down completely in regions in which the deformation gradient is large. Lattice Green's functions [89, 182] offer a more attractive alternative, at the expense of somewhat increased computational effort. Lattice Green's functions are, as their name implies, equivalent to the familiar continuum Green's functions in the continuum limit. More to the point, they have been shown to yield accurate atomic displacements in several circumstances involving extended defects, *e.g.* , Tewary and Thomson [183].

6.5 Appendix E

Let the system be perturbed from a state of static atomic force equilibrium. At the location of each atom δ is an electron gas of density ρ^δ in the static equilibrium state and $\tilde{\rho}^\delta = \rho^\delta + \Delta\rho^\delta$ in the perturbed state.

By simple chain rule considerations,

$$\begin{aligned}
\frac{\partial F}{\partial R^{\delta\varepsilon^2}} &= F'\left(\rho^\delta\right) f'\left(R^{\delta\varepsilon^2}\right) \\
\frac{\partial^2 F}{\partial\left(R^{\delta\varepsilon^2}\right)^2} &= F''\left(\rho^\delta\right)\left[f'\left(R^{\delta\varepsilon^2}\right)\right]^2 + F'\left(\rho^\delta\right) f''\left(R^{\delta\varepsilon^2}\right) \\
\frac{\partial^2 F}{\partial R^{\delta\varepsilon^2}\partial R^{\delta\beta^2}} &= F''\left(\rho^\delta\right) f'\left(R^{\delta\varepsilon^2}\right) f'\left(R^{\delta\beta^2}\right),\ \beta \neq \varepsilon.
\end{aligned} \tag{E.1}$$

From this, we construct the Taylor expansion for $F\left(\rho^\delta\right)$,

$$\begin{aligned}
\Delta F\left(\rho^\delta\right) &= F\left(\tilde{\rho}^\delta\right) - F\left(\rho^\delta\right) \\
&= F'\left(\rho^\delta\right) \sum_{\varepsilon=1,\varepsilon\neq\delta}^{N_A} f'\left(R^{\delta\varepsilon^2}\right)\Delta R^{\delta\varepsilon^2} + \\
&\quad \frac{1}{2}F''\left(\rho^\delta\right)\left[\sum_{\varepsilon=1,\varepsilon\neq\delta}^{N_A} f'\left(R^{\delta\varepsilon^2}\right)\Delta R^{\delta\varepsilon^2}\right]^2 + \\
&\quad \frac{1}{2}F'\left(\rho^\delta\right) \sum_{\varepsilon=1,\varepsilon\neq\delta}^{N_A} f''\left(R^{\delta\varepsilon^2}\right)\left(\Delta R^{\delta\varepsilon^2}\right)^2 + \cdots \\
&= F'\left(\rho^\delta\right) \sum_{\varepsilon=1,\varepsilon\neq\delta}^{N_A}\left[f'\left(R^{\delta\varepsilon^2}\right)\Delta R^{\delta\varepsilon^2} + \frac{1}{2}f''\left(R^{\delta\varepsilon^2}\right)\left(\Delta R^{\delta\varepsilon^2}\right)^2\right] + \\
&\quad \frac{1}{2}F''\left(\rho^\delta\right)\left[\sum_{\varepsilon=1,\varepsilon\neq\delta}^{N_A} f'\left(R^{\delta\varepsilon^2}\right)\Delta R^{\delta\varepsilon^2}\right]^2 + \cdots.
\end{aligned} \tag{E.2}$$

At this point, we make the observation that equation (E.2) involves the derivatives of $f\left(R^{\delta\varepsilon^2}\right)$. This function is akin to a two-body potential, and in fact, in the current implementation, has the same cutoff distance as does the two-body portion of the EAM potential. Hence it is meaningful to speak of an annulus surrounding Ω that contains a total of M interacting atoms, so that the contribution to the expansion of atoms lying outside this annulus may be ignored. Use the convention that $\alpha,\beta \in \Omega$, and that $\gamma \notin \Omega$ is an interacting atom. Thus only the quantities proportional to $\Delta R^{\alpha\beta^2}, \Delta R^{\alpha\gamma^2} \neq 0$. Starting from equation (6.4) and including only the nonzero contributions, we

have

$$\begin{aligned}\Delta\Psi_N &= \sum_{\alpha=1}^{N} F'(\rho^{\alpha}) \left\{ \sum_{\beta=1,\beta\neq\alpha}^{N} \left[f'\left(R^{\alpha\beta^2}\right)\Delta R^{\alpha\beta^2} + \frac{1}{2} f''\left(R^{\alpha\beta^2}\right)\left(\Delta R^{\alpha\beta^2}\right)^2 \right] + \right. \\ &\left. \sum_{\gamma=1}^{M} \left[f'\left(R^{\alpha\gamma^2}\right)\Delta R^{\alpha\gamma^2} + \frac{1}{2} f''\left(R^{\alpha\gamma^2}\right)\left(\Delta R^{\alpha\gamma^2}\right)^2 \right] \right\} + \\ &\sum_{\gamma=1}^{M} F'(\rho^{\gamma}) \sum_{\alpha=1}^{N} \left[f'\left(R^{\alpha\gamma^2}\right)\Delta R^{\alpha\gamma^2} + \frac{1}{2} f''\left(R^{\alpha\gamma^2}\right)\left(\Delta R^{\alpha\gamma^2}\right)^2 \right] + \\ &\frac{1}{2}\sum_{\alpha=1}^{N} F''(\rho^{\alpha}) \left[\sum_{\beta=1,\beta\neq\alpha}^{N} f'\left(R^{\alpha\beta^2}\right)\Delta R^{\alpha\beta^2} + \sum_{\gamma=1}^{M} f'\left(R^{\alpha\gamma^2}\right)\Delta R^{\alpha\gamma^2} \right]^2 + \\ &\frac{1}{2}\sum_{\gamma=1}^{M} F''(\rho^{\gamma}) \left[\sum_{\alpha=1}^{N} f'\left(R^{\alpha\gamma^2}\right)\Delta R^{\alpha\gamma^2} \right]^2 + \cdots . \end{aligned} \tag{E.3}$$

Now in terms of the displacement components, $\Delta R^{\alpha\beta^2} = 2R_i^{\alpha\beta}u_i^{\alpha\beta} + u_i^{\alpha\beta}u_i^{\alpha\beta}$, $\Delta R^{\alpha\gamma^2} = 2R_i^{\alpha\gamma}u_i^{\alpha} + u_i^{\alpha}u_i^{\alpha}$, where $u_i^{\gamma} = 0$ by hypothesis. Substitution into equation (E.3), gives:

$$\begin{aligned}\Delta\Psi_N &= \sum_{\alpha=1}^{N} F'(\rho^{\alpha}) \left\{ \sum_{\beta=1,\beta\neq\alpha}^{N} \left[f'\left(R^{\alpha\beta^2}\right)\left(2R_i^{\alpha\beta}u_i^{\alpha\beta} + u_i^{\alpha\beta}u_i^{\alpha\beta}\right) + \right. \right. \\ &\left. \left. \frac{1}{2} f''\left(R^{\alpha\beta^2}\right)\left(2R_i^{\alpha\beta}u_i^{\alpha\beta} + u_i^{\alpha\beta}u_i^{\alpha\beta}\right)^2 \right] + \right. \\ &\left. \sum_{\gamma=1}^{M} \left[f'\left(R^{\alpha\gamma^2}\right)\left(2R_i^{\alpha\gamma}u_i^{\alpha} + u_i^{\alpha}u_i^{\alpha}\right) + \frac{1}{2} f''\left(R^{\alpha\gamma^2}\right)\left(2R_i^{\alpha\gamma}u_i^{\alpha} + u_i^{\alpha}u_i^{\alpha}\right)^2 \right] \right\} + \\ &\sum_{\gamma=1}^{M} F'(\rho^{\gamma}) \sum_{\alpha=1}^{N} \left[f'\left(R^{\alpha\gamma^2}\right)\left(2R_i^{\alpha\gamma}u_i^{\alpha} + u_i^{\alpha}u_i^{\alpha}\right) + \frac{1}{2} f''\left(R^{\alpha\gamma^2}\right)\left(2R_i^{\alpha\gamma}u_i^{\alpha} + u_i^{\alpha}u_i^{\alpha}\right)^2 \right] + \\ &\frac{1}{2}\sum_{\alpha=1}^{N} F''(\rho^{\alpha}) \left[\sum_{\beta=1,\beta\neq\alpha}^{N} f'\left(R^{\alpha\beta^2}\right)\left(2R_i^{\alpha\beta}u_i^{\alpha\beta} + u_i^{\alpha\beta}u_i^{\alpha\beta}\right) + \right. \\ &\left. \sum_{\gamma=1}^{M} f'\left(R^{\alpha\gamma^2}\right)\left(2R_i^{\alpha\gamma}u_i^{\alpha} + u_i^{\alpha}u_i^{\alpha}\right) \right]^2 + \\ &\frac{1}{2}\sum_{\gamma=1}^{M} F''(\rho^{\gamma}) \left[\sum_{\alpha=1}^{N} f'\left(R^{\alpha\gamma^2}\right)\left(2R_i^{\alpha\gamma}u_i^{\alpha} + u_i^{\alpha}u_i^{\alpha}\right) \right]^2 + \cdots \end{aligned} \tag{E.4}$$

If we assume very small displacements (i.e. $u^{\alpha\beta} \ll R^{\alpha\beta}$), then we can approximate $\Delta\Psi_N$ by ignor-

ing terms higher than quadratic order in the displacement components,

$$\begin{aligned}
\Delta\Psi_N \approx & \sum_{\alpha=1}^{N} F'(\rho^{\alpha}) \left\{ \sum_{\beta=1,\beta\neq\alpha}^{N} \left[f'\left(R^{\alpha\beta^2}\right)\left(2R_i^{\alpha\beta}u_i^{\alpha\beta}+u_i^{\alpha\beta}u_i^{\alpha\beta}\right)+ \right.\right. \\
& \left.\frac{1}{2}f''\left(R^{\alpha\beta^2}\right)\left(2R_i^{\alpha\beta}u_i^{\alpha\beta}\right)^2\right] + \\
& \left.\sum_{\gamma=1}^{M}\left[f'\left(R^{\alpha\gamma^2}\right)\left(2R_i^{\alpha\gamma}u_i^{\alpha}+u_i^{\alpha}u_i^{\alpha}\right)+\frac{1}{2}f''\left(R^{\alpha\gamma^2}\right)\left(2R_i^{\alpha\gamma}u_i^{\alpha}\right)^2\right]\right\} + \\
& \sum_{\gamma=1}^{M} F'(\rho^{\gamma}) \sum_{\alpha=1}^{N}\left[f'\left(R^{\alpha\gamma^2}\right)\left(2R_i^{\alpha\gamma}u_i^{\alpha}+u_i^{\alpha}u_i^{\alpha}\right)+\frac{1}{2}f''\left(R^{\alpha\gamma^2}\right)\left(2R_i^{\alpha\gamma}u_i^{\alpha}\right)^2\right] + \\
& \frac{1}{2}\sum_{\alpha=1}^{N} F''(\rho^{\alpha})\left[\sum_{\beta=1,\beta\neq\alpha}^{N} f'\left(R^{\alpha\beta^2}\right)\left(2R_i^{\alpha\beta}u_i^{\alpha\beta}\right)+\right. \\
& \left.\sum_{\gamma=1}^{M} f'\left(R^{\alpha\gamma^2}\right)\left(2R_i^{\alpha\gamma}u_i^{\alpha}\right)\right]^2 + \frac{1}{2}\sum_{\gamma=1}^{M} F''(\rho^{\gamma})\left[\sum_{\alpha=1}^{N} f'\left(R^{\alpha\gamma^2}\right)\left(2R_i^{\alpha\gamma}u_i^{\alpha}\right)\right]^2
\end{aligned} \tag{E.5}$$

By assumption, the expansion is taken about a state in atomic force equilibrium, so that the linear term in this expansion vanishes. Thus, to quadratic order in the displacement components, we have

$$\begin{aligned}
\Delta\Psi_N = & \sum_{\alpha=1}^{N} F'(\rho^{\alpha}) \left\{ \sum_{\beta=1,\beta\neq\alpha}^{N} \left[f'\left(R^{\alpha\beta^2}\right)\delta_{ij}+2f''\left(R^{\alpha\beta^2}\right)R_i^{\alpha\beta}R_j^{\alpha\beta}\right]u_i^{\alpha\beta}u_j^{\alpha\beta}+ \right. \\
& \left.\sum_{\gamma=1}^{M}\left[f'\left(R^{\alpha\gamma^2}\right)\delta_{ij}+2f''\left(R^{\alpha\gamma^2}\right)R_i^{\alpha\gamma}R_j^{\alpha\gamma}\right]u_i^{\alpha}u_j^{\alpha}\right\} + \\
& \sum_{\gamma=1}^{M} F'(\rho^{\gamma}) \sum_{\alpha=1}^{N}\left[f'\left(R^{\alpha\gamma^2}\right)\delta_{ij}+2f''\left(R^{\alpha\gamma^2}\right)R_i^{\alpha\gamma}R_j^{\alpha\gamma}\right]u_i^{\alpha}u_j^{\alpha} + \\
& \frac{1}{2}\sum_{\alpha=1}^{N} F''(\rho^{\alpha})\left[2\sum_{\beta=1,\beta\neq\alpha}^{N} f'\left(R^{\alpha\beta^2}\right)R_i^{\alpha\beta}u_i^{\alpha\beta}+2\sum_{\gamma=1}^{M} f'\left(R^{\alpha\gamma^2}\right)R_i^{\alpha\gamma}u_i^{\alpha}\right]^2 + \\
& \frac{1}{2}\sum_{\gamma=1}^{M} F''(\rho^{\gamma})\left[2\sum_{\alpha=1}^{N} f'\left(R^{\alpha\gamma^2}\right)R_i^{\alpha\gamma}u_i^{\alpha}\right]^2
\end{aligned} \tag{E.6}$$

We note that in going from equation (E.5) to equation (E.6) we have expanded some of the quadratic displacement terms to use both dummy coordinate indices i and j, but that this was not done for the last few terms involving the square of sums of atoms. Our reasoning for doing so will become apparent shortly.

Our goal here is, by a series of algebraic manipulations, to place equation (E.6) in the quadratic

form

$$\Delta\Psi_N = \sum_{\alpha=1}^{N} K_{ij}^{\alpha} u_i^{\alpha} u_j^{\alpha} + \sum_{\alpha=1}^{N} \sum_{\beta=1,\beta\neq\alpha}^{N} L_{ij}^{\alpha\beta} u_i^{\alpha} u_j^{\beta}, \tag{E.7}$$

from whence it may be easily transformed into standard quadratic form.

We introduce a change of functional dependence $f\left(R^{\alpha\beta^2}\right) = \hat{f}\left(R^{\alpha\beta}\right)$ through the chain rule relations

$$\begin{aligned} \frac{\partial f}{\partial R^2} &= \frac{\partial \hat{f}}{\partial R}\frac{\partial R}{\partial R^2} = \frac{1}{2R}\frac{\partial \hat{f}}{\partial R} \\ \frac{\partial^2 f}{\partial \left(R^2\right)^2} &= \frac{\partial}{\partial R^2}\left(\frac{1}{2R}\frac{\partial \hat{f}}{\partial R}\right) = \frac{1}{4R^2}\left(\frac{\partial^2 \hat{f}}{\partial R^2} - \frac{1}{R}\frac{\partial \hat{f}}{\partial R}\right). \end{aligned} \tag{E.8}$$

Taking

$$\begin{aligned} U^{\alpha\beta} &= \frac{\hat{f}'\left(R^{\alpha\beta}\right)}{R^{\alpha\beta}} = 2f'\left(R^{\alpha\beta^2}\right) \\ W^{\alpha\beta} &= \frac{1}{R^{\alpha\beta^2}}\left(\hat{f}''\left(R^{\alpha\beta}\right) - \frac{\hat{f}'\left(R^{\alpha\beta}\right)}{R^{\alpha\beta}}\right) = 4f''\left(R^{\alpha\beta^2}\right), \end{aligned} \tag{E.9}$$

and substituting equations (E.8-E.9) into equation (E.6), we obtain

$$\begin{aligned} \Delta\Psi_N = {} & \frac{1}{2}\sum_{\alpha=1}^{N}\sum_{\beta=1,\beta\neq\alpha}^{N}\left[F'\left(\rho^{\alpha}\right)\left(U^{\alpha\beta}\delta_{ij} + W^{\alpha\beta}R_i^{\alpha\beta}R_j^{\alpha\beta}\right)\right]u_i^{\alpha\beta}u_j^{\alpha\beta} + \\ & \frac{1}{2}\sum_{\alpha=1}^{N}\sum_{\gamma=1}^{M}\left[\left(F'\left(\rho^{\alpha}\right) + F'\left(\rho^{\gamma}\right)\right)\left(U^{\alpha\gamma}\delta_{ij} + W^{\alpha\gamma}R_i^{\alpha\gamma}R_j^{\alpha\gamma}\right)\right]u_i^{\alpha}u_j^{\alpha} + \\ & \frac{1}{2}\sum_{\alpha=1}^{N}F''\left(\rho^{\alpha}\right)\left[\sum_{\beta=1,\beta\neq\alpha}^{N}U^{\alpha\beta}R_i^{\alpha\beta}u_i^{\alpha\beta} + \sum_{\gamma=1}^{M}U^{\alpha\gamma}R_i^{\alpha\gamma}u_i^{\alpha}\right]^2 \\ & + \frac{1}{2}\sum_{\gamma=1}^{M}F''\left(\rho^{\gamma}\right)\left[\sum_{\alpha=1}^{N}U^{\alpha\gamma}R_i^{\alpha\gamma}u_i^{\alpha}\right]^2. \end{aligned} \tag{E.10}$$

Using the definition $\mathbf{u}^{\alpha\beta} = \mathbf{u}^{\alpha} - \mathbf{u}^{\beta}$ and now expanding the terms involving the square of sums

of atoms, the expression becomes

$$\begin{aligned}
\Delta\Psi_N \;=\; & \frac{1}{2}\sum_{\alpha=1}^{N}\sum_{\beta=1,\beta\neq\alpha}^{N}\left[F'\left(\rho^{\alpha}\right)\left(U^{\alpha\beta}\delta_{ij}+W^{\alpha\beta}R_i^{\alpha\beta}R_j^{\alpha\beta}\right)\right]\left(u_i^{\alpha}u_j^{\alpha}+u_i^{\beta}u_j^{\beta}-u_i^{\alpha}u_j^{\beta}-u_j^{\alpha}u_i^{\beta}\right)+ \\
& \sum_{\alpha=1}^{N}\sum_{\gamma=1}^{M}Y_{ij}^{\alpha\gamma}u_i^{\alpha}u_j^{\alpha}+ \\
& \frac{1}{2}\sum_{\alpha=1}^{N}F''\left(\rho^{\alpha}\right)\left\{\sum_{\beta=1,\beta\neq\alpha}^{N}\sum_{\eta=1,\eta\neq\alpha}^{N}U^{\alpha\beta}U^{\alpha\eta}R_i^{\alpha\beta}R_j^{\alpha\eta}\left(u_i^{\alpha}u_j^{\alpha}-u_i^{\beta}u_j^{\alpha}-u_i^{\alpha}u_j^{\eta}+u_i^{\beta}u_j^{\eta}\right)+\right. \\
& \left.2\sum_{\beta=1,\beta\neq\alpha}^{N}\sum_{\gamma=1}^{M}U^{\alpha\beta}U^{\alpha\gamma}R_i^{\alpha\beta}R_j^{\alpha\gamma}\left(u_i^{\alpha}u_j^{\alpha}-u_i^{\beta}u_j^{\alpha}\right)+\sum_{\gamma=1}^{M}\sum_{\zeta=1}^{M}U^{\alpha\gamma}U^{\alpha\zeta}R_i^{\alpha\gamma}R_j^{\alpha\zeta}u_i^{\alpha}u_j^{\alpha}\right\}+ \\
& \frac{1}{2}\sum_{\gamma=1}^{M}F''\left(\rho^{\gamma}\right)\left\{\sum_{\alpha=1}^{N}U^{\alpha\gamma}U^{\alpha\gamma}R_i^{\alpha\gamma}R_j^{\alpha\gamma}u_i^{\alpha}u_j^{\alpha}+\sum_{\alpha=1}^{N}\sum_{\beta=1,\beta\neq\alpha}^{N}U^{\alpha\gamma}U^{\beta\gamma}R_i^{\alpha\gamma}R_j^{\beta\gamma}u_i^{\alpha}u_j^{\beta}\right\},
\end{aligned} \tag{E.11}$$

where $\eta \in \Omega$, $\zeta \notin \Omega$ and

$$Y_{ij}^{\alpha\gamma}=\frac{1}{2}\left[\left(F'\left(\rho^{\alpha}\right)+F'\left(\rho^{\gamma}\right)\right)\left(U^{\alpha\gamma}\delta_{ij}+W^{\alpha\gamma}R_i^{\alpha\gamma}R_j^{\alpha\gamma}\right)\right]. \tag{E.12}$$

In order to simply further, we exploit the symmetry of our quantities with respect to atomic indices, α, β, etc., and coordinate indices i and j. In particular, $R^{\alpha\beta}=R^{\beta\alpha}$, $U^{\alpha\beta}=U^{\beta\alpha}$ and $W^{\alpha\beta}=W^{\beta\alpha}$.

Similarly, $Y_{ij}^{\alpha\beta} = Y_{ji}^{\alpha\beta} = Y_{ij}^{\beta\alpha}$. Thus, simplifying our expression further we have

$$
\begin{aligned}
\Delta\Psi_N \;=\; & \sum_{\alpha=1}^{N}\sum_{\beta=1,\beta\neq\alpha}^{N} Y_{ij}^{\alpha\beta}\left(u_i^{\alpha}u_j^{\alpha} - u_i^{\alpha}u_j^{\beta}\right) + \sum_{\alpha=1}^{N}\sum_{\gamma=1}^{M} Y_{ij}^{\alpha\gamma}u_i^{\alpha}u_j^{\alpha} + \\
& \frac{1}{2}\sum_{\alpha=1}^{N}\sum_{\beta=1,\beta\neq\alpha}^{N}\left(\left[F''\left(\rho^{\alpha}\right) + F''\left(\rho^{\beta}\right)\right]U^{\alpha\beta}U^{\alpha\beta}R_i^{\alpha\beta}R_j^{\alpha\beta} + \right. \\
& \left. F''\left(\rho^{\alpha}\right)\sum_{\eta=1,\eta\neq\alpha,\beta}^{N} U^{\alpha\beta}U^{\alpha\eta}R_i^{\alpha\beta}R_j^{\alpha\eta}\right)u_i^{\alpha}u_j^{\alpha} - \\
& \sum_{\alpha=1}^{N} F''\left(\rho^{\alpha}\right)\sum_{\beta=1,\beta\neq\alpha}^{N} U^{\alpha\beta}U^{\alpha\beta}R_i^{\alpha\beta}R_j^{\alpha\beta}u_i^{\alpha}u_j^{\beta} - \\
& \sum_{\alpha=1}^{N} F''\left(\rho^{\alpha}\right)\sum_{\beta=1,\beta\neq\alpha}^{N}\sum_{\eta=1,\eta\neq\alpha,\beta}^{N} U^{\alpha\beta}U^{\alpha\eta}R_j^{\alpha\beta}R_i^{\alpha\eta}u_i^{\alpha}u_j^{\beta} + \\
& \frac{1}{2}\sum_{\alpha=1}^{N}\sum_{\beta=1,\beta\neq\alpha}^{N}\sum_{\eta=1,\eta\neq\alpha,\beta}^{N} F''\left(\rho^{\eta}\right)U^{\alpha\eta}U^{\beta\eta}R_i^{\alpha\eta}R_j^{\beta\eta}u_i^{\alpha}u_j^{\beta} + \\
& \sum_{\alpha=1}^{N} F''\left(\rho^{\alpha}\right)\sum_{\beta=1,\beta\neq\alpha}^{N}\sum_{\gamma=1}^{M} U^{\alpha\beta}U^{\alpha\gamma}\left(R_i^{\alpha\beta}R_j^{\alpha\gamma}u_i^{\alpha}u_j^{\alpha} - R_i^{\alpha\gamma}R_j^{\alpha\beta}u_i^{\alpha}u_j^{\beta}\right) + \\
& \frac{1}{2}\sum_{\alpha=1}^{N} F''\left(\rho^{\alpha}\right)\sum_{\gamma=1}^{M}\sum_{\zeta=1}^{M} U^{\alpha\gamma}U^{\alpha\zeta}R_i^{\alpha\gamma}R_j^{\alpha\zeta}u_i^{\alpha}u_j^{\alpha} + \\
& \frac{1}{2}\sum_{\alpha=1}^{N}\left(\sum_{\gamma=1}^{M} F''\left(\rho^{\gamma}\right)U^{\alpha\gamma}U^{\alpha\gamma}R_i^{\alpha\gamma}R_j^{\alpha\gamma}\right)u_i^{\alpha}u_j^{\alpha} + \\
& \frac{1}{2}\sum_{\alpha=1}^{N}\sum_{\beta=1,\beta\neq\alpha}^{N}\left(\sum_{\gamma=1}^{M} F''\left(\rho^{\gamma}\right)U^{\alpha\gamma}U^{\beta\gamma}R_i^{\alpha\gamma}R_j^{\beta\gamma}\right)u_i^{\alpha}u_j^{\beta}
\end{aligned}
\tag{E.13}
$$

Now collect these terms,

$$\begin{aligned}
\Delta\Psi_N &= \sum_{\alpha=1}^{N}\left\{\sum_{\beta=1,\beta\neq\alpha}^{N}\left[Y_{ij}^{\alpha\beta}+\frac{1}{2}\left(F''\left(\rho^{\alpha}\right)+F''\left(\rho^{\beta}\right)\right)U^{\alpha\beta}U^{\alpha\beta}R_i^{\alpha\beta}R_j^{\alpha\beta}+\right.\right. \\
&\frac{1}{2}F''\left(\rho^{\alpha}\right)\sum_{\eta=1,\eta\neq\alpha,\beta}^{N}U^{\alpha\beta}U^{\alpha\eta}R_i^{\alpha\beta}R_j^{\alpha\eta}+F''\left(\rho^{\alpha}\right)\sum_{\gamma=1}^{M}U^{\alpha\beta}U^{\alpha\gamma}R_i^{\alpha\beta}R_j^{\alpha\gamma}\Bigg]+ \\
&\left.\sum_{\gamma=1}^{M}\left(Y_{ij}^{\alpha\gamma}+\frac{1}{2}F''\left(\rho^{\gamma}\right)U^{\alpha\gamma}U^{\alpha\gamma}R_i^{\alpha\gamma}R_j^{\alpha\gamma}\right)+\frac{1}{2}F''\left(\rho^{\alpha}\right)\sum_{\gamma=1}^{M}\sum_{\zeta=1}^{M}U^{\alpha\gamma}U^{\alpha\zeta}R_i^{\alpha\gamma}R_j^{\alpha\zeta}\right\}u_i^{\alpha}u_j^{\alpha}+ \\
&\sum_{\alpha=1}^{N}\sum_{\beta=1,\beta\neq\alpha}^{N}\left\{-Y_{ij}^{\alpha\beta}-F''\left(\rho^{\alpha}\right)U^{\alpha\beta}U^{\alpha\beta}R_i^{\alpha\beta}R_j^{\alpha\beta}-\right. \\
&F''\left(\rho^{\alpha}\right)\sum_{\eta=1,\eta\neq\alpha,\beta}^{N}U^{\alpha\beta}U^{\alpha\eta}R_i^{\alpha\eta}R_j^{\alpha\beta}+\frac{1}{2}\sum_{\eta=1,\eta\neq\alpha,\beta}^{N}F''\left(\rho^{\eta}\right)U^{\alpha\eta}U^{\beta\eta}R_i^{\alpha\eta}R_j^{\beta\eta}+ \\
&\left.\left.\sum_{\gamma=1}^{M}\left(-F''\left(\rho^{\alpha}\right)U^{\alpha\beta}U^{\alpha\gamma}R_i^{\alpha\gamma}R_j^{\alpha\beta}+\frac{1}{2}F''\left(\rho^{\gamma}\right)U^{\alpha\gamma}U^{\beta\gamma}R_i^{\alpha\gamma}R_j^{\beta\gamma}\right)\right\}u_i^{\alpha}u_j^{\beta}
\end{aligned} \tag{E.14}$$

Equation (E.14) has the desired form given by equation (E.7). It is now simple to place it in the standard quadratic form

$$\Delta\Psi_N=\sum_{k=1}^{3N}\sum_{\ell=1}^{3N}A_{k\ell}v_kv_\ell, \tag{E.15}$$

where $u_i^{\alpha}=v_{3(\alpha-1)+i}$. From equation (E.14),

$$\begin{aligned}
A_{3(\alpha-1)+i,3(\alpha-1)+j} &= \sum_{\beta=1,\beta\neq\alpha}^{N}\left[Y_{ij}^{\alpha\beta}+\frac{1}{2}\left(F''\left(\rho^{\alpha}\right)+F''\left(\rho^{\beta}\right)\right)U^{\alpha\beta}U^{\alpha\beta}R_i^{\alpha\beta}R_j^{\alpha\beta}+\right. \\
&\left.\frac{1}{2}F''\left(\rho^{\alpha}\right)\sum_{\eta=1,\eta\neq\alpha,\beta}^{N}U^{\alpha\beta}U^{\alpha\eta}R_i^{\alpha\beta}R_j^{\alpha\eta}+F''\left(\rho^{\alpha}\right)\sum_{\gamma=1}^{M}U^{\alpha\beta}U^{\alpha\gamma}R_i^{\alpha\beta}R_j^{\alpha\gamma}\right]+ \\
&\sum_{\gamma=1}^{M}\left(Y_{ij}^{\alpha\gamma}+\frac{1}{2}F''\left(\rho^{\gamma}\right)U^{\alpha\gamma}U^{\alpha\gamma}R_i^{\alpha\gamma}R_j^{\alpha\gamma}\right)+\frac{1}{2}F''\left(\rho^{\alpha}\right)\sum_{\gamma=1}^{M}\sum_{\zeta=1}^{M}U^{\alpha\gamma}U^{\alpha\zeta}R_i^{\alpha\gamma}R_j^{\alpha\zeta}
\end{aligned} \tag{E.16}$$

and

$$\begin{aligned}
A_{3(\alpha-1)+i,3(\beta-1)+j} &= -Y_{ij}^{\alpha\beta}-F''\left(\rho^{\alpha}\right)U^{\alpha\beta}U^{\alpha\beta}R_i^{\alpha\beta}R_j^{\alpha\beta}- \\
&F''\left(\rho^{\alpha}\right)\sum_{\eta=1,\eta\neq\alpha,\beta}^{N}U^{\alpha\beta}U^{\alpha\eta}R_i^{\alpha\eta}R_j^{\alpha\beta}+\frac{1}{2}\sum_{\eta=1,\eta\neq\alpha,\beta}^{N}F''\left(\rho^{\eta}\right)U^{\alpha\eta}U^{\beta\eta}R_i^{\alpha\eta}R_j^{\beta\eta}+ \\
&\sum_{\gamma=1}^{M}\left(-F''\left(\rho^{\alpha}\right)U^{\alpha\beta}U^{\alpha\gamma}R_i^{\alpha\gamma}R_j^{\alpha\beta}+\frac{1}{2}F''\left(\rho^{\gamma}\right)U^{\alpha\gamma}U^{\beta\gamma}R_i^{\alpha\gamma}R_j^{\beta\gamma}\right).
\end{aligned} \tag{E.17}$$

To these must be appended the terms resulting from the two-body portion of the EAM potential. These are [41]

$$A_{3(\alpha-1)+i,3(\alpha-1)+j} = \sum_{\beta=1,\beta\neq\alpha}^{N} X_{ij}^{\alpha\beta} + \sum_{\gamma=1}^{M} X_{ij}^{\alpha\gamma} \tag{E.18}$$

and

$$A_{3(\alpha-1)+i,3(\beta-1)+j} = -X_{ij}^{\alpha\beta}, \tag{E.19}$$

where

$$X_{ij}^{\alpha\beta} = \frac{1}{2}\left(P^{\alpha\beta}\delta_{ij} + Q^{\alpha\beta}R_i^{\alpha\beta}R_j^{\alpha\beta}\right), \tag{E.20}$$

with

$$\begin{aligned} P^{\alpha\beta} &= = \frac{1}{R^{\alpha\beta}}\frac{\partial\hat{\psi}_2}{\partial R^{\alpha\beta}} \\ Q^{\alpha\beta} &= \frac{1}{R^{\alpha\beta 2}}\left(\frac{\partial^2\hat{\psi}_2}{\partial R^{\alpha\beta 2}} - \frac{1}{R^{\alpha\beta}}\frac{\partial\hat{\psi}_2}{\partial R^{\alpha\beta}}\right). \end{aligned} \tag{E.21}$$

The completed **A** matrix containing both the two-body and the N-body contributions is the sum of the terms given by equations (E.16) and (E.18), and those given by equations (E.17) and (E.19). It is worth pointing out that, in contrast to the two-body case [41], the resulting matrix is not symmetric.

6.6 Appendix F

As noted previously, the EAM potential is given as the sum of a two-body and an N-body term,

$$\Psi = \sum_{\delta=1}^{N_A} F(\rho^\delta) + \Psi_2 \tag{F.1}$$

where the quantity ρ^δ is given by

$$\rho^\delta = \sum_{\gamma=1,\gamma\neq\alpha}^{N_A} \hat{f}(R^{\alpha\gamma}). \tag{F.2}$$

Both Ψ_2 and $\hat{f}(R^{\alpha\gamma})$ are known explicitly. This is, however, typically not the case with the embedding function F as well as its derivatives. These values are instead obtained from lookup tables.

To generate these tables, we consider the situation in which the crystal is subjected to homogeneous stretching along all three crystallographic axes, a situation that is equivalent to varying the crystal lattice parameter a. In this case, each atom has the same environment, and the quantity $\rho^\delta = \rho$ is the same for each atom, with the superscript merely denoting a typical atom. Note

that for a homogeneously stretched perfect crystal, the interatomic spacings $R^{\delta\gamma}$ are related to the lattice constant a in simple linear form, *i.e.*,

$$R^{\delta\gamma} = b^{\delta\gamma} a, \tag{F.3}$$

where $b^{\delta\gamma}$ is a constant. Then from equation (F.2),

$$\rho = \rho^{\delta} = \sum_{\gamma=1,\gamma\neq\delta}^{N_A} \hat{f}\left(b^{\delta\gamma} a\right) \tag{F.4}$$

Hence equation (F.1) may be written as

$$\Psi = \Psi(a) = N_A F(\rho) + \frac{N_A}{2} \sum_{\gamma=1,\gamma\neq\delta}^{N} \hat{\psi}_2\left(b^{\delta\gamma} a\right), \tag{F.5}$$

so that

$$F(\rho) = \frac{\Psi(a)}{N_A} - \frac{1}{2} \sum_{\gamma=1,\gamma\neq\delta}^{N} \hat{\psi}_2\left(b^{\delta\gamma} a\right). \tag{F.6}$$

The approach taken by Voter and Chen [195] is to equate $\Psi(a)/N_A$ to the per atom Rose energy $E(a)$ [160], so that

$$F(\rho) = E(a) - \frac{1}{2} \sum_{\gamma=1,\gamma\neq\delta}^{N} \hat{\psi}_2\left(b^{\delta\gamma} a\right), \tag{F.7}$$

Voter and Chen made use of a slightly modified form of $E(a)$, which we adopt here. This is given by

$$E(a) = -E_{coh} \hat{e}\,(a^*), \tag{F.8}$$

where $E_{coh} = 3.93$ eV is the per atom crystal cohesive energy for Au and a^* is a nondimensional lattice constant given by

$$a^* = \left(\frac{a}{a_0} - 1\right)\left(\frac{E_{coh}}{9B\Omega}\right)^{1/2}. \tag{F.9}$$

Here $B = 1.67\text{x}10^5$ J/cm^3 is the bulk modulus for Au, Ω =1.698x10^{-23} cm^3 the atomic volume, and $a_o = 4.08$ Å the equilibrium lattice constant. The function $\hat{e}\,(a^*)$ is a modification of that originally proposed by Rose *et al.* [160] so as to achieve $E(a_c^*) = 0$, where $a_c^* = \sqrt{2}R_c$ is the value of a^* taken on when the nearest neighbor spacing between atoms in the FCC lattice reaches the cutoff distance. It is given by

$$\hat{e}\,(a^*) = \frac{f\left(\sqrt{1-\varepsilon}a^*\right) - \varepsilon}{1-\varepsilon}, \tag{F.10}$$

where $f(a^*)$ is the original function given by Rose *et al.* [160],

$$f(a^*) = (1 + a^*)\, e^{a^*}. \tag{F.11}$$

The parameter ε in equation (F.10) is determined numerically so as to yield $\hat{e}\,(a_c^*) = 0$.

Our approach, then, is to systematically vary the lattice parameter a and to calculate ρ from equation (F.4) and $F(\rho)$ from equation (F.7). This allows us to generate the required lookup tables for $F(\rho)$. We also require lookup tables for $F'(\rho)$ and $F''(\rho)$. We note that

$$\frac{da}{d\rho^\delta} = \left(\frac{d\rho^\delta}{da}\right)^{-1} = \left(\sum_{\gamma=1,\gamma\neq\delta}^{N_A} b^{\delta\gamma}\hat{f}'\right)^{-1}. \tag{F.12}$$

From equation (F.6),

$$\begin{aligned}\frac{dF}{d\rho^\delta} &= E'(a)\frac{da}{d\rho^\delta} - \frac{1}{2}\sum_{\gamma=1,\gamma\neq\delta}^{N}\hat{\psi}_2'\left(b^{\delta\gamma}a\right)b^{\delta\gamma}\frac{da}{d\rho^\delta} \\ &= \left(E'(a) - \frac{1}{2}\sum_{\gamma=1,\gamma\neq\delta}^{N}\hat{\psi}_2'\left(b^{\delta\gamma}a\right)b^{\delta\gamma}\right)\left(\sum_{\gamma=1,\gamma\neq\delta}^{N} b^{\delta\gamma}\hat{f}'\right)^{-1}.\end{aligned} \tag{F.13}$$

Likewise,

$$\begin{aligned}\frac{d^2F}{d\rho_h^2} &= \left(E''(a) - \frac{1}{2}\sum_{\gamma=1,\gamma\neq\delta}^{N}\hat{\psi}_2''\left(b^{\delta\gamma}a\right)\left(b^{\delta\gamma}\right)^2\right)\left(\frac{da}{d\rho^\delta}\right)^2 + \\ &\quad \left(E'(a) - \frac{1}{2}\sum_{\gamma=1,\gamma\neq\delta}^{N}\hat{\psi}_2'\left(b^{\delta\gamma}a\right)b^{\delta\gamma}\right)\frac{d^2a}{d\left(\rho^\delta\right)^2}.\end{aligned} \tag{F.14}$$

Let

$$\rho^\delta = \sum_{\gamma=1,\gamma\neq\delta}^{N_A}\hat{f}\left(b^{\delta\gamma}a\right) \equiv g(a) \tag{F.15}$$

Then

$$\begin{aligned}\frac{da}{d\rho^\delta} &= \frac{1}{g'(a)} \\ \frac{d^2a}{d\left(\rho^\delta\right)^2} &= -\frac{g''}{\left(g'\right)^2}\frac{da}{d\rho^\delta} \\ &= -\frac{g''}{\left(g'\right)^3}.\end{aligned} \tag{F.16}$$

Hence

$$\frac{d^2a}{d\left(\rho^\delta\right)^2} = -\left(\frac{d\rho^\delta}{da}\right)^{-3}\frac{d^2\rho^\delta}{da^2}, \tag{F.17}$$

where

$$\frac{d^2\rho^\delta}{da^2} = \sum_{\gamma=1,\gamma\neq\delta}^{N} b^{\delta\gamma^2}\hat{f}''. \tag{F.18}$$

From these expressions, we can construct lookup tables for $F'(\rho)$ and $F''(\rho)$, and can interpolate the tables to the desired degree of accuracy. Simple chain rule relations then give

$$\begin{aligned} \frac{dF}{dR^{\alpha\beta}} &= \frac{dF}{d\rho}\frac{d\hat{f}}{dR^{\alpha\beta}} \\ \frac{d^2F}{d\left(R^{\alpha\beta}\right)^2} &= \frac{d^2F}{d\rho^2}\left(\frac{d\hat{f}}{dR^{\alpha\beta}}\right)^2 + \frac{dF}{d\rho}\frac{d^2\hat{f}}{d\left(R^{\alpha\beta}\right)^2}. \end{aligned} \tag{F.19}$$

Chapter 7

Molecular-dynamics-based cohesive zone law for brittle interfacial fracture

Principal Authors: Xiaowang Zhou, Neville R. Moody, Reese E. Jones, Jonathan A. Zimmerman, and E. David Reedy Jr.

One approach for performing a finite element simulation of interfacial fracture is to use a cohesive zone model. The cohesive zone model defines the interfacial traction-separation relation. Experimental determination of such a relation has been difficult. Most past work is confined to tensile loading, and much less work is devoted to mixed-mode loading conditions. Even so, specific laws are often assumed rather than predicted. Our recent work has used molecular dynamics (MD) simulation methods to derive a general cohesive zone law for the fracture between two brittle materials under any mix-mode loading conditions. Here we extend our method and use it to explore the effect of elastic constant mismatch between the adjacent materials. In particular, we construct two bilayer structures where the cohesive energies and lattice constants of the constituent materials are kept the same, but the elastic constant mismatch of the two materials in one structure differs from that in the other. We then use MD simulations to study the fracture and to derive the cohesive zone laws for both structures. The effect of elastic constant mismatch on fracture will then be discussed.

7.1 Introduction

Many modern technologies require the use of multilayered material structures to achieve desired functionality. Examples include thermal [28] and chemical [147] protection systems, electronic packaging [38], ceramic multilayer actuators [70], thermoelectric superlattices [112, 208, 209], thermoelectrics and compliant substrate technologies [21]. As these structures become relatively large and geometrically more complex as well as being required to survive harsh environments, interfacial fracture is likely to occur, especially when at least one of the materials at the interface is brittle. This presents a critical problem for the application of these systems [44, 50]. Modeling of interfacial fracture is highly desired in order to design optimum systems.

Modern approaches to the modeling and simulation of fracture are typically based upon a cohesive zone law that defines the relation between traction and crack opening displacement [204]. Construction of such a law has been a challenging exercise for the past decade and a half [190, 203, 204]. Most past work is limited to tensile loading, and much less work is devoted to mixed-mode loading conditions. Because a direct experimental quantification is difficult, specific cohesive zone

laws are often assumed rather than predicted. In recent years, there have been numerous efforts aimed at studying fracture using atomistic simulations [61, 161, 162]. Advances in these areas have begun to enable calculations that can be used to define a physics-based cohesive zone separation model. For example, Spearot *et al.* [175] proposed interface separation constitutive laws based upon molecular dynamics (MD) simulations of interfacial debonding between Cu grain boundaries, although their work did not result in an explicit traction vs. displacement relation at the local fractured surfaces. Yamakov *et al.* [206], on the other hand, did extract a qualitative local traction vs. displacement relation from their MD simulations of intergranular fracture of an Al metal. Their approach, however, is only applicable to far field tensile (mode I) loading conditions and cannot be applied to mixed-mode loading conditions. They also did not give explicit functions for traction vs. displacement relations. By extending Yamakov *et al.* 's work, we recently developed an MD model of fracture between two brittle materials under any combinations of far field tensile (mode I) and shear (mode II) strains, and derived directly analytical functions relating local traction, local displacement, and local loading mode mixity [218]. This new approach provides an effective means to study the effects of material properties upon interfacial fracture.

Interfacial fracture is known to be sensitive to many material properties, most notably lattice mismatch that causes mismatch stress, thermal expansion coefficient mismatch that causes thermal and residual stresses, and cohesive (bonding) energy that may affect decohesion resistance. Other properties may also affect fracture but are less understood. For instance, some multilayers of practical interests, such as those with compliant substrates [211], are based upon materials with vastly different elastic constants. It is known from continuum solutions that elastic mismatch can have a significant effect on crack-tip stress fields. However, experimental studies that could help clarify the role of elastic constant mismatch are difficult to perform since elastic constants cannot be independently varied without concurrently changing other material properties (such as cohesive energy and lattice constants) in real materials. Here we will perform MD simulations to extract local traction-displacement-mixity relations during debonding between two brittle materials. The purpose of our work is threefold: (i) test our previous approach [218] against a larger database created through MD simulations; (ii) improve the analytical functions so that they better match the MD traction-displacement data; and (iii) identify the effects of elastic constant mismatch on the cohesive zone law.

7.2 Methods

This section presents our MD model of an interface between materials A and B. First, two binary interatomic potentials are constructed for the A-B system. Each potential produces a different elastic constant mismatch between the two materials, but both potentials predict the same lattice constants and cohesive energies. Details regarding computational system size, crystal orientation, geometry, and mixed-mode loading are also described.

7.2.1 Interatomic potential

To be consistent with the previous work [218], body-centered-cubic (bcc) materials are used to construct the brittle interfacial fracture model. To investigate the effect of a specific material property, an ideal interatomic potential should allow the targeted property to change while fixing other material properties. Here we develop a bcc pair potential model that allows independent change of lattice constants, cohesive energies, and elastic constants. Note that in the present study, this potential model is parameterized to fit different elastic constants at fixed lattice constants and cohesive energies. It can also be used to fit different lattice constants or cohesive energies while fixing other properties. With the pair potential model, the total energy of a computational system is expressed as

$$E = \sum_{i,j \neq i} \phi_{ij}(r_{ij}) \tag{7.1}$$

where $\phi_{ij}(r_{ij})$ is the pair energy between atoms i and j separated by a distance r_{ij}. Our pair potential between atom species pair ij is expressed using three splined cubic functions applied respectively in three different distance ranges:

$$\phi_{ij}(r_{ij}) = \begin{cases} a_{1,ij} + b_{1,ij}\left(r - r_{1,ij}\right) + \frac{1}{2}c_{1,ij}\left(r - r_{1,ij}\right)^2 + \frac{1}{6}d_{1,ij}\left(r - r_{1,ij}\right)^3 & 0 < r \leq r_{1,ij} \\ a_{2,ij} + b_{2,ij}r + c_{2,ij}r^2 + d_{2,ij}r^3 & r_{1,ij} < r \leq r_{2,ij} \\ c_{3,ij}\left(r - r_{3,ij}\right)^2 + d_{3,ij}\left(r - r_{3,ij}\right)^3 & r_{2,ij} < r \leq r_{3,ij} \\ 0, & r > r_{3,ij} \end{cases} \tag{7.2}$$

where parameters $a_{1,ij}$, $b_{1,ij}$, $c_{1,ij}$ and $d_{1,ij}$ are used for the short-range; $a_{2,ij}$, $b_{2,ij}$, $c_{2,ij}$ and $d_{2,ij}$ are used for the mid-range; $c_{3,ij}$ and $d_{3,ij}$are used for the long-range; $r_{1,ij}$ is the junction point between the short- and mid-ranges; $r_{2,ij}$ is the junction point between the mid- and long-ranges; and $r_{3,ij}$ is essentially the cutoff distance of the potential. As described in Appendix G, only four parameters, $a_{2,ij}$, $b_{2,ij}$, $c_{2,ij}$ and $d_{2,ij}$, are treated as independent and other parameters are determined from the requirement that the function be continuous and physical. Five pair functions, notated as ϕ_a, ϕ_b, ϕ_c, ϕ_d and ϕ_e, are derived from five sets of input properties summarized in Table G1. The parameters of these five pair functions are listed in Table G2. For a bilayer system composed of species A and B, three pair potentials are needed to define A-A, B-B, and A-B interactions. Here we assemble two sets of A-B binary potentials P1 and P2 using the five pair functions. The correspondence of the A-A, B-B, and A-B interactions to the ϕ_a, ϕ_b, ϕ_c, ϕ_d and ϕ_e functions are shown in Table 7.1.

To characterize the potentials, various properties were calculated based upon the bcc crystal and the results are included in Table 7.1. Here single crystalline elastic constants C_{ij} were calculated for the bcc crystal using the approach described in references [216, 217]. Work of adhesion, woa, was calculated the same way as our previous work [218]. It is defined as woa(i-j) = Γ_i + Γ_j - $\Gamma_{i/j}$, where i = A or B, Γ_i is the (001) surface energy of the bcc species i, and $\Gamma_{i/j}$ is the (001) interfacial energy between two bcc species i and j. Following the method by Zotov and Ludwig [225], Youngs modulus E, shear modulus G, and Poissons ratio ν were calculated respectively using the following equations:

$$E = \frac{9B \cdot G}{3B + G} \tag{7.3}$$

Table 7.1. Lattice constant a (Å), cohesive energy E_c (eV atom^{-1}), elastic constants C_{11}, C_{12} and C_{44} (eV Å^{-3}), Young's and shear moduli E and G (GPa), Poisson's ratio ν, and work of adhesion woa (J m^{-2}), predicted by potentials P1 and P2.

	Pair	Function	a	E_c	C_{11}	C_{12}	C_{44}	E	G	ν	woa
*P*1	A–A	ϕ_a	3.162	−4.45	3.25	1.15	1.15	444	177	0.25	5.968
	B–B	ϕ_a	3.162	−4.45	3.25	1.15	1.15	444	177	0.25	5.968
	A–B	ϕ_d	3.162	−1.78	1.26	0.48	0.48	177	71	0.25	2.336
*P*2	A–A	ϕ_b	3.162	−4.45	3.41	1.21	1.21	466	186	0.25	5.968
	B–B	ϕ_c	3.162	−4.45	1.64	0.57	0.57	222	89	0.25	6.032
	A–B	ϕ_e	3.162	−1.78	0.46	0.33	0.33	72	28	0.30	2.400

$$G = \frac{G_{voight} + G_{Reuss}}{2} \tag{7.4}$$

$$\nu = \frac{1}{2}\frac{3B - 2G}{3B + G} \tag{7.5}$$

where $G_{voight} = (2C' + 3C_{44})/5$, $G_{Reuss} = (10C' \cdot C_{44})/(6C' + 4C_{44})$, and $C' = (C_{11} - C_{12})/2$. From Table 7.1, it can be seen that P1 and P2 potentials predict the same cohesive energy of -4.45 eV/atom for species A and B, the same energy of -1.78 eV/atom for the A-B interaction, and the same lattice constant of 3.162 Å for all interactions. However, P1 predicts a zero elastic constant mismatch between materials A and B whereas P2 predicts a significant elastic constant mismatch.

7.2.2 Molecular dynamics model

The MD model of fracture was detailed previously [218], and is briefly described here. The geometry of the system used in our molecular dynamics simulations of the crack propagation is shown in Fig. 7.1. Test runs were first carried out to determine a sufficiently large system dimension so that the cohesive zone law extracted is independent of the crack length during the steady-state crack propagation stage. The crystal is in the cubic orientation (*i.e.* x [100], y [010], and z [001]) and is composed of 253 unit cells in the x-direction, 206 unit cells in the y-direction, and 10 unit cells in the z-direction, for a total of 1,042,360 atoms. Periodic boundary conditions were used in both x- and z-directions, and non-periodic boundary conditions were applied in the y-direction. As shown in Fig. 7.1, the crystal is divided into six regions. The top half of the crystal is composed of atoms A that fall into three regions marked respectively as 3, 1, and 3. The bottom half of the crystal is composed of atoms B that fall into other three regions marked respectively as 4, 2, and 4. Note that due to the periodic boundary condition used in the x-direction, the regions 3 and 4 at the left side join the corresponding regions 3 and 4 at the right. As a result, these contiguous regions are marked by the same numbers. Atoms that are marked in black color are boundary atoms through which tensile and shear loads were applied.

A crack in the middle of the A/B interface was created by omitting the interactions between

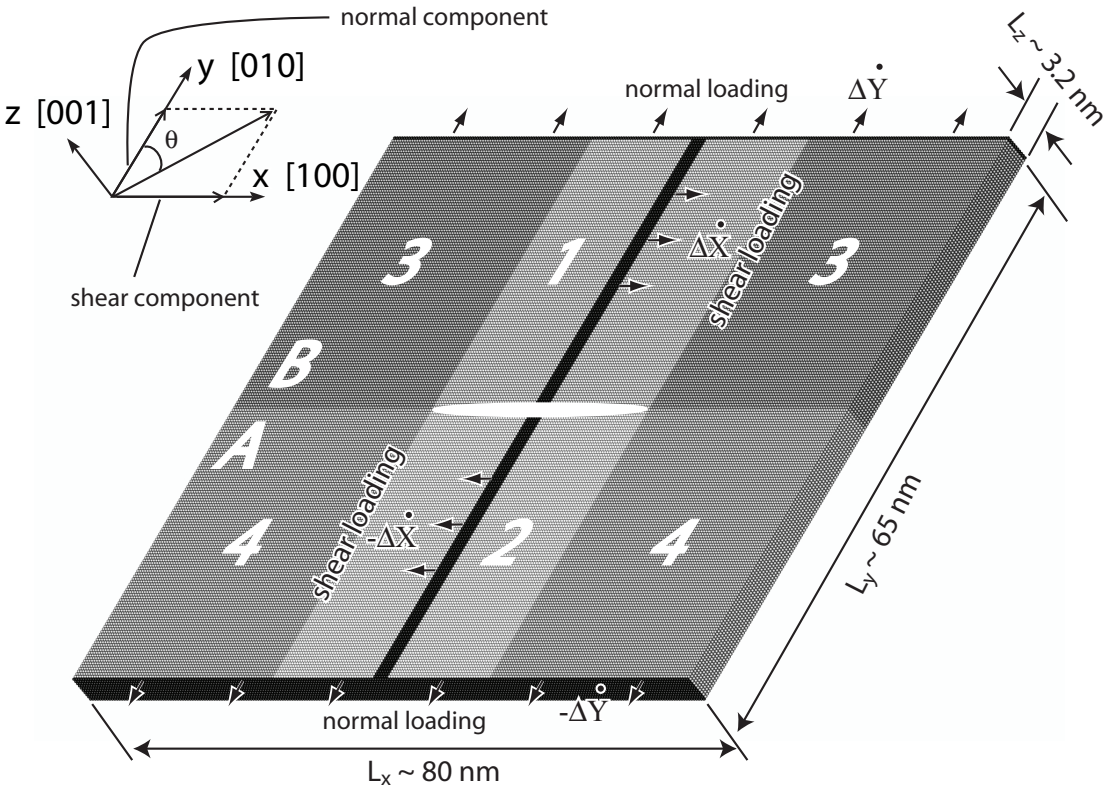

Figure 7.1. Geometry of molecular dynamics simulation

atoms in region 1 and atoms in region 2 while letting all other atoms interact. For mode I crack simulation where a tensile load normal to the crack plane is applied, crack propagation is associated with separation of regions 1 and 2. For mode II crack simulation where a shear load parallel to the crack plane is applied, the initial crack may be healed when region 1 is shifted to above region 4 or region 2 is shifted to below region 3. To overcome this problem, we initiate atom neighbors at the start of the simulations and do not redetermine neighbors. This means that atoms interact only with the neighbors that are identified at the start of the loading. It mimics the realistic scenario that once atoms near the crack tips break their bonds with their neighbors in the initial crystal configuration, they are quickly contaminated (e.g. via oxidation) so that they lose the ability to reform bonds with new neighbors. We emphasize that the approach is different from our early work19 where only interactions between atoms across the interface were not redetermined whereas the neighbors of all the other atoms are recalculated as in the conventional MD. Nonetheless, we have performed numerous tests and discovered that for the brittle interfacial model and the specific shear loading algorithm we used, only atoms at crack tips change their neighbors. As a result, not recalculating atom neighbors is a sufficiently accurate approximation. Readers are cautioned that this approximation cannot be applied to study ductile phenomena because reneighboring is essential for modeling dislocation formation and motion the mechanisms of plastic deformation. The only failure mechanism permitted by this approach is the nucleation of a vacancy when a bulk atom loses a neighbor without being replaced by a new neighbor, and the growth of such vacancies

into a void, or a crack (as simulated in our work).

During molecular dynamics simulations of mode I crack propagation, the system is uniformly stretched (by moving each atom a distance corresponding to a uniform normal strain increment) in the y-direction each time step. Numerical time integration approaches are then used to update the atom positions based upon interatomic potential and Newtons equations of motion under the condition that the y coordinates of the top and bottom horizontal layers of boundary atoms (marked black in Fig. 7.1) remain fixed. Unlike displacing boundary atoms alone, a uniform stretching of the system avoids the creation of shock wave during simulations.

During molecular dynamics simulations of mode II crack propagation, the upper and lower halves of the vertical layer of boundary atoms (marked black in Fig. 7.1) are displaced by a small distance in opposite directions along the x axis each time step. Newtons equations of motion are solved to update atom positions with the constraint that the x coordinates of the vertical layer of boundary atoms remain fixed. Mixed loading can be simulated by simultaneously applying normal and shear displacement. In all simulations, the rates at which the boundary atoms are displaced are determined from the simulated strain rates, which are on the order of 10^8 s^{-1}, characteristic of MD simulation techniques. Our simulations were performed using MD package LAMMPS [168] at a constant temperature of 300 K and fixed system dimensions in the x- and z-directions.

7.3 MD results

7.3.1 Simulation loading conditions

MD runs were carried out at constant boundary displacement rates, $\Delta\dot{X}$ and $\Delta\dot{Y}$, in the x- and y-directions (see Fig. 7.1). These correspond to constant engineering (global) shear and normal strain rates, $\dot{\varepsilon}_{xy} = 2\Delta\dot{X}/L_y$ and $\dot{\varepsilon}_{yy} = 2\Delta\dot{Y}/L_y$. The mixed loading condition can be approximately described by a loading angle, $\theta = \arctan\left(\Delta\dot{X}/\Delta\dot{Y}\right)$, Fig. 7.1. To extract the cohesive zone law as a function of mode-mixity, MD simulations were carried out at seven selected loading angles. The rates of boundary displacement in the x- and y-directions, $\Delta\dot{X}$ and $\Delta\dot{Y}$, the corresponding shear and normal strain rates, $\dot{\varepsilon}_{xy}$ and $\dot{\varepsilon}_{yy}$, and the loading angles, θ, are shown in Table 7.2.

7.3.2 Stress strain curves and crack propagation dynamics

Selected examples were examined to characterize stress-strain curves and crack propagation dynamics. Average atomic stresses based on the Virial theorem [222] were used to estimate global normal (yy) and shear (xy) stresses applied to the system. Corresponding engineering strains were calculated from the boundary displacement in the x- and y-directions, ΔX and ΔY. The results are used to map the stress vs. strain curves. To reduce thermal oscillation, values of stress, displacement, and strain are averaged over 10 time steps (each time step is 0.001 ps). A short averaging time of 0.01 ps was used to retain the time dependence of the properties. While this averaging time

Table 7.2. Boundary displacement rates $\Delta\dot{X}$ and $\Delta\dot{Y}$ (Åps^{-1}), strain rates $\dot{\varepsilon}_{xy}$ and $\dot{\varepsilon}_{yy}$ (10^8 s^{-1}), and loading angle $\theta(^\circ)$.

MD run	$\Delta\dot{X}/\Delta\dot{Y}$		$\dot{\varepsilon}_{xy}/\dot{\varepsilon}_{yy}$		θ
	Potential *P*1	Potential *P*2	Potential *P*1	Potential *P*2	
1	0.0000/0.0351	0.0000/0.0434	0.000/1.078	0.000/1.333	0.0
2	0.0098/0.0364	0.0113/0.0421	0.301/1.118	0.347/1.293	15.0
3	0.0210/0.0364	0.0237/0.0410	0.645/1.118	0.728/1.259	30.0
4	0.0279/0.0279	0.0336/0.0336	0.857/0.857	1.032/1.032	45.0
5	0.0390/0.0225	0.0441/0.0255	1.197/0.691	1.354/0.783	60.0
6	0.0510/0.0140	0.0560/0.0150	1.566/0.430	1.719/0.461	75.0
7	0.0646/0.0000	0.0630/0.0000	1.984/0.000	1.934/0.000	90.0

is small, it still helps mitigate thermal noises as the averaging is performed over many atoms. Example of a normal stress vs. normal strain curve obtained from a pure mode I ($\theta = 0^\circ$) simulation is shown in Fig. 7.2(a), and example of a shear stress vs. shear strain curve obtained from a pure mode II ($\theta = 90^\circ$) simulation is shown in Fig. 7.2(b).

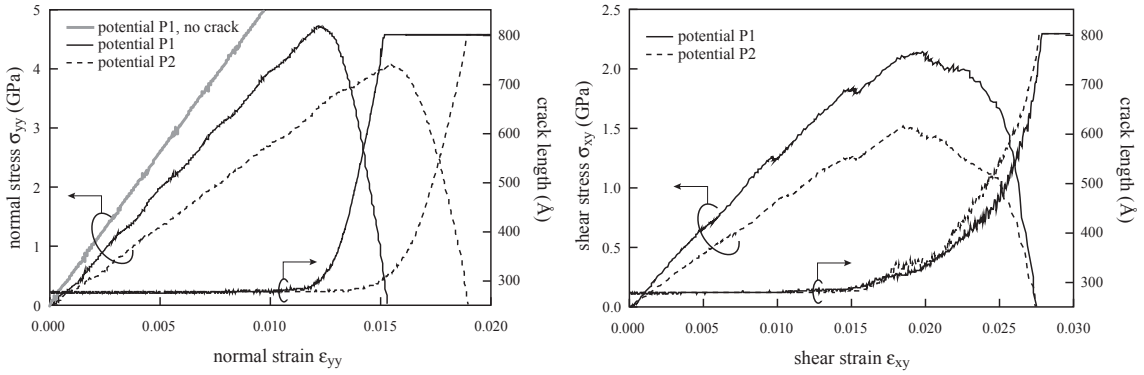

Figure 7.2. Stress and crack length as a function of strain. (a) tensile test ($\theta = 0^\circ$); and (b) shear test ($\theta = 90^\circ$).

Fig. 7.2(a) indicates that during the tensile test, the normal stress initially linearly increases as the normal strain is increased, corresponding to an elastic deformation of the system. To examine the effect of the presence of the crack, a similar normal stress vs. normal strain curve obtained from the P1 potential during a mode I loading of a crack-free sample is included in Fig. 7.2(a). The overall tensile elastic modulus of this crack-free sample is seen from Fig. 7.2(a) to be about 520 GPa. For a bilayer system with two equal-sized materials A and B, the overall elastic modulus can be calculated as $M = 2M_AM_B/(M_A + M_B)$, where M can be tensile (e.g., C_{11}, E etc.) or shear (e.g., C_{44}, G) modulus and the subscripts A and B refer to the materials. Using the C_{11} values listed in Table 7.1, we obtain an overall tensile elastic modulus of the crack-free, P1 prescribed sample as 3.25 eV/Å^3 = 520 GPa, which agrees well with Fig. 7.2(a). Fig. 7.2(a) clearly shows that the introduction of the crack significantly changes the overall compliance of the system. However,

these changes appear to be well correlated. For example, Fig. 7.2(a) shows that the stiffness of the cracked system using potential P1 is about 45% higher than that using P2. Interestingly, Table 7.1 indicates that the average C_{11} value of the bilayer is also about 45% higher for potential P1 than for P2.

After the normal stress reaches the maximum, it starts to decrease towards zero as the strain further increases. As will be discussed below, this decrease in stress was found to correlate well with the propagation of the crack. It can be seen that the maximum stress is about $\sigma_{\max} \approx 4.7$ GPa for potential P1 and about $\sigma_{\max} \approx 4.1$ GPa for potential P2, and the critical strain at which the maximum stress occurs is about $\varepsilon_c \approx 0.0122$ for potential P1 and $\varepsilon_c \approx 0.0154$ for potential P2. The stored elastic energy prior to the fracture, defined as $E_f = \sigma_{\max} \cdot \varepsilon_c/2$, was calculated to be 0.03 GJ m^{-3} for both potentials. Although P1 potential predicts a higher maximum stress, it also predicts a lower critical strain. As a result, both P1 and P2 potentials predict about the same stored energy.

According to Griffith theory [64], the critical stress of fracture of brittle materials can be expressed as

$$\sigma_{\max} = \sqrt{\frac{E \cdot \text{woa}}{\pi \cdot a_h}} \tag{7.6}$$

where a_h is half of the crack length and woa is work of adhesion. Using the Youngs modulus evaluated from Fig. 2 and an initial crack length of 278 Å, Eq. (7.6) predicts a fracture stress of $\sigma_{\max} \approx 4.6$ GPa for potential P1 and $\sigma_{\max} \approx 3.9$ GPa for potential P2. According to linear elastic equation, these stresses give a critical strain of $\varepsilon_c \approx 0.0118$ for potential P1 and $\varepsilon_c \approx 0.0144$ for potential P2. It can be seen that the results obtained from atomistic simulations agree quite well with Griffith theory.

A similar trend can be found in Figs. 7.2(b) for the shear test. Essentially an initial linear increase in the shear stress characteristic of the elastic deformation occurs as the shear strain begins to be applied. The overall shear modulus is seen to be about 128 GPa for potential P1 and about 87 GPa for P2, consistent with the C_{44} values listed in Table 7.1 as they both predict that the shear modulus is about 45% higher for potential P1 than for P2. Once the shear stress linearly increases to the maximum value, it starts to decrease as the shear strain further increases, signifying the fracture. The maximum stress is about $\sigma_{\max} \approx 2.1$ GPa for potential P1 and about $\sigma_{\max} \approx 1.5$ GPa for potential P2, and the critical strain at which the maximum stress occurs appears to be about $\varepsilon_c \approx 0.0192$ for both potentials. The higher maximum stress for P1 potential than for P2 potential is consistent with the tensile test and Griffiths theory described above. It should be noted that our shear loading is applied through the displacement of the vertical layer of boundary atoms as shown in Fig. 7.1. Such an approach can cause a stress concentration at the crack tip, and is necessary in order to isolate the crack phenomenon from slip. While the way in which the stress is introduced does not affect the local traction vs. crack opening displacement relation, the calculated global shear strain differs from the conventional definition. As a result, Fig. 7.2(b) should not be used to estimate the elastic energy prior to the fracture.

To examine the correlation between the observed stress vs. strain curves and fracture, the dynamic variation of crack length was monitored during simulations. It was recognized that atoms at

the cracked surface have significantly higher energy than those in the bulk. A threshold energy was then used to determine the crack length. Here we chose an atomic plane of "A" atoms immediately above the A/B interface and divided it evenly into ∼253 regions along the x-direction. An average potential energy was calculated over all atoms in each of the regions. If this average energy was larger than the threshold energy, the corresponding region was counted as cracked. The crack length was calculated as the sum of the width of all cracked regions. To reduce the statistical error due to dynamics, each crack length was averaged over 10 time steps that are centered at the time of crack length output. The results for crack length as a function of strain are included in Fig. 7.2 for both tensile and shear tests. It can be seen that crack did not propagate during the linear elastic deformation stage. When the stress reached the maximum value, the crack propagation is also seen to begin. A long steady-state crack propagation period is observed for the tensile case. Approximate steady-state (*i.e.* near-linear) crack propagation is observed for the shear case. We extract local traction and crack opening displacement data during these steady-state crack propagation periods to construct accurate cohesive zone laws.

7.3.3 Local traction and crack opening displacement

To quantify the cohesive zone law, stresses and displacements at local positions are analyzed in detail. As shown in Fig. 7.3, a horizontal layer that is centered at the crack (interface) plane but only has a height of $\delta_y \sim \pm 10$ Å was used for the analysis. The use of a small $\delta_y \sim \pm 10$ Å has been

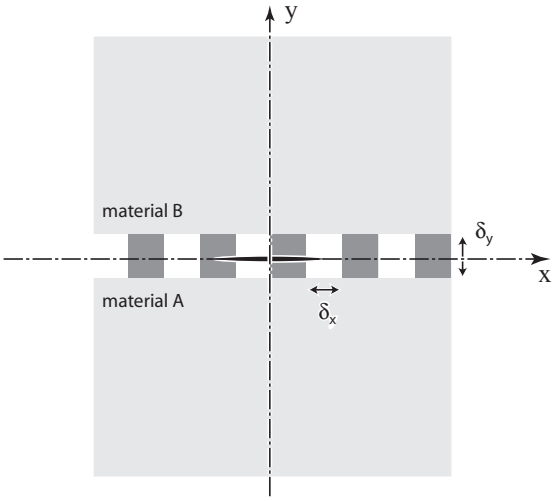

Figure 7.3. Schematic of regions used to calculate local traction and local displacement.

shown to represent well the local traction and displacement measurements [218]. The horizontal layer was further divided into regions with width δ_x. In this work, we used a constant δ_x of about 9.486 Å. This includes three $\{100\}$ planes, dividing the entire width of the system into about 84 regions. Normal and shear tractions at a local position (x coordinate) defined by a region were

calculated as the average atomic stresses of all atoms in that region, and the normal and shear components of the crack opening displacement, Δx and Δy, were calculated as the corresponding components of the average atom displacement in the upper half of the region with respect to that of the lower half. The total magnitude of the crack opening is defined as $\Delta r = \sqrt{\Delta x^2 + \Delta y^2}$. Stress and crack opening are calculated every 0.45 ps, which provides sufficient data for the analysis. Again to reduce dynamic statistics, stress and crack opening are averaged over 10 time steps that are centered at the time of output.

A large number of stress vs. crack opening data points (measured at different locations and times) are obtained during the steady-state crack propagation of each MD run. These data points are sorted according to the opening displacement. They are then binned with a bin size of 0.2 Å. The average traction and opening displacement associated with each bin were calculated using all the points in the bin. This effectively reduces the scatter of the data. Fig. 7.4 shows some examples of the traction as a function of displacement obtained using such an approach from both potentials, where Figs. 7.4(a) and 7.4(b) are the results of normal traction vs. displacement at two remote loading angles of $\theta = 0^\circ$ and $\theta = 60^\circ$, and Figs. 7.4(c) and 7.4(d) are the results of shear traction vs. displacement at two remote loading angles of $\theta = 45^\circ$ and $\theta = 90^\circ$.

Fig. 7.4 generally agrees well with the previous results [218]. It indicates that the stresses initially increased as the crack opening distance was increased until they reached a peak value. The stresses then decreased as the crack opening was further increased. For near normal tests such as Figs. 7.4(a) and 7.4(c), the stresses directly decayed to zero. However, when the tests are associated with a strong shear component, such as Figs. 7.4(b) and 7.4(d), a second stress peak occurred before the stress decayed to zero. Comparison of the stress vs. displacement curves between tensile ($\theta = 0^\circ$) and shear ($\theta = 90^\circ$) tests, Figs. 7.4(a) and 7.4(d), further indicates that the shear stress during shear loading has a considerably longer decaying tail than the normal stress during tensile loading whereas the peak stress is only slightly less. This suggests that shear fracture may be associated with a higher fracture toughness. Fig. 7.4 also shows that at least when the loading contains a high shear component [Fig. 7.4(d)], potential P1 predicts a higher shear stress than potential P2. Because the displacement is seen to be about the same, this suggests that potential P2 has a lower toughness when the loading is primary shear.

There is a plausible explanation for the occurrence of double peaks under near-shear loading conditions. Fig. 7.5(a) shows that during a tensile test along the vertical axis, atom B is pulled away from atom A until it moves to position B$'$. It can be seen that the bond between atoms A and B is constantly stretched until it is broken. Contrarily, Fig. 7.5(b) shows that during a near-shear loading test, atom B moves toward position B$'$ through an intermediate position B$''$. It can be seen that during this process, the bond between A and B can be shortened initially before it is stretched. Some bonds that undergo initial shortening before being stretched contribute to the second peak observed in Fig. 7.4.

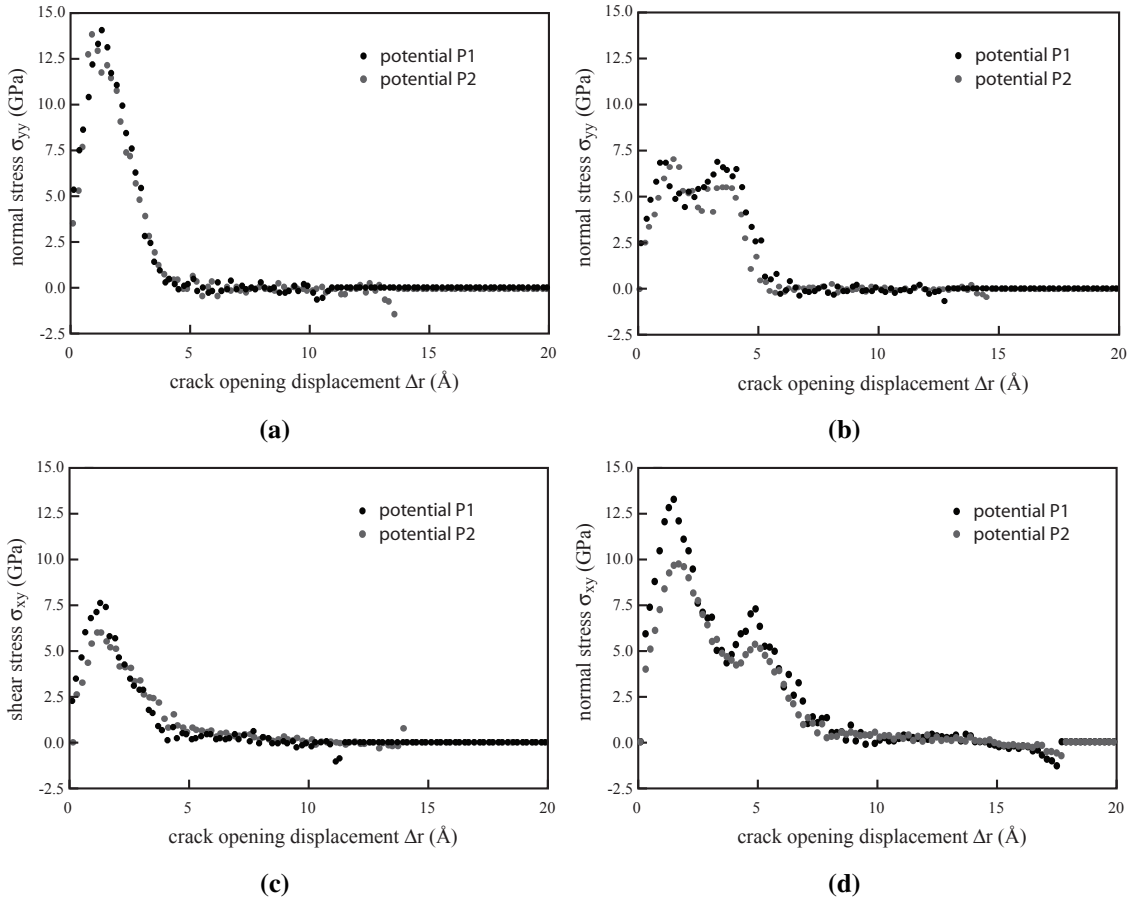

Figure 7.4. Traction as a function of displacement obtained from MD simulations. (a) normal stress at $\theta = 0^\circ$; (b) normal stress at $\theta = 60^\circ$; (c) shear stress at $\theta = 45^\circ$; and (d) shear stress at $\theta = 90^\circ$.

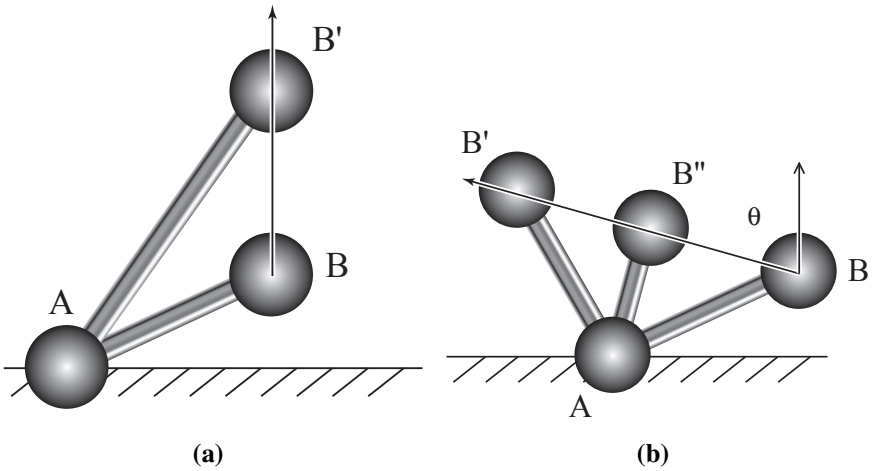

Figure 7.5. Change of bond length during test. (a) bond stretching during tensile loading; and (b) bond shortening-and-stretching during mixed mode loading.

7.4 Analytical cohesive zone law

The utility of the traction-displacement-loading angle data revealed from MD simulations can be greatly increased if these data can be described by analytical equations. Previous work has developed an algorithm to derive such equations [218]. Based upon a larger amount of MD data created in the present work, we seek to improve the analytical functions and their associated parameters over the previous work so that the analytical equations better reflect the MD data.

Detailed derivation of the analytical functions for traction-displacement-mixity relations is presented in Appendix H. The final traction as a function of displacement and mixity is described by Eq. (H.3). Since separate equations are used to describe normal and shear stresses and we have two potentials, four sets of parameters are needed. All four sets of parameters are given in Table H1.

To test the accuracy of the analytical equation, traction as a function of displacement was calculated using Eq. (H.3) for both normal and shear stresses and both potentials at a variety of loading angles, and the results are compared with the data obtained from the MD simulations in Fig. 7.6. It can be seen that the analytical prediction agrees very well with the MD data. In addition, the present analytical equation captures the second peak when the loading angles are high.

With accurate analytical equations for tractions as functions of displacement and mixity, three dimensional normal and shear stresses as functions of local normal (y) and shear (x) components of the crack opening displacement can be calculated. Results for normal and shear stresses are shown in Figs. 7.7(a) and 7.7(b) respectively, where the left column was obtained from potential P1 and the right column was obtained from P2. Fig. 7.7 gives insights on how local mixity affects traction. It can be seen that the trends predicted by both potentials are quite similar. When the local displacement is dominated by the shear component Δx (*i.e.* $\Delta y = 0$), the normal stress is negligible

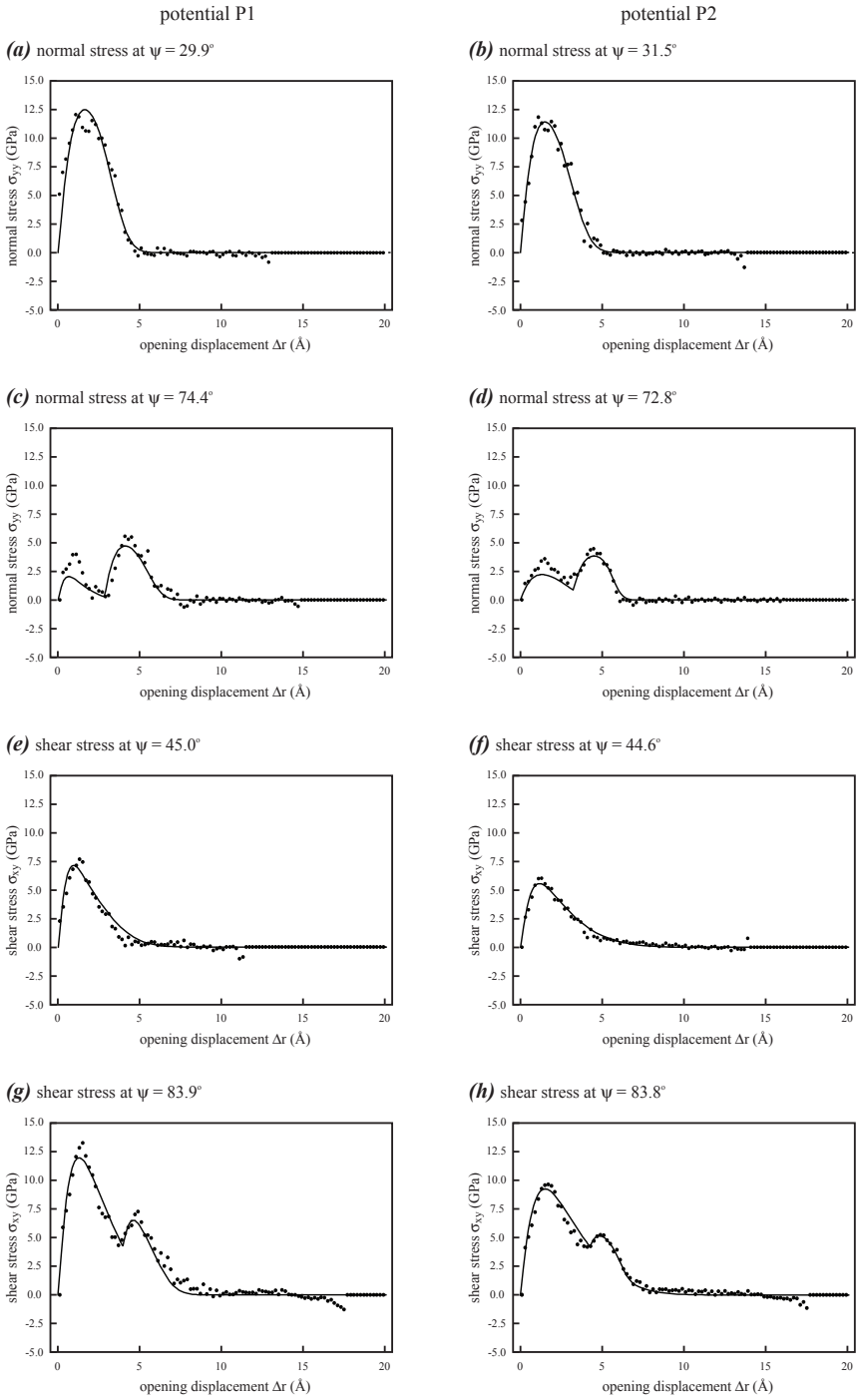

Figure 7.6. Comparison of traction as a function of displacement between MD data and fitted curves. (a) normal stress at $\psi \sim 29.9^\circ$ using potential P1; (b) normal stress at $\psi \sim 31.5^\circ$ using potential P2; (c) normal stress at $\psi \sim 74.4^\circ$ using potential P1; (d) normal stress at $\psi \sim 72.8^\circ$ using potential P2; (e) shear stress at $\psi \sim 45.0^\circ$ using potential P1; (f) shear stress at $\psi \sim 44.6^\circ$ using potential P2; (g) shear stress at $\psi \sim 83.9^\circ$ using potential P1; and (h) shear stress at $\psi \sim 83.8^\circ$ using potential P2. ψ is defined as $\arcsin\left(\sqrt{\Delta x^2/\left(\Delta x^2+\Delta y^2\right)}\right)$.

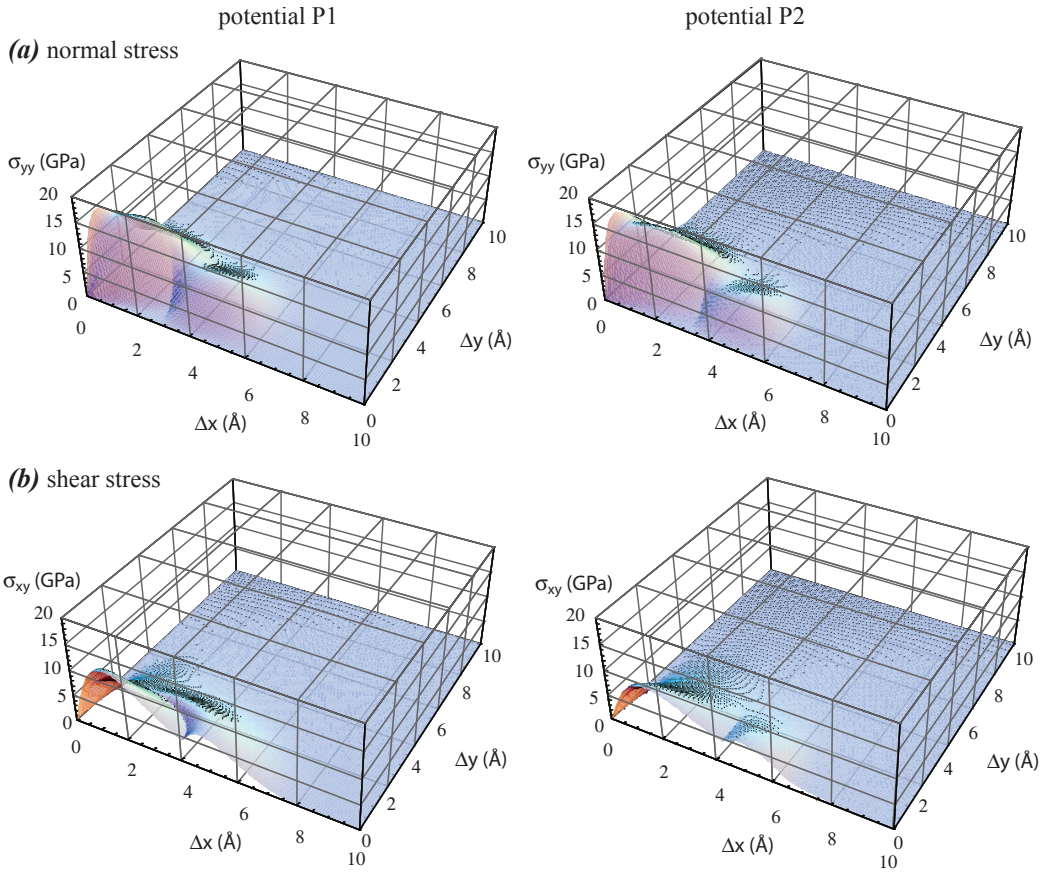

Figure 7.7. Stress as a function of crack opening displacement components Δx and Δy. (a) normal stress; and (b) shear stress.

and the shear stress is at maximum. On the other hand, when the local displacement is dominated by the normal component Δy ($\Delta x = 0$), the shear stress is negligible and the normal stress is at maximum. Fig. 7.7 can also be used to identify the critical mixity angle at which the second stress peak starts to occur. The shear stress predicted by potential P1, for example, appears to introduce the second peak at a smaller loading angle than that by potential P2.

7.5 Work of separation

Fracture toughness can be measured by the work of separation defined as follows:

$$w = w(\psi) = \int_0^\infty \sigma_{yy} \cdot d(\Delta y) + \int_0^\infty \sigma_{xy} \cdot d(\Delta x) \tag{7.7}$$

By integrating Eq. (7.7) at constant loading angle ψ, the work of separation was calculated as a function of ψ. The results of this calculation are shown in Fig. 7.8. As has been shown previously

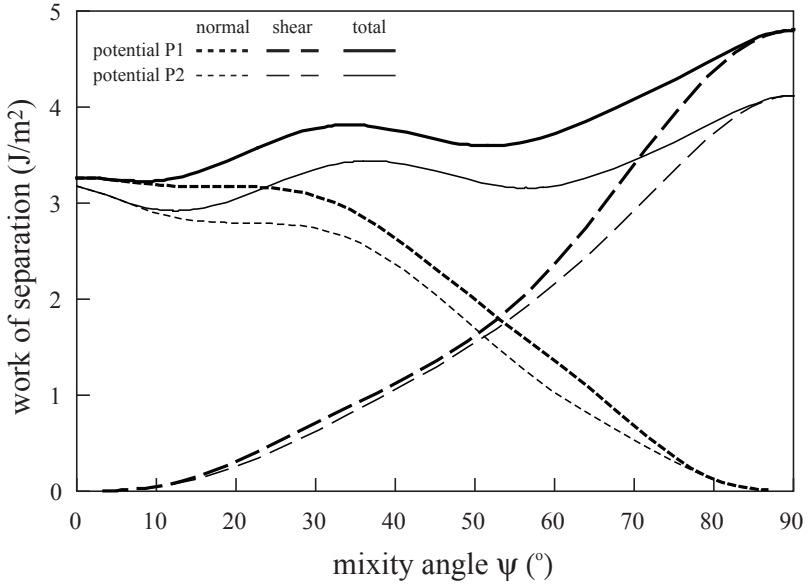

Figure 7.8. Work of separation as a function of loading angle ψ.

[218], Fig. 7.8 indicates that work of separation due to the normal stress is high when the loading angle is low, and it decreases to zero as the loading changes from tensile ($\psi = 0°$) to shear ($\psi = 90°$). The work of separation due to the shear stress is high when the loading angle is high, and it decreases to zero when the loading changes from shear to normal. The total work of separation composed of both normal and shear stress contributions exhibits some oscillations in Fig. 7.8. While these may be an artifact of the error of the fitted functions, the general trend is clear that the total work of separation increases as the loading becomes increasingly dominated by shear. Most interestingly, Fig. 7.8 clearly shows that potential P1 predicts a higher work of separation than

potential P2 at least for shear loading condition. This means that compared with an interface where the two materials have identical elastic constants, fracture is more likely to occur at the interface during a shear loading when the elastic modulus of one of the materials is reduced. Finally, the total work of separation roughly stays between 3.21 J m^{-2} and 4.84 J m^{-2} for potential P1 and between 2.92 J m^{-2} and 4.15 J m^{-2} for potential P2. The work of adhesion listed in Table 7.1 is in the 2.33 - 2.40 J m^{-2} range for both potentials. As expected, work of separation is higher than work of adhesion, and can vary as a function of elastic properties even work of adhesion remains fixed.

7.6 Discussion

The results presented above indicated that when the elastic constant of one material is decreased while the elastic constant of the other material is kept about the same or slightly increased, the work of separation between the two materials clearly decreases under the near-shear loading condition. This observation is further explored.

It is possible to calculate traction and crack opening displacement separately for materials A and B. For instance, tractions for A and B surfaces can be defined as the average atomic stresses for the lower and upper halves of the local unit shown in Fig. 7.3. Similarly, opening displacements for A and B surfaces can be derived from the average atomic displacement for the lower and upper halves of the local unit with respect to a reference point far away from the crack. Spatial distributions of such decomposed shear traction and shear displacement as well as the overall shear traction and shear displacement were calculated for shear tests using both potentials, and the results are shown in Fig. 7.9, where Fig. 7.9(a) is at a shear strain of 0.023 and Fig.7.9(b) is at a shear strain of 0.026. Numerous observations can be made from Fig. 7.9: (i) The traction distributions are consistent with classic continuum theories, namely, traction decays to zero (oscillates around zero due to thermal noise) for completely fractured surface sections where crack openings are large, and traction is largest near the crack tips and drops off away from the crack tips. (ii) Individual decomposed tractions and overall traction are about the same. In addition, the traction distributions near the crack tips do not have significant difference between the two strains (or equivalently, crack displacements), consistent with the steady-state condition achieved in the simulations. (iii) The total cracking opening displacement equals the sum of the displacements from surfaces A and B. For potential P1 where both materials have the same elastic modulus, displacements of surfaces A and B are equal within statistical errors. For potential P2 where the two materials have different elastic modulus, the material with the higher elastic modulus displaced significantly less than the one with the lower elastic modulus. (iv) Traction distributions near the crack tips are noticeably lower for potential P2 than potential P1, whereas the total displacements are about the same. It is therefore likely that the crack propagation was determined by the displacement during the shear loading. Because at a given displacement, a reduction in elastic modulus causes a reduction in stress. This reduced traction then resulted in a lower work of separation observed for the elastically mismatched system.

For comparison, spatial distributions of normal traction and normal displacement were also

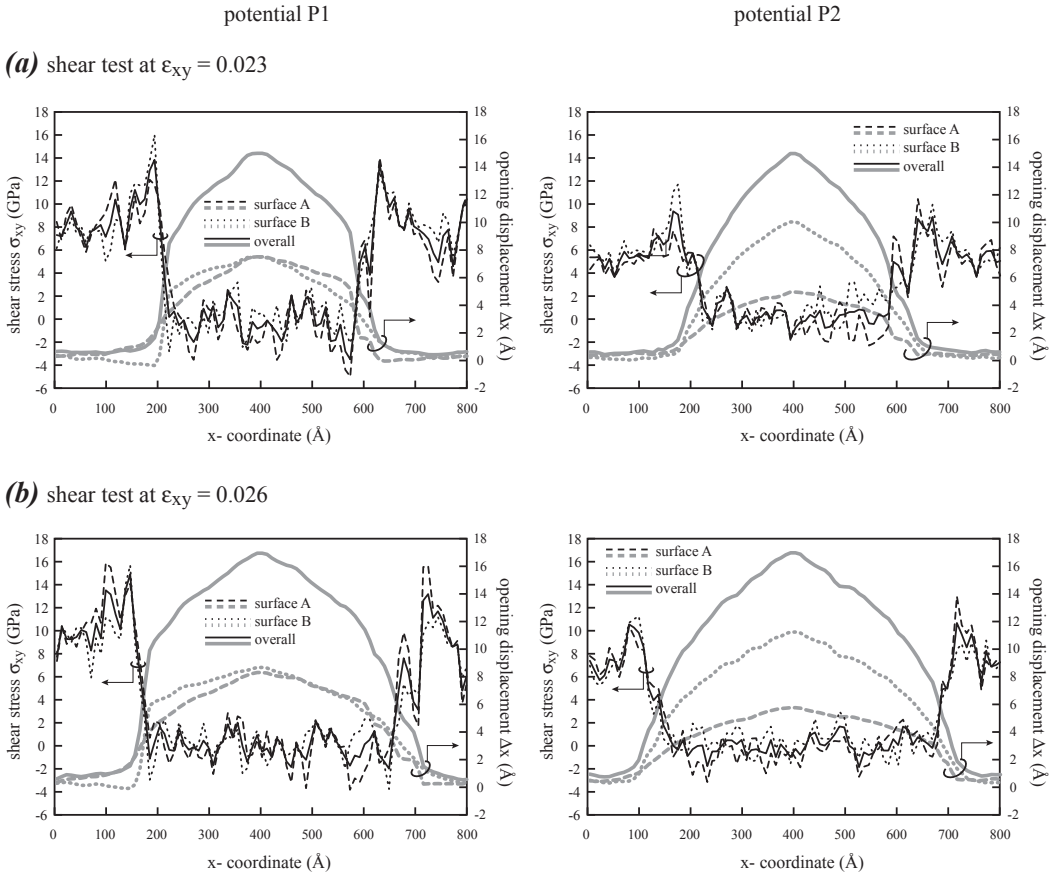

Figure 7.9. Spatial distributions of shear traction and shear opening displacement obtained from shear tests with both potentials. (a) at shear strain 0.023; and (b) at shear strain 0.026.

calculated for tensile tests using both potentials. Selected results are shown in Fig. 7.10 where Fig. 7.10(a) is obtained from potential P1 at a tensile strain of 0.013, and Fig. 7.10(b) is from potential P2 at a tensile strain of 0.017. These strains were chosen so that the crack lengths are

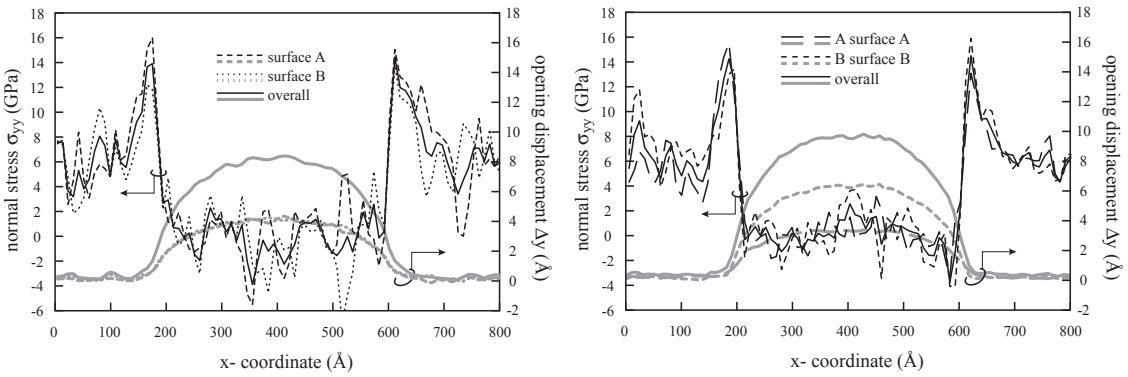

Figure 7.10. Spatial distributions of normal traction and normal opening displacement obtained from tensile tests with both potentials. (a) at tensile strain 0.013, potential P1; and (b) at tensile strain 0.017, potential P2.

about the same (around 400 Å) for Figs. 7.10(a) and 7.10(b). While the trend is very similar to the shear cases, Fig. 7.10 indicates that the traction distributions near the crack tips are very similar for the two potentials. As a result, the work of separation predicted by potential P2 is not significantly lower than that predicted by potential P1 during the tensile loading condition.

7.7 Conclusions

Molecular dynamics simulations have been carried out to study interfacial crack growth between two brittle materials with zero and large elastic constant mismatch at fixed lattice constants and cohesive energies. The dependence of local traction (both normal and shear stresses) and local crack opening displacement data was fully determined for a variety of remote loading angles. Analytical fits of these results are also presented. Work of separation was calculated as a function of mixity using these fits. The following conclusions were obtained:

1. The newly developed analytical fits of the calculated dependency of tractions on displacement and mixity accurately represent the MD data.
2. Normal traction vs. displacement relationships have a higher peak stress than the shear traction vs. displacement relationships, but they have a shorter tail.
3. Traction vs. displacement curves have a second peak under near-shear loading conditions that is thought to be due to the bond shortening-and-stretching mechanism.

4. As loading angle increases, the normal stress contribution to the work of separation decreases whereas shear stress contribution increases. The total work of separation remains between 2.92 N m^{-1} and 4.84 N m^{-1} and appears to be relatively high under the near-shear conditions compared with that under the near-normal conditions.

5. Under the conditions that materials have the same lattice constant, the same cohesive energy, the same surface energy or work of adhesion, and that the fracture occurs at the interface, the work of separation was found to vary as a function of elastic constant mismatch between the two materials. In particular, a decrease in the elastic constant of one material would result in a decrease in the work of separation especially under the shear loading condition. This was found to originate from a reduction in the traction near the crack tips during shearing loading.

7.8 Appendix G: Potential parameterization

In our pairwise potential functions, we constrain the radial parameters so that r_1 is shorter than the nearest neighbor distances of both bcc and face-centered-cubic (fcc) crystals, r_2 is longer than the second nearest neighbor distance of the bcc structure and the first nearest neighbor distance of the fcc structure, and r_3 is shorter than the third nearest neighbor distance of the bcc structure and the second nearest neighbor distance of the fcc structure. With these constraints, the model is essentially a second-nearest neighbor model for bcc and a first-nearest neighbor model for fcc, and the bulk properties are dependent only upon the mid-range function. The short- and long-range functions, therefore, are used for extrapolation purposes and can be determined after the mid-range function is fitted to material properties.

All pair functions, including those between similar species and those between dissimilar species, are parameterized to fit the properties of elemental bcc and fcc crystals [218]. The use of elemental structures to approximate interaction between dissimilar species greatly simplifies the problem and yet enables the characteristics of the interaction to be continuously adjusted. In this work, the mid-range function is fitted to four input properties: (i) bcc lattice constant, a; (ii) bcc cohesive energy, E_c; (iii) bcc bulk modulus, B; and (iv) relative cohesive energy difference between fcc and bcc crystals, $\Delta E \left(= E_c^{fcc} - E_c\right)$. Here the superscript "bcc" is omitted for the bcc properties. With the constraint $\Delta E > 0$, we can ensure a stable bcc structure.

Using Eqs. (7.1) and (7.2) and the constraints described above, the energy (per atom) of the bcc structure as a function of its nearest neighbor distance r can be expressed as $E(r) = 7a_2 + 2\left(2+\sqrt{3}\right)\cdot b_2 \cdot r + 8c_2 \cdot r^2 + \left(4+\frac{8\sqrt{3}}{3}\right) d_2 \cdot r^3$. The condition to fit the cohesive energy can then be expressed as

$$E_c = E(r_e) \tag{G.1}$$

where r_e is the equilibrium nearest neighbor distance in the bcc structure. The condition to fit the

lattice constant is equivalent to fit a zero pressure P at $r = r_e$, which can be written as

$$P = -\frac{dE(r)}{d\Omega} = -\frac{\sqrt{3}}{4r_e^2}\left.\frac{dE(r)}{dr}\right|_{r=r_e} \tag{G.2}$$

where Ω is atomic volume. The condition to fit the bulk modulus B is essentially the definition of bulk modulus:

$$B = \Omega\left.\frac{d^2E(r)}{d\Omega^2}\right|_{r=r_e} = \frac{\sqrt{3}}{12r_e^2}\left.\frac{d^2E(r)}{dr^2}\right|_{r=r_e} \tag{G.3}$$

Again using Eqs. (7.1) and (7.2) and the constraints, the energy of the fcc structure as a function of its nearest neighbor distance r can be expressed as $E^{fcc}(r) = 6\left(a_2 + b_2 \cdot r + c_2 \cdot r^2 + d_2 \cdot r^3\right)$. We do not have an input value of the (local) minimum energy nearest neighbor distance of the fcc structure, r_0^{fcc}. As a result, r_0^{fcc} is solved from the minimum energy condition $\left.\frac{dE^{fcc}(r)}{dr}\right|_{r=r_0^{fcc}} = 0$. The condition to fit the energy difference can then be expressed as

$$\Delta E = E^{fcc}(r_0^{fcc}) - E_c \tag{G.4}$$

Eqs. (G.1)-(G.4) provide four conditions to fit the four model parameters, a_2, b_2, c_2 and d_2. However, these conditions alone do not necessarily yield physically meaningful parameters. A physical pair function is repulsive at a short distance, reaches a minimum at an intermediate positive distance, and then smoothly decays to zero at the cutoff distance. Our analysis indicated that these conditions can be satisfied by the following constraints:

$$a_2 > 0, b_2 < 0, c_2 > 0, d_2 < 0, -3d_2 \cdot r_{3rd} > c_2 > -3d_2 \cdot r_{2nd} \tag{G.5}$$

where r_{2nd} and r_{3rd} are the second and the third nearest neighbor distances of the bcc structure.

An objective function, is defined as the sum of the weighted square deviation of Eqs. (G.1)-(G.4). Subject to the constraining conditions, Eq. (G.5), the fitting was carried out to minimize the objective function. Once the parameters of the mid-range function are known, the junction points can be chosen through visual judgment of the pair potential curves. The two parameters (c_3,d_3) of the long-range function are determined by matching the value and slope of the mid- and the long-range functions at r_2. The three parameters (a_1,b_1,c_1) of the short-range function are determined by matching the value, slope, and second derivative of the short- and the mid-range functions at r_1. This leaves the parameter d_1 undetermined. We arbitrarily chose d_1 to be a negative number of -150. It does not affect the equilibrium properties, but can be used to adjust the short-range repulsion.

With this process, we parameterized five pair potential functions according to five different sets of input properties shown in Table G1. These five pair functions are notated as ϕ_a, ϕ_b, ϕ_c, ϕ_d and ϕ_e, and their parameters are listed in Table G2. These functions exactly reproduce the targeted properties. The curves of the five functions are shown in Fig. 7.1(a). The curves for the energy of the bcc structure as a function of the nearest neighbor distance predicted by the five functions are shown in Fig. 7.1(b). Both pair function and bcc energy curves are seen to be fairly smooth.

Table G1. Targeted lattice constant a (Å), cohesive energy E_c (eV atom^{-1}), bulk modulus B, and structure energy difference ΔE (eV atom^{-1}) for five pair energy functions ϕ_a, ϕ_b, ϕ_c, ϕ_d and ϕ_e.

Pair functions	a	E_c	B	ΔE
ϕ_a	3.162	−4.45	1.85	0.053
ϕ_b	3.162	−4.45	1.94	0.023
ϕ_c	3.162	−4.45	0.93	0.344
ϕ_d	3.162	−1.78	0.74	0.020
ϕ_e	3.162	−1.78	0.37	0.127

Table G2. Parameters for the five pair functions ϕ_a, ϕ_b, ϕ_c, ϕ_d and ϕ_e.

Short-range	$a_{1,ij}$ (eV)	$b_{1,ij}$ (eV Å^{-1})	$c_{1,ij}$ (eV Å^{-2})	$d_{1,ij}$ (eV Å^{-3})	$r_{1,ij}$ (Å)
ϕ_a	−0.21656	−2.40149	6.10379	−150	2.46454
ϕ_b	−0.19531	−2.52481	6.42549	−150	2.46454
ϕ_c	−0.42714	−1.18974	2.99591	−150	2.46454
ϕ_d	−0.08249	−1.00621	2.67350	−150	2.46454
ϕ_e	−0.15169	−0.68749	2.27443	−150	2.46454
Mid-range	$a_{2,ij}$ (eV)	$b_{2,ij}$ (eV Å^{-1})	$c_{2,ij}$ (eV Å^{-2})	$d_{2,ij}$ (eV Å^{-3})	$r_{2,ij}$ (Å)
ϕ_a	33.05711	−28.178498	7.407284	−0.5890754	3.34511
ϕ_b	34.88508	−29.734689	7.827824	−0.6241984	3.32580
ϕ_c	15.72496	−13.590189	3.533603	−0.2753255	3.35507
ϕ_d	15.23574	−13.339492	3.667550	−0.3152450	3.34357
ϕ_e	15.62658	−15.028706	4.681823	−0.4794156	3.34180
Long-range	–	–	$c_{3,ij}$ (eV Å^{-2})	$d_{3,ij}$ (eV Å^{-3})	$r_{3,ij}$ (Å)
ϕ_a	–	–	−0.00882	1.13265	4.02937
ϕ_b	–	–	−0.03408	1.05933	4.02917
ϕ_c	–	–	−2.02171	−1.39366	4.03080
ϕ_d	–	–	−0.06216	0.38287	4.02207
ϕ_e	–	–	−1.22058	−1.12393	3.97111

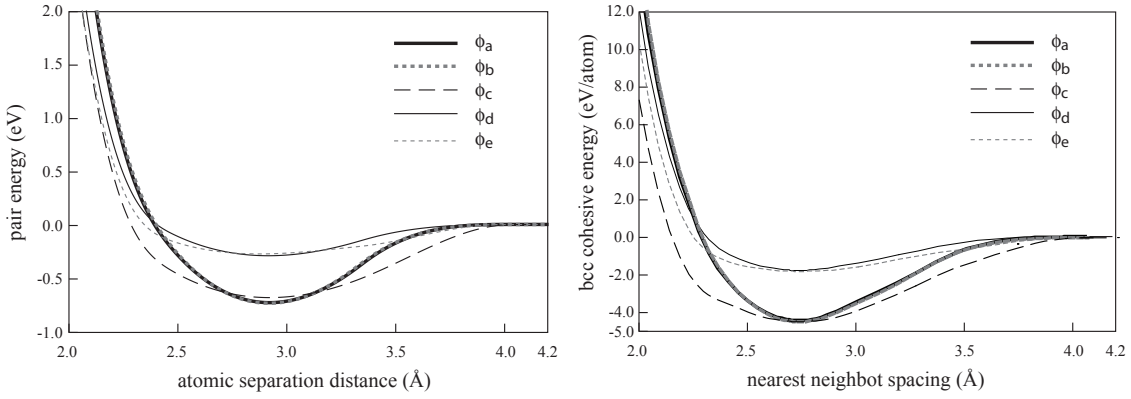

Figure G1. (a) Pair energy as a function of atomic spacing. (b) bcc cohesive energy as a function of the nearest neighbor distance.

7.9 Appendix H: Analytical formulation of traction-displacement-mixity relation

In this work, we have carried out seven MD simulations corresponding to seven remote loading angles $\theta = \arctan\left(\Delta\dot{X}/\Delta\dot{Y}\right) = 0^\circ,\ 15^\circ,\ 30^\circ,\ 45^\circ,\ 60^\circ,\ 75^\circ$ and 90°. We can also define a local loading angle $\psi = \arcsin\left(\sqrt{\Delta x^2/\left(\Delta x^2+\Delta y^2\right)}\right) = \arctan\left(\Delta x/\Delta y\right)$, where Δx and Δy are the shear and normal opening displacements measured within the volume unit used to calculate local properties. Alternatively, it is convenient to use a unitless local mode mixity parameter $m = \sin(\psi) = \sqrt{\Delta x^2/\left(\Delta x^2+\Delta y^2\right)}$. During the steady-state crack propagation, the points of the x and y components of the crack opening displacement, (Δx, Δy), were found to roughly fall on a straight line in each of these MD simulations. The MD run can therefore be characterized by an average "measured" mode mixity angle, $\overline{\psi} = \arcsin\left(\overline{\sqrt{\Delta x^2/\left(\Delta x^2+\Delta y^2\right)}}\right)$, or mixity parameter, $\overline{m} \approx \sin(\overline{\psi}) = \overline{\sqrt{\Delta x^2/\left(\Delta x^2+\Delta y^2\right)}}$, where $\overline{\sqrt{\Delta x^2/\left(\Delta x^2+\Delta y^2\right)}}$ is the average $\sqrt{\Delta x^2/\left(\Delta x^2+\Delta y^2\right)}$ value calculated from all the (Δx, Δy) points obtained during the steady-state crack propagation in an MD run. Values of θ and $\overline{\psi}$ are not exactly equal, but they are close. We found that for $\theta = 0^\circ$, 15°, 30°, 45°, 60°, 75° and 90°, $\overline{\psi}$ approximately equals 5.5°, 15.8°, 29.9°, 45.0°, 59.9°, 74.4° and 83.9° for the simulations using potential P1, and 5.4°, 16.0°, 31.5°, 44.6°, 58.5°, 72.8° and 83.8° for the simulations using potential P2.

Our purpose is to derive separate analytical functions that relate respectively the normal and shear components of local traction to local crack opening displacement and local mode mixity (m). Our approach involves two steps: (i) derive independent normal and shear stresses as functions of displacement at a fixed mixity ($m \approx \overline{m}$) for each of the MD runs; and (ii) consolidate the resultant array of traction vs. displacement functions through the dependence of the function parameters upon mixity.

Examination of results from individual MD runs indicates that regardless of mixity, the stress (either normal or shear) always initially increases to a peak when the magnitude of the crack opening, $\Delta r = \sqrt{\Delta x^2 + \Delta y^2}$, increases from zero. Stress always decays to zero when the opening Δr becomes large. The features of all traction vs. displacement relations appear to be sufficiently captured by four quantities: (i) the peak stress σ_p; (ii) the displacement Δr_p at which the peak stress occurs; (iii) the critical displacement Δr_c above which stress is negligible; and (iv) relative decay rates before and after the peak stress. We propose the following function $F(\alpha, \beta, \sigma_p, \Delta r_p, \Delta r_c, \Delta r)$ that can capture all these features:

$$F(\alpha, \beta, \sigma_p, \Delta r_p, \Delta r_c, \Delta r) = \frac{\Delta r_p^{\beta-\alpha} \beta^\beta \cdot \sigma_p \cdot \Delta r^\alpha}{[\Delta r_p \cdot (\beta - \alpha) + \alpha \cdot \Delta r]^\beta} \cdot f_c(\Delta r_p, \Delta r_c, \Delta r) \tag{H.1}$$

with

$$f_c(\Delta r_p, \Delta r_c, \Delta r) = \frac{1}{2} \cdot \mathrm{erfc}\left[\zeta_p + \frac{\zeta_c - \zeta_p}{\Delta r_c - \Delta r_p} \cdot (\Delta r - \Delta r_p)\right] \tag{H.2}$$

where $f_c(\Delta r_p, \Delta r_c, \Delta r)$ is a function defining the critical displacement Δr_c, and the known parameters $\zeta_p = -1.64498$ and $\zeta_c = 1.45222$ were solved from $\mathrm{erfc}[\zeta_p]/2 = 0.99$ and $\mathrm{erfc}[\zeta_c]/2 = 0.02$ respectively. It can be seen that when Δr is less than Δr_p, $f_c(\Delta r_p, \Delta r_c, \Delta r)$ is constantly close to one and therefore does not contribute to the value defined by Eq. (H.1). However, when Δr is close to Δr_c, $f_c(\Delta r_p, \Delta r_c, \Delta r)$ decays to near zero and therefore effectively enables Eq. (H.1) to become negligible at $\sim \Delta r_c$. Once $\alpha, \beta, \sigma_p, \Delta r_p, \Delta r_c$ are known, Eq. (H.1) is a function of displacement Δr. An advantage of Eq. (H.1) is that the parameters σ_p, Δr_p, and Δr_c are actually the physical quantities described above, and parameters α, β are two additional parameters that allow control of the decaying rate around the stress peak.

To capture the double peak phenomenon, we superimpose Eq. (H.2) with another similar function that is shifted in Δr. The resulting general traction function T (can be normal σ and shear τ stress) is expressed as:

$$\begin{aligned} &T(\alpha,\beta,\sigma_p,\Delta r_p,\Delta r_c,\sigma_{p2},\Delta r_{p2},\Delta r_{c2},\Delta r_s,\Delta r) \\ &\quad = F(\alpha,\beta,\sigma_p,\Delta r_p,\Delta r_c,\Delta r) + F(\alpha,\beta,\sigma_{p2},\Delta r_{p2},\Delta r_{c2},\Delta r - \Delta r_s) \cdot \delta(\Delta r - \Delta r_s) \end{aligned} \tag{H.3}$$

where $\delta(x)$ is a Heaviside step function. Eq. (H.3) involves nine parameters α, β, σ_p, Δr_p, Δr_c, σ_{p2}, Δr_{p2}, Δr_{c2} and Δr_s The additional parameters σ_{p2}, Δr_{p2}, Δr_{c2}, which have similar meaning to σ_p, Δr_p, Δr_c, are used to define the second peak. The parameter Δr_s is essentially the shifted distance between the two F functions.

Eq. (H.3) was parameterized against the data obtained at fixed mixity from each MD run (see, for example, Fig. 7.4). Examination of our fitted parameters at the seven MD runs with different mixity values indicated that there are well-defined trends between these parameters and m. This is not surprising because the nine parameters α, β, σ_p, Δr_p, Δr_c, σ_{p2}, Δr_{p2}, Δr_{c2} and Δr_s are all physical quantities rather than arbitrary parameters used to assist the fitting. Incorporation of the mixity dependence can therefore be achieved by identifying analytical equations of these nine parameters as a function of m. We found that σ_p and Δr_p can be well described by the polynomial function $\sum_{i=0}^{4} c_i \dot{m}^i$, σ_{p2} and Δr_s can be well described by another function $c_0 \cdot m^{c_1} \cdot (1-m)^{c_2} + c_3$, and all the other parameters can be treated as constants. By fitting to the parameter (α, β, σ_p, Δr_p,

Table H1. Parameters of analytical traction-displacement-mixity functions (stress in GPa and distance in Å).

Normal stress parameters predicted by potential $P1$											
α	β	σ_p					Δr_p				
		c_0	c_1	c_2	c_3	c_4	c_0	c_1	c_2	c_3	c_4
1.1800	8.0000	14.6974	−17.1730	49.4803	−47.0047	0.0000	1.0000	2.5885	−9.1000	21.4763	−15.7740
Δr_c	σ_{p2}				Δr_{p2}	Δr_{c2}	Δr_s				
	c_0	c_1	c_2	c_3			c_0	c_1	c_2	c_3	
5.2400	207.9726	12.9073	1.0000	0.0000	1.3600	4.3800	0.0000	–	–	2.8200	
Shear stress parameters predicted by potential $P1$											
α	β	σ_p					Δr_p				
		c_0	c_1	c_2	c_3	c_4	c_0	c_1	c_2	c_3	c_4
1.1800	8.0000	0.0000	−4.6725	86.4059	−148.1626	78.7212	0.7831	0.009410	2.3414	−5.3128	3.5079
Δr_c	σ_{p2}				Δr_{p2}	Δr_{c2}	Δr_s				
	c_0	c_1	c_2	c_3			c_0	c_1	c_2	c_3	
8.5600	4.3025	7.4069	0.0000	0.0000	0.9800	4.4000	2.0535	8.6867	0.0000	2.0016	
Normal stress parameters predicted by potential P2											
α	β	σ_p					Δr_p				
		c_0	c_1	c_2	c_3	c_4	c_0	c_1	c_2	c_3	c_4
1.1800	8.0000	14.0959	−16.9131	45.0036	−42.1864	0.0000	1.0146	1.6267	−8.8837	23.2643	−16.0450
Δr_c	σ_{p2}				Δr_{p2}	Δr_{c2}	Δr_s				
	c_0	c_1	c_2	c_3			c_0	c_1	c_2	c_3	
5.3200	201.2781	19.0041	1.0000	0.0000	1.4600	3.4700	0.0000	–	–	3.2200	
Shear stress parameters predicted by potential P2											
α	β	σ_p					Δr_p				
		c_0	c_1	c_2	c_3	c_4	c_0	c_1	c_2	c_3	c_4
1.1800	8.0000	0.0000	−3.0601	56.6927	−91.5108	47.3412	0.9833	−0.1565	1.3510	−1.9656	1.3420
Δr_c	σ_{p2}				Δr_{p2}	Δr_{c2}	Δr_s				
	c_0	c_1	c_2	c_3			c_0	c_1	c_2	c_3	
11.0900	2.6918	26.8255	0.0000	0.0000	1.0800	2.8800	0.0000	–	–	4.2410	

Δr_c, σ_{p2}, Δr_{p2}, Δr_{c2} and Δr_s) data derived from MD, we determined all these functions and the results are shown in Table H1.

Note that in Table H1, some Δr_s values may reduce to constants at the parameters used. The non-constant parameters are plotted in Fig. H1 as a function of m and are compared with the data derived from MD. It can be seen that the trends for the parameters as a function of mixity parameter m are very consistent for both normal and shear stresses and both potentials. As expected, σ_p decreases from the maximum value to zero for normal stress and increases from zero to the maximum value for shear stress as m is increased from 0 to 1. In addition, it is seen that σ_{p2} is negligible at small m values and becomes large at relatively large m values, consistent with the occurrence of the second peak when the loading involves a significant shear component. For normal stress, however, σ_{p2} drops again to zero at $m = 1$. This is because the normal stress vanishes during a shear loading. The analytical equations, therefore, quite well capture the traction-displacement-mixity relations revealed in the MD simulations.

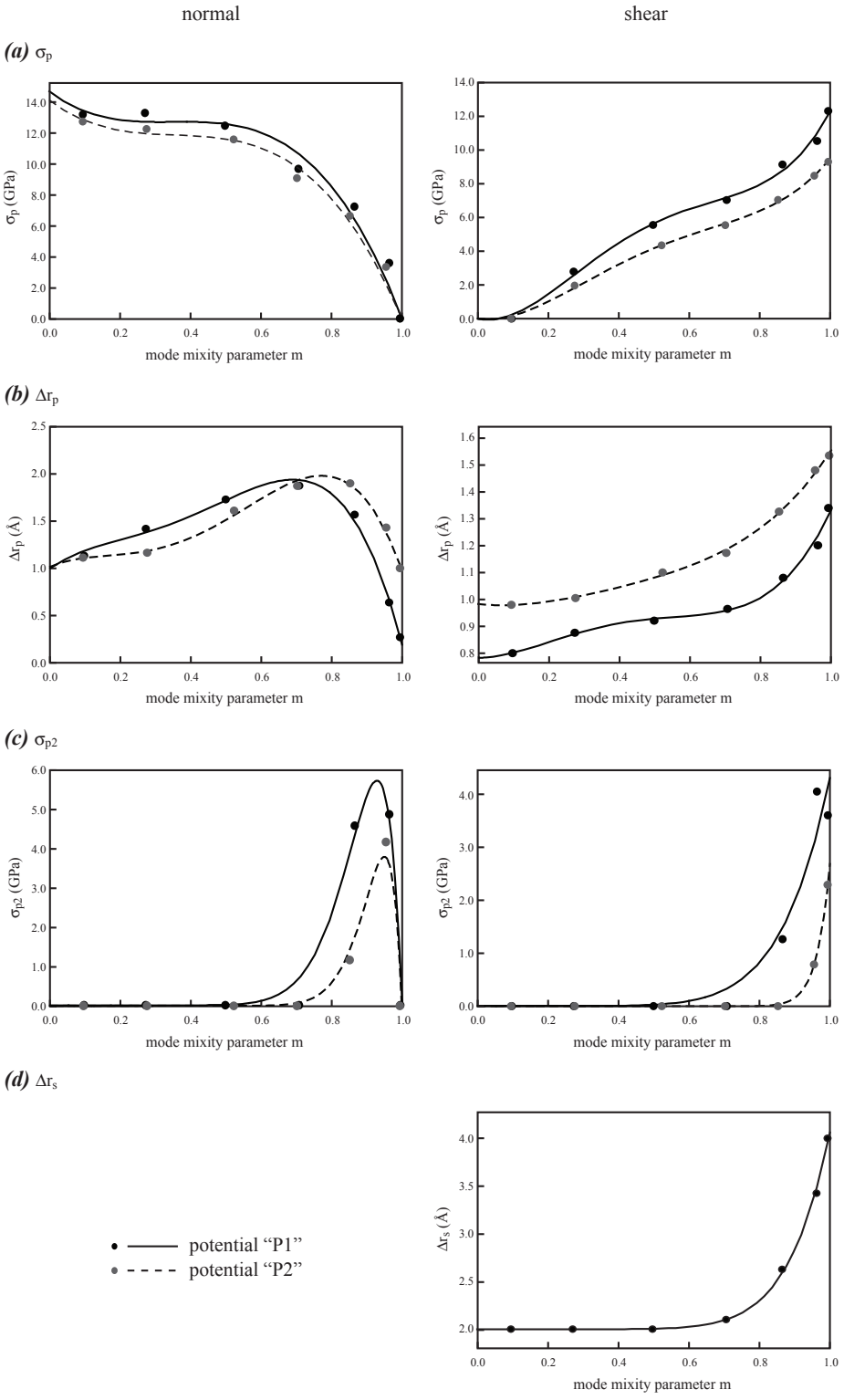

Figure H1. Comparison of the (a) σ_p, (b) Δr_p, (c) σ_{p2}, and (d) Δr_s MD data with analytical prediction.

Chapter 8

Finite element analysis of an atomistically-derived cohesive model for brittle fracture

Principal Authors: Jeffrey T. Lloyd, Jonathan A. Zimmerman, Reese E. Jones, Xiaowang Zhou, and David L. McDowell

In order to apply information from Molecular Dynamics (MD) simulations in problems governed by engineering length and time scales, a coarse graining methodology must be used. In Chapter 7, a traction-separation cohesive model was developed using results from MD simulations with atomistic-to-continuum measures of stress and displacement. Here, we implement this cohesive model within a combined finite element / cohesive surface element framework (referred to as a finite element approach or FEA), and examine the ability for the atomistically-informed FEA to directly reproduce results from MD. We find that FEA shows close agreement of both stress and crack opening displacement profiles at the cohesive interface, although some differences do exist that can be attributed to the stochastic nature of finite temperature MD. The FEA methodology is then used to study slower loading rates that are computationally expensive for MD. We find that the crack growth process initially exhibits a rate-independent relationship between crack length and boundary displacement, followed by a rate-dependent regime where, at a given amount of boundary displacement, a lower applied strain rate produces a longer crack length. Our method is also extended to larger length scales by simulating a compact tension (CT) fracture mechanics specimen with sub-micron dimensions. Such a simulation shows a computational speedup of approximately four orders of magnitude over conventional atomistic simulation, while exhibiting the expected fracture mechanics response. Finally, differences between FEA and MD are explored with respect to ensemble and temperature effects in MD, and their impact on the cohesive model and crack growth behavior. These results enable us to make several recommendations to improve the methodology used to derive cohesive laws from MD simulations. In light of this work, which has critical implications for efforts to derive continuum laws from MD simulations, it is shown care must be taken when using a similar approach, and effects of ensemble, temperature, and strain rate must be considered.

8.1 Introduction

A key challenge to material modeling and simulation is incorporating atomic-level physics into models that can be used at larger scales. One such example is the modeling of multilayered material structures in order to predict their performance and reliability in micro- and nano-scale devices. Often these materials exhibit brittle deformation behavior and failure mechanisms, making them attractive to model with a combined finite element (FE) / cohesive surface element (CSE) methodology. In such an approach, one constitutive relation is used to represent bulk deformation of the materials involved, while another complementary relation is used to model interfacial delamination. Historically, these relations have been phenomenological in their construction, fitted to experimentally determined values of cohesive strength and work of adhesion. At the nano-scale, however, the need arises for including atomic behavior in order to enhance the fidelity of predictive models.

To address this need, much research has recently been done to use atomistic simulations (either molecular dynamics (MD) simulations or quasistatic energy minimization analyses) to motivate the key features of traction-separation laws used with CSE analysis. For example, Spearot *et al.* [175] proposed an internal state variable (ISV) framework that uses interface separation constitutive laws motivated by MD simulations of materials modeled with embedded-atom method [59] (EAM) potentials. These authors considered both normal and tangential displacement loading, and developed a nonlinear elastic separation potential that included path-history dependent effects with active and passive ISV's.

Yamakov *et al.* [206] developed a cohesive surface model using MD simulations of intergranular fracture in an fcc metal, which displays both brittle and ductile fracture mechanisms. These authors developed a robust method to combine estimates of crack opening displacement with normal stress to construct a qualitative model of traction-separation for both mechanisms. This approach was later combined with a statistical method developed by Saether *et al.* [166] to couple an atomistic domain (10^6 atoms, MD, 300 K) that is embedded within a continuum domain [207]. The resulting coupled system was used to derive a cohesive zone model (CZM) for interface debonding via moving averages of stress and opening displacement. While the coupling and averaging methods were quite sophisticated, the resulting CZM consisted of a parameterized bilinear curve fitted only to peak stress and the amount of displacement at full debonding. This work leads one to speculate whether more complex traction-separation laws could be developed using MD simulation results.

These early efforts by Spearot *et al.* and Yamakov *et al.* also set a precedent for using atomistic simulation to derive cohesive laws for fcc metals, known to exhibit ductile behavior in most cases. Others have continued on this path such as Choi and Kim [29], who constructed a cohesive model for single crystal gold, and Krull and Yuan [102], who designed an exponential traction-separation law using parameters derived from MD simulations of crack tip blunting and void initiation. However, it is not clear whether this use of cohesive surface elements is appropriate as the methodology was originally developed to model fracture of brittle material interfaces. This point was recently underscored in work by Fan and Yuen [52], who performed MD simulations and parameterized a cohesive model of an epoxy network material / Cu interface. Their model of

a polymer-ductile metal interface showed poor agreement between simulation and experiment for the force-displacement curve of a deformed tapered double cantilever beam (TDCB). In particular, the so-called valve effect in ductile fracture underscores the importance of modeling cascade effects of crack tip dislocation nucleation [32, 153, 192, 220]. Further complicating this issue is recent work by Song *et al.* [174], who found that dislocation-crack tip interactions do not significantly affect the overall traction-separation response, *i.e.* stress-field interactions with other nearby defects do not alter the cohesive relation measured at the crack tip. Given this uncertainty when dealing with cohesive behavior of ductile materials, we therefore limit consideration here to brittle fracture processes.

Reconsidering cohesive models for fracture of brittle materials (and mindful of the aforementioned models for ductile materials), we note that Coffman *et al.* [33] compared atomistic simulation of Si polycrystal with a CSE simulation using piecewise, bilinear cohesive laws determined from atomistics. Although more appropriate, the application of a CSE to a brittle polycrystalline material showed that matching cohesive properties of interfaces (grain boundary energy and cohesive strength) with a cohesive law of simple form was insufficient to match the failure stresses predicted by atomistic simulation. In an attempt to increase the fidelity of an atomistically-derived cohesive law, Zhou *et al.* [218, 219] used the methodology of Yamakov *et al.* [206] to develop a model for an 'ideal' bcc metal subject to mixed mode loading conditions. This model is innovative as it predicts a mode-mixity dependent work of adhesion, a feature not common to phenomenological cohesive laws.

One issue not addressed in many of the efforts discussed above (including [218] and [219]) is assessing how an atomistically-derived cohesive law behaves once implemented within a pure finite element (FE) / cohesive surface element (CSE) framework. This includes verification analyses that confirm that the law accurately reflects the originating atomistic results. In addition, little has been done to characterize the developed relations in time and length regimes that are at best computationally expensive, and at worst inaccessible, to MD simulation.

In this chapter, we implement one of the cohesive models developed in [219] within a combined finite element / cohesive surface element framework (referred to as a finite element approach or FEA), and verify its performance by examining the original geometry and loading rate used in MD to derive the traction-separation relation. Our analyses show close agreement of both stress and crack opening displacement profiles at the cohesive interface, although some differences do exist that can be attributed to the stochastic nature of finite temperature MD. Our FEA methodology is then used to study slower loading rates that are computationally expensive for MD. We find that the crack growth process initially exhibits a rate-independent relationship between crack length and boundary displacement, followed by a rate-dependent regime where, at a given amount of boundary displacement, a lower applied strain rate produces a longer crack length. We further find that crack velocity at all times remains below the limiting speed above which unstable crack behavior is often noticed, *e.g.*branching. Our method is also extended to a larger length scale by simulating a compact tension (CT) fracture mechanics specimen with sub-micron dimensions. Our simulation shows a computational speedup of approximately four orders of magnitude over conventional atomistic simulation, while exhibiting the expected fracture mechanics response. Finally, differences between FEA and MD are explored with respect to ensemble and temperature effects

in MD, and their effect on the cohesive model and crack growth behavior. These results enable us to make several recommendations to improve the methodology used to derive cohesive laws from MD simulations.

8.2 Methodology

8.2.1 Cohesive law derived from molecular dynamics simulations

The cohesive model used was developed by Zhou *et al.* [219]. In that work, the authors used two sets of interatomic potentials to model a 'weak' interfacial plane between two halves of a bcc (body-centered-cubic) crystal. Here, we consider only the model based on potential 'P1' [219] for which the two halves of crystal possess the same lattice spacing, cohesive energy and elastic moduli. The weak interface has the same lattice spacing as the bulk material, but lower values of cohesive energy, elastic moduli, and work of adhesion. The geometry modeled is that of a rectangular plate of width (x-direction) 800 Å, height (y-direction) 650 Å, and thickness (z-direction) 32 Å. To study the fracture response, a two dimensional crack of length 280 Å was introduced along the center line with the crack tips pointing in the $\pm x$-directions and crack plane normal in the y-direction (as shown in Figure 1 of [219]). MD simulation is used to equilibrate the cracked system at a temperature of 300 K using a Nosé-Hoover thermostat, thereby creating an NVT ensemble. Designated boundary regions were used to induce tensile and shear displacements leading to extension of the center crack, and combinations of these displacements were used to prescribe specific mode mixities. The NVT thermostat continues to enforce a system temperature (excluding boundary regions) of 300 K during this deformation process. Averages of stress and displacement components were calculated within localized volumes adjacent to the interfacial plane at positions behind, at, and in front of the propagating crack tips. Further details regarding the simulations performed and averaging process used to construct a cohesive law can be found in [219]. It should be noted that while the MD simulations performed by Zhou *et al.* did not explicitly prohibit crack tip instability behavior such as oscillations and branching, the design and use of a weak interatomic potential across the interfacial plane may have contributed significantly to enforcing planar propagation.

After a suite of simulations at various mode mixities had been performed in which the traction-separation response along the interface was measured, analytical functions were fit for the normal stress σ_{yy} and shear stress τ_{xy} in terms of the magnitude of crack opening displacement $\delta = \sqrt{\delta_x^2 + \delta_y^2}$ and a mode-mixity parameter $m \equiv \sqrt{\delta_x^2/\delta^2}$:

$$\begin{aligned}\sigma_{yy}(\delta, m) =& F(\alpha, \beta, \sigma_p(m), \delta_p(m), \delta_c, \delta) \\ &+ F(\alpha, \beta, \sigma_{p2}(m), \delta_{p2}, \delta_{c2}, \delta - \delta_s(m)) \cdot H(\delta - \delta_s(m))\end{aligned} \tag{8.1}$$

$$\begin{aligned}\tau_{xy}(\delta, m) =& F(\alpha, \beta, \tau_p(m), \zeta_p(m), \zeta_c, \delta) \\ &+ F(\alpha, \beta, \tau_{p2}(m), \zeta_{p2}, \zeta_{c2}, \delta - \zeta_s(m)) \cdot H(\delta - \zeta_s(m)),\end{aligned} \tag{8.2}$$

where we have assumed the cohesive interface has a normal in the y-direction and undergoes normal (y) or transverse (x) displacement. Here,

$$F(\alpha,\beta,\sigma,\delta_a,\delta_b,\delta) = \frac{\beta^\beta \cdot \delta_a^{\beta-\alpha} \cdot \sigma \cdot \delta^\alpha}{[(\beta-\alpha)\cdot\delta_a + \alpha\cdot\delta]^\beta} \cdot f_c(\delta_a,\delta_b,\delta) \tag{8.3}$$

$$f_c(\delta_a,\delta_b,\delta) = \frac{1}{2}\cdot \text{erfc}\left[3.0972\cdot\frac{\delta-\delta_a}{\delta_b-\delta_a} - 1.64498\right] \tag{8.4}$$

$$\sigma_p(m) = 13.4738\left(1-m^4\right) \tag{8.5}$$

$$\delta_p(m) = 1 + 2.5885\,m - 9.1\,m^2 + 21.4763\,m^3 - 15.774\,m^4 \tag{8.6}$$

$$\sigma_{p2}(m) = 207.9726\,m^{12.9073}\,(1-m) \tag{8.7}$$

$$\delta_s(m) = 2.83 \tag{8.8}$$

$$\tau_p(m) = -4.6725\,m + 86.4059\,m^2 - 148.1626\,m^3 + 78.7212\,m^4 \tag{8.9}$$

$$\zeta_p(m) = 0.7831 + 0.00941\,m + 2.3414\,m^2 - 5.3128\,m^3 + 3.5079\,m^4 \tag{8.10}$$

$$\tau_{p2}(m) = 4.3025\,m^{7.4069} \tag{8.11}$$

$$\zeta_s(m) = 2.0535\,m^{8.6867} + 2.0016 \tag{8.12}$$

$\alpha = 1.18$, $\beta = 8$, $\delta_c = 5.24$, $\delta_{p2} = 1.36$, $\delta_{c2} = 4.38$, $\zeta_c = 8.56$, $\zeta_{p2} = 0.98$, $\zeta_{c2} = 4.4$, $H(x)$ is the Heaviside function, and where all stresses (σ and τ) are in GPa and all displacements (δ and ζ) are in Å.

All functions and parameter values are the same as those given in [219], with the exception of the function given for $\sigma_p(m)$. Refitting of $\sigma_p(m)$ was performed as the existing function from [219] appears to not fit the MD data well at very low mode mixities. Contour plots of Equations (8.1) and (8.2) (as functions of δ_x and δ_y instead of δ and m) are shown in Figure 8.1.

8.2.2 Implementation of cohesive law into a finite element / cohesive surface element framework

The cohesive traction-separation law given in the previous section was implemented in an Abaqus [172] UMAT (User-defined MATerial) for COH2D4 two-dimensional, zero thickness cohesive elements. Because the stress state is directly calculated from the displacements passed into the UMAT from Abaqus, arbitrarily complicated traction-separation laws derived from MD can be implemented with relative ease, making this approach appealing to fitting complex crack tip behavior.

For the finite element model of the bulk material, two-dimensional continuum CPE4 (plane strain) elements were used with isotropic material properties to represent the bulk elastic behavior. Isotropic elastic constants were given in [219] as Young's modulus $E = 444$ GPa, Poisson's ratio $\nu = 0.25$, and shear modulus $G = 177$ GPa. The assumption of isotropic behavior closely

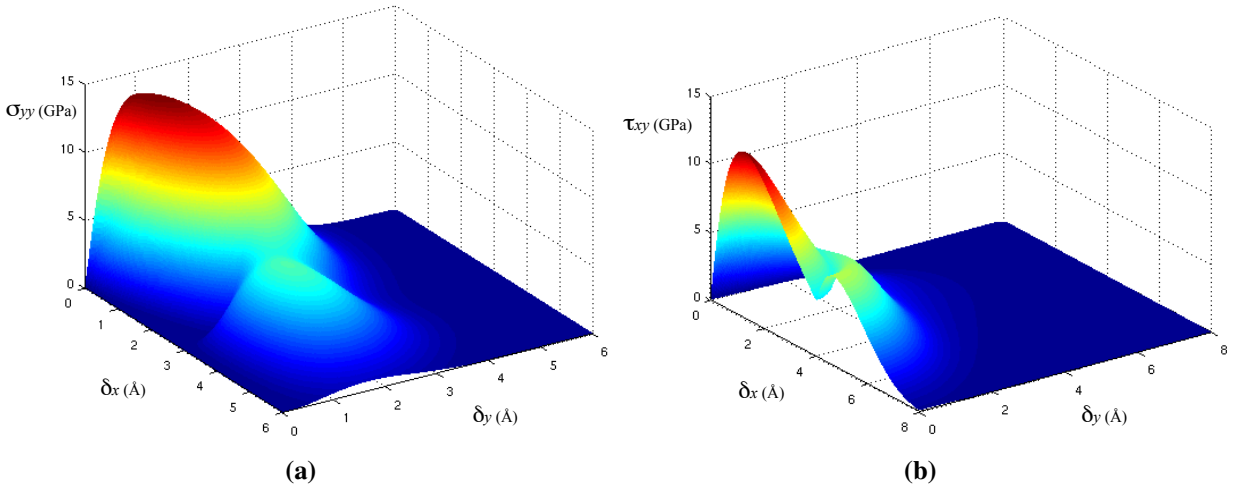

Figure 8.1. Contour plots of (a) normal and (b) shear stress for mixed-mode traction-separation law

approximates single crystal properties as determined from the elastic constants given in [219]. For example, for tension along a $\langle 100 \rangle$ direction, $E = C_{11} - \frac{2C_{12}^2}{C_{11}+C_{12}} = 424$ GPa. Likewise, for pure shear $G = C_{44} = 184$ GPa. The isotropic moduli suggested by Zhou *et al.* differ by less than 5% from these single crystal equivalents. Use of the isotropic assumption is also validated by calculating the anisotropy ratio $A = \frac{2C_{44}}{C_{11}-C_{12}} = 1.095$, a value close to unity.

Zero thickness cohesive elements were used along the predefined crack path along the mid-plane. An implicit dynamic analysis was used in order to ensure conditional stability, in which the loading rate of the boundary corresponded to exactly the same loading rates used in the MD simulations from [219] ($\sim 10^8$ s^{-1}). We used an equivalent density of 10.505 g/cm^3, based on the atomic weight of 100 amu and a lattice spacing of 3.162 Å for a bcc crystal structure, as was used in [219]. We note that since the same mass density is used in both FEA and MD, and as the elastic moduli are very close between the two analysis methods, by using the same loading rate differences in interfacial behavior due to elastic wave propagation are minimized.

For the cohesive law described in the previous section, the normal opening displacement δ_y is assumed to be positive. In the case of compressive loading, an elastic penalty an order of magnitude larger than E is used to prevent surface-surface penetration. In the case of shear loading, the response is not modified with regard to the sign of δ_x, other than producing a shear traction of opposite sign. The contact is assumed "frictionless" in that the shear response does not alter in the case of negative δ_y.

8.3 Results

8.3.1 Crack growth analysis of FEA and MD: direct comparison

Our first objective is to compare the crack opening behavior observed in MD with the analytical relationship implemented into Abaqus. The geometry considered is a rectangular plate of width 800 Å and height 650 Å. Unlike the MD system shown in Figure 1 of reference [219], which was three-dimensional of thickness 32 Å with periodic boundary conditions in the thickness direction, our FEA system is two-dimensional. Our continuum constitutive description is isotropic, with zero thickness cohesive elements inserted along the interface and represented by the dotted red lines in Figure 8.2(b) and 8.3(b). In contrast, the MD system utilized a non-local interatomic potential with a separate potential used for interactions across the cohesive interface of approximate range 4 Å. Both MD and FEA geometries contained a center crack of length 280 Å across which material does not interact (traction free). For our comparison, the system is loaded in pure normal (mode I) or pure shear (mode II) boundary displacement.

For normal loading, the displacement boundary conditions are slightly different in FEA than in MD. In the original MD simulations, loading was applied via a ramped displacement (*i.e.* homogeneous strain) field applied to the entire domain consistent with the boundary conditions in order to mitigate the effects of dynamic wave propagation through the material, as shown in Figure 8.2(a). In contrast, a uniform displacement is applied to nodes at the top and bottom boundary of the FEA system, as shown in Figure 8.2(b). For the horizontal direction boundaries, the MD system is subject to periodic boundary conditions while the FEA system is subject to symmetry boundary conditions. The differences in loading between MD and FEA for normal loading were determined to be negligible, as the MD simulation was re-run with comparable normal direction boundary conditions as the FEA analysis with little difference to the crack propagation response, as will be shown later. This result is anticipated as the velocity of the boundaries, approximately ± 0.0325 Å/ps, is far smaller than the elastic wave speed of the bulk material, about 65 Å/ps. We note that in Figure 8.2, the symbol $\overline{\Delta}_y$ represents the amount of normal displacement applied to the system boundary in contrast to δ_y, which denotes the normal opening displacement at the crack plane. This notation style is also used for transverse displacements ($\overline{\Delta}_x$ and δ_x) associated with shear loading, as shown in Figure 8.3.

For shear loading, in order to most easily replicate the boundary conditions of uniform loading along the center of the crack as was done in MD (shown in Figure 8.3(a)), an FEA model was constructed as seen in Figure 8.3(b) where uniform loading was applied to the edges, and two half cracks exist at the geometry side edges with cohesive elements defining the interface in the middle of the model. For post-processing, the FEA crack geometry is converted back to the same geometry that was used in the MD case using the symmetry of the boundary conditions in order to make a direct comparison between FEA and MD results.

For both normal and shear loading, a time increment of 2.0 ps is used for the implicit analyses performed. At the boundary displacement rate of 0.0325 Å/ps, this produces a displacement increment of 0.065 Å per analysis step.

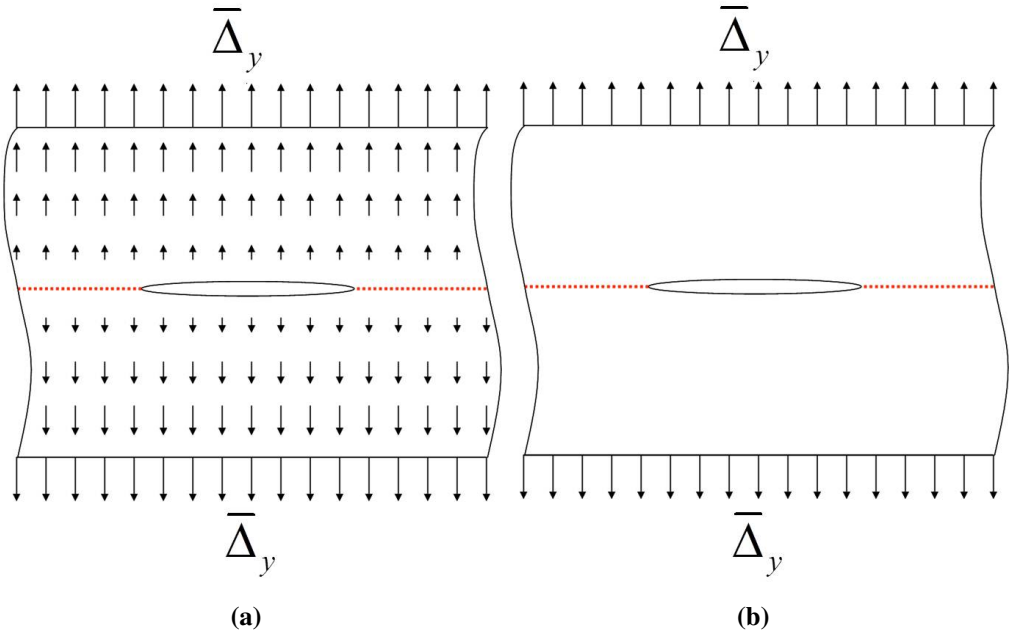

Figure 8.2. Geometry and boundary conditions for (a) MD and (b) FEA analyses - Normal loading.

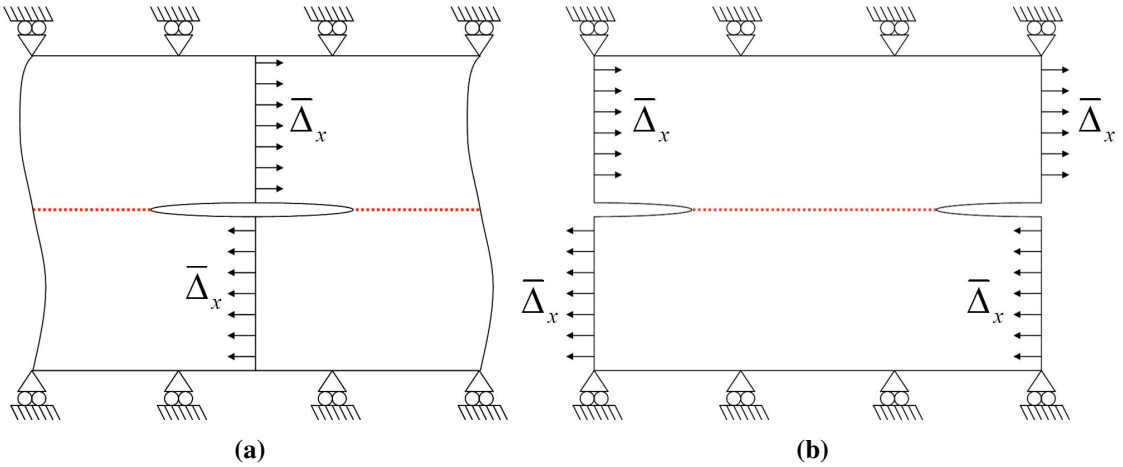

Figure 8.3. Geometry and boundary conditions for (a) MD and (b) FEA analyses - Shear loading.

The FEA system analyzed consists of a regular grid of linear quadrilateral elements 10 Å in height. Two meshes were considered: one with bulk and cohesive elements of width 1 Å, and one with elements of width 10 Å. Both of these meshes satisfy the instability criteria discussed by Foulk [80], namely that the mesh size h must be less than the quantity $h_{\max} = M\phi/\left(2\sigma_{\max}^2\right)$, where M is the relevant elastic modulus, ϕ is the energy required for fracture, and $\sigma_{\max}$ is the peak stress of the traction-separation law. Violation of this condition results in an inability to simulate stable crack growth. For normal loading of our system, $M = E = 444$ GPa, $\phi = 2.98$ J/m^2 and $\sigma_{\max} = 13.47$ GPa, giving $h_{\max} = 36.5$ Å. For shear loading, $M = G = 177$ GPa, $\phi = 4.75$ J/m^2 and $\sigma_{\max} = 12.29$ GPa resulting in $h_{\max} = 27.8$ Å. In addition to ensuring stability, these meshes must be capable of resolving the cohesive zone length. Visual and numerical analysis of the normal loading case reveals an approximate cohesive zone length of 30 Å, whereas for the shear loading case it is closer to 50 Å. Thus, consideration of both resolution and stability predict that both meshes should produce the same stable cohesive behavior. This was verified, as the stress and displacement profiles across the interface were the same for both mesh sizes.

Figure 8.4 shows the crack opening displacement and stress profiles for the case of mode I (normal) loading, where FEA (solid lines) denotes quantities from cohesive and finite elements along the crack plane and MD (dotted lines) denote results taken from the MD simulations performed in [219]. Note that for FEA, only stresses along the cohesive elements are shown as the stress across the cracked region not meshed by cohesive elements is always zero, whereas in MD thermal fluctuations can cause a non-zero measured stress across the crack face. Before the crack begins to grow at an applied remote loading of $\overline{\Delta}_y = 3.250$ Å there is very close agreement between both MD and FEA for the displacement and stress profile distributions across the specimen. After the crack grows in MD at $\overline{\Delta}_y = 4.225$ Å, however, the crack has not yet grown significantly in FEA for this same loading, and requires a larger remote applied loading of $\overline{\Delta}_y = 4.980$ Å in order to grow approximately the same amount. For each case in which the crack lengths are similar, the stress distribution across the interface is very similar, which gives confidence that the MD simulations are being replicated by our FEA model. Nevertheless, we note that the two simulation methods show some disagreement with regard to the amount of boundary displacement at which crack propagation initiates.

Figure 8.5 shows the crack opening displacement and stress profiles for the case of mode II (shear) loading. Here, both the stress and displacement profiles match closely for the case in which the crack has grown by approximately 130 Å ($\overline{\Delta}_x = 7.59$ Å), as well as for the case in which the crack has grown about 270 Å ($\overline{\Delta}_x = 8.45$ Å), almost doubling its initial length. For the left-hand side of the stress profile distribution, there is small disagreement between the FEA and MD; however, this can be clearly attributed to the stochastic nature of MD simulations resulting in the left crack tip initiating propagation earlier (*i.e.* at a slightly smaller boundary displacement) than the right crack tip. We note that stress profile shown in Figure 8.5(b) indicates that material points pass through a local maximum after reaching the peak stress value. This behavior reflects the secondary, lower maximum in the cohesive relation as shown in Figure 8.1.

Our FEA simulations show close agreement with the MD data with regards to both stress and crack opening displacement profiles at the cohesive interface. Simulation of mode I (tensile) loading displays the same stress profile when the crack length is aligned between the two simulation

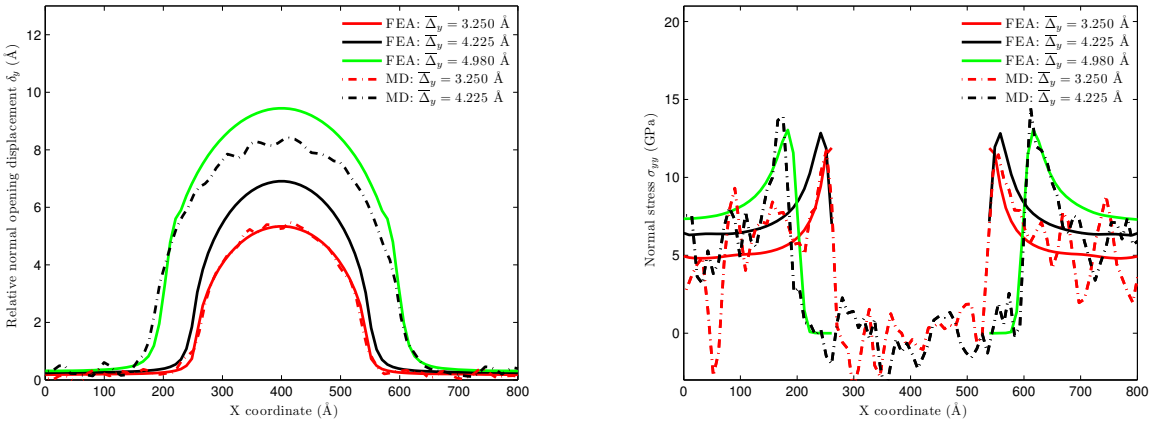

(a) **(b)**

Figure 8.4. (a) Crack opening displacement and (b) normal stress for mode I loading (pre- and post-crack propagation initiation shown).

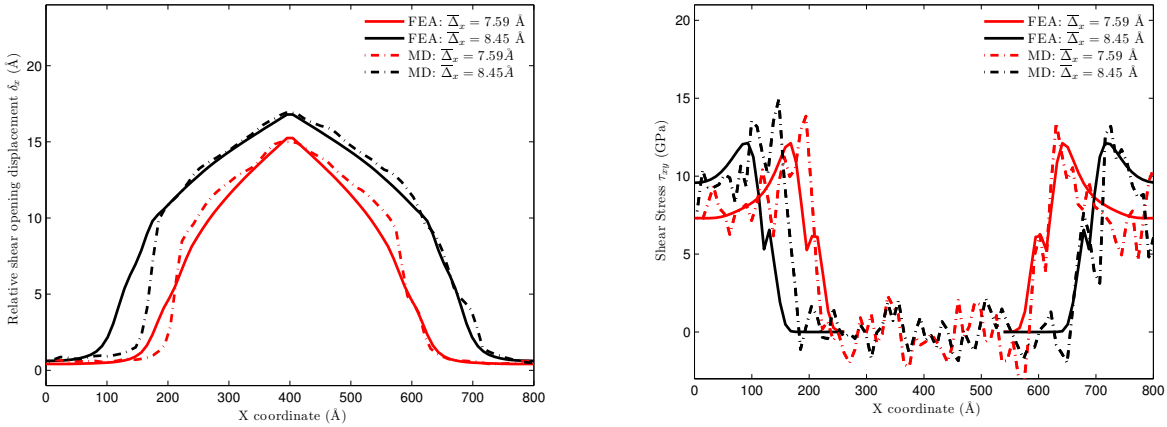

(a) **(b)**

Figure 8.5. (a) Displacement and (b) shear stress for mode II loading (pre- and post-crack propagation initiation shown).

methods, and has reasonable agreement in the crack opening displacement profile. A discrepancy does exist in that crack propagation begins at a lower boundary displacement in the MD simulation than in the FEA simulation. This type of discrepancy also appears for the left crack tip when the system undergoes mode II (shear) loading, albeit to a lesser degree and of opposite trend. That aside, the stress and crack opening displacement profiles for this case show good quantitative as well as qualitative agreement between the two simulation methods. Our results thus far indicate that while some discrepancies exist, there is potential that the FEA can be used to accurately coarse-grain MD behavior of brittle fracture at cracked interfaces.

8.3.2 Analysis of inertial effects

With some confidence that the atomistically informed FEA simulations are modeling the crack opening behavior observed in MD, we now examine simulations in which the computational speedup of FEA is exploited in order to better understand the role of loading rate on the crack growth process. In addition, such a study will hopefully help illuminate if the high loading rate at which the MD simulations were performed affected the parameterization of the cohesive law derived by Zhou *et al.* .

We repeat the FEA simulations discussed in section 8.3.1 with boundary displacement rates varied over two orders of magnitude (10^6/s - 10^8/s) and examine their consequence on the interfacial crack growth behavior. Because the shear loading case showed the best qualitative and quantitative agreement with MD simulations as shown in Figure 8.5, it will be used to examine whether or not rate effects are pertinent when deriving the cohesive law from a high strain rate MD simulation.

Figures 8.6 and 8.7 show crack opening displacement and stress profiles for several strain rates both before and after (respectively) crack propagation begins to occur. Here, strain rate is determined by dividing the boundary loading rate by the half-height of the simulation region. This strain rate represents an average quantity over the simulation region, noting that strain rate actually varies inhomogeneously throughout the system. In Figure 8.6, the profiles for a quasistatic analysis, *i.e.* strain rate of zero, are also shown.

Figure 8.6 clearly shows that there are no significant inertial effects introduced over multiple orders of magnitude. As mentioned earlier, the rates used in the MD simulations (10^8 sec^{-1}) and the others examined here result in boundary displacement velocities that are much lower than the relevant elastic wave speeds of the bulk material. As such, the same displacement and stress profiles are observed at all rates simulated. However, once the crack has started propagating, as shown in Figure 8.7, it is clear that significant inertial effects are introduced and that the crack growth behavior is affected by the loading rate applied.

In order to more directly quantify loading rate effects on crack growth, the crack length is plotted as a function of remote applied displacement for different strain rates in Figure 8.8(a). We note that in Figure 8.8 data is not plotted for crack lengths exceeding a 'threshold' value of 550 Å. This is done as beyond this threshold value, crack growth rate is influenced by the symmetric boundary

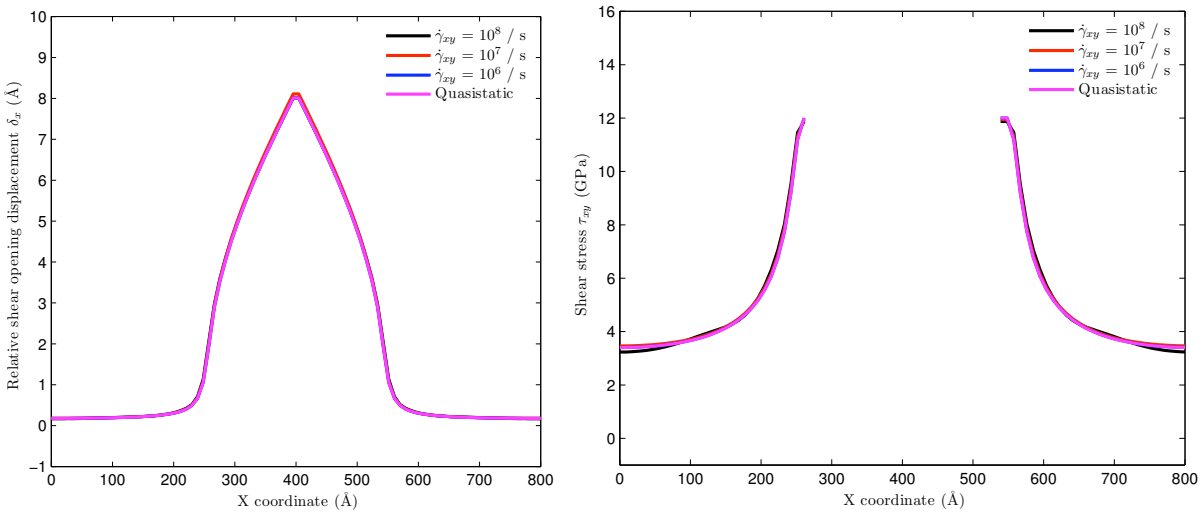

(a) **(b)**

Figure 8.6. (a) Displacement and (b) shear stress profile for mode II loading before crack propagation $\overline{\Delta}_y = 4.0$ Å.

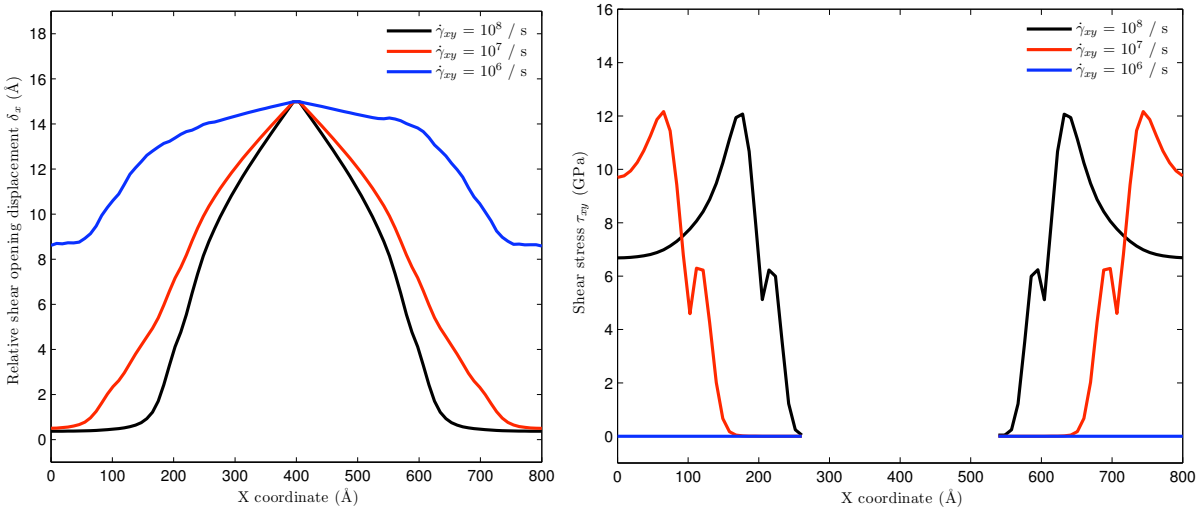

(a) **(b)**

Figure 8.7. (a) Displacement and (b) shear stress profile for mode II loading after crack propagation at $\overline{\Delta}_x = 7.475$ Å.

conditions in the x-direction. Figure 8.8(a) shows that when crack propagation first begins, its rate is not largely affected by strain rate. However, at a boundary displacement of about $\overline{\Delta}_x = 7.0$ Å, smaller loading rates result in a larger crack length for the same remote applied displacement. This trend qualitatively agrees with intuition that as the time that forces have to equilibrate increases (*i.e.* at lower strain rates), the crack growth behavior approaches that of quasistatic loading in which failure occurs immediately after some minimal extent of crack extension.

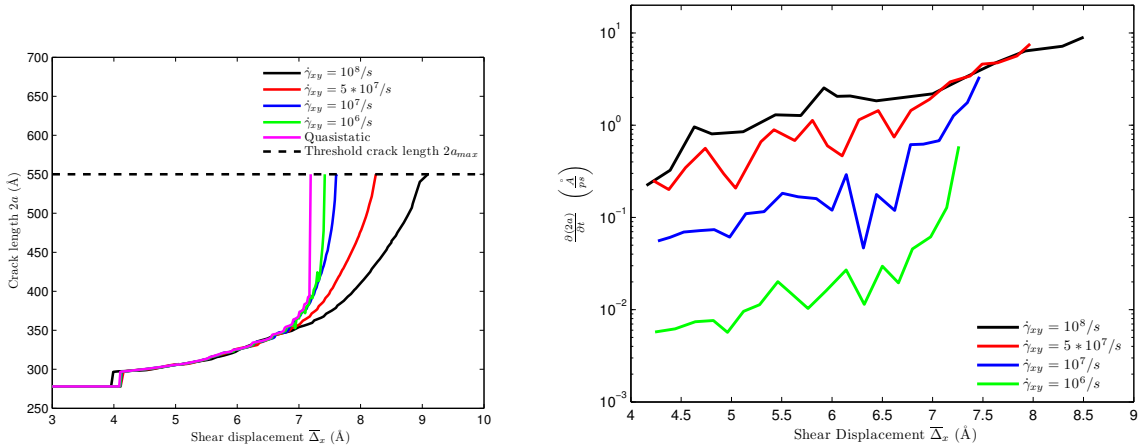

(a) **(b)**

Figure 8.8. (a) Crack length and (b) growth rate for FEA calculations of mode II loading at various loading rates. Subfigure (a) shows that crack propagation begins at a boundary displacement of 4 Å, when the stress within the cohesive elements exceeds the peak stress of the traction-separation law. Crack extension is nearly linear up to a displacement of about 7 Å, after which loading rate-dependent behavior is evident.

Work by Gao [62] and others suggests that cracks in a cohesive medium (such as that modeled by our traction-separation law) will reach a limiting speed of propagation, v_{lim}, above which cracks cease to propagate along a straight line and instead propagate in an oscillatory manner and/or result in branching. Such behavior is not enabled in our FEA, and was not observed to occur in the original MD simulations (as noted in section 8.2.1). The question arises as to whether this observed (for MD) / assumed (for FEA) behavior is physically valid. Figure 8.8(b), which also uses a threshold crack length cutoff of 550 Å, shows the rate of crack growth as a function of amount of boundary displacement. We note here that crack tip speed is half the growth rate for the double-tipped crack.

As suggested by Gao [62], the value of v_{lim} is typically found to be 30-40% of the Rayleigh wave speed, v_R. For our material, v_R = 37.77 Å/ps [151], making v_{lim} in the range 11.3-15.1 Å/ps. Gao also derived an estimate of v_{lim} as equal to $\sqrt{\sigma_{\text{max}}/\rho}$, where σ_{max} is the cohesive strength of the solid and ρ is its mass density. For our cohesive model subjected to mode II loading, $\sigma_{\text{max}} =$

12.29 GPa and $v_{\text{lim}} = 10.82$ Å/ps. Using either criteria, Figure 8.8(b) shows that crack growth in our simulations does not exceed these limits, thereby validating the observed behavior in MD and excusing our FEA from having to add cohesive zone elements along potential branching paths, a complex task. One might ask whether crack speed falling below v_{lim} is a direct consequence of constraining the crack to planar growth, as done in our FEA simulations. However, Abraham and Gao [1] showed that in such cases crack speed can surpass the limiting speed and even reach the longitudinal wave speed of the bulk material.

From the above analysis of Figures 8.6 - 8.8, we note that no rate effects are observed before crack propagation, and only after some threshold amount of crack propagation are rate effects evident. These effects may have some bearing on the traction-separation law derived from MD; however, Zhou *et al.* [219] remarked that local traction and crack opening displacement data used to parameterize the cohesive law were extracted only from a crack propagation length-displacement domain in which the shear crack exhibits approximate steady-state behavior (*i.e.* a nearly linear relationship exists between crack length and boundary displacement). As this domain coincides with the pre-threshold region shown in Figure 8.8(a), we conclude that the cohesive law displays appropriate rate-independent behavior in our FEA simulations. Certainly, more investigation is warranted to understand and verify the correctness of the post-threshold crack propagation behavior observed. For a deeper understanding of brittle fracture rate effects, the reader is referred to the comprehensive review by Marder and Gross [120].

8.3.3 Simulation of compact tension (CT) fracture test

Similar exploitation of the computational efficiency of our FEA can be used to analyze the extension of cohesive behavior derived from MD towards greater length scales. Additionally, in order to model stable crack growth under quasistatic loading, it is necessary to examine a scenario in which the effective stress intensity factor alters as crack growth occurs. Thus, we perform a simulation of crack growth for a compact tension (CT) specimen [11] subject to displacement loading via prescribed motion of loading pins. Fracture of a CT specimen serves as a good proof-of-concept problem to verify that the atomistically-derived cohesive law displays behavior consistent with linear elastic fracture mechanics, while simultaneously showing how much computational savings can be obtained over conventional atomistic simulation.

The geometry and mesh of our CT specimen is shown in Figure 8.9. The specimen is 384 nm wide by $H = 369$ nm tall, with an effective width (the distance between the pin holes and the uncracked edge) of $W = 307$ nm, an initial crack length of $a = 155$ nm ($a/W \approx 0.5$), and pin holes of radius 38.4 nm. Our initial geometry contains a zero-width crack rather than the finite-width notch and fatigue-induced crack used in a conventional CT specimen. Cohesive elements are placed along the pre-defined crack path, and are 1 Å wide. This element size enables the cohesive zone to be resolved over a length of approximately 45 Å (45 elements), and satisfies the stability criterion discussed earlier [80]. The specimen was loaded under displacement control with the pins fixed in the x-direction, and displacements in the $\pm y$-directions of up to 0.5 Å/step applied to the outer nodes of the top and bottom pin holes, respectively. The computational time for this simulation was 12 minutes on a 3.6 GHz Pentium (R) processor with 2 MB of RAM. This speedup

is approximately four orders of magnitude (10^4) faster than a similar MD simulation of the same size, assuming computational cost of the previously mentioned MD simulations is proportional to the number of atoms.

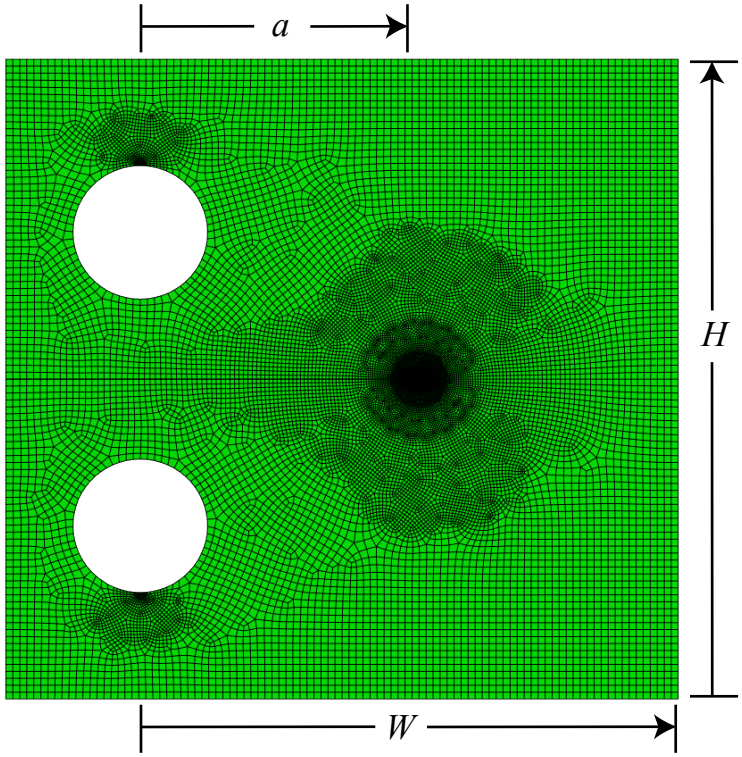

Figure 8.9. FEA mesh of Compact Tension specimen. The specimen's height $H = 369$ nm, its effective width $W = 307$ nm, and its initial crack length $a = 155$ nm ($a/W \approx 0.5$).

The crack opening behavior due to displacement of the top and bottom pins is observed in Figure 8.10. In this figure, the elements are colored according to their values of σ_{yy} as shown in the attached legend. Before crack propagation begins to occur, the cohesive zone begins to form, as seen in Figures 8.10(a) and 8.10(b). Once a critical displacement is reached crack propagation occurs and the mesh resolves the cohesive zone as well as the crack extension behavior as seen in Figures 8.10(c) and 8.10(d).

Figure 8.11 shows the loading-displacement trajectory seen by the top pin. We observe a linear regime before crack propagation, and once crack propagation begins to occur the unloading is reflected in the decrease in force with further displacement. This same trend of linear loading until crack extension is seen in traditional fracture-mechanics tests of brittle specimens and is evidence that there are no significant geometric non-linearities in this system.

We can further verify our analysis by taking the value of peak load in Figure 8.11, 66.21 N/m, and combining it with geometric dimensions of the system to obtain the stress intensity factor,

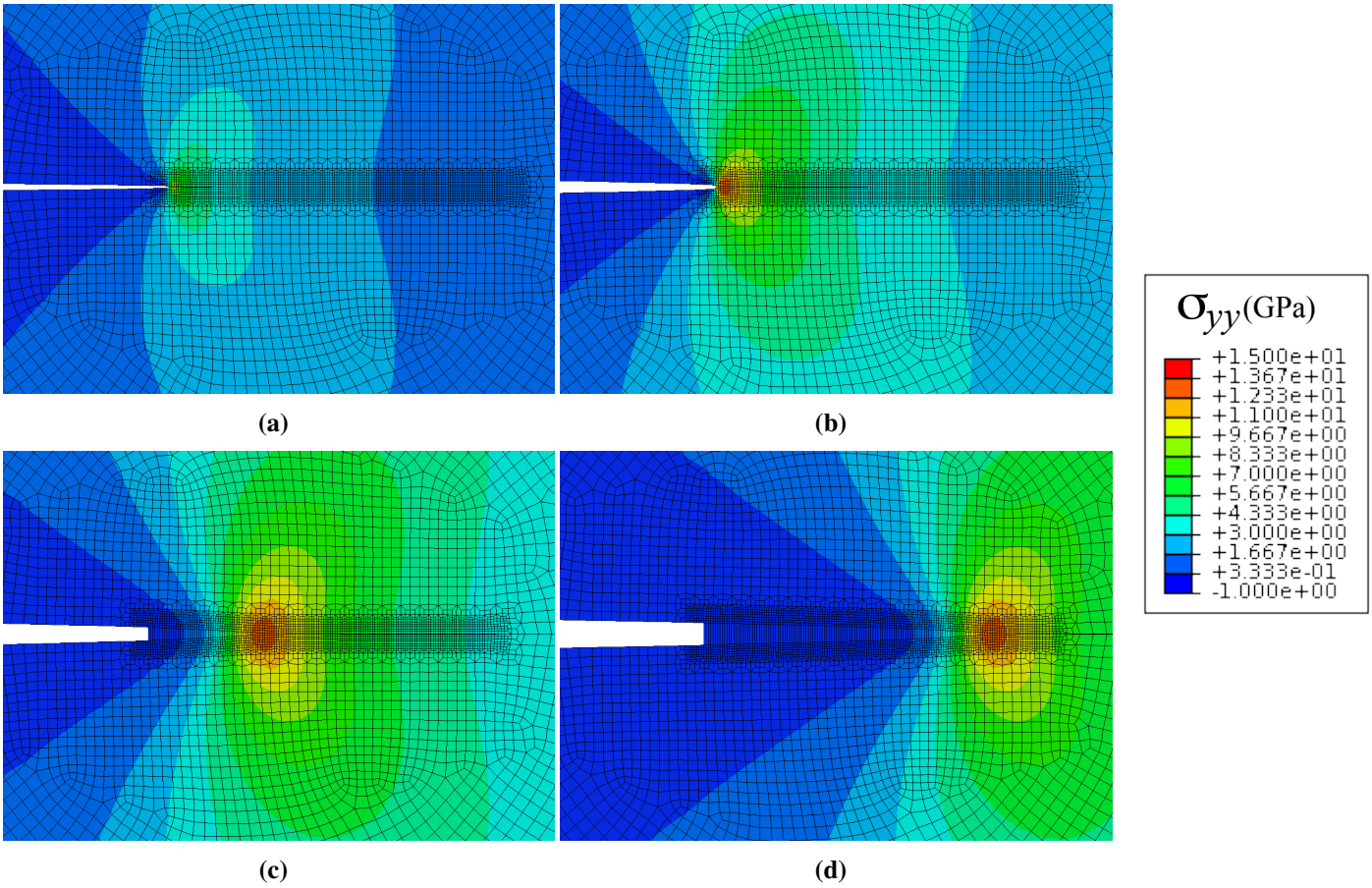

Figure 8.10. Quasistatic crack growth in the CT geometry. Loading-pin displacements of (a) 12.5 Å, (b) 24.0 Å, (c) 35.0 Å, and (d) 36.0 Å are shown. Plots are colored according to element values of σ_{yy} in units of GPa as shown in the legend.

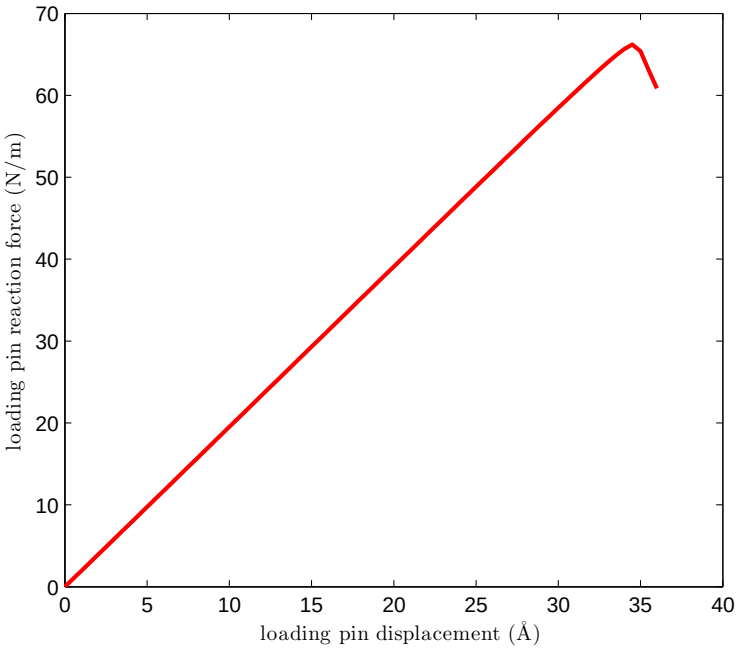

Figure 8.11. Reaction force vs loading-pin displacement for Compact Tension specimen.

K_I = 1.154 MPa $\cdot \sqrt{m}$ [6]. Using the linear elastic fracture mechanics relation between energy release rate and stress intensity factor, $J = K_I^2/E'$ where $E' = E/(1-\nu^2)$, we obtain a value for fracture toughness of $J = J_c = 2.813$ J/m^2. This value lies close to the mode I work of separation, calculated analytically using the relations in section 8.2.1 to be 2.984 J/m^2 (a difference of 5.7%).

Our analysis shows that the atomistically-derived cohesive law gives good agreement with predictions from linear elastic fracture mechanics. It shows the expected linear relationship between loading-pin displacement and reaction force. In addition, the observed peak load results in a fracture toughness estimate close to the work of separation predicted directly from the cohesive model for mode I loading. While certainly more complex fracture geometries can be analyzed (*i.e.* one without a solution known from linear elastic fracture mechanics), our analysis of the CT specimen verifies the correct behavior of both the cohesive law and our finite element implementation.

8.4 Discussion

In our earlier comparison between MD and FEA, we noted that some discrepancies existed in predicting crack propagation with the two methods. For the case of mode I (tensile) loading, crack propagation begins at a smaller boundary displacement in the MD simulation than in the FEA simulation. For mode II (shear) loading, this type of discrepancy also appears for the left crack tip although to a lesser degree and with an opposite trend (*i.e.* the FEA simulation initiates propagation at a smaller boundary displacement than for MD). As thermal effects are absent from the FEA simulations, it is tempting to attribute these discrepancies to such effects. However, it is not sufficient to leave this as simple conjecture. In this section, we present results from additional MD simulations conducted in order to develop some insights on how thermal aspects may affect the derivation of the cohesive law.

MD simulations were performed in a similar manner as described in [219], and the reader is referred to that work for further details. However, for the mode I loading case a uniform displacement is applied to atomic regions at the top and bottom of the system rather than in the ramped fashion previously used. This method of loading is more consistent with that used in our FEA simulations, as noted earlier. As well as performing isothermal (an NVT ensemble) simulations at 300 K, we also conducted isothermal calculations at 100 K. As use of a constraining thermostat to simulate NVT ensembles adds or subtracts energy directly to individual atoms, we also examined the response of constant energy (an NVE ensemble)[1] MD simulations at initial temperatures of 0 K, 100 K and 300 K. As in [219], our simulations were performed using the open-source MD package LAMMPS [168].

Figure 8.12 shows how temperature, ensemble type, and the use of a ramped displacement field (as done in the original MD simulations in [219] and shown in Figure 8.2(a)) affect the crack opening displacement and stress profiles for the normal (mode I) loading case. Note that the

[1]These simulations are not truly constant energy, as work is being done on the system through the displacing boundary regions. However, the equations of motion solved are those for an NVE ensemble, as is customary in much of the molecular dynamics literature.

ramped simulations are labeled as such. This figure shows three trends emerging for the same applied boundary displacement of $\overline{\Delta}_y = 4.225$ Å:

1. Ramping has no significant effect on the interfacial separation behavior.
2. The crack opens in the NVT ensemble before the NVE ensemble regardless of temperature.
3. As temperature decreases, crack opening is retarded for the same applied boundary displacement.

We note that at the chosen displacement of 4.225 Å, crack propagation had already begun in the original NVT-300 K simulation performed in [219].

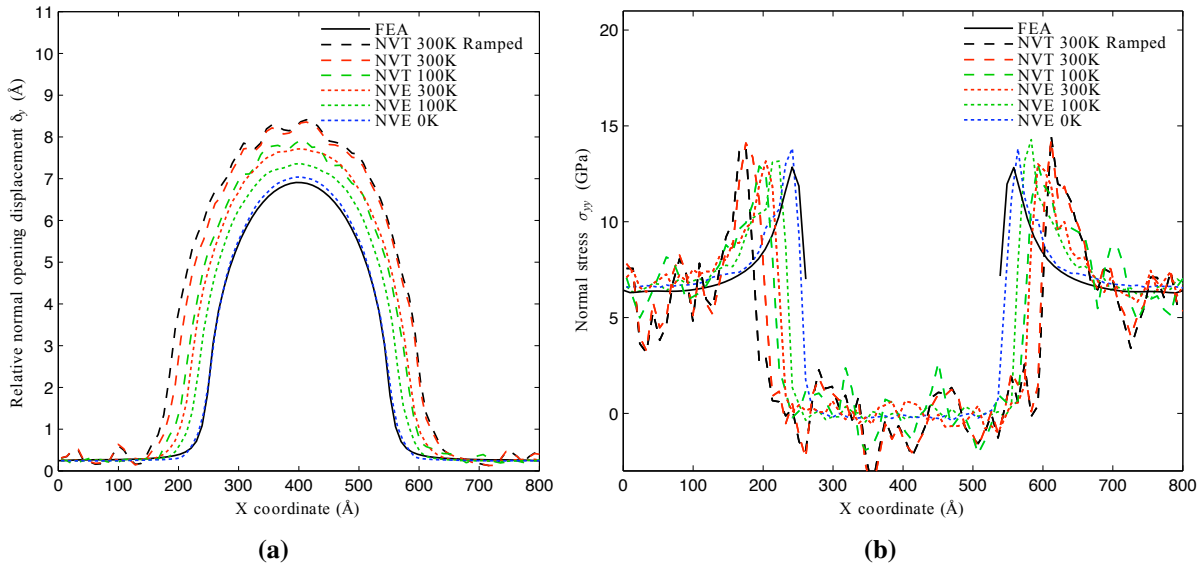

Figure 8.12. (a) Displacement and (b) normal stress profile for mode I loading at $\overline{\Delta}_y = 4.225$ Å for various MD ensembles.

Shear simulations were run with the same variations to temperature and ensemble type and are shown in Figure 8.13 at the applied boundary displacement of $\overline{\Delta}_x = 7.59$ Å. The ensemble and temperature affect the crack growth behavior in a similar fashion as noticed in the tensile simulations, where decreasing temperature retards crack growth and the use of NVT promotes crack growth compared with NVE. However, these figures also show that the FEA response for mode I loading is most similar to the MD simulation for the NVE-0 K system whereas the response for mode II loading is most similar to the MD simulation for the NVT-300 K system. In this regard, the behavior of the shear and normal cases are quite different.

In order to understand the discrepancies between FEA, NVT, and NVE simulations, multiple factors must be considered. It is clear that ensemble type and temperature lead to stress fluctuations that do not exist in FEA. Qualitatively, by looking at the stress distribution across the cracked and

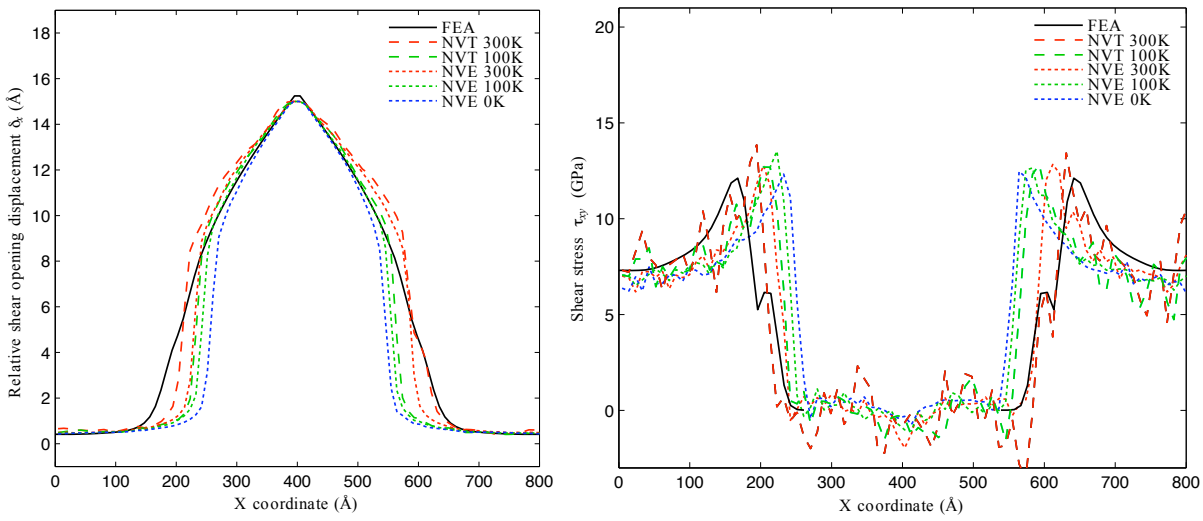

(a) **(b)**

Figure 8.13. (a) Displacement and (b) shear stress profile for mode I loading at $\overline{\Delta}_x = 7.59$ Å for various MD ensembles.

uncracked interfaces in Figures 8.12(b) and 8.13(b), regardless of the two temperatures, the NVT case has larger stress fluctuations than the NVE case. Also, as temperature is lowered, stress fluctuations decrease accordingly for each ensemble. It is clear that these fluctuations play a role in opening the crack that are absent in FEA, but this is not the only contribution. As can be seen from the crack opening stress profile in Figure 8.13(b), the traction profile is also dependent on the ensemble and temperature. The dual maxima observed in the NVT-300 K simulations is not present at lower temperatures or for the NVE ensembles. This observation indicates that the "dual hump" feature of the fitted traction-separation law from reference [219] may have been influenced by the choice of temperature and the use of an NVT ensemble.

Clearly, this analysis shows us that further examination is needed to definitively pinpoint the sources of discrepancy between FEA and MD, and to determine the relationship between temperature, fluctuations of stress and displacement fields, and the functional form and parameterization for a cohesive law. Our findings thus far suggest two possible options to undertake this task. One strategy would be to fit the cohesive law to low/zero temperature simulations to reflect the underlying athermal activation energy barriers for separation and introduce thermally-induced fluctuations as a temperature field in the FEA framework. Recent work by Ryu *et al.* [165] suggests that such energy barriers may include a temperature-dependent entropic contribution. However, using an athermal barrier that can be breached by thermally-induced fluctuations in stress fields would be a significant first step in constructing a more accurate model. Alternatively, one could incorporate temperature dependence into the cohesive law itself, and fit parameters using results from a series of isothermal (NVT) simulations of the temperature range of interest. Both of these strategies try to tackle fundamental discrepancies between aspects that exist in FEA and MD that clearly do not have a one to one correspondence. While further work is warranted, our efforts here have shown

that these issues must be considered when extracting information from MD and using it in any coarse-grained method such as was done with FEA in this work.

8.5 Conclusions and Future Work

In this work, an atomistically-derived cohesive traction-separation relation was implemented in a finite element / cohesive surface approach via an Abaqus [172] UMAT subroutine. The FEA model was compared against the original MD simulations used to design the cohesive relation for simulations of normal (mode I) and shear (mode II) loading of the same center-cracked specimen geometry with similar elastic properties. It shows close agreement with regard to both the stress and crack opening displacement profiles across the interface for the similar externally applied displacements. This reproduction and comparison of MD behavior with FEA has not been commonly done for other atomistically-derived cohesive relations, and presents both a methodology as well as an impetus for doing so. Our analysis also shows that certain discrepancies exist that limit the ability of our FEA model to reflect what happens in finite temperature MD simulations, which are most likely connected to thermal fluctuations of stress and displacement fields that cause the onset of crack propagation in a non-deterministic fashion.

Larger time scales were explored using an FEA model by examining the effect strain rate has on crack growth behavior. An acceptable regime that is relatively strain rate-insensitive was identified, and, since the traction-separation laws from MD were derived in this regime, it is reasonable to use these same laws for stable crack growth problems at lower strain rates. We also verified that while our FEA system is constrained against non-planar crack growth behavior (*e.g.*branching), crack speeds calculated fall below the limiting speed above which such behavior is expected. We acknowledge that more investigation is needed to verify that our model behaves correctly within a regime of displacements that shows a sensitivity to strain rate.

The applicability of this method to larger-than-atomistic length scales was also investigated using simulations of a compact tension fracture test. These simulations show a computational speedup of approximately four orders of magnitude, and produce results consistent with expectations from traditional fracture mechanics analysis. Thus, we believe our approach to be a viable coarse graining methodology. This said, one limitation apparent in our approach is that the cohesive zone length of our model is $\sim$ 10 Å due to its atomistic origins. Further, a stability analysis shows that use of our model to represent stable crack growth requires cohesive surface element sizes no larger than $\sim$ 30 Å. These requirements may induce a heavy computational burden for complex fracture problems with multiple crack paths as compared with phenomenologically-based cohesive laws used in finite element analysis. However, we maintain that the computational cost would still be far less than that for performing full-scale atomistic simulations, while hopefully incorporating the fidelity gained through such simulations.

Several paths and recommendations for future work are apparent based on the work presented here. First and foremost, an examination is warranted of how temperature, ensemble type, and loading rate affect the functional form and parameters of an atomistically-derived cohesive law.

More information regarding the sensitivity of the cohesive law fitting process to these factors is needed. Second, aspects that are not present in conventional finite element / cohesive surface element simulations but are present in MD simulations, such as thermal vibrations and material diffusion, should be incorporated into the FEA depending on the system being modeled. Third, features of material microstructure including crystal orientation and the differentiating structure of grain boundaries have not been considered in the development of the cohesive law. Information on how these features affect cohesion should be included in any advanced models. In addition, the methodology of our finite element approach can be used to compare atomistically-derived cohesive laws with traditional phenomenological relations. On this point, the FEA is best used to investigate brittle fracture phenomena in nanoscale devices. In particular, bcc metals, silicon and other materials commonly used in nanotechnology can be examined with regards to reliability and performance.

8.6 Appendix I: UMAT of atomistically-derived cohesive zone model

```
      SUBROUTINE UMAT(STRESS,STATEV,DDSDDE,SSE,SPD,SCD,
     & RPL,DDSDDT,DRPLDE,DRPLDT,
     & STRAN,DSTRAN,TIME,DTIME,TEMP,DTEMP,PREDEF,DPRED,CMNAME,
     & NDI,NSHR,NTENS,NSTATV,PROPS,NPROPS,COORDS,DROT,PNEWDT,
     & CELENT,DFGRD0,DFGRD1,NOEL,NPT,LAYER,KSPT,KSTEP,KINC)
C
      INCLUDE 'ABA_PARAM.INC'
C
      CHARACTER*80 CMNAME
      DIMENSION STRESS(NTENS),STATEV(NSTATV),
     & DDSDDE(NTENS,NTENS),DDSDDT(NTENS),DRPLDE(NTENS),
     & STRAN(NTENS),DSTRAN(NTENS),TIME(2),PREDEF(1),DPRED(1),
     & PROPS(NPROPS),COORDS(3),DROT(3,3),DFGRD0(3,3),DFGRD1(3,3)

      DIMENSION
     & STRESS0(NTENS) !Stress at beginning of time step


      STRESS0(1) = STRESS(1) !STORE INITIAL STRESSES AT START OF TIME STEP
      STRESS0(2) = STRESS(2) !STORE INITIAL STRESSES AT START OF TIME STEP
      EPS = PROPS(1) !READ IN THE CHARACTERISTIC EPSILON FOR CALCULATING
                     !THE TANGENT STIFFNESS MATRIX. A RULE OF THUMB FROM
                     !ALEJANDRO WAS TO USE ~ (10E-6 * ELEMENT LENGTH)

      !SNPX = NORMAL STRESS AT (DX + EPS,DY)
      !THINK STRESS NORMAL PERTURBED IN THE POSITIVE X
```

```
      !SNMX = NORMAL STRESS AT (DX - EPS,DY)
      !SNPY = NORMAL STRESS AT (DX,DY+EPS) .... ETC
      !STPX = TANGENT STRESS AT (DX+EPS,DY)



      IF ((TIME(2).EQ.0).AND.((DSTRAN(1).EQ.0).AND.
     &  (DSTRAN(2).EQ.0))) THEN !FIRST TIME STEP

C       CALCULATE TANGENT STIFFNESS MATRIX USING NUMERICAL PERTURBATION
        CALL CALC_STRESS_NORM(0+EPS,0,SNPX)
        CALL CALC_STRESS_NORM(0-EPS,0,SNMX)
        CALL CALC_STRESS_NORM(0,0+EPS,SNPY)
        CALL CALC_STRESS_NORM(0,0-EPS,SNMY)

        CALL CALC_STRESS_SHEAR(0+EPS,0,STPX)
        CALL CALC_STRESS_SHEAR(0-EPS,0,STMX)
        CALL CALC_STRESS_SHEAR(0,0+EPS,STPY)
        CALL CALC_STRESS_SHEAR(0,0-EPS,STMY)

        DDSDDE(1,1) = (SNPY-SNMY)/(2*EPS)
        DDSDDE(1,2) = (SNPX-SNMX)/(2*EPS)
        DDSDDE(2,1) = (STPY-STMY)/(2*EPS)
        DDSDDE(2,2) = (STPX-STMX)/(2*EPS)

C        PRINT*,"TIME:", TIME(2)

        STRESS(1)=0
        STRESS(2)=0

C        PRINT*,"SYY:", STRESS(1)
C        PRINT*,"SXX:", STRESS(2)
C        PRINT*,"DX:", DX
C        PRINT*,"DY:", DY

      ELSE !NOT FIRST TIME STEP

        DX = STRAN(2) + DSTRAN(2)
        DY = STRAN(1) + DSTRAN(1)

C       CALCULATE TANGENT STIFFNESS MATRIX USING NUMERICAL PERTURBATION
        CALL CALC_STRESS_NORM(DX+EPS,DY,SNPX)
        CALL CALC_STRESS_NORM(DX-EPS,DY,SNMX)
        CALL CALC_STRESS_NORM(DX,DY+EPS,SNPY)
```

```
        CALL CALC_STRESS_NORM(DX,DY-EPS,SNMY)

        CALL CALC_STRESS_SHEAR(DX+EPS,DY,STPX)
        CALL CALC_STRESS_SHEAR(DX-EPS,DY,STMX)
        CALL CALC_STRESS_SHEAR(DX,DY+EPS,STPY)
        CALL CALC_STRESS_SHEAR(DX,DY-EPS,STMY)

        DDSDDE(1,1) = (SNPY-SNMY)/(2*EPS)
        DDSDDE(1,2) = (SNPX-SNMX)/(2*EPS)
        DDSDDE(2,1) = (STPY-STMY)/(2*EPS)
        DDSDDE(2,2) = (STPX-STMX)/(2*EPS)

C        PRINT*,"TIME:", TIME(2)

        CALL CALC_STRESS_NORM(DX,DY,STRESS(1))
        CALL CALC_STRESS_SHEAR(DX,DY,STRESS(2))


C        PRINT*,"SYY:", STRESS(1)
C        PRINT*,"SXX:", STRESS(2)
C        PRINT*,"DX:", DX
C        PRINT*,"DY:", DY
C        PRINT*,"DDSDDE(1,1):", DDSDDE(1,1)
C        PRINT*,"DDSDDE(1,2):", DDSDDE(1,2)
C        PRINT*,"DDSDDE(2,1):", DDSDDE(2,1)
C        PRINT*,"DDSDDE(2,2):", DDSDDE(2,2)

      END IF

      RETURN
      END


      SUBROUTINE CALC_STRESS_NORM(X,Y,SY)

      IMPLICIT DOUBLE PRECISION (A-H,O-Z)
      DELTA_R = SQRT(X**2+Y**2)
      IF(X.EQ.0) THEN
        TT = 0.0
      ELSE
        TT = (X**2/(X**2+Y**2))**(0.5)
      END IF

C      PRINT*, "TT:", TT
```

```
      IF(Y.LT.0) THEN
        SY = 532.8*Y
      ELSE
        PSI_C = 1.45222
        PSI_P = -1.64498
        ALPHA_N = 1.18
        BETA_N = 8.00
        SIGP_N = 13.4738-13.4738*TT**4        !UPDATED NORMAL STRESS FIT
        SIGP2_N = 207.9726*(TT**12.9073)*(1-TT)
        DELRP_N = 1+2.5885*TT-9.1*TT**2+21.4763*TT**3-15.774*TT**4
        DELRS_N = 2.82
        DELRP2_N = 1.36
        DELRC_N = 5.24
        DELRC2_N = 4.38

        TERM1_N = (DELRP_N**(BETA_N-ALPHA_N)*BETA_N**BETA_N*SIGP_N*
     &    DELTA_R**ALPHA_N)/((DELRP_N*(BETA_N-ALPHA_N)+ALPHA_N*DELTA_R)
     &    **BETA_N)

        TERM2_N = 0.5*ERFC(PSI_P+(PSI_C-PSI_P)/(DELRC_N-DELRP_N)*
     &    (DELTA_R-DELRP_N))

        IF(DELTA_R-DELRS_N.GE.0) THEN
           TMULT_N = 1
        ELSE
           TMULT_N = 0
        END IF

        IF(DELTA_R.GE.DELRS_N) THEN
           TERM3_N = (DELRP2_N**(BETA_N-ALPHA_N)*BETA_N**BETA_N*SIGP2_N*
     &     (DELTA_R-DELRS_N)**ALPHA_N)/((DELRP2_N*(BETA_N-ALPHA_N)+
     &     ALPHA_N*(DELTA_R-DELRS_N))**BETA_N)

          TERM4_N = 0.5*ERFC(PSI_P+(PSI_C-PSI_P)/(DELRC2_N-DELRP2_N)*
     &     (DELTA_R-DELRS_N-DELRP2_N))
        ELSE
           TERM3_N = 0
           TERM4_N = 0
        END IF

        SY = TERM1_N*TERM2_N+TERM3_N*TERM4_N*TMULT_N
      END IF
      !CHANGE SIGN IF NORMAL LOADING IS COMPRESSIVE
      !THIS IS NOT USED IF ELASTIC COMPRESSION IS USED
C      IF (Y.LT.0) THEN
```

```
C        SY = -1*(EXP(-10*Y-2)+1)*SY
C        SY = -1*(EXP(-100*(Y+.03))+1)*SY
C      END IF

       RETURN
       END

       SUBROUTINE CALC_STRESS_SHEAR(X,Y,SX)

       IMPLICIT DOUBLE PRECISION (A-H,O-Z)
       DELTA_R = SQRT(X**2+Y**2)

       IF(X.EQ.0) THEN
         TT = 0.0
       ELSE
         TT = (X**2/(X**2+Y**2))**(0.5)
       END IF

       PSI_C = 1.45222
       PSI_P = -1.64498

       ALPHA_T = 1.18
       BETA_T = 8.00
       SIGP_T = -4.6725*TT+86.4059*TT**2-148.1626*TT**3+78.7212*TT**4
       SIGP2_T = 4.3025*(TT**7.4069)
       DELRP_T = .7831+.009410*TT+2.3414*TT**2-5.3128*TT**3+3.5079*
      &  TT**4
       DELRS_T = 2.0535*(TT**8.6867)+2.0016
       DELRP2_T = 0.980
       DELRC_T = 8.56
       DELRC2_T = 4.40

       TERM1_T = (DELRP_T**(BETA_T-ALPHA_T)*BETA_T**BETA_T*SIGP_T*
      &  DELTA_R**ALPHA_T)/((DELRP_T*(BETA_T-ALPHA_T)+ALPHA_T*DELTA_R)
      &  **BETA_T)

       TERM2_T = 0.5*ERFC(PSI_P+(PSI_C-PSI_P)/(DELRC_T-DELRP_T)*
      &  (DELTA_R-DELRP_T))

       IF(DELTA_R-DELRS_T.GE.0) THEN
          TMULT_T = 1
       ELSE
          TMULT_T = 0
       END IF
```

```
 IF(DELTA_R.GE.DELRS_T) THEN
   TERM3_T = (DELRP2_T**(BETA_T-ALPHA_T)*BETA_T**BETA_T*SIGP2_T*
&  (DELTA_R-DELRS_T)**ALPHA_T)/((DELRP2_T*(BETA_T-ALPHA_T)+
&  ALPHA_T*(DELTA_R-DELRS_T))**BETA_T)

   TERM4_T = 0.5*ERFC(PSI_P+(PSI_C-PSI_P)/(DELRC2_T-DELRP2_T)*
&  (DELTA_R-DELRS_T-DELRP2_T))
 ELSE
   TERM3_T = 0
   TERM4_T = 0
 END IF

 SX = TERM1_T*TERM2_T+TERM3_T*TERM4_T*TMULT_T

 !CHANGE SIGN IF DISP IN SHEAR IS NEGATIVE
 IF(X.LT.0) THEN
   SX = -1*SX
 END IF

 RETURN
 END
```

Chapter 9

An efficient non-reflecting boundary condition constructed via optimization of damped layers

Principal Authors: Reese E. Jones and Christopher J. Kimmer

In this chapter we use analytic and numerical techniques to construct optimal, nearly reflectionless boundary layers for lattice dynamics by tuning the mass, stiffness and damping of those layers. Using a one-dimensional, nearest-neighbor chain as a model system, we obtain new analytical results for the low and high frequency behavior of such boundary conditions, as well as a continued fraction solution for the reflection coefficient of multiple layers. In addition, we obtain optimal parameters for the one-dimensional system and a three dimensional system using wavepackets with normal incidence and compare the results to an implementation of the exact boundary condition in one dimension and optimal versions of the commonly used ramped damping in three dimensions.

9.1 Introduction

The need for reflectionless boundary conditions is clear in any simulation involving waves in a domain that is necessarily finite due to computational resources. Many treatments have been developed for waves in continuous media, e.g. acoustics and elasticity [45] as well as electromagnetics [15]. Here, we are concerned specifically with discrete lattice dynamics and our goal is to develop tuned, computationally inexpensive, easy-to-implement non-reflecting boundary conditions for molecular dynamics (MD) and MD-based multiscale applications that avoids storage of the history of the atomic trajectories and the computation of convolution integrals.

The form of an exact reflectionless boundary condition is known. Adelmann and Doll [2] derived a generalized Langevin equation based on a continued fraction representation [133] that is the exact solution to the problem of reflectionless wave propagation in a semi-infinite one dimensional (1D) chain of atoms. This treatment involves a convolution of a system-dependent kernel with the history of atomic displacements or velocities near the boundary of the system and was subsequently called the time history kernel (THK) when used in multiscale applications [196]. The THK is the optimal solution for propagation in linear media and, with perfect precision arithmetic and an arbitrarily long history, it is reflectionless. For more complex, three-dimensional (3D) systems the

kernel can be determined numerically [22] or analytically [91], although evaluation of the analytical expressions for typical 3D systems remains a challenge. In all cases, the kernel unfortunately has a very slow and oscillatory decay in time and therefore is very expensive computationally.

E and co-workers were apparently the first to form an optimal approximate boundary condition in order to increase efficiency [43]. With their variational boundary condition (VBC), they generalized the problem to finding the optimal coefficients of a finite kernel. The particular form of the VBC subsumes the THK and allows for trade-offs in the length of kernel history versus the number of boundary layers [114]. The coefficients of the terms that comprise the kernel, which is non-local in time and space, are derived based on the minimization of the reflection coefficient across the Brillouin zone. In their perfectly-matched multiscale simulation (PMMS) method [113, 185], Li and co-workers took an alternate approach by forming the discrete analog to the well-known perfectly matched layer (PML) of continuum wave propagation [15]. The discrete PML [113], and its extension MD-PML [65], attempt to create a reflectionless boundary layer by employing complex-valued elastic constants that vary in space. The change in elastic properties allows one to tune the impedance of the boundary condition while introducing dissipation through the damping caused by the imaginary parts of the constants. In the simplest versions of the PMMS method, the impedance matching is not exact although the boundary condition is local in time and consequently relatively simple to implement in existing MD frameworks. However, the method is predicated on determining an optimal damping function which, to date, has not been determined; only *ad hoc* forms of this function have been used. The MD-PML method more closely matches the impedance of the original MD system at the cost of a considerably more complicated, coupled dynamics in the region where the boundary condition is applied. Comparative studies of the various methods can be found in the literature [113, 114, 210].

Our proposed method is also motivated by finding an efficient, optimal approximate boundary condition using essentially the same objective function as Li and E [114], namely the obvious one of minimum average reflection coefficient over a range of frequencies.[1] Unlike E and co-workers we limit ourselves to multi-layer treatments that are local in time, *i.e.* no storage of history nor convolution, in an effort to produce a method that could be applied in an MD simulation without modification of the underlying code. For instance, the proposed method was constructed in the well-known LAMMPS code [150] without modification. It relies on treating the mass, damping constant and stiffnesses of atoms participating in the boundary condition as parameters which may be varied to optimize the reflection coefficient. The optimization process we employed is a combination of analytical and numerical methods for simpler systems and is fully numerical for more complex systems. To this end, we present new results yielding an analytic expression for the reflection coefficient as a function of frequency for an arbitrary boundary condition in a 1D harmonic chain. Moreover, we introduce the use of multiple Gaussian wave-packets in a single MD simulation as a new method for determining the frequency response of the boundary condition. Given the free parameters and dynamics of our simple one-dimensional model system, the boundary layer can be interpreted as a sequence of second order filters. In this context, we observe that the optimal layer is constructed by evenly spacing the zeros of the reflection function

[1] This approach differs from the original work of E and Huang [43] where only the reflection coefficient in the neighborhood of zero frequency was used to determine the damping coefficients.

in the frequency range of interest.[2] This effects a collocation of the reflection function to zero at specific frequencies.

In Section 9.2 we summarize early results for reflection in 1D systems and present new analytical results that represent a considerable generalization of the previous analysis [176]. These expressions are used to derive the behavior of a general boundary condition in the high- and low-frequency limits. In Section 9.3 we put the boundary treatment into practice and apply our numerical optimization scheme. We give some rationale for choosing among the various permutations the modified damped layer can have, *i.e.* modification of mass; spring stiffness, either per atom or per bond; and damping, either per atom or per bond. With 1D simulation results based on a discrete sampling of the reflection spectrum using wave packets, we are able to show good correspondence with the novel analytical results. Then we apply the same methodology to a 3D system with a more complex lattice and introduce the multiple wave-packet method for MD as a novel means to efficiently quantify the behavior of a specific boundary condition. We conclude with discussion of future work including the treatment of general three-dimensional problem where normal incidence on a planar boundary is not assumed.

9.2 1D chain analysis

The model system we consider for analytical treatment is a monatomic, harmonic 1D chain with mass m, nearest-neighbor interactions and spring constant κ. The equation of motion for atom n in the chain, with displacement u_n, is given by

$$m\ddot{u}_n = \kappa(u_{n+1} + u_{n-1} - 2u_n) \tag{9.1}$$

whose Fourier transform determines the dispersion relation

$$\omega(k)^2 = 2\omega_0^2(1-\cos(ka)) = \omega_{max}^2 \sin^2\left(\frac{1}{2}ka\right) \tag{9.2}$$

with the maximum frequency twice the natural frequency of a bond: $\omega_{max} = 2\sqrt{\frac{\kappa}{m}} \equiv 2\omega_0$. Here a is the lattice constant. Periodic boundary conditions allow one to guess that the steady state solution is the real part of

$$u_n = A_i e^{i(kna-\omega t)} \tag{9.3}$$

where A_i is a complex amplitude determining the overall phase of the wave and the energy in the wave (which is proportional to $|A_i|^2\omega^2$). The velocity is simply the real part of $v_n = -i\omega u_n$.

[2] By looking at the reflection minimization problem as a generic optimization problem, this behavior can be understood. An unmodified, fixed boundary gives a reflection function of one for all frequencies. When zeros are added by damping/stiffness/mass modification, these zeros act as collocation points for the reflection function. Since it appears that each damping element adds a single zero at an independent frequency, the optimal solution for a finite number of collocations in minimizing a function that responds in a regular and uniform fashion is to have those collocation points be regularly spaced across the function's finite range.

9.2.1 Reflectionless boundary condition

As mentioned in the Introduction, the time history kernel (THK) [2] is a linear operator on the velocity or displacement history. It effects the linear response of semi-infinite lattice and, consequently, it is a perfectly reflectionless boundary condition for small amplitude waves. The THK is derived by separating an infinite one-dimensional chain into two parts, the explicit ($n \leq 0$) and the implicit ($n > 0$); solving, with transforms, for the trajectories of the implicit half in terms of the trajectories of the explicit half; and then substituting these equations in the equations of motion of the explicit atoms to eliminate unwanted degrees of freedom as in the Mori-Zwanzig formalism [132]. For a nearest-neighbor one dimensional chain, the equation for the last explicit atom (index $n = 0$) is

$$\begin{aligned} m\ddot{u}_0 &= \kappa(u_{-1} - u_0) + \int_0^t \theta(t-\tau)u_0(t)\,d\tau + r \\ &= \kappa(u_{-1} - u_0) + \kappa u_0 - \int_0^t \beta(t-\tau)\dot{u}_0(t)\,d\tau + r_\beta \end{aligned} \tag{9.4}$$

where the kernels are: $\theta(t) = -\frac{2\kappa}{t}J_2(2\omega_0 t) = \dot{\beta}(t)$, and $\beta(t) = \frac{\kappa}{\omega_0 t}J_1(2\omega_0 t)$. Here, J_1 and J_2 are the first order and second order Bessel functions of the first kind, respectively. Note that the terms, $r = \theta(t)\dot{u}_1(0) - \dot{\theta}(t)u_1(0)$ and $r_\beta(t) = r(t) + \beta(t)\dot{u}_1(0)$, that collect the initial conditions are zero if the removed part of the chain is quiescent at $t = 0$.[3] The approach we consider in this work essentially amounts to simplifying the history kernel while not treating the initial conditions, which are temperature-dependent. Consequently, any available method in the literature of treating the finite-temperature effects in these terms could potentially be used without modification in our method. Here we define

$$\bar{\beta} = \int_0^\infty \beta(t)\,dt = \frac{\kappa}{\omega_0} \tag{9.5}$$

and note that $\beta(0) = \kappa$. For a linear chain with a quiescent start, (9.4) reduces to

$$m\ddot{u}_0 = \kappa(u_1 - u_0) - \bar{\beta}\int_0^t \frac{1}{t-\tau}J_1(2\omega_0(t-\tau))\dot{u}_0(\tau)\,d\tau\,. \tag{9.6}$$

It is often approximated as

$$m\ddot{u}_0 = \kappa(u_1 - u_0) - \bar{\beta}\,\dot{u}_0 \tag{9.7}$$

to avoid the convolution integral.

In practice, the integral in (9.4) needs to be approximated by a quadrature based on the discrete time history of the numerical integrator

$$m\ddot{u}_0(i\Delta t) = \kappa\big(u_1(i\Delta t) - u_0(i\Delta t)\big) - \bar{\beta}\sum_{j=0}^{\min(N,i-1)} \frac{1}{i-j}J_1(2\omega_0\Delta t(i-j))\dot{u}_0(j\Delta t) \tag{9.8}$$

where Δt is the time step and the current time $t = i\Delta t$. As we see in Figure 9.1, the performance of the THK truncated at a finite length degrades with decreasing kernel size N and eventually behaves

[3] We are not considering thermalized lattices in this work.

like a simple damped boundary condition. Here we have defined the reflection coefficient as the ratio of reflected energy to incident energy as a function of frequency of the incident waveform. It is also noteworthy that the high-frequency response is considerably worse than the low-frequency response. Finally, we remark that this boundary condition in 1D requires storage of order N and additional floating point operations of order N at each timestep. Moreover, as the timestep Δt is decreased, N must be increased in inverse proportion to Δt in order to achieve similar performance to the $N = 2000$ case pictured here. In three dimensions, the scaling is the same, although the absolute storage required and computational expense is greater. In contrast, the method we propose below is independent of the time-step and requires additional storage and computation of order the number of boundary layers used, which will typically be a much smaller integer than the history kernel length.

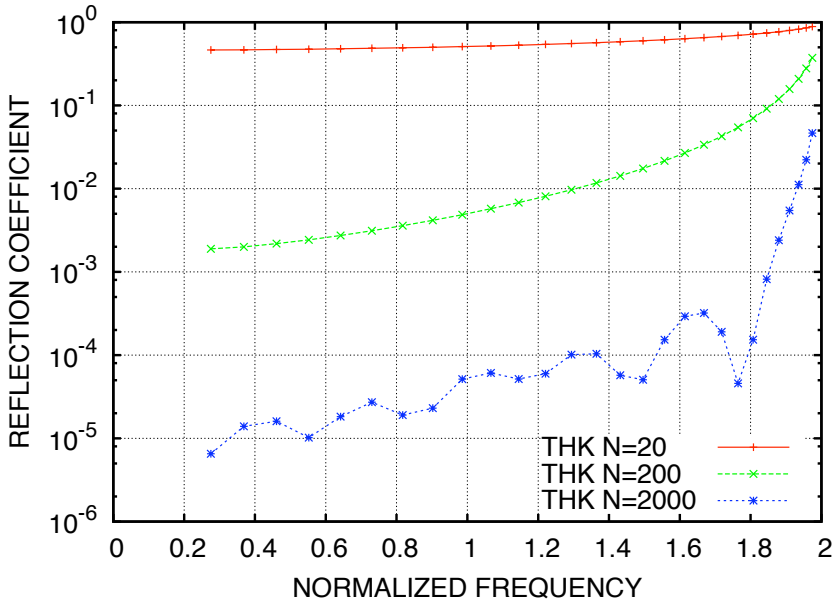

Figure 9.1. (Color online) Comparison of the (energy) reflection coefficient as a function of frequency for truncated, finite THKs of varying convolution length. Frequencies have been normalized by ω_0.

9.2.2 Interfaces

An imperfect boundary condition will inevitably create a change of impedance at the interface between the explicit region $n < 0$ where the dynamics are important and the implicit region $n \geq 0$ which tries to mimic a semi-infinite chain. Scattering off an interface between regions with different force constants has been solved algebraically. For an interface at $n = 0$ between regions

with force constants κ and κ_+ Eq. 9.1 becomes

$$m\ddot{u}_n = \kappa(u_{n+1} + u_{n-1} - 2u_n), \qquad n < 0 \tag{9.9}$$
$$m\ddot{u}_0 = \kappa(u_{-1} - u_0) + \kappa_+(u_1 - u_0) \tag{9.10}$$
$$m\ddot{u}_n = \kappa_+(u_{n+1} + u_{n-1} - 2u_n), \quad n > 0. \tag{9.11}$$

The solution to these equations was first presented in the literature by Steinbrüchel [176], whose approach we summarize here. For an incident wave traveling from negative n in the direction of increasing n, the ansatz is

$$u_n = \mathrm{e}^{\mathrm{i}(k_i na - \omega_i t)} + R\mathrm{e}^{\mathrm{i}(k_r na - \omega_r t)}, n < 0 \tag{9.12}$$
$$u_n = T\mathrm{e}^{\mathrm{i}(k_t na - \omega_t t)}, \qquad n \geq 0. \tag{9.13}$$

Continuity of displacement and its time derivatives for all times yields the condition

$$\omega_i = \omega_r = \omega_t \equiv \omega \tag{9.14}$$

while the dispersion relation for $n < 0$ yields

$$k_r = -k_i. \tag{9.15}$$

The wave vector of the transmitted wave is determined by the condition of equal frequencies using the dispersion relations of the two semi-infinite crystals so that we finally have

$$u_n = \mathrm{e}^{\mathrm{i}(k_i na - \omega t)} + R\mathrm{e}^{\mathrm{i}(-k_i na - \omega t)}, n < 0 \tag{9.16}$$
$$u_n = T\mathrm{e}^{\mathrm{i}(k_t na - \omega t)}, \qquad n \geq 0. \tag{9.17}$$

Using Eq. 9.9 for $n = -1$, substituting in the ansatz of Eqs. 9.16 and 9.17, and using $m\omega^2 = \kappa(\mathrm{e}^{\mathrm{i}k_i a} + \mathrm{e}^{-\mathrm{i}k_i a} - 2)$ yields a statement of displacement continuity at the interface

$$1 + R = T. \tag{9.18}$$

Eq. 9.10 with similar substitutions of the ansatz and the dispersion relation for the semi-infinite crystal with force constant κ_+ yields

$$T\left[\kappa_+\left(\mathrm{e}^{\mathrm{i}k_t a} - 1\right) + \kappa\right] = \kappa\left(\mathrm{e}^{-\mathrm{i}k_i a} + R\mathrm{e}^{\mathrm{i}k_i a}\right). \tag{9.19}$$

There are now two equations (9.18) and (9.19) in two unknowns, T, R, which give the amplitude of the reflected wave

$$R = \frac{\kappa\left(1 - \mathrm{e}^{-\mathrm{i}k_i a}\right) + \kappa_+\left(\mathrm{e}^{-\mathrm{i}k_t a} - 1\right)}{\kappa\left(\mathrm{e}^{\mathrm{i}k_i a} - 1\right) - \kappa_+\left(\mathrm{e}^{-\mathrm{i}k_t a} - 1\right)}. \tag{9.20}$$

9.2.3 A Single Boundary Layer

A central idea of non-reflecting methods is that the response of a large, effectively semi-infinite region $n \geq 0$ to incoming waves can be approximated by an appropriate boundary condition acting on

a small portion of this region. To this end, we consider the effect of replacing the semi-infinite region with force constant κ_+ (i.e all $n \geq 0$) by a series of so-called "boundary layers" with modified mechanical and elastic properties, see Figure 9.2. When these modifications yield linear equations of motion, a similar method to Steinbrüchel's allows the determination of the reflections from this boundary region. For instance, if viscous damping only is applied to this terminating atom at $n = 0$ Eq. 9.10 becomes

$$m_0 \ddot{u}_0 = \kappa(u_{-1} - u_0) - \gamma \dot{u}_0 \tag{9.21}$$

On the other hand, if the boundary atom is also bonded rigidly to a fixed atom, *i.e.* to maintain the lattice constant and prevent relaxation at the terminating layer, Eq. 9.10 becomes

$$m_0 \ddot{u}_0 = \kappa(u_{-1} - 2u_0) - \gamma \dot{u}_0 \tag{9.22}$$

Indeed, these equations are specific cases of the general equation of motion

$$m_0 \ddot{u}_0 = \kappa(u_{-1} - u_0) + \lambda u_0 - \gamma \dot{u}_0, \tag{9.23}$$

where an elastic force with force constant λ and a viscous damping force with damping constant γ acts on the boundary particle.

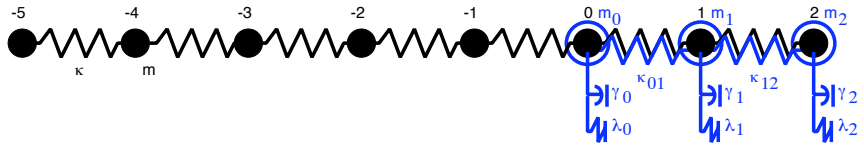

Figure 9.2. (Color online) 1D chain of atoms with nearest neighbor interactions where properties of the atomic layers for $n \geq 0$ have been modified.

To determine R for these boundary conditions, one recognizes that for an incident wave traveling in the direction of increasing n, the ansatz is unchanged from Eqs. 9.12 and 9.13. Substituting the ansatz into the equation of motion for $n = -1$ yields Eq. 9.18 again so that the displacement of atom 0 is now known in terms of R. Substituting into the equation of motion for $n = 0$ and solving for R yields:

$$R = \frac{\kappa\left(1 - \frac{m_0}{m}\right)\left(1 - e^{-ik_i a}\right) + \kappa\frac{m_0}{m}\left(e^{ik_i a} - 1\right) - \lambda - i\omega\gamma}{\kappa\left(1 - \frac{m_0}{m}\right)\left(e^{ik_i a} - 1\right) + \kappa\frac{m_0}{m}\left(1 - e^{-ik_i a}\right) + \lambda + i\omega\gamma}. \tag{9.24}$$

In the case where $m_0 = m$ and for the specific ω that satisfies $\lambda + i\omega\gamma = -\kappa_+(e^{-ik_t a} - 1)$, the boundary condition has matched the impedance of the semi-infinite region with lattice constant κ and Eqs. 9.20 and 9.24 are equivalent expressions. Only for this particular frequency will the boundary condition have a zero reflection coefficient $R(\omega) = 0$.

For a multiscale simulation, the response of the boundary to long wavelength (*i.e.* continuum-scale) excitations may be of particular concern. In the limit of zero frequency, $e^{\pm ik_i a} \sim 1 \pm i\omega ca$

where $c \equiv a\omega_0$ is the speed of sound in the 1D material. Eq. 9.24 becomes

$$R = \lim_{\omega \to 0} \frac{i\kappa\omega ca - \lambda - i\omega\gamma}{i\kappa\omega ca + \lambda + i\omega\gamma}, \tag{9.25}$$

indicating that the presence or absence of an elastic force at the boundary governs the long-wavelength response of the boundary *irrespective of the value of the mass* m_0. Specifically, a non-zero elastic force λu_0 leads to $R(\omega = 0) = -1$ indicating an inversion of the wave at the boundary while $\lambda = 0$ yields a value less than 1 for $\gamma > 0$ (i.e. for dissipative damping). Similarly, the short-wavelength, high-frequency limit occurs when $k_i a = -\pi$ and $\omega = \omega_{max}$ yielding

$$R = \lim_{\omega \to \omega_{max}} \frac{2\kappa - 4\kappa\frac{m_0}{m} - \lambda - i\omega\gamma}{-2\kappa + 4\kappa\frac{m_0}{m} + \lambda + i\omega\gamma} = -1. \tag{9.26}$$

This result shows that complete reflection (accompanied by inversion) of the highest-frequency waves occurs independently of the parameters chosen for the boundary condition.

Figure 9.3 shows the frequency response of a chain of atoms where the addition of a harmonic well, $\lambda > 0$, at the end of the chain creates a zero in $R^2(\omega) \equiv |R(\omega)|^2$ near the middle of the Brillouin zone. We also see that $R^2(0) = 1$ and $R^2(\omega_{max}) = 1$, as predicted. By examining the form of the THK (9.6), we see that the stiffness of the THK goes to zero for slow disturbances, *i.e.* $\omega \to 0$. Clearly, the addition of a harmonic well at the end of the chain does not have this property. The choice of what modifications to the boundary layers are optimal will be treated more fully in Section 9.3.

9.2.4 Multiple Boundary Layers

A straightforward extension of Steinbrüchel's method can be used to determine the reflected amplitude for a more general, and more typical, system with a multiple-layer boundary region terminating the chain. However, the algebra quickly becomes cumbersome as the number of boundary layers increases, and one must consider the different dispersion relations accompanying any change in the elastic properties of a layer in the boundary region. Here we show that a simpler method may be used to solve the general problem when one need only determine the value of the reflection coefficient R.

For a series of N damped layers, take the interface between the undamped and damped layers once again to be at $n = 0$. The boundary region is specified by the N equations of motion

$$\begin{aligned}
m_0\ddot{u}_0 &= \kappa(u_{-1} - u_0) + \kappa_{0,1}(u_1 - u_0) + \lambda_0 u_0 - \gamma_0 \dot{u}_0 && (9.27)\\
&\vdots \\
m_n\ddot{u}_n &= \kappa_{n,n+1}(u_{n+1} - u_n) + \kappa_{n-1,n}(u_{n-1} - u_n) + \lambda_n u_n - \gamma_n \dot{u}_n && (9.28)\\
&\vdots \\
m_{N-1}\ddot{u}_{N-1} &= \kappa_{N-2,N-1}(u_{N-2} - u_{N-1}) + \lambda_{N-1} u_{N-1} - \gamma_{N-1}\dot{u}_{N-1}. && (9.29)
\end{aligned}$$

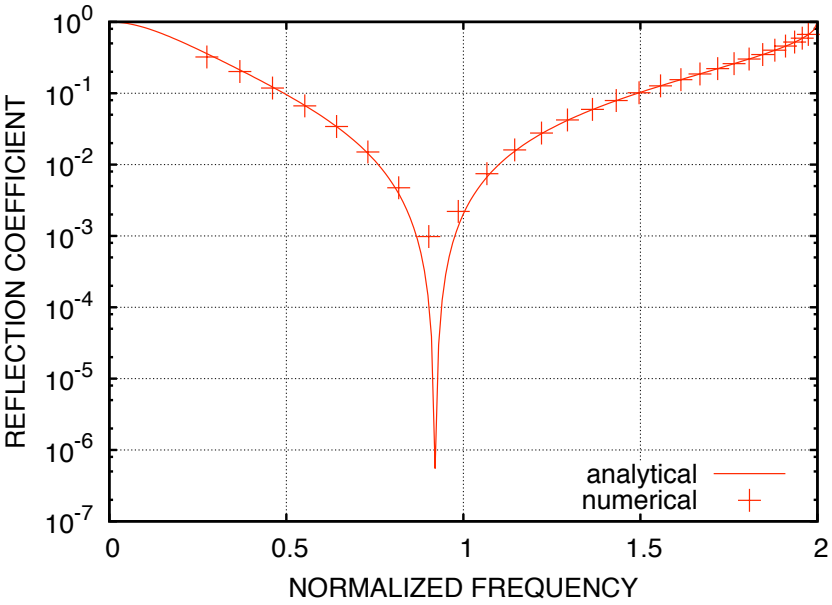

Figure 9.3. (Color online) The reflection coefficient R^2 as a function of frequency for a chain with a terminal spring $\lambda = 0.4235\,\kappa$ and damper $\gamma = 0.8866\,\tilde{\beta}$, which happens to be the optimal boundary condition of this type. Frequencies have been normalized by ω_0.

The N layers are considered to have arbitrary bond stiffnesses $\kappa_{i,j} = \kappa_{j,i}$ as well as arbitrary single-body forces (elastic + viscous) and arbitrary masses m_i. In this manner, one has considerable freedom to optimize the boundary condition with respect to these parameters, tailoring it to the desired properties.

For the Steinbrüchel method the ansatz of Eq. 9.12 is unchanged, recognizing that R is the superposition of the waves reflected at the interface between atom -1 and 0, 0 and 1, 1 and 2, ... $N-2$ and $N-1$. Eq. 9.13 is correct for only the terminating atoms and is consequently generalized to the following N ansatzes

$$u_n = T_n e^{i(k_n na - \omega t)} + R_n e^{i(-k_n na - \omega t)}, \;\; 0 \leq n < N-1 \tag{9.30}$$

$$u_{N-1} = T_{N-1} e^{i(k_{N-1}(N-1)a - \omega t)}. \tag{9.31}$$

where it should be noted that the wave with amplitude T_n propagates in the positive x direction and the one with amplitude R_n propagates in in negative x. These equations can be solved algebraically; simplifications abound because the phase factors $e^{\pm k_n na}$ always occur as a factor with T_n (upper sign) or R_n (lower sign). However, if one is only interested in R, as is the case here, then the displacements u_n may simply be eliminated beginning with u_{N-1} and ending with u_0 to determine R. For this solution, the initial relation of Eq. 9.18 is replaced by

$$1 + R = R_0 + T_0 \tag{9.32}$$

when Eqs. 9.16 and 9.30 for $n = 0$ are substituted into Eq. 9.9. Rewriting u_{N-1} in terms of u_{N-2} via Eq. 9.29 yields

$$u_{N-1} = \frac{\kappa_{N-2,N-1}}{(\kappa_{N-2,N-1} - m_{N-1}\omega^2 - \lambda_{N-1} - i\omega\gamma_{N-1})} u_{N-2} \equiv G_{N-1} u_{N-2}. \tag{9.33}$$

Indeed, u_n may generally be written in terms of u_{n-1} as

$$u_n = G_n u_{n-1}, \;\; 0 \leq n \leq N-1. \tag{9.34}$$

The functions G_n are determined from the recurrence relation

$$G_n = \frac{\kappa_{n-1,n}}{(\kappa_{n-1,n} + \kappa_{n,n+1}(1 - G_{n+1}) - m_n\omega^2 - \lambda_n - i\omega\gamma_n)}, 0 \leq n < N-1 \tag{9.35}$$

which is a continued fraction in the functions G. The recursion is terminated using G_{N-1} given in Eq. 9.33 or alternatively by defining $G_N \equiv 1$ and using Eq. 9.35. Finally, given $u_0 = G_0 u_{-1}$ along with u_0 and u_{-1} being known in terms of R, one has

$$R = \frac{G_0 e^{-ik_i a} - 1}{1 - G_0 e^{ik_i a}}. \tag{9.36}$$

In the high-frequency limit $\omega \to \omega_{max}$ we have $\exp^{\pm ik_i a} \to -1$ once again yielding $R \to -1$ irrespective of the parameters used for the boundary region.

9.3 Optimization of damped layers

The analytical results from the previous section can be used to study the 1D chain in great detail, but their applicability to typical 3D systems of interest is more limited. In this section we determine the optimal parameters for various types of boundary conditions using our analytical results as well as numerical techniques that will be introduced in this section.

We first apply the purely analytical results of the previous section to the PMMS/PML method [113, 185] in order to determine optimal damping functions for that method. We then turn to molecular dynamics (MD) [5] simulations in both one (1D) and three dimensions (3D). We employ Gaussian wave-packets to sample $R(\omega)$ and then use this information to optimize the parameters of a particular boundary treatment. Our technique uses wave-packets at many frequencies in the same simulation for efficient sampling.

Briefly, MD uses Newtonian dynamics with a numerical integration (in our case velocity Verlet) to simulate the particle trajectories subject to interatomic forces, see *e.g.* Frenkel and Smit's text [60]. The first MD system we consider is a simple chain with a monatomic basis. The second system is a 3D silicon crystal with a "long" direction along the x-axis and periodic boundary conditions in the $y-$ and $z-$ directions. The interface between atoms of interest and the atoms for the boundary condition lies in the $y-z$ plane at the high x end of the simulation cell. For the excitations studied here, the 3D system is analogous to the 1D system although its dynamics are more complex.

Each optimization is used to validate the next. We use the optimal, analytically derived 1D damped boundary condition to validate the numerical results that are derived independently using the wave-packet method. With the wave-packet method we treat a richer set of configurations of the boundary layer and we carry over the best of these treatments to the 3D system. The 3D system is then used to test the applicability of this method to a more typical system of interest.

9.3.1 Minimization of the reflection coefficient

Here we define the optimum set of parameters $\mathcal{P}$ to be that set which minimizes $\overline{R^2}$, the average value of $R^2(\omega)$ over the Brillouin zone. This is certainly not the only possible definition; but it is the simplest which incorporates information about the performance of the boundary condition across the entire frequency spectrum. Alternatively, one may wish to focus on performance in a specific frequency band or one may consider thermal systems where it may be more appropriate to compute thermodynamic averages and incorporate the density of states.

Although $R(\omega)$ is known analytically for the 1D case, the integral of R over frequency is not, so we use numerical integration to determine $\overline{R^2}$ and to optimize this value as a function of the free parameters. The actual values of R for any frequency ω may be determined directly from analytical

expressions or using wave-packet MD simulation. Formally, the optimization problem is given by

$$\min_{\mathcal{P}} \overline{R^2} \equiv \min_{\mathcal{P}} \frac{1}{\omega_{max}} \int_0^{\omega_{max}} R^2(\omega)\, d\omega \approx \min_{\mathcal{P}} \frac{1}{\sum_i \Delta\omega_i} \sum_i R^2(\omega_i)\, \Delta\omega_i \tag{9.37}$$

where the rightmost expression is appropriate for the discrete sampling inherent in numerical integration methods. This is a nonlinear optimization which we perform with a local optimizer (a Newton-Raphson variant with a finite-difference Hessian). The solution to any local optimization scheme depends on the starting set of parameters. Hence, as we determine the optimal solutions for a sequence to treatments of increasing number of layers, we use the previous solution for a similar treatment with fewer layers (and parameters) which is subsumed in the current treatment. In addition, we bound the range of the parameters so that the critical time step of the explicit time integration is not affected by the boundary treatment.

Specifically, we can optimize with respect to a subset of the free parameters treated in Section 9.2.4: (a) damping only $\mathcal{P} = \{\gamma_i\}$, (b) interatomic spring plus per-atom damping $\mathcal{P} = \{\gamma_i, \kappa_{ij}\}$, (c) mass modification plus damping $\mathcal{P} = \{\gamma_i, m_i\}$, and (d) mass, stiffness and damping modification $\mathcal{P} = \{\gamma_i, m_i, \kappa_{ij}\}$. Since the harmonic oscillators representing the motion of the atoms in the lattice are coupled, each of these parameters, namely mass, damping and stiffness, are independent. In terms of the linear system, mass scales the diagonal of the dynamical matrix, *i.e.* the left-hand side of Eqs. (9.27-9.29) reduced by mass and in matrix form, whereas interatomic spring stiffness also scales off-diagonal entries. We did not investigate the addition of harmonic well stiffness since it precludes $R^2(0) < 1$, as discussed in Section 9.2.3, nor the addition of interatomic dampers. Interatomic dampers were discarded as a candidate modification mainly due to the fact they were not available in our target 3D code LAMMPS [150] and are also relatively complex to implement due to the dependence on neighbor lists.

9.3.2 Perfectly Matched Layers

The free parameters of masses, stiffnesses, and damping constants provide considerable freedom in constructing a boundary condition. Indeed, the perfectly-matched multiscale (PMMS) method using discrete PML [113, 185] for the boundary region is a special case of this method. For the 1D chain, the PMMS boundary condition can be addressed analytically using the results of Section 9.2. Following To and Li [185], we use a so-called "damping function" d_i to define the parameters for layer i. Li *et al.* [113] present two possible boundary conditions that are local in time (and one that is non-local in time that we will not treat here). The boundary conditions differ by the choice of exponent in a scaling function used to modify the dynamics of the atoms in the boundary layer. For the simplest case, each boundary atom experiences a viscous force with damping constant $\gamma_i = m d_i$, and we refer to this PMMS model as the "linear model." In the "quadratic model" the scaling is the square of that in the linear model and one has the nonzero parameters $\lambda_i = m d_i^2$ and $\gamma_i = 2 m d_i$. The mass is not considered variable in the PMMS method, so only a single mass m is defined for the chain. Likewise, the bond stiffness is held constant so that $\kappa_{ij} = \kappa$ for all layers. Given these definitions, the reflection coefficient as a function of the damping function is given by substitution into Eq. 9.36.

Given the analytical expression for $R(\omega)$, the *ad-hoc* expressions for the damping function used in PMMS may be critically evaluated. The damping function $d_i = d\,i^2$ used in PMML in the literature is due to Collino and Tsogka (CT) [34], and has a single free parameter d. We optimize this semi-empirical damping function with respect to its free parameter for both the linear and quadratic stretching functions. An optimization is also carried out for each stretching function where no functional form is imposed on the damping function, *i.e.* each $\{d_i, i = 1...N\}$ is treated as a free parameter. The results of this optimization are shown in Fig. 9.4, and for comparison we show the optimal result for "ramped damping" where the damping constant varies linearly from the first to the last boundary atom $\gamma_i = \gamma i$. As seen in the Figure, PML outperforms ramped damping, and the simplest method with linear stretching, which corresponds to each atom being damped with no other modification, yields the overall minimum of $\overline{R^2}$. As the number of layers N increases, we observe a power-law decay in $\overline{R^2}$ with $\overline{R^2} \sim N^{-0.76}$. For comparison, the CT damping function with linear stretching decays as $N^{-0.58}$, while the quadratic stretching decays as $N^{-0.64}$ in the optimal case and as $N^{-0.54}$ using the semi-empirical damping function.

The optimal damping parameters as a function of the number of boundary layers N are shown in Fig. 9.5. Interestingly, the optimal damping constants approach $\bar{\beta}$ for the last (rightmost) boundary atom and approximately follow a linear, ramped damping profile for the rest of the boundary atoms. Alternately, it is apparent from Figure 9.5b that the locus of damping values decays with nearly power law trend from the free end to the interface. However neither approximation is sufficiently accurate to allow us to ascertain the exact functional form of the optimal damping profile. The amplitude of the reflection coefficient as a function of frequency $R^2(\omega)$ is shown in Fig. 9.6. The effect of increasing N is to introduce additional local minima into the reflection coefficient, thereby lowering the average over frequency. Also, as N increases zeros in $R(\omega)$ appear near the high frequency end of the Brillouin zone, as evidenced by the cusp-like minima above normalized frequency 1.8.

9.3.3 Wavepackets

For more complicated systems, the frequency response of the boundary can be determined via MD simulations using the multiple wave-packet method [94]. In this method, a set of wave-packets, each with a central wave-vector $\vec{k}_i$ and central frequency ω_i, propagate at their group velocities $\frac{\partial\omega}{\partial\vec{k}}|_{\vec{k}=\vec{k}_i}$. In particular for a central wave-vector $\vec{k}_i$, normal mode amplitudes $\xi_{\vec{k}\zeta}$ given by

$$\xi^i_\zeta(\vec{k}_i + (\delta k_x)\hat{x}) = A_i e^{-\eta_0^2 \delta k_x^2} e^{-i\left(\vec{k}_i + (\delta k_x)\hat{x}\right)\cdot\vec{R}_i} \tag{9.38}$$

are combined to generate a single wave-packet [169]. The subscript ζ labels the phonon branch, which is fixed for a given simulation. The arbitrary complex amplitude A_i determines the overall energy in the wave-packet, and the δk_x–dependent phase shifts yield non–zero displacements and velocities localized about $\vec{R}_i$ in real space. The spatial extent of the localization varies inversely with η_0, which is chosen so that the wave-packets do not overlap in frequency content. The initial

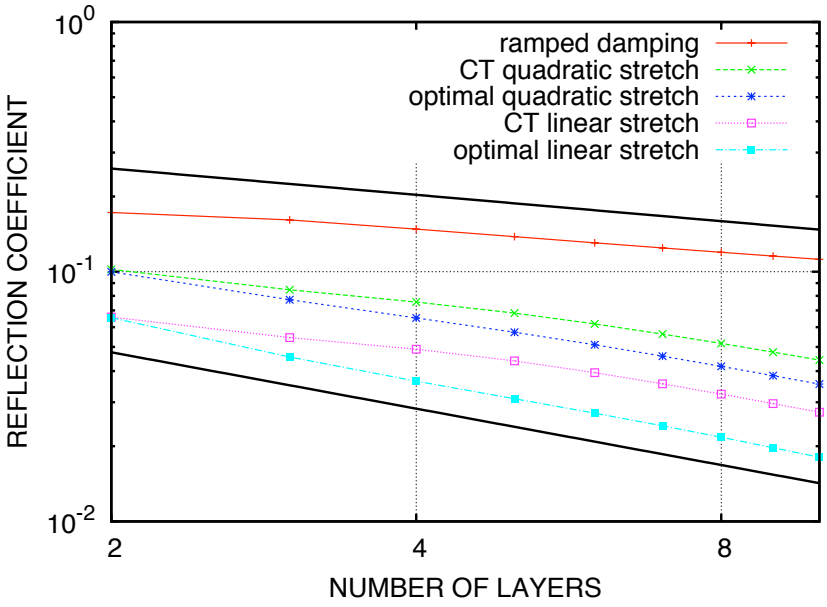

Figure 9.4. (Color online) Average reflection coefficient $\overline{R^2}$ as a function of the number of boundary layers. The curves denoted with "CT" use the one parameter damping function, while the curves denoted as "optimal" have free parameters equal to the number of layers employed. The upper black trend line has an exponent of $-\frac{1}{3}$ and the lower trend line has an exponent of $-\frac{3}{4}$.

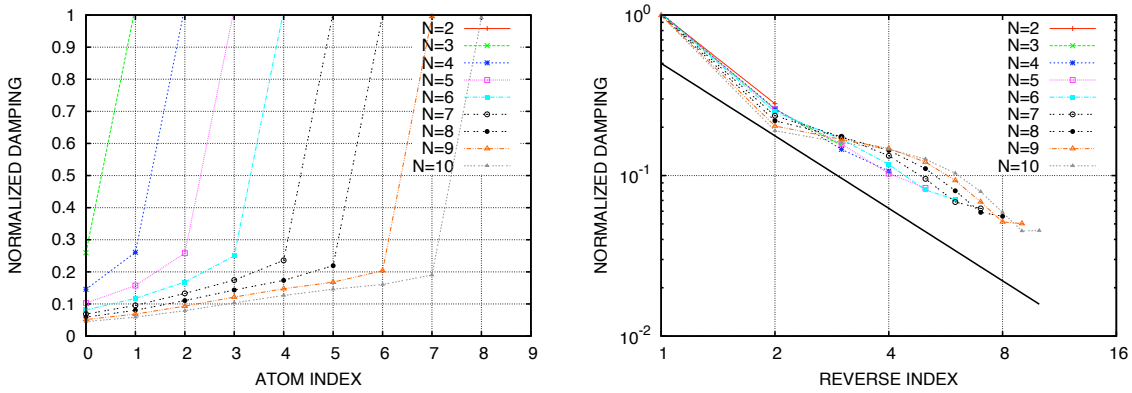

Figure 9.5. (Color online) Optimal values of the PML damping parameters as a function of the number of boundary layers, (a) counting from the interface and (b) counting from the free end. The black trend line has an exponent of $-\frac{3}{2}$. Damping values γ_i have been normalized by $\bar{\beta}$.

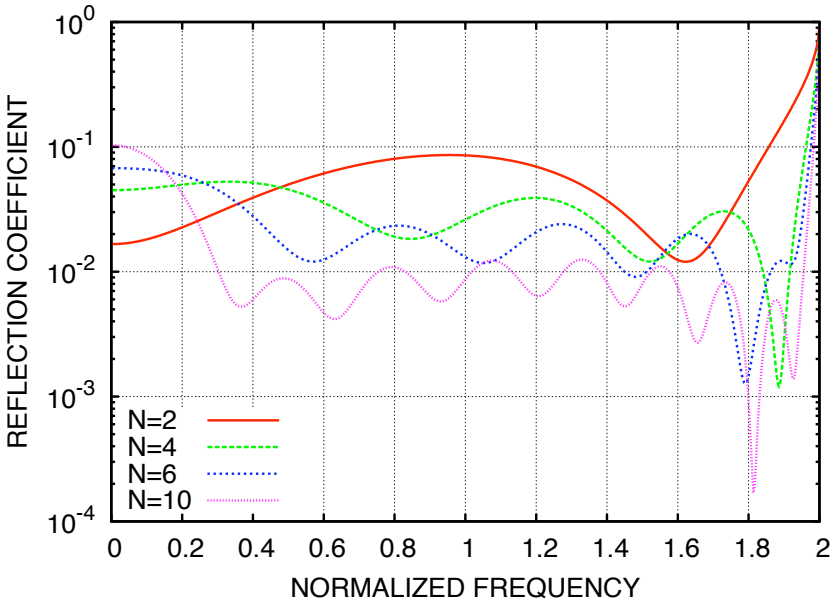

Figure 9.6. (Color online) Reflection coefficient R^2 versus frequency ω for the optimal PML solution with 2,4,6, and 10 boundary layers. Frequency has been normalized by ω_0.

atomic displacements are given by

$$\vec{u}_{il}(t=0) = \mathrm{Re}\sum_i \sum_{\vec{k},\zeta} \xi^i_\zeta(\vec{k})\vec{\varepsilon}_{i\zeta}(\vec{k})\mathrm{e}^{\mathrm{i}\vec{k}\cdot\vec{R}_l - i\omega_\zeta(\vec{k})t}\Big|_{t=0} \tag{9.39}$$

where $\vec{u}_{il}(t)$ represents the displacement for atom i in the unit cell labeled by l. The polarization vector $\vec{\varepsilon}_{i\zeta}(\vec{k})$ is determined by diagonalizing the dynamical matrix of the bulk perfect crystal, as are the frequencies $\omega_\zeta(\vec{k})$, *i.e.* they are the eigenvectors and corresponding eigenvalues. The initial velocities $\vec{v}_{il}$ are given by the time derivative of Eq. 9.39 at $t = 0$.

To determine the energy transmission coefficients as a function of branch and frequency, the final displacements and velocities after transmission through the interface are analyzed in terms of the normal modes of the perfect crystal lattice. The inverse of Eq. 9.39 is used to calculate the normal mode amplitudes $\xi_\zeta(\vec{k})$ after reflection from the boundary condition. Frequency space is binned with a bin centered on each central frequency of the multiple wave-packets. The ratio of the energy reflected by the boundary in a given frequency bin to the initial energy in the same bin yields the discrete approximation to $R^2(\omega)$ sampled over branch ζ. Given that the group velocities of the wave-packets depend on their central frequencies, care was necessary in assuring that the reflected packets all returned from the boundary within a given time window. In the following, the number of wave-packets employed will be apparent from the number of points used in the graphs of $R^2(\omega)$.

9.3.4 Optimal damped layers

As mentioned at the beginning of this section, we use 1D MD together with the wave-packet method validated with analytical results in order to have a fully tested numerical optimization algorithm for our 3D system. To this end, we use a 1000 atom chain interacting with a Lennard-Jones (LJ) potential ($\varepsilon = 1.0$ and $\sigma = 1.0$) as an efficient test case for optimizing boundary treatments of fixed type and given number of layers. It is also an analogous system in all but the non-linearity to the one analyzed in Section 9.2 and identical to the one treated in Section 9.3.2. The mass of all the atoms in the unmodified part of the chain was $m = 1.0$. The zero temperature stiffness of the chain $\kappa = 72.0$ gives a natural frequency $\omega_0 = \sqrt{72.0}$ and $\omega_0/100 \approx 0.0012$ was chosen as a suitable time-step. Wave packets with positive propagation directions were generated at the negative end of the (non-periodic) chain, please refer again to the schematic in Figure 9.2.

Optimal solutions

Figure 9.7 shows the spectral response of the optimal boundary conditions for the four types of damping layers described in Section 9.3.1, namely : (a) damping only, (b) interatomic spring plus per-atom damping, (c) mass modification plus damping, and (d) mass, stiffness and damping modification. Corresponding analytical solutions for some of the treatments are plotted for comparison and to show the behavior at the ends of the Brillouin zone. It is evident from Figure 9.7 that the

numerical scheme replicates the analytical results in an acceptable fashion given the discrete frequency sampling. The error is seen to be negligible in most cases and greatest when the function being sampled has a large derivative with respect to frequency. This trend can be attributed to the finite spread in frequencies comprising a single wave packet, and the error may be reduced by reducing this spread at the expense of a larger MD system size. For reference, the response of THK with a 2000 step history and total reflection coefficient of $\overline{R^2} = 0.0031$ is also shown. Clearly, the addition of stiffness or mass allows the optimal placement of zeros in the reflection spectrum $R^2(\omega)$ as evidenced by the cusp-like minima. As more layers are added the zeros appear to be approximately evenly spaced across the Brillouin zone which effects a collocation of the reflection response to zero at discrete frequencies. For this particular system there appears to be a one-to-one correspondence with the number of zeros and the number of layers.

Table 9.1 summarizes the actual values determined by MD and numerical optimization for the various boundary treatments considered. As observed in Section 9.3.2, the set of parameters $\{\gamma_i\}$ for the damping-only optimal solutions does not display the linearity of a ramp but there is a marked increase in γ_i from nearly zero to a value nearly equal to $\bar{\beta}$ as the layer index i increases away from the interface and toward the free end. Comparing with Sec. 9.3.2, it is evident that the fully numerical approach has independently determined the optimal damping function for the linear PML stretching function, which provides validation of the MD wave-packet approach in the present context. The monotonic trend of $\{\gamma_i\}$ can also be seen in the mass-damping and mass-spring-damping treatments but not in the mass-spring boundary condition. From the data in Table 9.1, we can see that the trend is nearly a power-law in the damping-only and damping with mass adjustment, which is consistent with the findings of Sec. 9.3.2. From Figure 9.8 we can see that, for the mass-damping treatment, as N increases the damping per layer approaches a similar power law trend to a damping alone treatment albeit with a slightly faster decay. The mass, although clearly showing a smooth decay, is not well approximated by a power law (nor an exponential).

The table shows that the optimal solution for a single layer of damping is $\gamma = \bar{\beta}$, the velocity coefficient in the approximate β form of the THK, Eq. (9.7). It is also apparent from the table that changing the mass to (approximately) half the normal mass (and the damping to approximately $\frac{3}{4}\bar{\beta}$) leads to about five times better reflection coefficient than an optimal single layer treatment with damping alone. Consequently, the optimal PMMS methods treated here are not globally optimal, *i.e.* the variation of additional free parameters such as mass leads to significantly less reflection.

Figure 9.9 shows the convergence of $\overline{R^2}$ with increasing number of layers for the four types of treatments. It is apparent that the convergence rate of spring-damping is comparable to damping alone and, similarly, mass-spring-damping is comparable to just mass-damping, albeit with better leading coefficients. This observation is corroborated by fact that the optimal modified stiffnesses are near the value κ of the unmodified part of the chain. This first result is quite surprising since spring-damping clearly affords the optimal placement of zeros in $R^2(\omega)$ that are absent in damping alone for a small number of boundary layers. Lastly, it is interesting to note that total reflection coefficient for the THK with a 2000 sample kernel is higher than the $N > 2$ layer mass-damper and mass-spring-damper solutions mainly due to the high frequency behavior which has been manipulated by placing a zero near ω_{max}.

N	$\overline{R^2}$	γ_0	m_0	$\kappa_{0,1}$	γ_1	m_1	$\kappa_{1,2}$	γ_2	m_2	$\kappa_{2,3}$	γ_3	m_3
1	0.1476	1.000	-	-	-	-	-	-	-	-	-	-
2	0.0650	0.288	-	-	1.059	-	-	-	-	-	-	-
3	0.0424	0.164	-	-	0.282	-	-	1.114	-	-	-	-
4	0.0311	0.122	-	-	0.172	-	-	0.303	-	-	1.167	-
1	0.1476	1.000	-	-	-	-	-	-	-	-	-	-
2	0.0434	0.420	-	1.167	1.121	-	-	-	-	-	-	-
3	0.0265	0.508	-	1.188	0.140	-	0.767	1.185	-	-	-	-
4	0.0189	0.376	-	1.148	0.349	-	0.896	0.129	-	0.743	1.317	-
1	0.0316	0.749	0.504	-	-	-	-	-	-	-	-	-
2	0.0068	0.066	0.856	-	0.799	0.412	-	-	-	-	-	-
3	0.0021	0.004	0.938	-	0.114	0.823	-	0.789	0.351	-	-	-
4	0.0008	0.000	0.967	-	0.028	0.927	-	0.140	0.790	-	0.772	0.307
1	0.0316	0.749	0.504	-	-	-	-	-	-	-	-	-
2	0.0040	0.168	0.893	1.086	0.823	0.392	-	-	-	-	-	-
3	0.0013	0.000	0.985	1.039	0.199	0.843	1.086	0.798	0.328	-	-	-

Table 9.1. Optimal non-dimensional parameters per layer. Masses m_i have been divided by the mass of a regular atom m, damping constants γ_i by $\bar{\beta} = \sqrt{m\kappa}$ and the stiffnesses κ_{ij} by the zero temperature stiffness of the LJ bonds κ. For comparison, a THK with a kernel of size 2000 has $\overline{R^2} = 0.0031$.

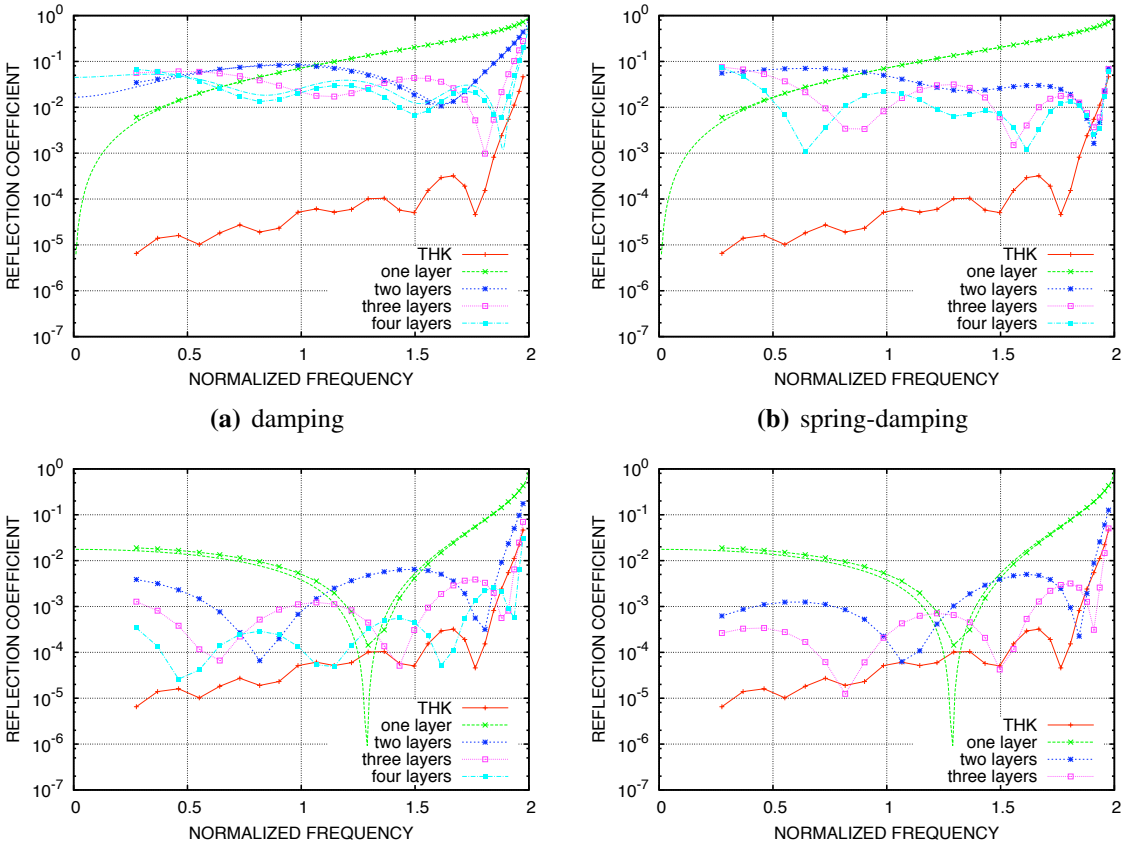

(a) damping

(b) spring-damping

(c) mass-damping

(d) mass-spring-damping

Figure 9.7. (Color online) Reflection coefficient as a function of frequency for optimal damping and stiffness compared to the THK: (a) damping only, (b) spring and damping, (c) mass and damping, and (d) mass spring and damping. The curves that extend from normalized frequency 0 to 2 were generated from the analytic solution which was optimized independently.

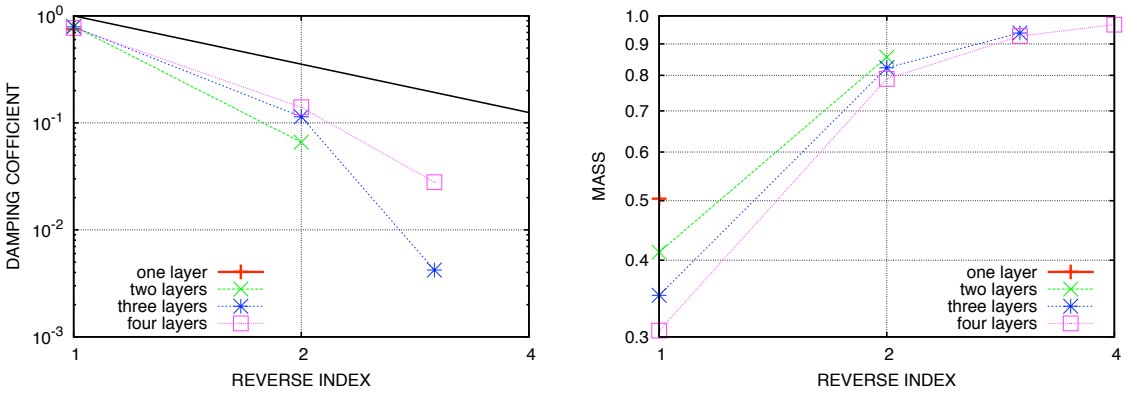

(a) damping **(b)** mass

Figure 9.8. (Color online) Optimal values of damping and mass for a mass-damper boundary layer counting from the free end. Damping values have been normalized by $\bar{\beta}$ and mass values by m. The black trend line has an exponent of $-\frac{3}{2}$ which facilitates comparison with Fig. 9.5.

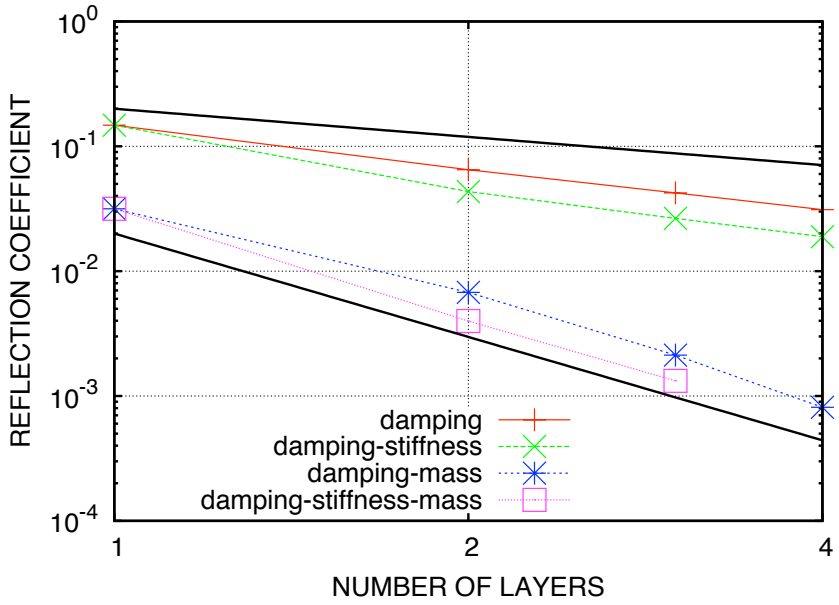

Figure 9.9. (Color online) Average reflection coefficient $\overline{R^2}$ as a function of number of layers. The upper black trend line has an exponent of -1 and the lower trend line $-\frac{11}{4}$.

Shock

We tested our tuned boundary conditions with a broadband disturbance created by a large amplitude velocity impulse in the nonlinear regime, where the amplitude of the resultant shock was roughly one hundred times that of the wave-packets. This simulation was chosen over, for example, a fracture simulation since it was much simpler to construct and analyze while at the same time replicating most of the qualitative features of an isolated fracture event. We compared the optimal $N = 3$ layer mass-spring-damper treatment (refer to Table 9.1) to a THK with a 2000 sample kernel.

Figure 9.10a shows the frequency response of the THK and optimal damping. A fast Fourier transform (FFT) of the incident velocity waveform was taken after shock developed but before it interacted with the boundary. Similarly, FFTs of the reflected waveform were taken after all the significant part of the wave form had left the vicinity of the boundary. Figure 9.10a clearly reflects the relationship $E_{reflected}(\omega) = R^2(\omega)E_{incident}(\omega)$ and that both treatments are ineffective at removing the high frequency content with nearly zero group velocities.[4] Figure 9.10b shows the temporal response of the THK and damped layers to the velocity impulse, where both are characteristic of the THK's β kernel (9.4) damped oscillations. Clearly, the exponential envelope of the layer solution falls inside the envelop of the THK. As a point of reference for this particular system, the THK treatment took 2.941 seconds to complete 100,000 time steps, compared to 0.990 seconds for the layers solution which represents approximately a factor of 3 speed-up for essentially the same performance.

9.3.5 Optimal layers in a three dimensional system

In this simulation we employ a $500 \times 1 \times 1$ unit cell silicon system with Stillinger-Weber interactions [177]. Although the long direction of the system draws comparison to the 1D chain, the potential includes three body interactions and the silicon lattice has a polyatomic basis, leading to the presence of optical branches in the phonon spectra. We consider the response of the boundary to longitudinal acoustic (LA) wave packets which have normal incidence on the $y-z$ boundary plane, *i.e.* the incident wave packets have central wave vectors of the form $(k_x 00)$, yielding a dispersion relation functionally equivalent to the 1D chain. Although the dispersion relation of the 3D system is much richer than the 1D system, we optimize $\overline{R^2}$ only over the LA branch $\omega(k_x 00)$ and note that we do not observe conversion between branches as wave packets scatter off the boundary. In this case we only consider damping or mass and damping modification per quarter cell layer, since these boundary treatments are as effective as those that modify the stiffness and required no modification of LAMMPS [150].

[4] In a finite temperature simulation these frequencies would be interpreted as thermal vibrations and arguably demand separate treatment.

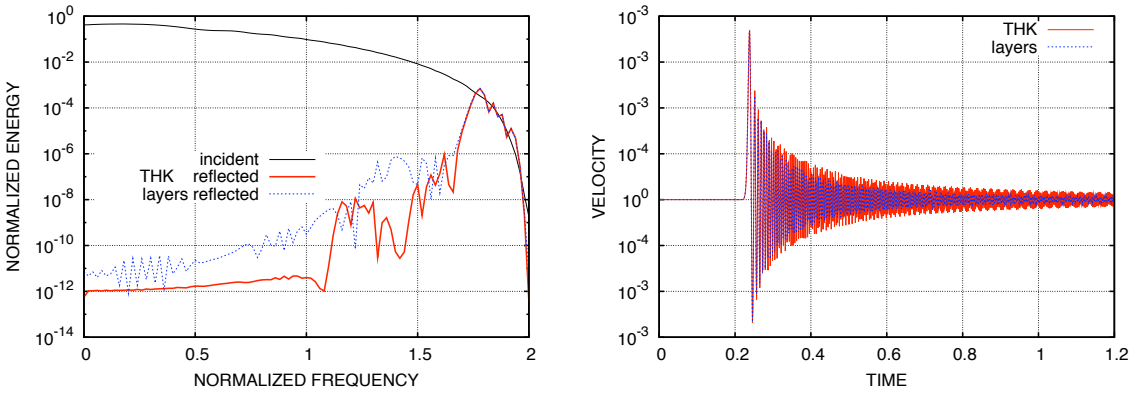

(a) frequency response **(b)** temporal response

Figure 9.10. (Color online) Shock incident and reflected energy normalized by the total energy of the incident waveform (a) and temporal response (b) for the optimal three layer mass-spring-damper boundary condition and a 2000 step long THK. Frequency has been normalized by ω_0.

Optimized layers

Figure 9.11 shows the frequency response of the optimal filters which are tuned for the full longitudinal acoustic (LA) spectrum. From Figure 9.11 it is not apparent that the reflection coefficient for any of the boundary layer treatments is approaching one at the high frequency end of the Brillouin zone as in the one-dimensional case without a basis, although this may just be an artifact of our ability to resolve frequencies at the ends of the Brillouin zone with wave-packets. Clearly, mass-damping is more effective across the full spectrum than damping alone due to adding zeros of the reflection coefficient near the middle of the Brillouin zone. This fact is demonstrated by the convergence rates shown in Figure 9.12. The mass-damping treatment is also more effective than an optimized linearly ramped damping, which has a convergence rate comparable to optimal per layer damping. However, unlike per-layer optimized treatments which tend to be more effective at lower frequencies, ramped damping is particularly effective at damping high frequencies. Table 9.2 shows that the trends in the optimal parameters are similar but not quite the same as the 1D system of Section 9.3.4 summarized in Table 9.1. In fact, the optimal damping for this system is not always monotonic with increasing layer index i. Figure 9.12 also shows that the rates of convergence for similar boundary treatments are also substantially lower in this quasi-3D setting.

Shock

As in Section 9.3.4, we generate a velocity impulse at the low x end of the system that propagates toward the damped boundary at the high x end as a test of the ability our tuned layer to handle

N	$\overline{R^2}$	γ_0	m_0	γ_1	m_1	γ_2	m_2	γ_3	m_3
1	0.0412	1.000	-	-	-	-	-	-	-
2	0.0379	0.099	-	1.020	-	-	-	-	-
3	0.0286	0.164	-	0.084	-	1.000	-	-	-
4	0.0267	0.076	-	0.168	-	0.081	-	1.006	-
1	0.0035	0.917	0.555	-	-	-	-	-	-
2	0.0015	0.073	1.031	0.936	0.575	-	-	-	-

Table 9.2. Optimal non-dimensional parameters per layer. Masses m_i have been divided by the mass of a regular atom m, damping constants γ_i by $\bar{\beta}$. For reference, the optimal ramped solution are: one layer $\gamma = 1.000$ with $\overline{R^2} = 0.0412$, two layers $\gamma = 0.8602$ with $\overline{R^2} = 0.0664$, three layers $\gamma = 0.7493$ with $\overline{R^2} = 0.0578$, four layers $\gamma = 0.7234$ with $\overline{R^2} = 0.0532$.

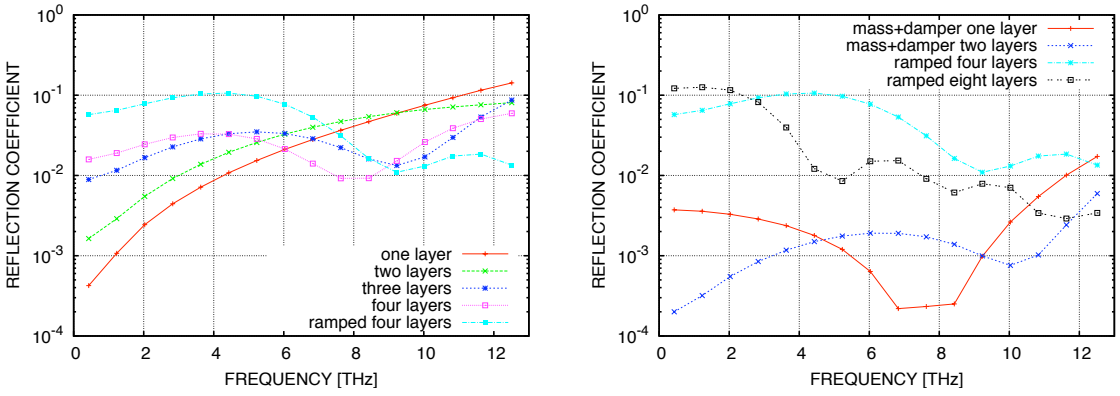

(a) damping **(b)** mass-damping

Figure 9.11. (Color online) Reflection coefficient as a function of frequency for optimal damping and mass compared to ramped. (a) damping only, (b) mass and damping.

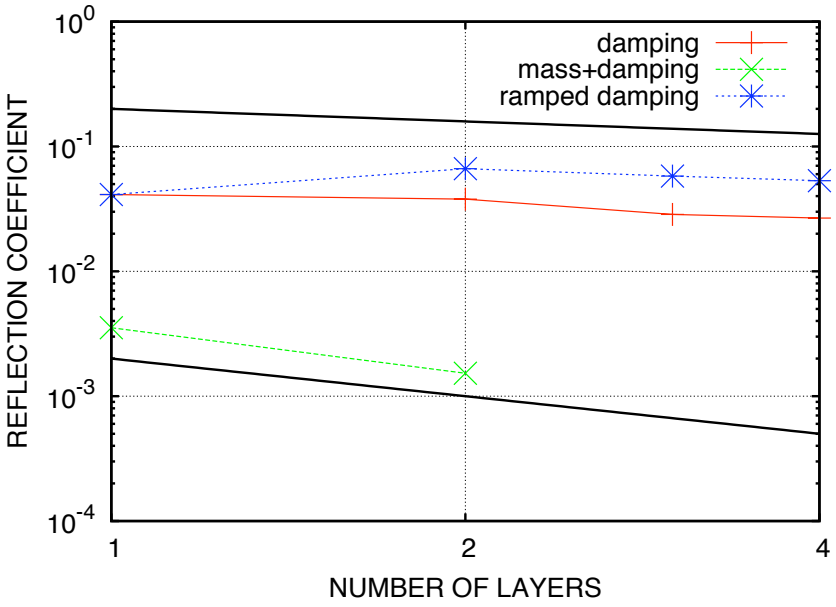

Figure 9.12. (Color online) Total reflection coefficient as a function of number of layers. Upper black trend line exponent $-\frac{1}{3}$, lower trend line -1.

a broadband disturbance characteristic of a fracture event. Figure 9.13 shows discrete Fourier transforms of the displacement waveform after it has reflected from the end for both: (a) an optimal two layer mass-damper treatment and (b) a simple fixed end condition. The fixed end clearly preserves the frequency content of the waveform whereas the damped layer decreases the main displacement components significantly. The reflection coefficient obtained from this waveform is, at least qualitatively, consistent with the frequency response obtained from the wave-packets, as shown in Figure 9.11. Both the longitudinal optical (LO) and longitudinal acoustic (LA) branches show similar behavior despite the fact that the boundary treatment was only tuned to LA wave-packets. Another observation of interest is : there are many more zeros to the reflection response than would be expected from the number of layers and the 1D results of Section 9.3.4 (In 1D we observed one zero per layer for low number of layers of mass-damping).

9.4 Discussion

We have provided analysis and a numerical methodology to create efficient, effective, nearly reflectionless boundary treatments. The methodology can be trivially extended to band-pass filtering for the low frequency / high frequency split necessary for multiscale domain decompositions. The one obvious downside to our approach is that it is apparently dependent on the particular impedance properties of the system of interest and in principle requires an optimization step to determine

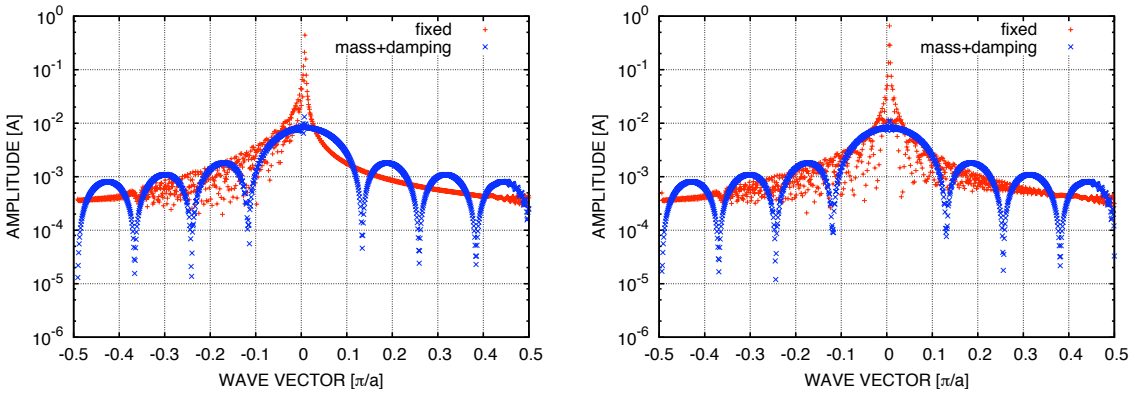

(a) LA **(b)** LO

Figure 9.13. (Color online) Shock in Si (a) longitudinal acoustic (LA) branch, (b) longitudinal optical (LO) branch. The wave vector has been normalized by π over the lattice constant $a = 5.43094 \mathring{A}$.

effective parameters for damping. However, this step may at worst be performed once for a system which is used for many different simulations, i.e. for Stillinger-Weber silicon with an (001) boundary plane. Also, effective but not optimal boundary conditions may be employed without the optimization process, by applying known parameters from one system to a similar system. Although we have not explored the sensitivity of the parameters in the optimal solutions, we conjecture that the reflection properties are not extremely sensitive to the exact values of damping, additional mass and interatomic stiffness per layer. Moreover, the clear trend in optimal PMMS solutions for the 1D system suggest a better-performing alternative to the current damping functions commonly used in that method. With that being said it seems practical to construct a useful damped boundary treatment by just understanding where added mass or stiffness places zeros in the reflection spectrum in the frequency band of interest.

One perspective that may help in this endeavor is the idea that each of the damped boundary layers governed by second order ordinary differential equations characteristic of coupled, damped harmonic oscillators which can be interpreted in the context of a sequence of second order filters. In the optimization problem, we adjust mass, damping and stiffness of the exterior layers in order to effect zeros in the transfer function defined by the reflection coefficient $R(\omega)$ in analogy with the design of a filter. Although there is no history or convolution explicitly in this type of treatment, the propagation of a waveform through a finite number of layers adds delays that are also characteristic of a sequential filter. Basic filter design relies on "zero-pole" analysis of the transfer function $R(\omega)$ which starts with a factorization of the numerator and denominator of the transfer function. We will pursue this analysis this in future work. Like all other treatments known to the authors, our analysis is done in continuous time and connects to analog filters. In future work we intend to explore the discrete time aspects of the MD reflectionless boundary condition problem.

The analogy between wave propagation and signal propagation is actually an old one going back to Brillouin [20, Chapter 3]. Specifically Brillouin states that a boundary layer with half the mass of the normal chain leads to a vanishing real part of impedance, a fact that our results corroborate, refer to Table 9.1. In the event that a full optimization is not warranted for the system of interest, a single layer of damping with half the mass and a damping coefficient of approximately the spring constant times the natural frequency should be effective as a non-reflecting boundary condition. For a multiple-layer boundary condition, the optimal linear PML may be used where the final damped atom is damped by the same value suggested for a single-layer and a ramped damping profile is used for all other layers.

We have not touched on the issues implicit in truly three dimensional configurations with waveforms with non-normal incidence, nor on lattices with more than nearest neighbor interactions. We leave these topics for future work. Extension of this work to finite temperature systems should be relatively straightforward since the creation of the damping kernel or its efficient approximation, as in this work, is independent of the generation of the random force term used in generalized Langevin treatments to maintain the temperature at the boundary. Of course the fluctuation-dissipation theorem does link the two together and establishing this connection precisely for the proposed represents the primary challenge.

Chapter 10

Publications and Presentations

This project has produced the following articles and presentations:

"A material frame approach for evaluating continuum variables in atomistic simulations", Jonathan A. Zimmerman, Reese E. Jones, and Jeremy A. Templeton, *Journal of Computational Physics*, **229**, pp. 2364-2389, 2010.

"Prediction of instabilities at the atomic scale", T J Delph and J A Zimmerman, *Modelling and Simulation in Materials Science and Engineering*, **18**, p. 045008, 2010.

"The construction and application of an atomistic **J**-integral via Hardy estimates of continuum fields", Reese E. Jones and Jonathan A. Zimmerman, *Journal of the Mechanics and Physics of Solids*, **58**, pp. 1318-1337, 2010.

"An atomistic **J**-integral at nite temperature based on Hardy estimates of continuum fields", Reese E. Jones, Jonathan A. Zimmerman, Jay Oswald, and Ted Belytschko, *Journal of Physics: Condensed Matter*, **23**, p. 015002, 2011.

"Finite Element Analysis of an Atomistically-Derived Cohesive Model for Brittle Fracture", Jeffrey T. Lloyd, Jonathan A. Zimmerman, Reese E. Jones, Xiaowang Zhou, and David L. McDowell, *Modelling and Simulation in Materials Science and Engineering*, **19**, p. 065007, 2011.

"A Material Frame Approach for Evaluating Continuum Variables Within Atomistic Simulations", Presented at the International Symposium on Plasticity, St. Thomas, U.S. Virgin Islands (January 3-8, 2009).

"Challenges of and Variations on Coupled Atomistic-Continuum Simulation", Presented at the Joint U.S. Russia Conference on Advances in Materials Science, Prague, Czech Republic (August 31 September 4, 2009).

"Extracting Continuum Variables from Atomistic Simulation", J.A. Zimmerman, Presented at Invited Seminars at Washington State University (July 9, 2009), the University of Houston (October 29, 2009) and the University of Colorado at Boulder (April 8, 2010).

"Evaluating Continuum Variables Within Atomistic Simulations: A Material Frame Approach", J.A. Zimmerman, R.E. Jones and J.A. Templeton, 2009 MRS Spring Meeting, San Francisco, CA (April 13-17, 2009).

"A Criterion for Predicting Instabilities in Nanostructures", Jonathan A. Zimmerman and Terry J.

Delph, Presented at the 16^{th} US National Congress of Theoretical and Applied Mechanics (USNCTAM 2010), State College, PA (June 27 - July 2, 2010).

“The construction of an atomistic J-integral via estimates of continuum fields”, R. Jones, J. Zimmerman, J. Oswald, and T. Belytschko, Presented at the 2011 US National Congress of Computational Mechanics (USNCCM 2011), Minneapolis, MN (July 25 - July 28, 2011).

“Application of an Atomistically-Derived Cohesive Model of Brittle Fracture”, Jeffrey T. Lloyd, Jonathan A. Zimmerman, Reese E. Jones, Xiaowang Zhou, and David L. McDowell, Presented at the 2011 US National Congress of Computational Mechanics (USNCCM 2011), Minneapolis, MN (July 25 - July 28, 2011).

References

[1] F. F. Abraham and H. Gao. How fast can cracks propagate? Phys. Rev. Lett., 84(14): 3113–3116, 2000.

[2] S. A. Adelmann and J. D. Doll. Generalized Langevin equation approach for atom-solid surface scattering: General formulation for classical scattering off harmonic solids. J. Chem. Phys., 64(6):2375–2388, 1976.

[3] N.C. Admal and E.B. Tadmor. A unified interpretation of stress in molecular systems. Journal of Elasticity, 2010. In Press.

[4] I. Alber, J. L. Bassani, M. Khantha, V. Vitek, and G. J. Wang. Grain boundaries as heterogeneous systems: atomic and continuum elastic properties. Phil. Trans. R. Soc. Lond. A, 339:555–586, 1992.

[5] M.P. Allen and D.J. Tildesley. Computer Simulation of Liquids. Clarendon Press, Oxford, 1989.

[6] T. L. Anderson. Fracture Mechanics: Fundamentals and Applications. CRC Press, Inc., Boca Raton, FL, 2^{nd} edition, 1995.

[7] P C Andia, F Costanzo, and G L Gray. A lagrangian-based continuum homogenization approach applicable to molecular dynamics simulation. International Journal of Solids and Structures, 42:6409–6432, 2005.

[8] Pedro C Andia, Francesco Costanzo, and Gary L Gray. A classical mechanics approach to the determination of the stress-strain response of particle systems. Modelling and Simulation in Materials Science and Engineeing, 14:741–757, 2006.

[9] F. Armero and J. C. Simo. A new unconditionally stable fractional step method for non-linear coupled thermomechanical problems. Int. J. Num. Meth. Eng., 35:737–766, 1992.

[10] N. W. Ashcroft and N. D. Mermin. Solid State Physics. Holt, Rinehart and Winston, New York, NY, 1976.

[11] Standard test method for linear-elastic plane-strain fracture toughness K_{Ic} of metallic materials. ASTM, E399-09 edition, 2009.

[12] T.H.K. Barron and M.L. Klein. Perturbation theory of anharmonic crystals. In G.K. Horton and A.A. Maradudin, editors, Dynamical Properties of Solids, volume 1. North Holland, Amsterdam, 1974.

[13] M. F. Beatty. Topics in finite elasticity: hyperelasticity of rubber, elastomers, and biological tissues – with examples. Appl. Mech. Rev., 40:1699–1734, 1987.

[14] R. Bellman. Introduction to Matrix Analysis. McGraw-Hill, New York, 2^{nd} edition, 1970.

[15] J.P. Bérenger. A perfectly matched layer for the absorption of electromagnetic-waves. J. Comp. Phys., 114(2):185–200, 1994.

[16] X. Blanc, C. Le Bris, F. Legoll, and C. Patz. Finite-temperature coarse-graining of one-dimensional models: Mathematical analysis and computational approaches. J. Nonlinear Sci., 20(2):241–275, 2010.

[17] M. Born. On the stability of crystals I. Proc. Cambridge Phil. Soc., 36:160–172, 1940.

[18] M. Born and K. Huang. Dynamical Theory of Crystal Lattices. Oxford University Press, Oxford, UK, 1954.

[19] Max Born. Thermodynamics of crystals and melting. J. Chem. Phys., 7:591, 1939.

[20] L. Brillouin. Wave propagation in periodic structures, 2nd ed. Dover, New York, 1953.

[21] A. S. Brown and W. A. Doolittle. The status and promise of compliant substrate technology. Appl. Surf. Sci., 166(1-4):392–398, 2000.

[22] W Cai, M de Koning, VV Bulatov, and S Yip. Minimizing boundary reflections in coupled-domain simulations. Phys. Rev. Lett., 85(15):3213–3216, 2000.

[23] H. B. Callen. Thermodynamics and an Introduction to Thermostatistics. Wiley, Hoboken, NJ, 2nd edition, 1985.

[24] Youping Chen. Local stress and heat flux in atomistic systems involving three-body forces. Journal of Chemical Physics, 124:054113, 2006.

[25] Youping Chen and James D Lee. Connecting molecular dynamics to micromorphic theory. (I). instantaneous and averaged mechanical variables. Physica A, 322:359–376, 2003.

[26] Youping Chen and James D Lee. Connecting molecular dynamics to micromorphic theory. (II). balance laws. Physica A, 322:377–392, 2003.

[27] K S Cheung and S Yip. Atomic-level stress in an inhomogeneous system. Journal of Applied Physics, 70(10):5688–5690, 1991.

[28] S. R. Choi, J. W. Hutchinson, and A. G. Evans. Delamination of multilayer thermal barrier coatings. Mech. Mater., 31:431–447, 1999.

[29] S. T. Choi and K-S Kim. Nanoscale planar field projections of atomic decohesion and slip in crystalline solids. Part I. A crack-tip cohesive zone. Phil. Mag., 87(12):1889–1919, 2007.

[30] S. T. Choi and K. S. Kim. Nanoscale planar field projections of atomic decohesion and slip in crystalline solids. part I. A crack-tip cohesive zone. Phil. Mag., 87(12):1889–1919, 2007.

[31] R J E Clausius. On a mechanical theorem applicable to heat. Philosophical Magazine, 40: 122–127, 1870.

[32] H. H. M. Cleveringa, E. Van der Giessen, and A. Needleman. A disrete dislocation analysis of mode I crack growth. J. Mech. Phys. Solids, 48:1133–1157, 2000.

[33] V. R. Coffman, J. P. Sethna, G. Heber, M. Liu, A. Ingraffea, N. P. Bailey, and E. I. Barker. A comparison of finite element and atomistic modeling of fracture. Modelling Simul. Mater. Sci. Eng., 16:065008, 2008.

[34] F Collino and C Tsogka. Application of the perfectly matched absorbing layer model to the linear elastodynamic problem in anisotropic heterogeneous media. Geophysics, 66(1): 294–307, 2001.

[35] J Cormier, J M Rickman, and T J Delph. Stress calculation in atomistic simulations of perfect and imperfect solids. Journal of Applied Physics, 89(1):99–104, 2001.

[36] F Costanzo, G L Gray, and P C Andia. On the definitions of effective stress and deformation gradient for use in md: Hill's macro-homogeneity and the virial theorem. International Journal of Engineering Science, 43:533–555, 2005.

[37] Francesco Costanzo, Gary L Gray, and Pedro C Andia. On the notion of average mechanical properties in md simulation via homogenization. Modelling and Simulation in Materials Science and Engineeing, 12:S333–S345, 2004.

[38] X. Dai, M. V. Brillhart, and P.S. Ho. Adhesion measurement for electronic packaging applications using double cantilever beam method. IEEE Trans. Compon. Pack. Technol., 23 (1):101–116, 2000.

[39] G. De Lorenzi and G. Jacucci. Adequacy of lattice dynamics for high-temperature point-defect properties. Phys. Rev. B, 33(3):1993–1996, 1986.

[40] T J Delph. Conservation laws for multibody interatomic potentials. Modelling and Simulation in Materials Science and Engineering, 13:585–594, 2005.

[41] T. J. Delph, J. A. Zimmerman, J. M. Rickman, and J. M. Kunz. A local instability criterion for solid-state defects. J. Mech. Phys. Sol., 57:67–75, 2009.

[42] L.M. Dupuy, E.B. Tadmor, R.E. Miller, and R. Phillips. Finte-temperature quasicontinuum: Molecular dynamics without all the atoms. Phys. Rev. Lett., 95(6):060202, 2005.

[43] W. E and Z. Huang. Matching conditions in atomistic-continuum modeling of materials. Phys. Rev. Lett., 87(13):135501/1–135501/4, 2001.

[44] A. T. English and C. M. Melliarsmith. Reliability and failure mechanisms of electronic materials. Annu. Rev. Mater. Sci., 8:459–495, 1978.

[45] B Engquist and A Majda. Radiation boundary-conditions for acoustic and elastic wave calculations. Comm. Pure Appl. Math., 32(3):313–357, 1979.

[46] A C Eringen. Microcontinuum Field Theories I: Foundations and Solids. Springer-Verlag, New York, 1999.

[47] A Cemal Eringen and Charles B Kafadar. Polar field theories. In A Cemal Eringen, editor, Continuum Physics: Volume IV - Polar and Nonlocal Field Theories. Academic Press, New York, 1969.

[48] J. D. Eshelby. The force on an elastic singularity. Phil. Trans. Roy. Soc. Lon. A, 244(877): 87–112, 1951.

[49] J.D. Eshelby. The elastic energy-momentum tensor. Journal of Elasticity, 5(3-4):321–35, 1975.

[50] A. G. Evans and J. W. Hutchinson. The thermomechanical integrity of thin-films and multilayers. Acta Metall. Mater., 43(7):2507–2530, 1995.

[51] M. Fago, R. L. Hayes, E. A. Carter, and M. Ortiz. Density-functional-theory-based local quasicontinuum method: Prediction of dislocation nucleation. Phys. Rev. B, 70:100102R, 2004.

[52] H. B. Fan and M. M. F. Yuen. A multi-scale approach for investigation of interfacial delamination in electronic packages. Microelectronics Reliability, 50:893–899, 2010.

[53] D. Farkas. Atomistic studies of intrinsic crack-tip plasticity. Materials Research Society Bulletin, 25(5):35–38, 2000.

[54] D. Farkas. Bulk and integranular fracture behaviour of Ni-Al. Philosophical Magazine A, 80(6):1425–1444, 2000.

[55] D. Farkas, M.J. Mehl, and D.A. Papaconstantopoulos. Lattice trapping of cracks in Fe using an interatomic potential derived from experimental data and *ab initio* calculations. In Multiscale Modeling of Materials, volume 653 of Materials Research Society Symposium Proceedings, pages Z.6.4.1–Z.6.4.6. Materials Research Society, 2001.

[56] S. M. Foiles. Evaluation of harmonic methods for calculating the free energy of defects in solids. Phys. Rev. B, 49(21):14930–14939, 1994.

[57] S M Foiles, M I Baskes, and M S Daw. Embedded-atom-method functions for the fcc metals Cu, Ag, Au, Ni, Pd, Pt, and their alloys. Phys. Rev. B, 33:7983–7991, 1986.

[58] S.M. Foiles and J.J. Hoyt. Computer Simulation of Bubble Growth in Metals Due to He. Technical Report SAND2001-0661, Sandia National Laboratories, 2001.

[59] S.M. Foiles, M.I. Baskes, and M.S. Daw. Embedded-atom-method functions for the fcc metals cu, ag, au, ni, pd, pt, and their alloys. Phys. Rev. B, 33:7983–7991, 1986.

[60] D. Frenkel and B. Smit. Understanding Molecular Simulation. Academic Press, San Diego, 2001.

[61] K. Gall, M. Horstemeyer, M. Van Schilgaarde, and M. Baskes. Atomistic simulations on the tensile debonding of an aluminum-silicon interface. J. Mech. Phys. Solids, 48(10):2183–2212, 2000.

[62] H. Gao. A theory of local limiting speed in dynamic fracture. J. Mech. Phys. Solids, 44(9): 1453–1474, 1996.

[63] L. Gomez, C. Gazza, H. Dacharry, L. Penaranda, and A. Dobry. Pressure dependence of the melting mechanism at the limit of overheating in lennard-jones crystals. Phys. Rev. B, 71: 134106, 2005.

[64] A. A. Griffith. The phenomena of rupture and flow in solids. Philos. Trans. Roy. Soc. Lond. A, 221:163–198, 1920.

[65] M. N. Guddati and S. Thirunavukkarasu. Phonon absorbing boundary conditions for molecular dynamics. J. Comput. Phys., 228(21):8112–8134, 2009. ISSN 0021-9991. doi: http://dx.doi.org/10.1016/j.jcp.2009.07.033.

[66] P M Gullett, M F Horstemeyer, M I Baskes, and H Fang. A deformation gradient tensor and strain tensors for atomistic simulations. Modelling and Simulation in Materials Science and Engineering, 16:015001, 2008.

[67] P. Gumbsch and G.E. Beltz. On the continuum versus atomistic descriptions of dislocation nucleation and cleavage in nickel. Modelling and Simulation in Materials Science and Engineering, 3:597–613, 1995.

[68] M. E. Gurtin. An Introduction to Continuum Mechanics. Academic Press, Inc., San Diego, California, 1981.

[69] M. E. Gurtin. Configurational forces as basic concepts of continuum physics. Springer, New York, NK, 2000.

[70] T. H. Hao, X. Gong, and Z. Suo. Fracture mechanics for the design of ceramic multilayer actuators. J. Mech. Phys. Solids, 44(1):23–48, 1996.

[71] R J Hardy. Formulas for determining local properties in molecular-dynamics simulations: Shock waves. Journal of Chemical Physics, 76(1):622–628, 1982.

[72] R J Hardy and A M Karo. Stress and energy flux in the vicinity of a shock front. In Shock Compression of Condensed Matter, Proceedings of the American Physical Society Topical Conference, pages 161–164. American Physical Society, 1990.

[73] R J Hardy, S Root, and D R Swanson. Continuum properties from molecular simulations. In 12th International Conference of the American-Physical-Society-Topical-Group on Shock Compression of Condfensed Matter, volume 620, Pt. 1 of AIP Conference Proceedings, pages 363–366. American Institute of Physics, 2002.

[74] R. Hill. Acceleration waves in solids. J. Mech. Phys. Sol., 10:1–16, 1962.

[75] R. Hill and F. Milstein. Principles of stability analysis of ideal crystals. Phys. Rev. B, 15: 3087, 1977.

[76] J.P. Hirth and J. Lothe. Theory of Dislocations. Krieger Publishing Company, Malabar, Florida, 2nd edition, 1982.

[77] W. G. Hoover. Canonical dynamics: Equilibrium phase-space distributions. Phys. Rev. A, 31:1695–1697, 1985.

[78] M F Horstemeyer and M I Baskes. Strain tensors at the atomic scale. In Multiscale Phenomena in Materials - Experiments and Modeling, volume 578 of Materials Research Society Symposium Proceedings, pages 15–20. Materials Research Society, 2000.

[79] M F Horstemeyer, M I Baskes, V C Prantil, J Philliber, and S Vonderheide. A multi-scale analysis of fixed-end simple shear using molecular dynamics, crystal plasticity, and a macroscopic internal state variable theory. Modelling and Simulation in Materials Science and Engineering, 11(3):265–286, 2003.

[80] J. W. Foulk III. An examination of stability in cohesive zone modeling. Comput. Meth. Appl. Mech. Eng., 199:465–470, 2010.

[81] H Inoue, Y Akahoshi, and S Harada. A fracture parameter for molecular-dynamics method. Intl. J. Frac., 66(4):R77–R81, 1994.

[82] H Inoue, Y Akahoshi, and S Harada. A molecular dynamics-aided fracture mechanics parameter and its application to a tensile problem. Computational Mechanics, 16:217–222, 1995.

[83] J H Irving and J G Kirkwood. The statistical mechanical theory of transport processes. iv. the equations of hydrodynamics. Journal of Chemical Physics, 18(6):817–829, 1950.

[84] E P Isoardi, N L Allan, and G D Barrera. Quasiharmonic free energy and derivatives for many-body interactions: The embedded atom method. Phys. Rev. B, 69(2), 2004.

[85] H. Jiang, Y. Huang, and K.C. Hwang. A finite–temperature continuum theory based on interatomic potentials. J. Eng. Mat. Tech., 127:408, 2005.

[86] Y Jin and F G Yuan. Atomistic simualtions of j-integral in 2d graphene nanosystems. Journal of Nanoscience and Nanotechnology, 5:2099–2107, 2005.

[87] Z.H. Jin, P. Gumbsch, K. Lu, and E. Ma. Melting mechanisms at the limit of superheating. Phys. Rev. Lett., 87:055703, 2001.

[88] R. E. Jones and J. A. Zimmerman. The construction and application of an atomistic j-integral via hardy estimates of continuum fields. Journal of the Mechanics and Physics of Solids, 2010. In Press.

[89] H. Kanzaki. Point defects in face-centered cubic lattice - I. Distortion around defects. Phys. Chem. Solids, 2:24–36, 1957.

[90] E. G. Karpov, H. S. Park, and Wing Kam Liu. A phonon heat bath approach for the atomistic and multiscale simulation of solids. Int. J. Num. Meth. Eng., 70(3):351–378, 2007.

[91] EG Karpov, GJ Wagner, and WK Liu. A Green's function approach to deriving non-reflecting boundary conditions in molecular dynamics simulations. Int. J. Num. Meth. Engin., 62(9):1250–1262, 2005.

[92] C L Kelchner, S J Plimpton, and J C Hamilton. Dislocation nucleation and defect structure during surface indentation. Physical Review B, 58(17):11085–11088, 1998.

[93] R. Khare, S.L. Mielke, J.T. Paci, Sulin Zhang, R. Ballarini, G.C. Schatz, and T. Belytschko. Coupled quantum mechanical/molecular mechanical modeling of the fracture of defective carbon nanotubes and graphene sheets. Physical Review B (Condensed Matter and Materials Physics), 75(7):75412–1–12, 2007.

[94] C. J. Kimmer and R. E. Jones. Continuum constitutive models from analytical free energies. J. Phys.-Cond. Mat., 19(32), 2007.

[95] J. G. Kirkwood. Statistical mechanics of fluid mixtures. Journal of Chemical Physics, 3: 300–313, 1935.

[96] T. Kitamura, Y. Umeno, and R. Fushino. Instability criterion of inhomogeneous atomic system. Mat. Sci. Eng. A, 379:229–233, 2004.

[97] T. Kitamura, Y. Umeno, and N. Tsuji. Analytical evaluation of unstable deformation criterion of atomic structure and its application to nanostructure. Comp. Mat. Sci., 29:499–510, 2004.

[98] C. Kittel and H. Kroemer. Thermal Physics. W.H. Freeman and Company, New York, 2nd edition, 1980.

[99] P. Klein and H. Gao. Crack nucleation and growth as strain localization in a virtual-bond continuum. Eng. Frac. Mech., 61(1):21–48, 1998.

[100] P.A. Klein and J.A. Zimmerman. Coupled atomistic-continuum simulations using arbitrary overlapping domains. Journal of Computational Physics, 213:86–116, 2006.

[101] K. Kolluri, M. R. Gungor, and D. Maroudas. Molecular dynamics simulations of martensitic fcc-to-hcp phase transformations in strained ultrathin metallic films. Phys. Rev. B, 78: 195408, 2008.

[102] H. Krull and H. Yuan. Suggestions to the cohesive traction-separation law from atomistic simulations. Eng. Fract. Mech., 78(3):525–533, 2011.

[103] A-Y Kuo and P. C. Riccardella. Path-independent line integrals for steady-state, two-dimensional thermoelasticity. Intl. J. Fracture, 35:71–79, 1987.

[104] D.J. Lacks and R.C. Shukla. Molecular dynamics simulations of the effects of truncation of the Taylor expansion of the potential energy on the thermodynamic properties of a crystal. J. Chem. Phys., 105:4185, 1996.

[105] P Lancaster and K Salkauskas. Surfaces generated by moving least squares methods. Mathematics of Computation, 37:141–158, 1981.

[106] A. Latapie and D. Farkas. Molecular dynamics investigation of the fracture behavior of nanocrystaline α-Fe. Phys. Rev. B, 69:134110, 2004.

[107] B. Lawn. Fracture of Brittle Solids. Cambridge University Press, Cambridge, UK, 2nd edition, 1993.

[108] B. Lebouvier, A. Hairie, F. Hairie, G. Nouet, and E. Paumier. Calculation of the free energy of different configurations of $\{001\}$ $\sigma = 13$ grain boundary in Silicon by the quasiharmonic method. Solid State Phen., 37-38:85–90, 1994.

[109] J.E. Lennard-Jones. The determination of molecular fields I. From the variation of the viscosity of a gas with temperature. Proceedings of the Royal Society (of London), 106A: 441, 1924.

[110] J.E. Lennard-Jones. The determination of molecular fields II. From the equation of state of a gas. Proceedings of the Royal Society (of London), 106A:463, 1924.

[111] R. LeSar, R. Najafabadi, and D.J. Srolovitz. Finite–temperature defect properties from free-energy minimization. Phys. Rev. Lett., 63:624–627, 1989.

[112] D. Li, Y. Wu, R. Fan, P. Yang, and A. Majumdar. Thermal conductivity of si/sige superlattice nanowires. Appl. Phys. Lett., 83(15):3186–3188, 2003.

[113] SF Li, XH Liu, A Agrawal, and AC To. Perfectly matched multiscale simulations for discrete lattice systems: Extension to multiple dimensions. Phys. Rev. B, 74(4):045418, 2006.

[114] X. Li and W. E. Variational boundary conditions for molecular dynamics simulations. Comm. Comp. Phys., 1(1):136–176, 2006.

[115] Bin Liu and Xinming Qiu. How to Compute the Atomic Stress Objectively? J. Comp. Theo. Nanosci., 6(5):1081–1089, 2009.

[116] J. Lu and L. Zhang. An atomistic instability condition and applications. J. Mech. Mat. Struct., 1:633–648, 2006.

[117] J. Lu and L. Zhang. Analysis of failure of single-wall carbon nanotubes. Comp. Mat. Sci., 35:432–441, 2006.

[118] J F Lutsko. Stress and elastic constants in anisotropic solids: Molecular dynamics techniques. Journal of Applied Physics, 64(3):1152–1154, 1988.

[119] L E Malvern. Introduction to the Mechanics of a Continuous Medium. John Wiley & Sons, Inc., New York, 1969.

[120] M. Marder and S. Gross. Origin of crack tip instabilities. J. Mech. Phys. Solids, 43(1):1–48, 1995.

[121] J. Marian, G. Venturini, B. L. Hansen, J. Knap, M. Ortiz, and G. H. Campbell. Finite-temperature extension of the quasicontinuum method using langevin dynamics: entropy losses and analysis of errors. Modell. Sim. Matls. Sci. Eng., 18(1), 2010.

[122] J. M. Martin. Many-body forces in metals and the brugger elastic constants. J. Phys. C, 8: 2837–2857, 1975.

[123] G. A. Maugin. Material Inhomogeneities in Elasticity. CRC press, Boca Raton, FL, 1993.

[124] G. A. Maugin. Material forces: Concepts and applications. Appl. Mech. Rev., 48(5):213–245, 1995.

[125] J C Maxwell. On reciprocal figures, frames and diagrams of forces. Transactions of the Royal Society Edinborough, XXVI:1–43, 1870.

[126] J C Maxwell. Van der waals on the continuity of the gaseous and liquid states. Nature, pages 477–480, 1874.

[127] D. A. McQuarrie. Statistical Mechanics. Harper and Row, New York, NY, 1976.

[128] R. E. Miller and D. Rodney. On the nonlocal nature of dislocation nucleation during nano-indendation. J. Mech. Phys. Sol., 56:1203–1223, 2008.

[129] F. Milstein and R. Hill. Theoretical properties of cubic crystals at arbitrary pressure—III. Stability. J. Mech. Phys. Sol., 27:255–279, 1979.

[130] F. Milstein and K. Huang. Theory of the response of an FCC crystal to [110] uniaxial loading. Phys. Rev. B, 18:2529–2541, 1978.

[131] Y Mishin, M R Sorensen, and A F Voter. Calculation of point-defect entropy in metals. Phil. Mag. A, 81(11):2591–2612, 2001.

[132] H Mori. Transport collective motion and Brownian motion. Prog. Theo. Phys., 33(3):423–, 1965.

[133] H Mori. A continued-fraction representation of time-correlation functions. Prog. Theo. Phys., 34(3):399–, 1965.

[134] J. R. Morris and X. Song. The melting lines of model systems calculated fro coexistence simulations. J. Chem. Phys., 116:9352, 2002.

[135] J. W. Morris, Jr. and C. R. Krenn. The internal stability of an elastic solid. Phil. Mag. A, 80 (12):2827–2840, 2000.

[136] A Ian Murdoch. On the microscopic interpretation of stress and couple stress. Journal of Elasticity, 71:105–131, 2003.

[137] A Ian Murdoch. Some primitive concepts in continuum mechanics regarded in terms of objective space-time molecular averaging: The key role played by inertial observers. Journal of Elasticity, 84:69–97, 2006.

[138] A Ian Murdoch. A critique of atomistic definitions of the stress tensor. Journal of Elasticity, 88:113–140, 2007.

[139] R. Najafabadi and D.J. Srolovitz. Evalution of the accuracy of the free-energy minimization method. Phys. Rev. B, 52:9229, 1995.

[140] K. Nakatani, A. Nakatani, and H. Kitagawa. Molecular dynamics study on fracture mechanisms of Fe-amorphous metal (J integral near mode I crack tip). In H. Kitagawa, T. Jr. Aihara, and Y. Kawazoe, editors, Mesoscopic dynamics of fracture. Computational materials design, pages 88–98. Springer, Berlin, Germany, 1998.

[141] K Nakatani, A Nakatani, Y Sugiyama, and H Kitagawa. Molecular dynamics study on mechanical properties and fracture in amorphous metal. AIAA Journal, 38(4):695–701, 2000.

[142] V. N. Nikolaevskii. Contour invariants in the theory of fracture of thermoelastic bodies. PMM U.S.S.R. - J. Appl. Math. Mech., 45(3):428–431, 1984.

[143] W Noll. Die herleitung der grundgleichungen der thermomechanik der kontinua aus der statistischen mechanik. Journal of Rational Mechanics and Analysis, 4(5):627–646, 1955.

[144] A. A. Pacheco and R. C. Batra. Instabiliites in shear and simple shear deformations of gold crystals. J. Mech. Phys. Sol., 56:3116–6143, 2008.

[145] J. Panova and D. Farkas. Atomistic simulation of fracture in TiAl. Metallurgical and Materials Transactions A, 29A:951–955, 1998.

[146] H. S. Park and J. A. Zimmerman. Modeling inelasticity and failure in gold namowires. Phys. Rev. B, 72:054106, 2005.

[147] M. J. Park, A. Leyland, and A. Matthews. Corrosion performance of layered coatings produced by physical vapor-deposition. Surf. Coat. Technol., 43-44(1-3):481–492, 1990.

[148] A. Paskin, D.K. Som, and G.J. Dienes. Computer simulation of crack propagation: lattice trapping. Journal of Physics - Part C: Solid State Physics, 14:L171–L176, 1981.

[149] M. Peach and J. S. Koehler. The forces exerted on dislocations and the stress fields produced by them. Phys. Rev., 80(3):436–439, 1950.

[150] S. Plimpton. Fast parallel algorithms for short-range molecular dynamics. J. Comput. Phys., 117(1):1–19, 1995. See also http://lammps.sandia.gov.

[151] M. Rahman and T. Michelitsch. A note on the formula for the Rayleigh wave speed. Wave Motion, 43:272–276, 2006.

[152] J. R. Rice. A path independent integral and approximate analysis of strain concentration by notches and cracks. J. Appl. Mech., 35(2):379–386, 1968.

[153] J. R. Rice. Dislocation nucleation from a crack tip: an analysis based on the Peierls concept. J. Mech. Phys. Solids, 40(2):239–271, 1992.

[154] J. M. Rickman and R. LeSar. Free-energy calculations in materials research. Annual Reviews of Materials Research, 32:195–217, 2002.

[155] J. M. Rickman and D. J. Srolovitz. A modified–local–harmonic model for solids. Phil. Mag. A, 67:1081–1094, 1993.

[156] J. M. Rickman, R. Najafabadi, L. Zhao, and D. J. Srolovitz. Finite–temperature properties of perfect crystals and defects from zero–temperature energy minimization. J. Phys.: Condens. Matter, 4:4923–4934, 1992.

[157] J.M. Rickman and D.J. Srolovitz. A modified–local–harmonic model for solids. Phil. Mag. A, 67:1081–1094, 1993.

[158] O Rodríguez de la Fuente, J A Zimmerman, M A González, J de la Figuera, J C Hamilton, W W Pai, and J M Rojo. Dislocation emission around nanoindentations on a (001) fcc metal surface studied by scanning tunneling microscopy and atomistic simulations. Physical Review Letters, 88(3):036101, 2002.

[159] S Root, R J Hardy, and D R Swanson. Continuum predictions from molecular dynamics simulations: Shock waves. Journal of Chemical Physics, 118(7):3161–3165, 2003.

[160] J. H. Rose, J. R. Smith, F. Guinea, and J. Ferrante. Universal features of the equation of state of metals. Phys. Rev. B, 29:2963–2969, 1984.

[161] J. Rottler and M.O. Robbins. Molecular simulations of deformation and failure in bonds formed by glass polymer adhesives. J. Adhesion Sci. Technol., 17(3):369–381, 2003.

[162] J. Rottler, S. Barsky, and M.O. Robbins. Cracks and crazes: On calculating the macroscopic fracture energy of glassy polymers from molecular simulations. Phys. Rev. Lett., 89(14): 148304–4, 2002.

[163] J S Rowlinson and B Widom. Molecular Theory of Capillarity. Clarendon Press, Oxford, 1989.

[164] R.E. Rudd and J.Q. Broughton. Coarse–grained molecular dynamics: Nonlinear finite elements and finite temperature. Phys. Rev. B, 72:144104, 2005.

[165] S. Ryu, K. Kang, and W. Cai. Entropic effect on the rate of dislocation nucleation. Proc. Natl. Acad. Sci., 108(13):5174–5178, 2011.

[166] E. Saether, V. Yamakov, and E. H. Glaessgen. An embedded statistical method for coupling molecular dynamics and finite element analysis. Int. J. Numer. Meth. Engng., 78:1292–1319, 2009.

[167] Sandia National Laboratories. ParaDyn, Sandia National Laboratories: http://www.cs.sandia.gov/∼sjplimp/, 2009.

[168] Sandia National Laboratories. LAMMPS : Large-scale Atom/Molecular Massively Parallel Simulator, Sandia National Laboratories: http://lammps.sandia.gov, 2011.

[169] P. K. Schelling, S. R. Phillpot, and P. Keblinski. Kapitza conductance and phonon scattering at grain boundaries by simulation. J. Appl. Phys., 95:6082, 2004.

[170] P Schofield and J R Henderson. Statistical mechanics of inhomogeneous fluids. Proceedings of the Royal Society of London A, 379:231–240, 1982.

[171] V. Shastry and D. Farkas. Molecular statics simulation of fracture in α-iron. Modelling and Simulation in Materials Science and Engineering, 4:473–492, 1996.

[172] Simulia, Inc. Abaqus/Standard, version 6.8. http://www.simulia.com/products/abaqus_fea.html, 2010.

[173] J.E. Sinclair. Atomistic computer simulation of brittle-fracture extension and closure. Journal of Physics - Part C: Solid State Physics, 5:L271–L274, 1972.

[174] J. Song, W. A. Curtin, T. K. Bhandakkar, and H. J. Gao. Dislocation shielding and crack tip decohesion at the atomic scale. Acta Mater., 58:5933–5940, 2010.

[175] D.E. Spearot, K.I. Jacob, and D.L. McDowell. Non-local separation constitutive laws for interfaces and their relation to nanoscale simulations. Mech. Mater., 36:825–847, 2004.

[176] C. Steinbrüchel. The scattering of phonons of arbitrary wavelength at a solid-solid interface: Model calculation and applications. Zeitschrift fur Physik B Condensed Matter, 24:293–299, 1976.

[177] F H Stillinger and T A Weber. Computer simulation of local order in condensed phases of silicon. Physical Review B, 31:5262–5271, 1985.

[178] Arun K. Subramaniyan and C. T. Sun. Continuum interpretation of virial stress in molecular simulations. Int. J. Solid Struct., 45(14-15):4340–4346, 2008.

[179] A. P. Sutton. Temperature–dependent interatomic forces. Phil. Mag. A, 60(2):147–159, 1989.

[180] J Tersoff. New empirical model for the structural properties of silicon. Physical Review Letters, 56:632–635, 1986.

[181] J Tersoff. Modeling solid-state chemistry: interatomic potentials for multicomponent systems. Physical Review B, 39:R5566–R5568, 1989.

[182] V. K. Tewary. Green-function method for lattice statics. Adv. Phys., 22:757–810, 1973.

[183] V. K. Tewary and R. Thomson. Lattice statics of interfaces and interfacial cracks in bimaterial solids. J. Mater. Res., 7:1018–1028, 1992.

[184] R. Thomson, C. Hsieh, and V. Rana. Lattice trapping of fracture cracks. Journal of Applied Physics, 42(8):3154–3160, 1971.

[185] A.C. To and Shaofan Li. Perfectly matched multiscale simulations. Phys. Rev. B, 72(3): 35414–1–8, 2005.

[186] Albert C. To, Wing Kam Liu, and Adrian Kopacz. A finite temperature continuum theory based on interatomic potential in crystalline solids. Comput. Mech., 42(4):531–541, 2008.

[187] C. Truesdell and W. Noll. The non-linear field theories of mechanics. Encyclopedia of Physics, III, 1965. S. Flugge, ed.

[188] D H Tsai. The virial theorem and stress calculation in molecular dynamics. J. Chem. Phys., 70:1375–1382, 1979.

[189] J-L Tsai, S-H Tzeng, and Y-J Tzou. Characterizing the fracture parameters of a graphene sheet using atomistic simulation and continuum mechanics. International Journal of Solids and Structures, 47(3-4):503–509, 2010.

[190] V. Tvergaard and J.W. Hutchinson. The influence of plasticity on mixed mode interface toughness. J. Mech. Phys. Solids, 41(6):1119–1135, 1993.

[191] R. Guido Della Valle and E. Venuti. Quasiharmonic lattice dynamics and molecular dynamics calculations for the Lennard–Jones solids. Phys. Rev. B, 58:206–212, 1998.

[192] E. Van der Giessen and A. Needleman. Dislocation plasticity effects on interfacial fracture. Interface Science, 11:291–301, 2003.

[193] K. J. VanVliet, J. Li, T. Zhu, S. Yip, and S. Suresh. Quantifying the early stages of plasticity through nanoscale experiments and simulations. Phys. Rev. B, 67:104105, 2003.

[194] A Voter. Embedded atom method potentials for seven FCC metals: Ni, Pd, Pt, Cu, Ag, Au and Al. Technical Report LA-UR 93-3901, Los Alamos National Laboratories, 1993.

[195] A. F Voter and S. P. Chen. Accurate interatomic potentials for Ni, Al and Ni_3Al. volume 82 of MRS Symposium Proc., pages 175–180, 1987.

[196] G. J. Wagner and W. K. Liu. Coupling of atomistics and continuum simulations using a bridging scale decomposition. J. Comp. Phys., 190:249–274, 2003.

[197] G J Wagner, R E Jones, J A Templeton, and Parks M L. An atomistic-to-continuum coupling method for heat transfer in solids. Computer Methods in Applied Mechanics and Engineering, 197:3351–3365, 2008.

[198] D. C. Wallace. Thermodynamics of Crystals. Dover, Mineola, NY, 1972.

[199] J. Wang, J. Li, S. Yip, S. Phillpot, and D. Wolf. Mechanical instabilities of homogeneous crystals. Phys. Rev. B, 52:12627–12635, 1995.

[200] Edmund B Webb III, Jonathan A Zimmerman, and Steven C Seel. Reconsideration of continuum thermomechanical quantities in atomic scale simulations. Mathematics and Mechanics of Solids, 13:221–266, 2008.

[201] J H Weiner. Statistical Mechanics of Elasticity. Dover Publications, Inc., Mineola, New York, 2^{nd} edition, 2002.

[202] S. Xiao and W. Yang. Temperature–related Cauchy–Born rule for multiscale modeling of crystalline solids. J. Comp. Phys., 36, 2006.

[203] X.-P. Xu and A. Needleman. Void nucleation by inclusion debonding in a crystal matrix. Modelling Simul. Mater. Sci. Eng., 1:111–132, 1993.

[204] X.-P. Xu and A. Needleman. Numerical simulations of fast crack growth in brittle solids. J. Mech. Phys. Solids, 42(9):1397–1434, 1994.

[205] YG Xu, K Behdinan, and Z Fawaz. Molecular dynamics calculation of the J-integral fracture criterion for nano-sized crystals. Intl. J. Frac., 130(2):571–582, 2004.

[206] V. Yamakov, E. Saether, D. R. Phillips, and E. H. Glaessgen. Molecular-dynamics simulation-based cohesive zone representation of intergranular fracture process in aluminum. J. Mech. Phys. Sol., 54:1899–1928, 2006.

[207] V. Yamakov, E. Saether, and E. H. Glaessgen. Multiscale modeling of intergranular fracture in aluminum: constitutive relation for interface debonding. J. Mater. Sci., 43:7488–7494, 2008.

[208] B. Yang, J. L. Liu, K. L. Wang, and G. Chen. Measurements of anisotropic thermoelectric properties in superlattices. Appl. Phys. Lett., 80(10):1758–1760, 2002.

[209] B. Yang, W. L. Liu, J. L. Liu, K. L. Wang, and G. Chen. Measurements of anisotropic thermoelectric properties in superlattices. Appl. Phys. Lett., 81(19):3588–3590, 2002.

[210] JZ Yang and XT Li. Comparative study of boundary conditions for molecular dynamics simulations of solids at low temperature. Phys. Rev. B, 73(22):224111, 2006.

[211] H. H. Yu and J. W. Hutchinson. Influence of substrate compliance on buckling delamination of thin films. Inter. J. Fract., 113(1):39–55, 2002.

[212] L. Zhao, R. Najafabadi, and D. J. Srolovitz. Finite-temperature vacancy formation thermodynamics - local harmonic and quasi-harmonic studies. Modell. Sim. Matls. Sci. Eng., 1(4): 539–551, 1993.

[213] M Zhou. A new look at the atomic level virial stress: on continuum-molecular system equivalence. Proceedings of the Royal Society of London, Series A, 459:2347–2392, 2003.

[214] M Zhou. Thermomechanical continuum representation of atomistic deformation at arbitrary size scales. Proceedings of the Royal Society of London, Series A, 461:3437–3472, 2006.

[215] M Zhou and D L McDowell. Equivalent continuum for dynamically deforming atomistic particle systems. Philosophical Magazine A, 82:2547–2574, 2002.

[216] X. W. Zhou and H. N. G. Wadley. A potential for simulating the atomic assembly of cubic elements. Comp. Mater. Sci., 39:340–348, 2007.

[217] X. W. Zhou and H. N. G. Wadley. A potential for simulating the atomic assembly of ab compounds. Comp. Mater. Sci., 39:541–551, 2007.

[218] X. W. Zhou, J. A. Zimmerman, E. D. Reedy Jr., and N. R. Moody. Molecular dynamics simulation based cohesive surface representation of mixed mode fracture. Mechanics of Materials, 40:832–845, 2008.

[219] X. W. Zhou, N. R. Moody, R. E. Jones, J. A. Zimmerman, and E. D. Reedy. Molecular-dynamics-based cohesive zone law for brittle interfacial fracture under mixed loading conditions: Effects of elastic constant mismatch. Acta Materialia, 57:4671–4686, 2009.

[220] T. Zhu, W. Yang, and T. Guo. Quasi-cleavage processes driven by dislocation pileups. Acta Mater., 44(8):3049–3058, 1996.

[221] J A Zimmerman. Continuum and Atomistic Modeling of Dislocation Nucleation at Crystal Surface Ledges. PhD thesis, Stanford University, 2000.

[222] J A Zimmerman, E B Webb III, J J Hoyt, R E Jones, P A Klein, and D J Bammann. Calculation of stress in atomistic simulation. Modelling and Simulation in Materials Science and Engineering, 12:S319–S332, 2004.

[223] Jonathan A Zimmerman, Douglas J Bammann, and Huajian Gao. Deformation gradients for continuum mechanical analysis of atomistic simulations. International Journal of Solids and Structures, 46:238–253, 2009.

[224] Jonathan A. Zimmerman, Reese E. Jones, and Jeremy A. Templeton. A material frame approach for evaluating continuum variables in atomistic simulations. J. Comp. Phys., 229 (6):2364–2389, 2010.

[225] N. Zotov and A. Ludwig. First-principles calculations of the elastic constants of fe-pt alloys. Intermetallics, 16(1):113–118, 2008.

DISTRIBUTION:

1 C.J. Kimmer, Indiana University Southeast, New Albany, IN 47150
1 T.J. Delph, Lehigh University, Bethlehem, PA 18015
1 J. Oswald, Northwestern University, Evanston, IL 60208
1 T. Belytschko, Northwestern University, Evanston, IL 60208
1 J.T. Lloyd, Georgia Institute of Technology, Atlanta, GA 30332
1 D.L. McDowell, Georgia Institute of Technology, Atlanta, GA 30332

1 MS 0110 J.M. Phillips, 1200
1 MS 0110 J.E. Johannes, 1220
1 MS 0346 R.S. Chambers, 1524
1 MS 0346 E.D. Reedy Jr., 1526
1 MS 0372 H.E. Fang, 1524
1 MS 0372 N.L. Breivik, 1524
1 MS 0372 E. Corona, 1524
1 MS 0372 J.M. Emery, 1524
1 MS 0372 J. Gorman, 1524
1 MS 0372 S. Grange, 1524
1 MS 0372 K.W. Gwinn, 1524
1 MS 0372 T.D. Hinnerichs, 1524
1 MS 0372 J. Koester, 1524
1 MS 0372 C.S. Lo, 1524
1 MS 0372 K.N. Long, 1524
1 MS 0372 K.E. Metzinger, 1524
1 MS 0372 S.T. Montgomery, 1524
1 MS 0372 W.M. Scherzinger, 1524
1 MS 0372 G.W. Wellman, 1525
1 MS 0376 J.M. Emery, 1524
1 MS 0384 D.B. Dimos, 1500
1 MS 0429 S.K. Griffiths, 2100
1 MS 0431 J. Pott, 0231
1 MS 0824 J.E. Bishop, 1525
1 MS 0824 J.V. Cox, 1524
1 MS 0824 J.M. Redmond, 1525
1 MS 0824 L.W. Tuttle, 1525
1 MS 0847 P.J. Wilson, 1520
1 MS 0885 T.L. Aselage, 1810
1 MS 0887 C.L. Jones Adkins, 1800
1 MS 0889 C.C. Battaile, 1814
1 MS 0889 T.E. Buchheit, 1814

1 MS 0889 M.E. Chandross, 1814
1 MS 0889 J.M. Lane, 1814
1 MS 1070 C.C Wong, 1526
1 MS 1070 J.E. Massad, 1526
1 MS 1070 H. Sumali, 1526
1 MS 1185 A.S. Gullerud, 5417
1 MS 1314 S. Cheng, 1814
1 MS 1315 A. Dickey, 1814
1 MS 1315 M.J. Stevens, 1814
1 MS 1322 J.B. Aidun, 1425
1 MS 1322 R.P. Muller, 1425
1 MS 1322 A.P. Thompson, 1425
1 MS 1411 A. Dickey, 1814
1 MS 1411 S.M. Foiles, 1814
1 MS 1411 A.L. Frischknecht, 1814
1 MS 1411 L.M. Hall, 1814
1 MS 1411 E.A. Holm, 1814
1 MS 1411 E. Homer, 1814
1 MS 1411 J.D. Madison, 1814
1 MS 1411 G.J. Tucker, 1814
1 MS 1411 F.B. Van Swol, 1814
1 MS 1411 C.R. Weinberger, 1814
1 MS 1411 R.A. Roach, 1823
1 MS 9001 R.H. Stulen, 8000
1 MS 9042 J.W. Foulk III, 8246
1 MS 9042 C.D. Moen, 8246
1 MS 9042 J. Ostien, 8246
1 MS 9042 T.J. Vogler, 8246
1 MS 9042 A.A. Brown, 8249
1 MS 9042 M.L. Chiesa, 8249
1 MS 9042 A. Lindblad, 8249
1 MS 9042 M. Yip, 8249
1 MS 9153 R.G. Miller, 8200
1 MS 9154 W.P. Ballard, 8200
1 MS 9154 M.E. Gonzales, 8240
1 MS 9402 D. Ward, 8131
1 MS 9403 B.M. Wong, 8223
1 MS 9403 L.M. Hale, 8246
1 MS 9404 T.E. Felter, 8222
1 MS 9404 H.F. Jackson, 8222
1 MS 9404 N.R. Moody, 8222

1	MS	9404	C.W. San Marchi, 8222
1	MS	9404	B.P. Somerday, 8222
1	MS	9404	H. Jin, 8246
1	MS	9404	R.E. Jones, 8246
1	MS	9404	A. Mota, 8246
1	MS	9404	X. Zhou, 8246
1	MS	9404	J.A. Zimmerman, 8246
1	MS	9409	N.R. Fornaciari, 8365
1	MS	9409	J. Deng, 8365
1	MS	9409	L. Crowl Erickson, 8365
1	MS	9409	P.E. Gharagozloo, 8365
1	MS	9409	J.A. Templeton, 8365
1	MS	9409	G.J. Wagner, 8365
1	MS	9161	R.H. Nilson, 8365
1	MS	9161	C.R. Tewell, 8222
1	MS	0899	Technical Library, 8944 (electronic copy)

Sandia National Laboratories